DETERMINATION OF HARTEBEESTHOEK RADIO ASTRONOMY OBSERVATORY (HARTRAO) VLBI ANTENNA PARAMETERS AND LOCAL TIE FOR IMPROVED GLOBAL REFERENCE FRAMES

by

Marisa Nickola

Submitted in partial fulfilment of the requirements for the degree
Doctor of Philosophy in Geoinformatics

in the

Department of Geography, Geoinformatics & Meteorology
Faculty of Natural and Agricultural Sciences

UNIVERSITY OF PRETORIA

August 2022

SUMMARY

DETERMINATION OF HARTEBEESTHOEK RADIO ASTRONOMY OBSERVATORY (HARTRAO) VLBI ANTENNA PARAMETERS AND LOCAL TIE FOR IMPROVED GLOBAL REFERENCE FRAMES

by

Marisa Nickola

Supervisor: Prof. W.L. Combrinck

Department of Geology, Geoinformatics and Meteorology, University of Pretoria

Co-supervisor: Dr A. de Witt

Hartebeesthoek Radio Astronomy Observatory (HartRAO)

Degree: Doctor of Philosophy in Geoinformatics

Keywords: very long baseline interferometry, station-specific errors, meteorological data, antenna calibration, antenna pointing, antenna axis offset, local tie

Astrometric and geodetic Very Long Baseline Interferometry (VLBI) at the Hartebeesthoek Radio Astronomy Observatory (HartRAO) contribute to the realisation of the International Celestial Reference Frame (ICRF) and determination of the International Terrestrial Reference Frame (ITRF). Geodetic VLBI also provides the reference point of the HartRAO 26 m antenna used in co-location of the 15 m antenna and three other space geodetic techniques and also as reference datum for South Africa's national surveying system. The VLBI Global Observing System (VGOS) is currently being introduced worldwide to form part of the Global Geodetic Observing System (GGOS). The HartRAO VGOS antenna will soon become operational and will have to be tied accurately to the 26 m and 15 m antennas. If HartRAO is to contribute to GGOS and continue participating

in ICRF realisation and ITRF determination, GGOS requirements of 1 mm accuracy and 0.1 mm/yr stability on global baselines will have to be met, and station-specific errors degrading the accuracy of astrometric/geodetic VLBI results will have to be minimised. Station-specific errors addressed in this study relate to meteorological data, antenna calibration and pointing, antenna axis offset (AO) and the local tie between the 26 m and 15 m antennas.

The quality of HartRAO meteorological data used in VLBI and single-dish analysis was investigated by comparing it with meteorological data from a Global Navigation Satellite System (GNSS) station and a test installation. The opacity correction applied to 22 GHz observations on the 26 m antenna was investigated by comparison of precipitable water vapour (PWV) values calculated from HartRAO and GNSS meteorological data as well as Suominet integrated PWV. The 26 m antenna is one of only a few antennas capable of CRF realisation in the Southern Hemisphere at 22 GHz, the latter requiring accurate pointing. The 26 m antenna's pointing performance and gain at 22 GHz were determined from gain calibration observations. A possible correlation between heating of the antenna structure and degraded pointing was investigated.

The AO of the HartRAO 26 m and 15 m antennas and the baseline length between the antennas were estimated in geodetic VLBI data analysis with the Vienna VLBI and Satellite Software (VieVS) for comparison with the more accurate ground survey values to determine whether it is possible to estimate these values with the required accuracy in VLBI analysis. Possible seasonal variation of the AO and baseline length were also investigated. The antenna axis offset altitude correction (AOAC), which accounts for the effect of the orientation of the equatorially mounted 26 m antenna on the tropospheric path delay, was simulated in VieVS to study its effect on the estimated AO of the 26 m antenna. Short baseline (SBL) experiments between the two HartRAO antennas were also scheduled and analysed with VieVS in order to estimate the local tie vector between the antennas more accurately and to determine whether the GGOS goal of 1 mm accuracy is achievable on such a short baseline at the very least. The results for baseline components and baseline length were compared with the corresponding results from the most recent ground survey.

RESEARCH OUTPUTS

The first of the following contributions has been accepted for publication in a peer-reviewed journal and the remainder were published in proceedings, as part of this work or related to it:

1. **Nickola, M.**, Krásná, H., de Witt, A., Combrinck, W.L. and Böhm, J. (Accepted). Hartebeesthoek Radio Astronomy Observatory (HartRAO) antenna axis offset determined by geodetic VLBI analysis and ground survey. *South African Journal of Geomatics.*
2. **Nickola, M.**, de Witt, A., Botha, R. C. and van Zyl, P. 2021. HartRAO weather data. In *Proceedings of the 25th European VLBI Group for Geodesy and Astrometry Working Meeting*, Haas, R. (ed.), 100-104.
3. **Nickola, M.**, de Witt, A., Schartner, M., Botha, R.C., Jacobs, C.S., Gruber, J., Krásná, H., Combrinck, W.L. and Böhm, J. 2019. HartRAO site tie measurements: VLBI and ground survey. In *Proceedings of the 24th European VLBI Group for Geodesy and Astrometry Working Meeting*, Haas, R., Garcia-Espada, S. and López Fernández, J.A. (eds.), 162-166.
4. **Nickola, M.**, de Witt, A., Krásná, H., Combrinck, W.L., Böhm, J., Schartner, M. and Jacobs, C.S. 2018. Antenna parameters and local tie between HartRAO 15 m and 26 m antennas. In *IVS 2018 General Meeting Proceedings*, Armstrong, K.L., Baver, K.D. and Behrend, D. (eds.), 155-159.
5. **Nickola, M.**, de Witt, A., Krásná, H., Jacobs, C.S., Combrinck, W.L. and Böhm, J. 2017. HartRAO antenna axis offset and its effect on troposphere modelling and antenna coordinates. In *Proceedings of the 23rd European VLBI Group for Geodesy and Astrometry Working Meeting*, Haas, R. and Elgered, G. (eds.), 148-151.

DECLARATION

I declare that the dissertation/thesis, which I hereby submit for the degree Doctor of Philosophy in the Faculty of Natural and Agricultural Sciences at the University of Pretoria, is my own work and has not previously been submitted by me for a degree at this or any other tertiary institution.

ETHICS STATEMENT

The author, whose name appears on the title page of this dissertation/thesis, has obtained, for the research described in this work, the applicable research ethics approval.

The author declares that s/he has observed the ethical standards required in terms of the University of Pretoria's Code of Ethics for Researchers and the Policy guidelines for responsible research.

Marisa Nickola
August 2022

ACKNOWLEDGEMENTS

This thesis is the result of research I carried out at the Hartebeesthoek Radio Astronomy Observatory under the Space Geodesy and Fundamental Astronomy programmes while registered at the University of Pretoria.

I would like to thank the following people and institutions for their assistance with the research:

- Prof Ludwig Combrinck and Dr Aletha de Witt
- Prof Johannes Böhm, Dr Hana Krásná, Dr Matthias Schartner and Dr Jakob Gruber from the Technical University of Vienna (TUW), Austria as well as Dr David Mayer and Dr Andreas Hellerschmied (both previously from TUW) and Chris Jacobs from the Jet Propulsion Laboratory, California Institute of Technology/NASA, USA
- Dr Roelf Botha, Dr Jonathan Quick, Dr George Nicolson, Philip Mey, Pieter Stronkhorst and all other staff of the Hartebeesthoek Radio Astronomy Observatory (HartRAO)
- Prof Serena Coetzee and the administrative staff of the Geology, Geoinformatics and Meteorology Department at the University of Pretoria (UP) as well as the late Prof George Djolov
- The IVS family all over the world, from Ny Ålesund to Syowa, from Kokee Park to Warkworth
- Glenda Coetzer, Leslie Nickola and my parents, Golda and Tewie Muller

TABLE OF CONTENTS

LIST OF TABLES

LIST OF FIGURES

LIST OF ABBREVIATIONS AND ACRONYMS

ADC	: analogue-to-digital converter
AGGO	: Argentinean-German Geodetic Observatory
AO	: axis offset
AOAC	: axis offset altitude correction
ASI	: Agenzia Spaziale Italiana / Centro di Geodesia Spaziale
az-el	: azimuth-elevation
BBC	: base-band channel
BKG	: Germany's Federal Agency for Cartography and Geodesy
BL	: baseline length
CIMO	: Commission for Instruments and Methods of Observation
CONT	: continuous (VLBI campaign)
CPWLO	: continuous piece-wise linear offset
CRF	: celestial reference frame
DBBC	: digital base-band converter
Dec	: declination
DGFI	: German Geodetic Research Institute
DiFX	: distributed FX-architecture software
DLR	: German Aerospace Centre
DORIS	: Doppler Orbitography and Radiopositioning Integrated by Satellite
DOY	: day-of-year
DPFU	: degrees-per-flux-unit
DRAN	: Drift scan Reduction and ANalysis program
EOP	: Earth Orientation Parameters
ESA	: European Space Agency
FEA	: finite element analysis
FEM	: finite element model
FS	: Field System
Gaia	: ESA's Astrometric mission
GGOS	: Global Geodetic Observing System
GNSS	: Global Navigation Satellite System

GPS : Global Positioning System
GSFC : Goddard Space Flight Center
GUI : graphical user interface
HA : hour angle
HartRAO : Hartebeesthoek Radio Astronomy Observatory
HOPS : Haystack Observatory Postprocessing System
HPBW : half-power beamwidth
HPN : half-power North
HPS : half-power South
IAG : International Association of Geodesy
IAU : International Astronomical Union
ICRF : International Celestial Reference Frame
IERS : International Earth Rotation Service
IGN : National Institute of Geographic and Forest Information (France)
IGS : International GNSS Service
ITRF : International Terrestrial Reference Frame
IVS : International VLBI Service for Geodesy and Astrometry
IVSCC : IVS Combination Centre
JPL : NASA Jet Propulsion Laboratory
KAT : Karoo Array Telescope
LCP : left circular polarisation
LLR : Lunar Laser Ranging
LNA : low noise amplifier
LO : local oscillator
LOD : length of day
NASA : National Aeronautics and Space Administration
NGS : National Geodetic Survey
NMA : Norwegian Mapping Authority
NNR : no-net-rotation
NNT : no-net-translation
OSO : Onsala Space Observatory
OTT : Onsala twin telescopes
PSS : point source sensitivity

PWV : precipitable water vapour
RA : right ascension
RCP : right circular polarisation
RF : radio frequency
RFI : radio-frequency interference
RINEX : Receiver INdependent EXchange format
Roscosmos : Russian Federal Space Agency
SBL : short baseline
SEFD : system-equivalent flux density
SLR : Satellite Laser Ranging
S/LLR : Satellite/Lunar Laser Ranging
SNR : signal-to-noise ratio
Ta : antenna temperature
Ta On : on-source antenna temperature
Tcal : noise diode calibration temperature
TPI : total power integration
TRF : terrestrial reference frame
Tsys : system temperature
TUWIEN : Technical University of Vienna
UAS : unmanned aerial system
UT : Universal Time
UTC : Coordinated Universal Time
VGOS : VLBI Global Observing System
vgosDB : VGOS database
VieVS : Vienna VLBI and Satellite Software
VLBA : Very Long Baseline Array
VLBI : Very Long Baseline Interferometry
VMF : Vienna mapping function
WMO : World Meteorological Organization
wx : weather information
ZHD : zenith hydrostatic delay
ZWD : zenith wet delay

CHAPTER 1 INTRODUCTION

Geodesy is the scientific discipline that deals with the measurement and representation of the Earth, its gravitational field, and other geodynamic phenomena, such as crustal and polar motion as well as ocean tides (Committee on the National Requirements for Precision Geodetic Infrastructure, Committee on Seismology and Geodynamics and National Research Council, 2010). The Hartebeesthoek Radio Astronomy Observatory (HartRAO) performs both radio astronomy and space geodetic research. The HartRAO Space Geodesy Programme focuses on the four major space geodesy techniques – Very Long Baseline Interferometry (VLBI), Global Navigation Satellite Systems (GNSS), Satellite Laser Ranging (SLR) and Doppler Orbitography and Radiopositioning Integrated by Satellite (DORIS).

The HartRAO 26 m and 15 m radio antennas regularly participate in astrometric and geodetic VLBI observations at the standard S/X dual-band frequencies (2.3/8.4 GHz) and at the higher K-band frequency (22 GHz). Astrometric VLBI provides the International Celestial Reference Frame (ICRF), realised through the measurements of positions of extragalactic reference radio sources. These same radio sources are observed in geodetic VLBI to determine station positions and velocities, tectonic plate motion, Earth orientation parameters (EOP) and tropospheric parameters, amongst others, as well as to contribute to the realisation of the International Terrestrial Reference Frame (ITRF) (Schuh and Böhm, 2013). According to Combrinck *et al*. (2015), geodetic VLBI at HartRAO also provides "… absolute reference points and ties between collocated geodetic instruments to act as constraints in global solutions using different techniques and as control point for the geodetic survey system of SA (Hartebeesthoek94 datum)".

As part of the Global Geodetic Observing System (GGOS), which aims to combine the major geodetic techniques into a single highly accurate observing system (Gross, Beutler and Plag, 2009), a next generation VLBI system, the VLBI Global Observing System (VGOS), is currently being introduced worldwide. In accordance with GGOS requirements, VGOS aims at an order of magnitude improvement in astrometric and geodetic precision. Global baselines need to be accurate to 1 mm and stable to 0.1 mm/yr (Niell *et al*., 2006). The VGOS antennas are often co-located with legacy antennas, allowing VGOS antennas to be linked to the legacy antennas and for the antennas to be accurately tied together (Petrachenko, 2015). The legacy antennas provide long stable time series, in some instances more than 20 years of VLBI observations (Petrachenko *et al*., 2009). However, while VGOS observations will take over geodetic VLBI observations, operations of legacy antennas will be maintained for astronomical VLBI and for some time also for ICRF astrometric VLBI observations which require high sensitivity. According to Petrachenko *et al*. (2014) "… more Southern Hemisphere stations are required to support ICRF definition, and, in general, a more uniform global distribution of stations is required to support ITRF definition." A VGOS antenna has been installed at HartRAO recently and is expected to become operational in due course.

Astrometric VLBI enables the determination of precise and accurate positions of extragalactic radio sources at the sub-milliarcsecond (nanoradian) level. These same radio sources are observed in geodetic VLBI to determine positions and velocities of radio antennas in the global network at an accuracy level of several millimetres. The positions and velocities can be inferred from the difference in the arrival time of a radio signal emitted by an extragalactic radio source, such as a quasar (quasi-stellar object), at the different antennas forming the baseline. This geometric delay, together with additional contributions which affect the propagation of the radio wave or that change its path, constitute the primary observable of astrometric/geodetic VLBI, the group delay. This delay observable is corrupted by various station-specific structural, instrumental and propagation error sources, degrading the accuracy of astrometric and geodetic VLBI results (Schuh and Behrend, 2012).

In this study, station-based effects that could be corrupting the VLBI delay observable at HartRAO were identified and, where possible, investigated in order to discover possible courses of action to eliminate or at least mitigate these sources of error with a view to meeting GGOS accuracy requirements and improving ITRF and ICRF realisation. Whilst it was not possible to investigate certain of the error budget contributors that were identified, such as an outdated pointing model, failing bearing and aged encoders, antenna structural effects (particularly gravitational and thermal deformation), unstable antenna foundations and instrumental effects (specifically the stability of the hydrogen maser clock and phase and cable calibration systems), error sources related to degraded meteorological surface data, antenna calibration and pointing, antenna axis offset (AO) and the local tie between the antennas were investigated in this study. Although the current study focused on the HartRAO 26 m and 15 m antennas, it is anticipated that findings from this study may also be utilised towards improved VGOS operations at HartRAO in the near future.

1.1 RATIONALE

At HartRAO, the long-term monitoring of Earth processes with four space geodesy techniques from the very same site provides a trusted long-term data record. The co-location of the four space geodetic techniques makes HartRAO one of only twelve fiducial geodetic sites worldwide (GGOS, 2022). It is also the only fundamental station in Africa. Located in Africa as well as the Southern Hemisphere, the station location is of strategic importance in the worldwide space geodesy network (Combrinck and Combrink, 2004). HartRAO is not only a key fiducial station in the global geodetic network, but also provides the absolute reference point for South Africa's survey system (Combrinck *et al*., 2015). The HartRAO 26 m antenna's VLBI reference point serves as the reference point for the co-location of the 15 m antenna, GNSS and SLR stations on-site and as reference datum for South Africa's surveying system.

HartRAO is one of only a few astrometric and geodetic VLBI capable stations in the Southern Hemisphere and the only such station on the African continent and is one of only two stations in the South that participate in ICRF observations at 22 GHz. HartRAO is soon to become one of only two stations in the Southern Hemisphere with VGOS

operability. The HartRAO station is thus an indispensable contributor to improving the ITRF and ICRF in the South. To meet GGOS accuracy requirements and contribute to improved ITRF and ICRF realisation, HartRAO has to deliver accurate astrometric and geodetic VLBI results. It is therefore essential that local station-based error sources corrupting the VLBI delay observable be identified and minimised. Error budget contributors of particular concern at HartRAO currently and detailed in this study, are as follows: (1) degraded meteorological surface data used to determine tropospheric delay, antenna thermal deformation as well as atmospheric absorption (opacity) and refraction corrections; (2) inaccurate antenna pointing in the 22 GHz frequency band used for celestial reference frame (CRF) work; (3) a possible change in antenna AO due to an antenna bearing replacement; and (4) the need for accurate local ties between the HartRAO antennas, especially with a view to tying the VLBI reference point of the VGOS antenna to that of the 26 m legacy antenna. These station-based errors (as well as the other error budget contributors mentioned in the previous section that were also identified but not investigated in this study), ultimately lead to less accurate station and source coordinates and thus also to less accurate measurements of local and global baselines and therefore need to be addressed.

1.2 PROBLEM STATEMENT

In order to meet the more stringent accuracy requirements set by GGOS and towards improved ITRF and ICRF realisation, station-specific error sources corrupting the VLBI delay observable and degrading VLBI results need to be identified, and their error contributions reduced. Such error sources therefore need to be investigated and mitigated at HartRAO. Suspected degraded *in situ* meteorological surface data at HartRAO could lead to inaccurate modelling of the troposphere and antenna thermal deformation, as well as to inaccurate atmospheric absorption and refraction corrections being applied. The pointing of the HartRAO 26 m antenna is not sufficiently accurate, especially not for higher-frequency observations at 22 GHz. Degraded declination pointing and differential heating of the support structure could be contributing factors. With a critical main-shaft bearing failure that occurred in 2008 and with yet another bearing failure imminent, the life expectancy of the HartRAO 26 m legacy antenna is uncertain. The bearing failure could

have caused a change in AO. The 15 m antenna is also exhibiting signs of reaching the end of its lifetime. The VGOS antenna urgently needs to be tied to these older antennas, especially to the 26 m legacy antenna with its long stable time series. It will be possible to isolate problems to a specific antenna by observing with all three antennas simultaneously. The VGOS antenna is, however, not operational yet. This allows for time to identify, investigate and mitigate error sources connected to the station and antennas before conducting local tie observations with the VGOS antenna included. It is also necessary to accurately determine the AO of the antennas. The most accurate method of determining the AO and the local tie is by terrestrial survey, but these surveys are not performed on a regular basis, with the last co-location survey having been conducted at HartRAO in 2014. It is therefore important to establish whether it is possible to estimate the AO and local tie in VLBI analysis with the required accuracy in order that AO and local tie observations may be pursued as soon as the VGOS antenna does become operational.

Research questions are as follows:

1. HartRAO error sources:
   a) Which station-specific error sources are possibly corrupting the VLBI delay observable at HartRAO?
   b) What course of action is required to reduce the size of the errors involved?
2. HartRAO weather data:
   a) What is the state of HartRAO's *in situ* meteorological surface sensors?
   b) What is the quality of meteorological data used in astrometric/geodetic VLBI and single-dish calibration?
3. Antenna calibration and pointing:
   a) What is the HartRAO 26 m antenna's pointing performance and gain at 22 GHz?
   b) Could there be a correlation between degraded declination pointing and differential heating of the support structure?
4. Antenna AO:
   a) What are the values estimated in VLBI analysis for the AO of the HartRAO 26 m antenna, before bearing failure and after bearing replacement, as well as for the 15 m antenna?

b) How do these estimated values compare with values measured in the most recent ground survey?
c) Are GGOS accuracy goals achievable with the estimation of AO in VLBI analysis?
d) Is there any seasonal variation in AO?
e) What is the effect of the antenna axis offset altitude correction (AOAC) on the estimated AO of the HartRAO 26- antenna?

5. Baseline length and local tie:
   a) What is the value estimated in VLBI analysis for the baseline length between the HartRAO 26 m and 15 m antennas?
   b) How does the estimated value compare with the value measured in the most recent ground survey?
   c) Are GGOS accuracy goals achievable with the estimation of the local tie and baseline length in VLBI analysis?
   d) Is there any seasonal variation detectable in baseline length?

1.3 AIMS AND OBJECTIVES

The aim of this study is to identify and investigate HartRAO station-specific error sources corrupting the VLBI delay observable and to establish a possible course of action to mitigate the adverse effect of such error sources towards meeting GGOS accuracy requirements and improving ITRF and ICRF realisation. It is also aimed at determining whether the AO of the HartRAO 26 m and 15 m antennas as well as the local tie between the two antennas can be estimated in VLBI analysis in accordance with GGOS accuracy requirements.

Objective 1:

Identify HartRAO station-specific error sources corrupting the VLBI delay observable, and suggest possible courses of action to mitigate them.

Objective 2:

Assess the state of of HartRAO *in situ* meteorological surface sensors and the quality of their data used for astrometric and geodetic VLBI and single-dish calibration purposes.

Objective 3:

Investigate the HartRAO 26 m antenna's pointing performance and gain at 22 GHz.

Objective 4:

Estimate the AO for the HartRAO 26 m and 15 m antennas in VLBI analysis and compare these values with those measured in the 2014 co-location survey. Investigate possible seasonal variation.

Objective 5:

Estimate the baseline length between the HartRAO 26 m and 15 m antennas in VLBI analysis and compare these values with that obtained in the 2014 co-location survey. Investigate possible seasonal variations in baseline length between the antennas.

1.4 METHODOLOGY

The methodology followed to answer the Research questions and to meet the Aims and Objectives of this study is to, firstly, in *Chapter 3*, and in line with *Research question 1* and *Objective 1*, identify HartRAO station-specific error sources considered to be of the highest priority for mitigation by the HartRAO station itself or by the wider International VLBI Service for Geodesy and Astrometry (IVS) community. The error sources to be investigated in this study are identified by consulting with HartRAO Engineering, Operations and astronomers as well as by taking IVS requirements into consideration. Each of the these sources of error are then investigated individually in subsequent chapters as follows:

- HartRAO surface meteorological data as possible source of error are investigated in *Chapter 4*, in line with *Research question 2* and *Objective 2*, by comparing the quality of historical and current meteorological data from HartRAO meteorological sensors used to provide *in-situ* measurements of ambient temperature, relative humidity and barometric pressure, and its possible degradation over time, with long-term meteorological data provided by a Paroscientific MET3 unit of the HartRAO GNSS reference station as well as with short-term data from a new Paroscientific MET4 test installation. The opacity correction applied in gain calibration observations of the

HartRAO 26 m antenna at 22 GHz is also investigated by comparing the effect of making use of precipitable water vapour (PWV) values calculated from surface measurements of temperature and humidity provided by the HartRAO meteorological sensors and the GNSS MET3 unit as well as estimated values of PWV integrated along the Global Positioning System (GPS) signal path as provided by Suominet for the HartRAO GNSS station.

- Pointing performance and gain of the HartRAO 26 m antenna at 22 GHz as possible source of error are investigated in *Chapter 5*, in line with *Research question 3* and *Objective 3*, by conducting and analysing gain calibration observations with Jupiter as calibrator source. A possible correlation between differential heating of the support structure and an observed deterioration of the pointing during the gain curve observations is investigated by comparing differential heating of temperature sensors mounted on the antenna support structure during the gain curve observations with the time range over which the pointing correction degraded.
- In *Chapter 6*, *Research question 4* and *Objective 4* are addressed by estimating antenna AO values for the HartRAO 26 m and 15 m antennas in geodetic VLBI data analysis and comparing it with the more accurate ground survey values, including those of the most recent co-location survey performed in 2014, in order to establish whether the AO can be estimated in VLBI analysis with the sub-millimetre accuracy required for meeting the GGOS/VGOS goal of 1 mm accuracy in station coordinates. Possible seasonal variation of the AO is investigated by dividing sessions into seasonal groupings for VLBI analysis. The effect of the AO altitude correction (AOAC) on the estimated AO and coordinates of the equatorially mounted HartRAO 26 m antenna is also investigated by simulation as well as by VLBI session analysis.
- In *Chapter 7*, *Research question 5* and *Objective 5* are addressed by estimating the baseline length between the HartRAO 26 m and 15 m antennas in VLBI analysis of local short baseline (SBL) experiments and comparing it with the more accurate 2014 co-location survey value, in order to establish whether it is possible to estimate the local short baseline in VLBI analysis with the sub-millimetre accuracy required for meeting the GGOS/VGOS goal of 1 mm accuracy on global baselines. Possible seasonal variation of the baseline length is investigated by dividing sessions into seasonal groupings for VLBI analysis.

1.5 STUDY CONTRIBUTIONS

This study contributes to understanding and, where possible, identifying solutions to mitigate error sources afflicting astrometric and geodetic VLBI operations at HartRAO, a core geodetic site and indispensable contributor to improving global reference frames in the South. Identifying and understanding station-specific error sources at HartRAO contribute to improved VLBI modelling and analysis. Mitigation of error sources or improved modelling would contribute to more accurate high-precision global astrometric and geodetic VLBI measurements. Based on the results from this study, stations should, for example, upgrade or replace outdated or faulty meteorological equipment. Analysts can adjust values, strategies and methods and/or update models accordingly, for example, updating HartRAO's *a priori* antenna AO values or taking unreliable meteorological surface data at HartRAO into account. The study also contributes towards ensuring HartRAO's continued relevance in global networks for astrometric and geodetic VLBI and especially towards preparing for VGOS operations at HartRAO and being able to meet the stringent GGOS accuracy requirements.

The study contributes specifically to understanding the:

1) accuracy and continuity requirements of meteorological surface data for astrometric and geodetic VLBI;
2) pointing accuracy required of the 26 m antenna at 22 GHz for continued contribution to CRF realisation in the South;
3) the impact of bearing replacement on antenna AO and the possibility of estimating AO with the required accuracy in the VLBI analysis; and
4) requirements for dedicated short baseline sessions to accurately tie the VGOS antenna to the 26 m legacy antenna and of estimating baseline length in VLBI analysis with the required accuracy.

The various investigations motivate for:

1) the upgrade / replacement of HartRAO meteorological sensors / equipment;

2) an update of the pointing (and incorporated) models, preceded by bearing replacement and installation of high-resolution encoders, as well as for comprehensive amplitude calibration of the 26 m antenna; and
3) implementation of an automated total station for continuous measurement of the VLBI reference points, AO and local tie to: (a) investigate possible correlation of AO with various station-based effects towards improvement of the AO model used in the VLBI analysis; (b) identify technique-dependent parameters that adversely affect the accuracy of either VLBI or total station measurements; (c) improve the local ties between the various techniques on site; and (d) improve our understanding of the HartRAO complex.

1.6 LIMITATIONS

The outdated pointing model of the HartRAO 26 m antenna was identified as being one of the station-specific error sources requiring the most urgent attention. The pointing model can however not be updated before the faulty bearing has not been replaced, and in addition, higher resolution encoders have not yet been installed. The effect of degraded meteorological surface data on the atmospheric refraction correction, which forms part of the antenna pointing model, was not addressed in this study. Other possible sources of error that were only shortly described but not investigated in this study are the 26 m antenna's bearing and encoders, structural effects (including gravitational and thermal deformation) and antenna foundations for both the 26 m and 15 m antennas, the hydrogen maser clock used by both antennas as well as the phase (both antennas) and cable (26 m antenna only) calibration systems.

Global astrometric and geodetic VLBI sessions in which both the HartRAO 26 m and 15 m antennas participated were required for determining the local tie (baseline) between the antennas. Since the start of the 15 m antenna's operations in October of 2012, most of these sessions have been offloaded to the 15 m antenna. There are therefore not that many sessions in which both antennas participated ("dual" sessions). Furthermore, very few simultaneous same-source observations are scheduled in such dual sessions, which would preclude more accurate estimation of the local tie vector for two antennas observing

through the same troposphere. Only eleven of the twenty SBL experiments conducted between the two antennas have been correlated thus far. Correlation is required to provide the processed VGOS database (vgosDB) files used in the VLBI analysis. Investigating seasonal variation in baseline length was therefore curtailed by the paucity of dual global sessions and the SBL experiment lacking correlated sessions for October and November as well as any seasonal overlap. The automated total station for continuous monitoring of vector ties has not been implemented yet. This precluded the planned comparison of the local tie obtained from continuous ground survey measurements with that estimated in the VLBI analysis of SBL experiments running in tandem.

1.7 ETHICAL CONSIDERATIONS

The Vienna VLBI and Satellite Software (VieVS) that was used in the VLBI data analysis is developed and maintained by the Department of Geodesy and Geoinformation, Vienna University of Technology. It is made freely available and should be referenced by citing Böhm *et al*. (2018). Processed geodetic VLBI data from observing sessions are freely available from the International VLBI Service for Geodesy and Astrometry (IVS) data centres. Use of VLBI data and results are acknowledged by citing Nothnagel *et al*. (2017) – http://ivscc.gsfc.nasa.gov/publications/citation.html

1.8 OVERVIEW OF STUDY

Chapter 2 provides background to astrometric and geodetic VLBI with respect to data acquisition and analysis, parameter estimation in VieVS, reference frames and the IVS and GGOS/VGOS. Station-specific error sources at HartRAO, limiting the accuracy of VLBI results, are identified and described briefly in *Chapter 3*. The state of HartRAO meteorological sensors and quality of *in situ* meteorological surface data are investigated, and the impact of degraded data on astrometric and geodetic VLBI is briefly discussed in *Chapter 4*, while its impact on single-dish calibration is explored further. Pointing problems of the HartRAO 26 m antenna at 22 GHz are addressed by investigating pointing corrections and antenna gain in *Chapter 5*. A possible correlation between degraded declination pointing and differential heating of the support structure is also explored. In

Chapter 6, the AO estimates for the HartRAO 26 m and 15 m antennas determined in VLBI analysis are compared with the AO values measured in the most recent ground survey. The effect of the AOAC on the AO estimated in VLBI analysis for the HartRAO 26 m equatorially mounted antenna is also examined. Local tie results estimated in the VLBI analysis of IVS global sessions in which both the HartRAO 26 m and 15 m antennas participated as well as of SBL experiments conducted between the two antennas, are compared with results from the most recent ground survey in *Chapter 7*. Plans for the implementation of an automated local tie measuring system are also discussed. *Chapter 8* provides a summary of findings, recommendations and future work as well as conclusions reached related to this study.

CHAPTER 2 VERY LONG BASELINE INTERFEROMETRY

Very Long Baseline Interferometry (VLBI) is one of the four major space geodetic techniques used to observe changes in the Earth's shape, rotation and gravity field. Astrometric and geodetic VLBI contribute to realisation of the International Celestial Reference Frame (ICRF), establishment and maintenance of the International Terrestrial Reference Frame (ITRF), to linking these reference frames by observing the full set of Earth orientation parameters (EOP) as well as to uniquely providing direct measurements of nutation parameters and the Earth's rotation angle (UT1-UTC) (Schuh and Böhm, 2013). In the following, background to the VLBI technique as employed in astrometry and geodesy is provided, based on an overview by Schuh and Böhm (2013) and comprehensive works by Sovers, Fanselow and Jacobs (1998), Takahashi *et al.* (2000) and Nothnagel (2018).

2.1 GEOMETRIC PRINCIPLE OF VLBI

The geometric principle of VLBI is depicted in Figure 2.1. Signals from an extra-galactic space-fixed radio source, such as a quasar, billions of light years away, arrive as planar wavefronts at two Earth-fixed antennas (1 and 2), separated by baseline vector $\underline{b}$ and simultaneously pointing in the direction of the radio source, $\underline{s}_0$. The wavefront first arrives at antenna 1 at time t_1 and sometime later, t_2, at antenna 2. The difference in arrival times, $t_2 - t_1$, is the time delay, τ, the primary observable of VLBI as given by the fundamental equation of VLBI (Schuh and Böhm, 2013):

$$\tau = -\frac{\underline{b} \cdot \underline{s}_0}{c} = t_2 - t_1 \tag{2.1}$$

where $\underline{b}$ is the baseline vector from antenna 1 to antenna 2 and $\underline{s}_0$ is the direction to the radio source, c the velocity of light and t_1 and t_2 the arrival times of the signal at antennas 1 and 2 respectively.

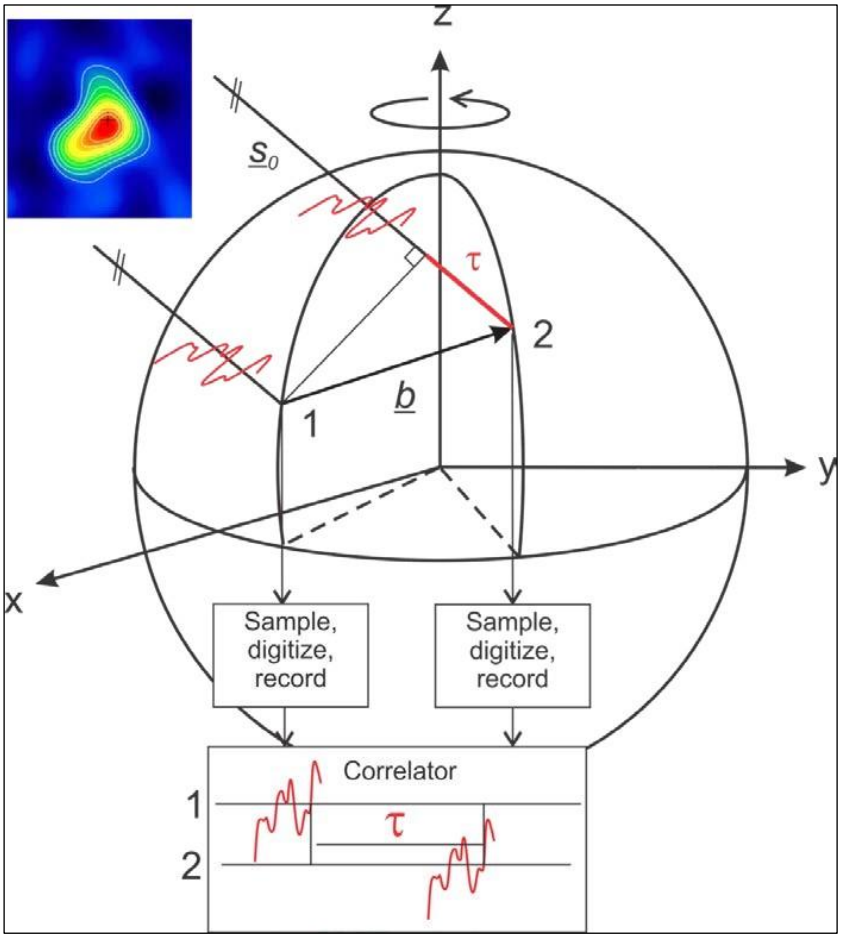

Figure 2.1 Geometric principle of VLBI – wavefronts emitted by an extra-galactic radio source, such as a quasar, located at position $\underline{s}_0$, are received at antennas 1 and 2, separated by baseline $\underline{b}$, at different times. The time delay between the wavefront's arrival at antenna 1 and antenna 2, τ, is the scalar product of the baseline ($\underline{b}$) and source ($\underline{s}_0$) vectors and is the primary observable of VLBI (Schuh and Böhm, 2013).

2.2 DATA ACQUISITION

Data acquisition proceeds from scheduling of observations, through observing the radio sources according to the schedule and recording the data, to sending the data to correlators for cross-correlation, fringe-fitting and post-processing, finally producing the database files containing the observed delays used in the VLBI analysis software for parameter estimation.

The first step in the data acquisition process is *scheduling* of observations. An observing schedule is generated for each, typically 24-hour session, comprising antennas selected from a global network of stations, together observing multiple stable and compact radio sources of high flux density with optimal sky-coverage at various azimuth and elevation angles, in numerous scans. During each scan, a network or sub-network/s of the participating antennas simultaneously observe the same source. The aim is for antennas to participate in the maximum number of scans with minimum slewing time between scans, but not compromising on optimal sky coverage, which provides for estimation of troposphere delays. Each scan must be of sufficient duration for the required signal-to-noise ratio (SNR) to be reached. Specialised scheduling software packages, such as SKED (Gipson, 2018) and VieSched++ (Schartner and Böhm, 2019), allow for schedules to be optimised to achieve the specific session objectives.

The next step in the data acquisition process entails *observing* the radio sources together with other participating stations following the schedule for that particular session. In geodetic VLBI, observations are conducted at frequencies of 2.3 GHz (S-band, $\lambda = 13$ cm) and 8.4 GHz (X-band, $\lambda = 3.5$ cm) simultaneously. While the primary observing frequency is at 8.4 GHz, observations at 2.3 GHz are used for ionospheric calibration—the ionosphere is a dispersive medium at radio frequencies and the dual-frequency observations allow for mitigating its effect on the observed delay. The radio source signal (radio frequency, RF signal) arrives at the antenna and is reflected into the antenna's feedhorn where it is converted into a voltage. Phase calibration tones are also injected at the feedhorn to calibrate system delays and detect variations in signal phase. A cable calibration system monitors changes in cable length caused by temperature variations and

flexing of cables. The RF signal is amplified with a low-noise amplifier (LNA), mixed with a local oscillator (LO) signal, heterodyned to intermediate frequencies, and then down-converted to base-band frequency channels (BBC) in the digital base-band converter (DBBC) where it is also digitised, time-tagged with a highly stable hydrogen maser clock and formatted, before being transferred to the recorder where the data are recorded to hard drive.

In the final step of the data acquisition process, data from all stations participating in a session are shipped to the correlator via electronic data transfer for *correlation* and fringe-fitting. The correlator makes use of the distributed FX (DiFX) software to first Fourier transform (F) and then cross-correlate (X) signals from the participating antenna pairs forming a baseline. The signals recorded at the antennas are combined pairwise. The difference in the signal arrival times at the two antennas, the time delay, is provided by the peak of the interference pattern. The correlator finds this peak by shifting the two bit streams, representing the voltages of the two antennas as functions of time, in time relative to each other, until their cross-correlation function is maximised. The correlation process is carried out simultaneously for all frequency channels. Each of the channels produces average amplitudes and phases every 1-2 seconds for each of the stations (Sovers, Fanselow and Jacobs, 1998). During *fringe-fitting*, the phase samples from the frequency channels are Fourier transformed from the frequency and time domain to the delay and delay rate domain respectively, which are then searched for peaks. The peaks provide *a priori* values for the least-squares fit which determines the phase and group delay as well as phase rate observables (Sovers, Fanselow and Jacobs, 1998). The group delay is the fundamental observable in astrometric and geodetic VLBI. The data are further prepared for analysis by removing ionospheric effects, and correcting for instrumental delays by applying the phase calibration tones. In further post-processing, database files which include ambiguity resolution as well as station cable calibration and meteorological data, are created. The database files are now ready for use by VLBI analysis software.

2.3 DATA ANALYSIS

As depicted in Figure 2.2, the flow diagram for geodetic VLBI data analysis at first follows two separate paths which eventually converge for parameter estimation in a least-squares adjustment.

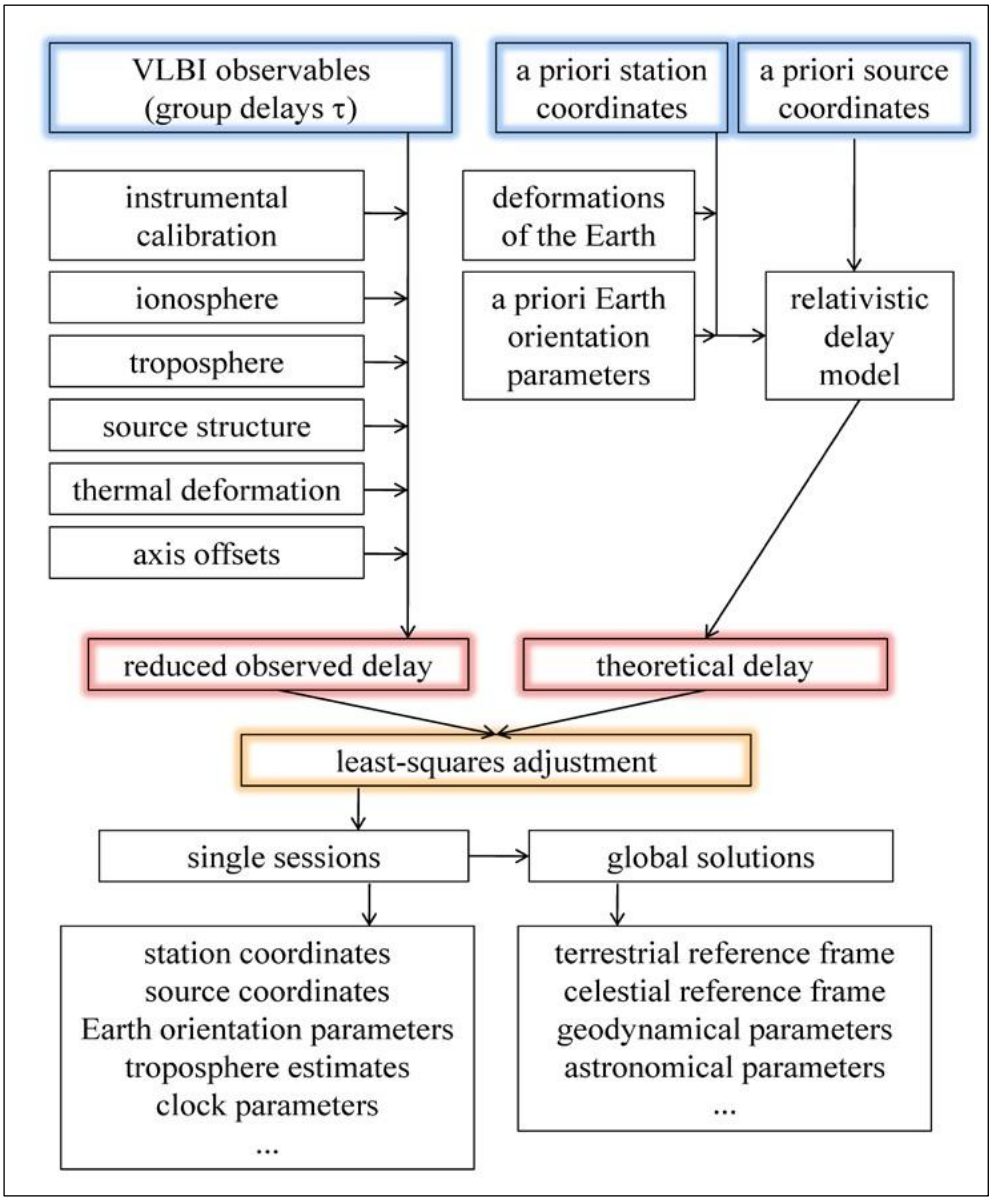

Figure 2.2 Flow diagram depicting the VLBI analysis process – the difference between the reduced observed delay and calculated theoretical delay (O-C) is used in a least-squares adjustment to estimate the parameters of interest (Schuh and Böhm, 2013).

In the path on the left in Figure 2.2, corrections and models to account for instrumental and environmental effects are applied to the observed group delay, τ, delivered by the correlator, to produce the *reduced observed delay (O)*. Corrections for instrumental calibration include those pertaining to systematic clock instabilities, electronic delays in equipment such as cable delays, and group delay ambiguities due to the multichannel frequency setup used in geodetic VLBI. Ionospheric corrections obtained from differences in the S- and X-band group delays are applied to the primary X-band observations. The delay caused by the hydrostatic part of the troposphere is modelled. Thermal and gravitational deformation of the antenna structure are also modelled for, as is the antenna AO, which exists for antennas with non-intersecting rotation axes. Extended structure in radio sources causes a change in source coordinates and has to be corrected for. In the path on the right in Figure 2.2, models are applied to *a priori* values of VLBI model parameters to calculate a *theoretical delay (C)* in close agreement with the reduced observed delay. The Consensus model (Eubanks, 1991), as recommended by the International Earth Rotation Service (IERS) Conventions 2010 (IERS, 2010), is followed. The *a priori* station coordinates are corrected for Earth deformations at the time of observation by applying station displacement models for tectonic motion, solid Earth tides and station dependent loading effects, such as ocean and atmosphere loading, pole tides and ocean pole tides, as well as for other local station motion. The station coordinates are then transformed from the terrestrial into a celestial reference system by a series of rotations using the *a priori* EOP in order to connect source and station positions. A general relativistic delay model is applied to account for gravitational delay of the radio source signal passing near massive celestial bodies. In order to determine the total theoretical delay, models have to be applied also for the hydrostatic part of the troposphere delay and delays caused by thermal and gravitational deformation of the antennas as well as the antenna axis offset (AO). The difference between the reduced observed delay and the calculated theoretical delay (observed minus computed, O – C) is determined for each observation in a VLBI session. These residuals are then entered into a least-squares adjustment for estimation of the parameters of interest. Parameter estimation is discussed in the following section as it relates to the geodetic VLBI analysis software package used in this study, i.e. the Vienna VLBI and Satellite Software (VieVS, Böhm *et al.*, 2018).

2.4 PARAMETER ESTIMATION IN THE VIENNA VLBI AND SATELLITE SOFTWARE

Several software packages exist for the analysis of geodetic VLBI data. Since VieVS was used for the analysis of geodetic VLBI data in this study, the estimation of geodetic parameters as it relates to the use of VieVS in this study is discussed here. Various geodetic target and auxiliary parameters can be estimated in VieVS, by making use of iterative least-squares adjustment following the Gauss-Markoff model (Koch, 1999), in which the squared sum of the residuals is minimised. Accurate *a priori* information is required for small adjustments to these values to be estimated. Parameters can be estimated in either single-session analysis or in a global solution of multiple sessions. In single-session analysis, local parameters, which change over time, are estimated for the specific observing session, while for the global solution, global parameters, which remain constant over time, are estimated for a batch of sessions in its entirety.

The VieVS software is modular in structure (see Figure 2.3) with each module consigned to a specific task and able to operate independently but also in combination with the other modules. In addition to the control module, VIE_SETUP, which includes the graphical user interface (GUI), there are three main modules—VIE_INIT, VIE_MOD and VIE_LSM—and three supplementary modules— VIE_GLOB, VIE_SCHED and VIE_SIM.

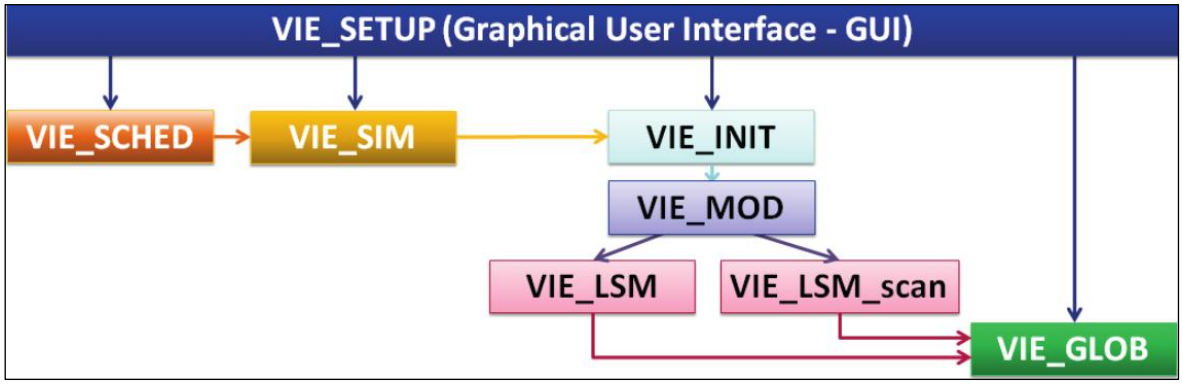

Figure 2.3 Modular structure of VieVS (Madzak et al., 2013).

Database files containing the observed delay and delay rate are loaded and read by the *VIE_INIT* (initialising) module of VieVS. In this study, database files in the National Geodetic Survey (NGS) format, Version 4 or higher, were used. The Version 4 NGS card files contain the total time delay with ionospheric correction already applied and group delay ambiguities already resolved. Also included are station meteorological measurements for modelling of troposphere delay, station cable delay to be added to the observed delay, as well as other antenna-related information. The VIE_INIT module retrieves station and source coordinates from terrestrial and celestial reference frame (TRF and CRF) catalogues in VieVS, respectively. This module is also tasked with the exclusion of problematic stations, sources, baselines and station cable calibration as well as elimination of outliers.

In the *VIE_MOD* (modelling) module of VieVS, the theoretical delays and their partial derivatives are calculated from models recommended in the IERS Conventions 2010 (IERS, 2010).

The least-squares estimation of geodetic parameters is performed by the *VIE_LSM* (least squares matching) module of VieVS. Various geodetic target parameters, such as station coordinates and velocities, source coordinates, EOP, antenna AO and baseline vectors, can be estimated. Parameters can either be estimated or fixed to *a priori* values. Auxiliary parameters, such as tropospheric zenith wet delay (ZWD) and gradients as well as station clock offset and drift, propagate into the target parameters and have to be estimated as they cannot be observed or modelled with the required accuracy. For datum definition in the estimation of station coordinates, since it is possible for the entire network of observing stations to be translated or rotated without changing the distances measured by VLBI, it is necessary to constrain the *a priori* station coordinates of all stations or a selection of at least three stable stations in the observing network by no-net-rotation (NNR) and no-net-translation (NNT) conditions. Stations that have experienced non-linear motion due to an earthquake, for example, are excluded from the datum. Radio source coordinates are usually fixed to *a priori* values in the ICRF-3 (Charlot *et al*., 2020) but can be estimated for radio sources with positional instability due to structural variation, for example. For datum definition in estimation of radio source coordinates, only the NNR condition is applied to stable radio sources, as the sources are considered to be at an infinite distance.

Sources with positional instability are excluded from the datum. For a 24-hour observing session, station coordinates and EOP (polar motion, Earth rotation angle and precession-nutation) are typically estimated over the 24-hour interval. For each of the stations in the observing network, the troposphere ZWD and horizontal gradients are estimated with continuous piece-wise linear offsets (CPWLO), typically at 30-minute and 3-hourly intervals, respectively. Differences between the station clocks and a fixed reference clock (the most stable station clock in the observing network) are estimated as quadratic polynomial functions with CPWLOs, typically at hourly intervals. If a clock break is detected at a station, the station and epoch at which the clock break occurred are specified in the OPT file, and separate quadratic polynomial functions are estimated for before and after the break. A change in reference clock is also specified in the OPT file. Outliers identified in the VIE_LSM module are removed in VIE_INIT.

In multi-session analysis, a global solution of multiple sessions is performed in the *VIE_GLOB* (global) module of VieVS. Single sessions are combined by stacking the normal equation systems of the single sessions into a global normal equation system. A global adjustment is then performed to estimate global parameters that are constant over time, such as station and source coordinates, EOP as well as antenna AO. Although these parameters can be estimated in single-session analysis, a long time series is required to estimate them with high accuracy. Terrestrial and celestial reference frames (TRF and CRF) are determined by global solution. In addition to constraints for datum definition as applied in single-session analysis, velocity constraints can be applied where the same velocity is estimated for two antennas at the same site with a known local tie. For stations with position discontinuities, it is also possible to estimate constant velocities over all intervals.

Automated observation schedules for astrometric and geodetic VLBI sessions can be generated with the *VIE_SCHED* (scheduling) module of VieVS. Catalogue files containing information related to the sources, and antennas and equipment at the stations in the observing network, as well as the experimental setup for the particular session serve as input. The scheduling software is automated to construct the schedule scan-by-scan, optimising for the number of scans, sky-coverage and scan duration. The schedule

produces a list of scans in time-sequence for the particular session, indicating which sources should be observed at a specific time for a specific duration by the antennas in the observing network.

Simulated observations are performed in the *VIE_SIM* (simulating) module of VieVS. Monte Carlo simulations are carried out in which the three main stochastic error sources in VLBI—tropospheric ZWD and station clock and instrumental errors—are simulated using random numbers in each of a large number of simulations, and subsequently combined with the theoretical delay to generate realistic observations. The output is saved in the format of National Geodetic Survey (NGS) card files, and the simulated time delay can be analysed in either single-session analysis or within a global solution to estimate geodetic parameters of interest and obtain statistical information for comparison.

2.5 REFERENCE FRAMES

Reference frames provide the link between the three pillars of geodesy—the Earth's shape, rotation and gravity field (Angermann, Seitz and Drewes, 2013). Accurate and stable reference frames are therefore of vital importance for accurate geodetic results. The reference frames have to be determined at the level of Global Geodetic Observing System (GGOS) accuracy and stability requirements for global baselines of 1 mm and 0.1 mm/year, respectively, which were set as such specifically to be able to monitor sea-level rise.

The International Celestial Reference Frame (ICRF) and International Terrestrial Reference Frame (ITRF) provide the metrological basis of all Earth observations (Plag *et al*., 2009) and allow for connecting measurements separated in space and/or time (Gipson, 2020). The ICRF provides accurate positions for extragalactic radio sources. The ITRF provides accurate terrestrial geodetic station coordinates and velocities. The VLBI technique uniquely realises the ICRF and contributes towards determining the ITRF, together with Satelite Laser Ranging (SLR) defining its scale (Schuh and Böhm, 2013). The ICRF and ITRF are connected by the EOP (UT1-UTC, precession and nutation, and

Department of Geology, Geoinformatics and Meteorology
University of Pretoria

polar motion), which describe irregularities in the Earth's rotation, and are also uniquely defined by VLBI.

These reference frames are used for, amongst others: determining the Earth's orientation in space, planetary ephemerides and satellite orbits; studying tectonic plate motion, loading effects, land subsidence and sea-level rise; testing the theories of special and general relativity; for atmospheric and climatological studies; as well as for navigation, both on Earth and in Space (Plag *et al*., 2009; Angermann, Seitz and Drewes, 2013). The ICRF and ITRF also contribute to the realisation of 'A Global Geodetic Reference Frame for Sustainable Development' (United Nations General Assembly Resolution 69/266, 2015).

The latest realisation of the ICRF is ICRF-3 (Charlot *et al*., 2020). It was adopted in 2018 by the International Astronomical Union (IAU) and is based on ~40 years of astrometric and geodetic VLBI data observed at S/X-, K- and X/Ka-band radio frequencies and is the first realisation of a multi-wavelength frame (De Witt *et al*., 2022). The ICRF-3 contains positions for 4588 sources with positions of 600 of these sources available in all three frequency bands. Its axes are defined by a subset of 303 uniformly distributed sources, the so-called ICRF-3 defining sources. These sources are the most stable, compact and most observed sources at S/X-band and their positions are thus known with high accuracy. Looking towards a future ICRF, further improvement can be expected from densifying observations and spatial coverage in the South and increasing the observations on north-south baselines, monitoring source structure variation and mitigating its effects as well as the integration of the radio frames with the Gaia optical frame.

The latest realisation of the ITRF by the IERS is ITRF2020 (Altamimi *et al*., 2022). It is based on extended time series of station positions and EOP observed by the four space-geodetic techniques, VLBI, GNSS, SLR and DORIS, as well as on inter-technique local ties at co-location sites where more than one of these techniques are operational. The inter-technique combination utilises the specific capabilities of each technique, thus providing for high accuracy and robustness (Plag *et al*., 2009). The International VLBI Service for Geodesy and Astrometry (IVS) contribution to ITRF2020 consisted of solutions from eleven IVS analysis centres using six different VLBI analysis software packages to analyse

VLBI data from ~6600 24-hour IVS sessions for the period 1980.0 – 2021.0 (Gipson, 2020). The analysis centre solutions were then combined into single solutions for the individual sessions by the IVS Combination Center (IVSCC) and submitted to the IERS.

Co-location of instruments from the different techniques and the inter-technique ties between their reference points are crucial for establishing a unique and common reference frame for the various techniques, for detecting technique-specific biases and for separating signals of various Earth system processes (Rothacher *et al*., 2009; Angerman, Seitz and Drewes, 2013). The local ties between co-located instruments have thus far been determined in co-location ground surveys. However, with the advent of GGOS and its demand for higher accuracy, it is now required that local tie measurements "be performed with 0.1 mm accuracy, in a fully automated way and on an almost continuous basis" (Rothacher *et al*., 2009). It is further required that other co-located instruments, such as meteorological sensors, water vapour radiometers, gravimeters, etc. at core sites also be tied in.

2.6 INTERNATIONAL VLBI SERVICE FOR GEODESY AND ASTROMETRY

The International VLBI Service for Geodesy & Astrometry (IVS) coordinates astrometric and geodetic operational activities of a global station network and supports geophysical research (IVS, 2022). As a service of the International Association of Geodesy (IAG) and International Astronomical Union (IAU), it is mandated to deliver high-quality ITRF, ICRF and EOP products. This mandate is fulfilled by close cooperation of the various IVS components—network stations and correlators as well as operation, analysis, data, technology development, outreach and communications and coordinating centres.

The IVS observing network comprises ~50 stations throughout the world. Antennas from these stations participate in the IVS observing sessions on a best-effort basis. Only nine of these IVS network stations are located in the Southern Hemisphere—the Argentinean-German Geodetic Observatory (AGGO), Fortaleza in Brazil, HartRAO in South Africa, Hobart, Katherine and Yarragadee in Australia, Warkworth in New Zealand and O'Higgins and Syowa in Antarctica—which leads to a weak network geometry,

skewing the data towards the North, thereby reducing the accuracy of the estimated astrometric and geodetic parameters and compromising the quality of the VLBI products.

The IVS schedules and coordinates astrometric and geodetic VLBI sessions which are typically 24 hours in duration (excluding the hour-long Intensive sessions). The IVS observing programme encompasses several different types of sessions, each with a specific purpose in mind, be it to provide results for determining TRF, CRF, EOP *etc*. The observation network configuration and observing strategy depend on the purpose of the particular type of session.The Rapid turnaround and Intensive sessions are observed most frequently.

The *Rapid turnaround* IVS-R1 and IVS-R4 sessions are aimed at providing EOP results twice weekly, and are observed on Mondays (R1) and Thursdays (R4) for 24 hours each. The observing network preferably consists of at least eight globally distributed core stations supplemented by up to six other stations, all depending on the availability of antennas. The network geometry for the R1 and R4 sessions differ somewhat and the 3-day separation between the start of these sessions allows for monitoring of periodicity in tides and nutation. In addition to EOP determination, the R1 and R4 sessions also contribute to strengthening of the TRF.

The IVS *Intensive* sessions are of 1-hour duration and are performed on a daily basis to provide a daily UT1 measurement. Three types of Intensive sessions are observed throughout the week on East-West baselines sensitive to changes in UT1. The IVS-INT1 sessions are observed from Monday to Friday on baselines between two or three stations, usually on the baseline between Kokee Park (Hawai'i, USA) and Wettzell (Germany). The IVS-INT2 sessions are observed on Saturday and Sunday on either the single baseline between the Very Long Baseline Array (VLBA) station, MK-VLBA (Mauna Kea, Hawai'i), and Wettzell (Germany) or on additional baselines between these stations and Ishioka (Japan). The IVS-INT3 sessions are observed on Monday on baselines connecting Ishioka (Japan) (or Seshan, China), Ny-Ålesund (Norway) and Wettzell (Germany). Since the start of 2022, the above mentioned Intensives, conducted on East-West baselines between Northern Hemisphere stations only, have been augmented by Southern Intensive

(SI) sessions. The SI sessions were initially observed on baselines between the southern IVS network stations, HartRAO, Hobart and Yarragadee, but once it had been established that the HartRAO-Hobart baseline produced results comparable to those of the three-station network, Yarragadee, being unable to deliver the recorded data within the short time frame required for daily UT1 determination, was excluded from the observations. The SI sessions are currently being observed on Mondays at 06:30 UT to provide an overlap with the IVS-INT3 sessions (Böhm *et al*., 2022).

The IVS *Reference frame* sessions are divided into sessions for determining the CRF and the TRF. The IVS CRF and CRF deep-south (CRDS) sessions consist of astrometric VLBI observations aimed at improving the current realisation of the CRF as well as at extending and densifying the CRF by observing new radio sources not included in the existing CRF realisation. The IVS-CRF sessions are observed six times a year with at least three, and sometimes up to seven, participating stations from both the Northern and Southern Hemispheres. Due to the dearth of southern network stations, the IVS-CRDS sessions are a concerted effort to expand sky-coverage and densify sources and observations in the South. These sessions are observed six times a year with as many as possible of the southern stations—from a pool consisting of AGGO, HartRAO, Hobart, O'Higgins, Warkworth and Yarragadee—participating. In IVS-T2 sessions, the TRF is monitored approximately bi-monthly. All network stations participate in at least two T2 sessions a year with between 10 and 14 stations participating in any one session. Stations which infrequently observe are tied to stations observing on a regular basis and station coordinates are determined for all the stations. In order to determine highly accurate station coordinates, as many as possible of the stable legacy antennas are included in the T2 sessions. Since 2021, two IVS-T2P (or T2++) sessions have been added to the yearly observing schedule, in which the number of participating stations has been increased to between 20 and 25 and the observing mode enhanced for yet higher accuracy in station coordinates (Kotary, 2021).

The IVS *Research & Development* (IVS-R&D) sessions are special-purpose sessions with specific scientific goals and also aimed at improving the VLBI technique and its products. Currently, ten R&D sessions are observed throughout the year with six to nine stations participating in the sessions focused on observing optically-bright ICRF3 sources selected

from the Gaia optical catalogue (Gaia transfer sources) in order to align the ICRF-3 determined by VLBI with the Gaia optical CRF. The *Research and Development VLBA* sessions are astrometric/geodetic sessions observed six times a year with the 10-station VLBA together with eight IVS network stations with a long history. The purpose of these sessions is to determine and maintain high-accuracy CRF, TRF and EOP. Sources are imaged and source structure is studied to provide a core set of reference sources with known structure and precisely known positions.

The IVS *regional campaigns* include, amongst others, sessions dedicated to improving the VLBI technique in the Southern Hemisphere, such as the AUSTRAL and OHIGGINS sessions. The AUSTRAL sessions are observed at least once a month with stations of the AuScope VLBI array—Hobart, Katherine and Yarragadee—together with the HartRAO and Warkworth (New Zealand) stations. Intially, AUSTRAL astrometric and geodetic VLBI sessions were focused primarily on strengthening the CRF and TRF in the Southern Hemisphere (Plank *et al.*, 2017). Recently, the AUSTRAL mixed-mode (AUM/AUA) observing sessions were introduced, in which the Hobart and Katherine 12-m antennas, already fitted with VGOS wideband receivers, observe in the standard dual-frequency S/X mode along with the rest of the antennas in the AUSTRAL sessions to provide an uninterrupted position time series for the two antennas before they transition to full VGOS wideband operations. The OHIGGINS sessions (IVS-OHG) are observed six times throughout the year by the IVS network stations in Antarctica—O'Higgins and Syowa—together with the other southern network stations. The Kokee Park station (Hawai'i, USA), the southern-most of the northern stations, is also included to ensure a robust network geometry and an increased number of observations per scan. These sessions are aimed at providing an optimal tie of the stations in the Southern Hemisphere and a highly accurate regional TRF around the South Pole and also further improve the CRF in the South.

The IVS *continuous (CONT) campaigns* are conducted roughly every three years and consist of 15 days of consecutive 24-hour sessions observed with geographically well-distributed stations configured in a strong network geometry. The aim is to produce state-of-the-art data sets for testing the accuracy limits of the VLBI system as well as the performance limit of the network. The most recent CONT campaign, CONT17, featured

three independent observing networks which included two legacy networks observing at S/X-band and a VGOS network observing in VGOS wideband mode. The two legacy networks provided for two independent data sets which allowed for comparison of results and network geometry. The VGOS network was aimed at demonstrating VGOS capabilities. One of the legacy networks comprised fourteen IVS network stations while the other comprised four IVS network stations together with the ten VLBA stations. The VGOS demonstration network consisted of six VGOS-capable stations. The high-quality data sets derived from the continuous observations allow for studies of phenomena such as high-frequency EOP variations, ocean and atmosphere tidal loading, sub-daily site motions, reference frame stability as well as for investigating atmospheric effects and testing theoretical models (Behrend *et al*., 2020).

The *IVS products* derived from the session data are made available through the IVS data centres and include the following products:

- EOP results;
- TRF (station positions, velocities);
- CRF (updates to the ICRF);
- analysis products for combination within the IVS or with other other space techniques (allows for estimation of polar motion, UT1, UT1-TAI, LOD and station positions);
- tropospheric parameters (total and wet zenith path delays and station meteorological data); and
- time series of baseline lengths

Observing schedules for all IVS sessions can be downloaded by the stations participating in the sessions from the IVS data centre servers. Station-specific instructions are generated from the schedule file by processing it with the *VLBI Field System (FS)* software package (Himwich *et al*., 2003). During the session, the FS provides automated control of the antenna and other data acquisition hardware, steering the antenna according to the station's observing schedule. The FS furthermore records auxiliary data, such as station timing, cable delay and meteorological data, in a station log file for each scan in the observing schedule. The auxiliary data are used for station corrections and modelling in subsequent correlation and analysis.

2.7 GLOBAL GEODETIC OBSERVING SYSTEM

In 2007, the IAG established the *Global Geodetic Observing System (GGOS)* to meet an increasing demand for open, reliable and timely Earth observation data of the spatial and temporal changes of the shape and gravity field of the Earth and temporal variations of the Earth's rotation, towards an improved understanding of global change phenomena (GGOS, 2022). In order to achieve the aforementioned, GGOS aims at integrating the various geodetic techniques to provide geodetic reference frames with an accuracy of 1 mm and stability of 0.1 mm/year. The geodetic VLBI community, in the form of the IVS, responded to meeting the increased accuracy required for the VLBI technique to form part of GGOS by initiating a project for a next-generation geodetic VLBI system, now known as the *VLBI Global Observing System (VGOS)*. The VGOS goals were set at 1 mm position and 1 mm/year velocity accuracies, continuous measurements for EOP, and rapid generation and distribution of IVS products, remaining focused on providing the uniquely VLBI-defined CRF as well as UT1 and nutation products (Niell *et al*., 2005). New VGOS observing systems consisting of small (~12 m) fast-slewing antennas with broadband receivers covering the frequency range 2-14 GHz are currently being introduced worldwide in order to meet these goals. A VGOS observing network of at least 20 geographically well-distributed VGOS antennas is required for continuous EOP measurement. Currently, nine stations, all located in the Northern Hemisphere, regularly participate in VGOS observing, which includes VGOS Operational, Intensive, Research & Development and Test sessions (Behrend, 2021). An additional 14 VGOS stations are either being planned, under construction or in the process of installing a VGOS receiver. Six of these stations are located in the Southern Hemisphere, with Australia hosting three (Hobart, Katherine and Yarragadee), Africa (HartRAO, South Africa) and South America (Fortaleza, Brazil) one each, and Tahiti in French Polynesia another. Legacy antennas need to be upgraded and maintained for TRF continuation and CRF realisation (Niell *et al*., 2005). Where VGOS antennas are co-located with legacy antennas, the VGOS antenna has to be tied to the VLBI reference point of the legacy antenna. The VGOS stations are required to install an automated system for continuous measurement of antenna position and antenna location with respect to the reference point at the site with

sub-millimetre accuracy. Systematic instrumental, mechanical, loading and radio source structure errors have to be minimised and/or calibrated for.

CHAPTER 3 HARTRAO ERROR SOURCES

Station-specific errors limit the accuracy of astrometric and geodetic VLBI results by corrupting the signal delay, displacing the antenna VLBI reference point and reducing antenna pointing accuracy. Station-specific error sources will have to be eliminated or at least mitigated for the HartRAO antennas to be able to contribute to "continuity of the TRF and … enhancement and maintenance of the CRF" (Niell *et al*., 2005) and to meet Global Geodetic Observing System (GGOS) requirements of baseline accuracy and stability of 1 mm and 0.1 mm/yr respectively. HartRAO station-dependent errors specific to both the 26 m and 15 m antennas were investigated to determine a possible course of action to mitigate the sources of these errors. Station-specific errors either of particular concern at the station or in the wider IVS community currently were identified by consulting with Engineering, Operations and the astronomers at HartRAO as well as by giving consideration to recent IVS resolutions requiring IVS network stations to address specific station-related issues (IVS, 2019; IVS, 2021a,b).

3.1 BACKGROUND AND SCOPE

The K-band collaboration for the realisation of the CRF reported non-detection of radio sources in K-band astrometric observations on the single baseline between the HartRAO and Hobart 26 m (Australia) antennas (C. Jacobs, personal communication, 1 September 2016). HartRAO Operations indicated that spot calibrator measurements showed K-band pointing on the 26 m antenna to sometimes be off by up to a quarter of a half-power beamwidth (HPBW) and also reported significant declination pointing offsets of up to 30 mdeg in K-band pointing observations. Astronomers at HartRAO detected steps and a repeating pattern in the 26 m antenna's point source sensitivity (PSS) determined from Jupiter gain calibration observations at 22 GHz. Recent Jupiter gain curve

observations on the 26 m antenna at 22 GHz revealed the appearance of extended first sidelobes below the antenna's main beam on both Jupiter rising and setting (see Figure 3.1) as well as an unexplained decrease in antenna gain.

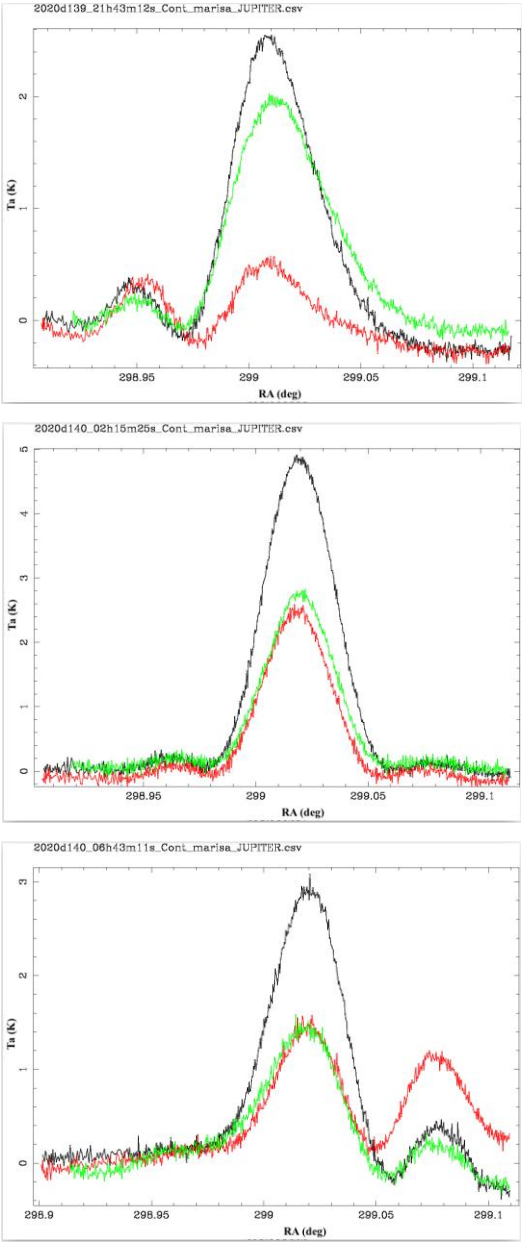

Figure 3.1 Extended first sidelobes – Jupiter gain curve observations on the HartRAO 26 m antenna at 22 GHz in right circular polarisation (RCP) for observations at ON (black), half-power North (HPN, red) and half-power South (HPS, green) positions – as Jupiter rises in the east, an extended first sidelobe appears on the left (top), becomes less pronounced as the antenna moves through zenith (middle) and then reforms on the right with Jupiter setting in the west (bottom).

The Bonn correlator reported non-detection of radio sources during geodetic VLBI sessions at S/X-band, particularly at X-band and on the baseline between the HartRAO 15 m antenna and AGGO (Argentina) 12 m antenna for recent sessions. AGGO reported a possible dependency of the signal-to-noise ratio (SNR) on elevation for the HartRAO 15 m antenna for two of the four sources with significant non-detections in a recent IVS geodetic session, R11014 (H. Hase, personal communication, 13 October 2021). The plot of SNR versus elevation for the few scans of the four sources that were detected seems to confirm an increase in the baseline SNR with increasing elevation of the HartRAO 15 m antenna for two of the four sources, 0332-403 and 2052-474 (see Figure 3.2).

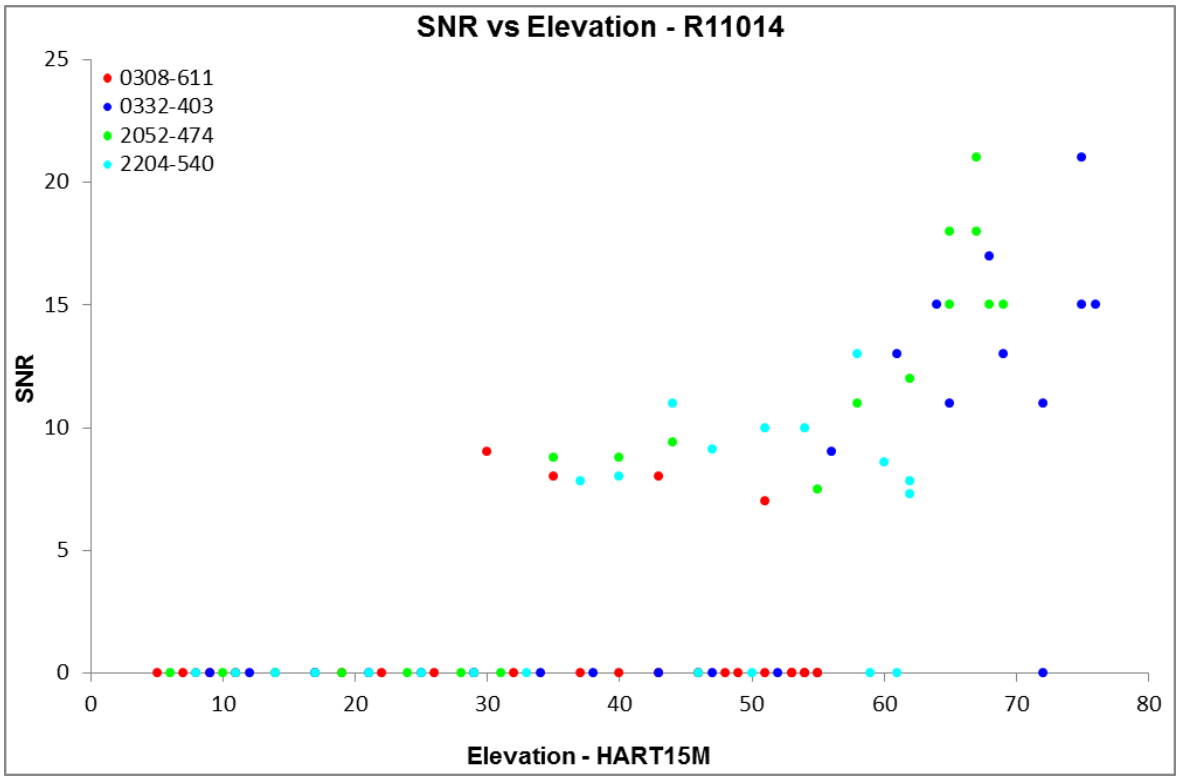

Figure 3.2 Non-detections in scans of the four sources 0308-611, 0332-403, 2052-474 and 2204-540 on the HART15M-AGGO baseline are indicated by a baseline signal-to-noise ratio (SNR) of zero. The baseline SNR seems to increase with the elevation of the HartRAO 15 m antenna in the few scans of the two sources 0332-403 and 2052-474 that had been detected.

In 2019, HartRAO Engineering reported a failing bearing on the west declination shaft of the 26 m antenna, discovered whilst installing and testing a new encoder at the end of the shaft (see Figure 3.3). The bearing was observed to be sliding back and forth axially along the shaft by ± 10 mm (see Figure 3.4). Installation of new higher resolution encoders was necessitated by intermittent failure of current encoders. HartRAO Operations indicated that the current encoders also were not able to provide sufficient resolution for K-band pointing.

The IVS has recently brought out resolutions requiring stations to monitor weather data and conduct gravitational deformation surveys. It was indicated that thermal expansion modelling could be improved by making use of temperature sensors mounted on the antenna structure. Instrumental stability, such as that of the hydrogen maser clock and phase and cable calibration systems, should be monitored on a continuous basis. Stations are also required to conduct local tie surveys to accurately determine the axis offset (AO), VLBI reference point and position of all antennas on site and to accurately tie the antennas together.

Figure 3.3 HartRAO 26 m antenna west end of declination shaft with encoder removed. Photo credit: J. Grobler.

Figure 3.4 Bearing at west end of declination shaft shows displacement of ± 10 mm. Photo credit: P. Mey.

3.2 POSSIBLE SOURCES OF ERROR IDENTIFIED BUT NOT INVESTIGATED IN THIS STUDY

Sources of error identified as requiring priority treatment, but not forming part of this study, are briefly discussed here and possible courses of action are suggested.

3.2.1 Pointing model

In an attempt to compensate for pointing inaccuracies, a pointing model is applied in observations of the HartRAO 26 m and 15 m antennas. A pointing model attempts to correct for pointing offsets due to systematic (repeatable) errors, such as mechanical misalignment and gravitational deformation of the antenna. The pointing model is determined by observing a large number of well distributed radio sources with accurately known positions and performing a least-squares fit on the pointing offset data to derive coefficients for the terms of the pointing equation, which normally comprise the RF collimation error, axis skew and tilt, encoder fixed offset, gravitational sag and residual error due to refraction as well as any other systematic errors unique to the antenna (*ad hoc* terms). The pointing model cannot correct for stochastic (random) errors caused by wind

Department of Geology, Geoinformatics and Meteorology
University of Pretoria

and thermal loading, and pointing observations should therefore be conducted on a regular basis under varying environmental conditions.

One of the highest priorities for the HartRAO 26 m antenna is to update the current pointing model, which has not been updated since July 2015. The pointing model can however only be updated once the bearing has been replaced and the new encoders have been installed. In the meantime, it should be investigated whether the bearing's movement might be contributing to pointing errors. After the recent spate of non-detections on the HartRAO 15 m and AGGO 12 m baseline, the Bonn correlator requested that HartRAO Operations investigate the 15 m antenna's pointing. A new pointing model was subsequently generated and installed on the 15 m antenna, but the correlator report for the first session after the update to the pointing model once again indicated several non-detections in both S- and X-band. A possible error in the atmospheric refraction correction component of the pointing model is currently under investigation. It might be responsible for the 15 m antenna's persisting non-detections and would also degrade the pointing of the 26 m antenna.

3.2.2 Bearing and encoders

Antenna axes rotate on bearings, and encoders measure the position of the rotation axes and thus of the antenna. Mechanical inaccuracy of bearings as well as encoder errors and resolution therefore influence the pointing accuracy of an antenna.

In an upgrade of the main parabolic reflector of the 26 m antenna during 1998 to 2005, perforated surface panels were replaced with solid panels, which increased the load on the bearings and can influence the expected lifetime of the bearings. After 47 years of operation, the 26 m antenna suffered a critical failure of the south polar bearing in 2008, which caused the polar shaft to sag by more than 1 cm. There were also pointing anomalies observed around the time of the failure which can be attributed to the degradation of the polar shaft bearing. After the 26 m antenna was repaired and a new bearing installed, a survey was conducted in 2010 to confirm that the polar shaft had been returned to the correct position. A failing west declination shaft bearing on the 26 m antenna was

discovered in 2019, whilst testing the resolution and accuracy of a new encoder. Damage to a flexible coupling connecting the encoder to the west declination shaft indicated a shift along the shaft. A micrometer dial gauge shows the bearing to be sliding back and forth axially along the declination shaft by ± 10 mm with a change in antenna orientation.

The current aged encoders have been failing and misreading intermittently. After increasing a marginal power supply voltage and further software improvements, the reliability of the encoders returned to acceptable levels in 2020. However, the current 19-bit encoders on the declination and polar shafts provide insufficient resolution for K-band pointing. New higher resolution 26-bit encoders were procured before discovery of the failing bearing. The failing bearing is however preventing the new encoders from being tested. It would also make sense to implement a more accurate pointing model only after installation of the new encoders.

A sensor has been installed to monitor the movement of the declination bearing to determine whether it is deteriorating and to motivate for its repair. The sensor is measuring along the declination axis. Movement along the axis would not have a significant effect on pointing offsets, unlike movement orthogonal to the axis. A strategy should therefore be developed to investigate possible orthogonal motion of the failing bearing and its impact on the 26 m antenna's pointing.

3.2.3 Structural effects

Dish surface accuracy and antenna pointing accuracy are degraded by panel fabrication errors and misalignments, optical misalignment as well as by distortions, deformations and deflections caused by thermal, gravitational and wind loading effects. These loading effects give rise to antenna structural instabilities, displacing the VLBI reference point and introducing path delay errors at the millimetre level.

Due to the stringent requirements placed on dish surface accuracy at the higher K-band observing frequency, it is the 26 m antenna's performance at 22 GHz that is impacted most by these sources of error. The replacement of the perforated surface panels of the 26 m

antenna's main parabolic reflector with solid panels with lower surface error was completed in 2003. It was followed by initial mechanical panel alignment with theodolite and tape measure and realignment of the sub-reflector in 2004. Microwave holography was performed in 2007 and indicated that the dish's accuracy now allowed for higher frequency observations at 22 GHz (Klein, 2008). Holography tests, during which the 22 GHz receiver had been removed and two surface panels adjusted, were also conducted at the end of 2017 but was not completed, providing insufficient data for a high-resolution image. Recent non-detection of radio sources during ICRF K-band observations as well as a significant declination pointing offset (suspected of being caused by differential heating of support beams) and the appearance of extended coma sidelobes (caused by gravitational deformation of the dish surface) during 22 GHz gain calibration observations, indicate that the 26 m antenna is no longer able to attain the required dish surface accuracy at 22 GHz. Further suspected causes for the mediocre performance at 22 GHz are surface panels that might not have been reset accurately after the 2017 holography campaign as well as gravitational deflection of the sub-reflector relative to the primary reflector and its focus.

For the smaller 15 m antenna, operating exclusively at the lower geodetic S/X frequency bands, a measurement campaign and finite element analysis (FEA) conducted in 2007 (Bester, 2007) and a microwave holography campaign conducted in 2010 during its experimental operation as Karoo Array Telescope (KAT) prototype, confirmed that it was performing within specification. Recent non-detections in geodetic VLBI sessions are suspected to be due to pointing issues. Dry patches on the 15 m antenna's composite reflector surface caused water ingress, necessitating a surface repair in 2016 which could have impacted on the surface accuracy. Structural and performance analyses of the VGOS antenna conducted in 2016 and 2017 (Eisenträger, Herold and Hartmann, 2016 and Eisenträger, Herold and Kreth, 2017), making use of FEA, indicated that the VGOS antenna satisfied design and performance specifications.

The smaller 15 m and VGOS antennas with their solid concrete pedestals are less affected by gravitational and thermal deformation than the much larger 26 m antenna with its steel structure. The VGOS antenna was designed to minimise the effects of gravitational and thermal deformations. However, thermal expansion is now a conventional model in IVS

data analysis, while a recent IVS resolution requires that all IVS antennas be surveyed for modelling of gravitational deformation. A possible course of action for modelling thermal and gravitational deformation of the HartRAO antennas is discussed forthwith.

Thermal deformation:

Thermal deformation causes differential expansion and contraction of the antenna structure, which displaces the VLBI reference point, and requires modelling in VLBI data analysis. A thermal expansion model derived for the 26 m antenna (Nothnagel, Pilhatsch and Haas, 1995) was improved and extended to include all antennas in the IVS network (also the HartRAO 15 m antenna) and is now a conventional model in IVS data analysis (Nothnagel, 2009). This model incorporates dimensions for the antenna construction elements, expansion coefficients for the material of the antenna structure (steel, concrete), *in-situ* measurements of air temperature, time delay between change in air temperature and expansion of the antenna structure, and a global reference temperature, to arrive at a delay correction. Wresnik *et al*. (2007) recommended the installation of temperature sensors on antenna structures. They found modelled corrections to agree better with local thermal deformation measurements when they used the temperature of the antenna structure rather than that of the surrounding air. The 26 m antenna already has 10 temperature sensors mounted at various points on its support structure. These sensors were installed to determine whether any correlation could be found between structural temperature variations and an observed diurnal pointing variation. The VGOS antenna also has several temperature sensors mounted on its structure, which could be used to derive a thermal expansion model for the antenna. Temperature sensors should be installed on the 15 m antenna's structure. The IVS thermal expansion models for the 26 m and 15 m antennas should be investigated and compared with local thermal deformation measurements to arrive at improved models for thermal deformation. It might also be possible to employ thermal imaging to determine thermal deformation of the three antennas.

Gravitational deformation:

Gravitational deformation of antenna structures introduces elevation-dependent variations in the signal path length and height of the VLBI reference point at the centimetre-level for large antennas. The IVS has brought out a resolution in 2019 recommending that all IVS antennas be surveyed for modelling of gravitational deformation. Such a survey should at the very least include measurements of elevation-dependent focal length and variations in the distance between the vertex of the main reflector and sub-reflector or prime-focus feedhorn (IVS, 2019). Gravitational deformation models do not exist for any of the HartRAO antennas. However, models have been produced for six IVS antennas surveyed thus far. These models are all based on the model by Clark and Thomsen (1988) in which gravitational deformation causes signal path length variations due to displacements of the primary reflector and receiver and changes in focal length. If certain input parameters, such as the focal length and edge tapering of the illumination function (Sarti and Abbondanza, 2010), are known, some of these models (*e.g.* Sarti *et al.*, 2011; Artz, Springer and Nothnagel, 2014) could possibly be applied to at least the 15 m azimuth-elevation (az-el) antenna. For the az-el mounted 15 m and VGOS antennas, the elevation axis bears the gravitational load and gravity acts normal to the horizontal azimuth axes. For the polar-mounted 26 m antenna, gravity does not act in the same plane and the gravity vector rotates relative to the backing structure of the dish and with respect to the quadrupod legs. Gravitational deformation of the 26 m antenna is therefore more complex and will have to be calculated using a finite element model (FEM). A gravitational deformation model has been derived for one of the VGOS Onsala twin telescopes (OTT) (Lösler, Haas and Eschelbach, 2019). The possibility of adapting this model to the HartRAO VGOS antenna, which is of similar design, should be investigated.

Except for thermal and gravitational surveys that should be conducted for all the HartRAO antennas, a comprehensive holography campaign would probably also be necessary for determining dish surface accuracy and possible panel misalignment as well as alignment of the primary reflector, sub-reflector and feed on the 26 m antenna. However, the first step in determining the contribution of structural effects to the error budget of astrometric and geodetic VLBI would be to investigate the various techniques employed to measure the

position, dimensions, separation, deformation, distortion, deflection, displacement and misalignment of antenna structural components, including the antenna optics – primary reflector, sub-reflector (quadrupod), vertex and feed/receiver. The most suitable and cost-effective measurement techniques, instruments and sensors should then be identified from current techniques in use – holography, photogrammetry (also using unmanned aerial system (UAS) / drone), terrestrial survey, terrestrial laser scanner, laser tracker, total station, thermal imaging, thermal and electronic distance measurement sensors and inclinometers. Although wind speeds at HartRAO are for the most part very low and wind gusts occur infrequently, wind loading effects on the antenna structure, especially that of the larger 26 m antenna, should also be investigated.

3.2.4 Antenna foundations

Stable antenna foundations are required for stable antenna positions. Geotechnical surveys have been conducted for each of the HartRAO antennas to ensure founding on the same solid bedrock connecting to the continental plate. There is however some concern regarding possible ground instability and hydrology loading associated with the foundation of the 15 m antenna. The engineering geological investigation for the 15 m antenna recommended founding on unweathered, medium-hard andesite volcanic rock at a depth of ~1.8 m (Holland-Muter, 2006). According to Combrinck and Schmidt (1998), andesite's weathering leaves boulders suspended in the soil that could be founded on by mistake. Kleinhans (2002) also notes that irregular weathering of andesite causes solid outcrops to occur within metres of a deep soil profile and warns that andesite core-stones and 'floaters' could result in a misleading interpretation of the bedrock depth and geotechnical conditions. One of the test boreholes was drilled through a 'floater', next to which the foundation was eventually laid. The geological investigation also revealed a fluctuating water table to be present during the rainy season. A Satellite Laser Ranging (SLR) calibration pier in close proximity to the 15 m antenna recently displayed a sudden positional shift of several centimetres, believed to be caused by the movement of underlying clay material during the rainy season. Seasonal variation in underlying groundwater may cause antenna positions to vary. Seasonal variation of ground water and soil moisture and their effect on foundation stability and antenna position should be

investigated with a view towards determining a local hydrological loading model for HartRAO. For determining intra-complex baseline vectors, such as for the short baseline ties between the HartRAO antennas, it is essential that the antennas are attached to the same stable bedrock and that their positions remain stable (Jacobs *et al*., 2017). Local instabilities may be revealed by site velocities that differ between the antennas (Munghemezulu *et al*., 2014).

3.2.5 Hydrogen maser clock

The hydrogen maser clock provides the necessary accuracy and stability as reference timing system for VLBI observations and analysis, and is the currently preferred fundamental frequency standard in astrometric and geodetic VLBI. However, these station reference clocks may exhibit instabilities and drifts, contributing to the instrumental error and corrupting delay measurements. The performance of the HartRAO hydrogen maser clock currently being used for astrometric and geodetic VLBI on both the 15 m and 26 m antennas, the iMaser72 clock, was evaluated in 2016 by comparison with a GNSS UTC time receiver and a frequency comparator (Munghemezulu *et al*., 2016). It was reported to be performing at the required level for astrometric/geodetic VLBI. However, residuals displayed a pattern which may have been caused by thermal variations in the maser room, and it was cautioned that the room should be kept at constant temperature to minimise frequency fluctuations. It was also advised that the hydrogen maser clock performance be monitored and corrected for drifts and ageing characteristics. A similar performance evaluation of the HartRAO maser clock should be carried out on a regular basis.

3.2.6 Phase and cable calibration systems

Phase and cable calibration systems (phase-cal and cable-cal) allow for monitoring and calibration of instrumental phase and delay changes as well as cable length changes. The cable-cal system measures cable length changes in all signal-carrying cables, including those of the phase-cal system and cable wrap as well as in the cable carrying the frequency reference signal from the hydrogen maser. Phase and delay variations, due to temperature changes and flexing of cables, cause errors in the receiving systems' instrumentation,

electronics and cabling, which affect the VLBI signal delay and limit the accuracy of astrometric and geodetic VLBI results. Intermittent phase-cal and local oscillator (LO) instability in 2015 pointed at possible damage to the 15 m antenna's cables through the antenna's cable wrap mechanism. In the following years, various cables were damaged by the faulty cable wrap mechanism and had to be replaced before the azimuth wrap was finally upgraded in 2019. The 26 m antenna displayed intermittent phase-cal and cable-cal values due to a loose connection in the cable between the antenna and the ground units in 2016. Cables subjected to frequent twisting, bending and stretching should be investigated for possible correlation between phase-cal delay and cable-cal measurements with antenna orientation, as this could bias the delay in a specific direction which may result in an error in the estimated station position. Cables should be inspected for damage and faulty connections on a regular basis and should be well-insulated from thermal effects. The diurnal variation of the phase-cal phase and cable-cal amplitude and phase should be monitored to display the expected thermal variations. Spurious signals that corrupt phase-cal phase and amplitude should be detected and ameliorated. IVS procedures for phase calibration and cable measurement system tests (as detailed in the VLBI System Documentation for the Mark IV Field System, GSFC, 1993) as well as general Field System (FS) *systests* procedures for instrumental and stability tests (as detailed in various station VLBI equipment testing documentation for continuous (CONT) VLBI campaigns and also in IVS Technical Operation Workshops Notes), should be carried out on a frequent basis. The FS *systests overnite* procedure allows for extended automated monitoring of the stability of station auxiliary data, such as phase and cable calibration. The possibility of installing a cable calibration system for the 15 m antenna should be investigated.

3.3 POSSIBLE SOURCES OF ERROR INVESTIGATED IN THIS STUDY

It was possible to investigate the following sources of error in this study. These are briefly discussed here and more thoroughly addressed in the chapters to follow.

Department of Geology, Geoinformatics and Meteorology
University of Pretoria

3.3.1 Meteorological surface data

Observations at higher frequencies, such as 22 GHz, are also degraded by inclement weather conditions. This requires an opacity correction to be applied in the analysis of 22 GHz gain curve calibration observations for determining the 26 m antenna's PSS, which is used to convert from antenna temperature (gain) due to an observed source to a source flux density. The PSS is an indicator of the antenna's aperture efficiency and, except in those instances where antenna hardware changes have taken place, is supposed to remain constant. Since the opacity correction is calculated from surface meteorological measurements, unreliable meteorological data would lead to incorrect antenna gain and PSS values for the 26 m antenna and ultimately to incorrect source flux densities. Unexplained steps and a recurring pattern observed in the PSS as well as a decrease in antenna gain during recent gain calibration observations with the 26 m antenna prompted an investigation of HartRAO meteorological data as a possible source of error. Surface meteorological data are also used in astrometric/geodetic VLBI for determining troposphere delay and thermal deformation models for all of the HartRAO antennas. In these instances, degraded meteorological data could lead to inaccurate determination of station heights and VLBI reference points. A resolution regarding monitoring and submission of meteorological data has already been approved by the IVS Directing Board. HartRAO surface meteorological data as a possible error source is addressed in *Chapter 4 – HartRAO Weather Data*.

3.3.2 Antenna calibration and pointing

Of particular concern at the HartRAO station currently is the imminent failure of a bearing on the declination shaft of the 26 m antenna and its influence on the pointing accuracy, especially at the higher observing frequencies. The failing bearing is also preventing the installation of high-resolution encoders and an update of the antenna pointing model. Astrometric observations towards celestial reference frame (CRF) realisation at the higher 22 GHz observing frequency place great demands on the 26 m antenna's pointing accuracy. Most of the error sources identified are therefore associated with the larger 26 m antenna. Non-detection of radio sources as well as a significant declination pointing offset

at K-band prompted an investigation of the pointing performance and gain of the 26 m antenna and are addressed in *Chapter 5 – Antenna Calibration and Pointing*. Also investigated in the aforementioned chapter are optimal settings for the sub-reflector focus position of the 26 m antenna as well as a possible correlation between degraded pointing and differential heating of the 26 m antenna support structure.

3.3.3 Antenna axis offset

The VLBI reference point of an antenna is located at the intersection of the antenna's rotation axes. In cases where the rotation axes do not intersect, such as for the HartRAO 26 m and 15 m antennas, an antenna AO exists. An error in the AO would affect the antenna's VLBI reference point and cause an error in the station coordinates. Although the AO is considered to be fixed, major antenna repairs, such as the bearing replacement on the 26 m antenna in 2010, could conceivably cause a change in the AO. In order to reach the VGOS goal of 1 mm accuracy in station coordinates, the AO needs to be known with sub-millimetre accuracy. In *Chapter 6 – Antenna Axis Offset*, the AO of the HartRAO 26 m and 15 m antennas are estimated by VLBI analysis and compared with AO values measured in a local ground survey.

3.3.4 Local tie

The ability to reach the VGOS goal of 1 mm baseline accuracy on the short ~113 m baseline between the HartRAO 26 m and 15 m antennas at least, is addressed in *Chapter 7 – Baseline Length and Local Tie*. The 26 m antenna's VLBI reference point serves as reference point for the co-location of the 15 m and VGOS antennas. The VLBI reference points of the 15 m and VGOS antennas need to be accurately tied to the VLBI reference point of the 26 m legacy antenna with its much longer and stable position time series. Short baseline (SBL) sessions were conducted to determine the local tie and measure the baseline length between the HartRAO 26 m and 15 m antennas. The baseline length estimated in VLBI data analysis was compared with that measured in a local ground survey. By running the local tie sessions between the 26 m and 15 m antennas before and after bearing repair/replacement on the 26 m antenna, it should be possible to ascertain whether any

change has occurred in AO, VLBI reference point and ultimately antenna position. Such local baseline experiments also allow for monitoring local ground motions and for discovering station-specific errors (Plank, 2014).

3.4 SUMMARY

In this chapter, HartRAO station-specific errors of particular concern at the station or in the wider IVS community were identified in consultation with HartRAO Engineering, Operations and astronomers as well as by taking IVS requirements into consideration. These errors are summarised in Table 3.1 Possible sources of error specific to the HartRAO site and HartRAO 26 m and 15 m antennas, which could be limiting the accuracy of astrometric/geodetic VLBI results. Entries in bold are further investigated in this study.Entries in bold are further investigated in this study.

Table 3.1 Possible sources of error specific to the HartRAO site and HartRAO 26 m and 15 m antennas, which could be limiting the accuracy of astrometric/geodetic VLBI results. Entries in bold are further investigated in this study.

Error source	Problem	Antenna
Pointing model	outdated; error in atmospheric refraction correction	26 m, 15 m
Bearing and encoders	failing; insufficient resolution (encoders)	26 m
Structural effects	dish surface inaccuracy; panel and optical misalignments; thermal and gravitational deformation	26 m, 15 m
Antenna foundations	ground instability; hydrology loading	15 m
Hydrogen maser clock	instability; drift	Station
Phase and cable calibration systems	instability; dependence on antenna orientation	26 m, 15 m
Weather data	**inaccurate, unreliable; errors in opacity and refractions corrections, troposphere delay and thermal deformation models**	**Station**
Antenna calibration and pointing	**non-detections; significant declination pointing offset; extended first sidelobes; optimal sub-reflector focus position; differential heating of support structure**	**26 m**
Antenna axis offset	**possible change in due to antenna repairs (26 m); inaccurate VLBI reference point, station coordinates**	**26 m, 15 m**
Local tie	**accurate tie of 15 m VLBI reference point to that of 26 m required**	**26 m, 15 m**

Department of Geology, Geoinformatics and Meteorology
University of Pretoria

CHAPTER 4 HARTRAO WEATHER DATA

Accurate and continuous meteorological data are of great importance in geodetic and astrometric VLBI processing and analysis as well as in the processing and analysis of data from other space geodetic techniques and from astronomical single-dish and VLBI. The meteorological sensors at HartRAO provide *in-situ* measurements of barometric pressure, ambient temperature, relative humidity as well as wind speed and direction.

The IVS Network Coordinator recently requested updated information regarding IVS station meteorological data. This request was followed by a newly approved IVS resolution which recommended continuous recording of meteorological data at network stations and delivery of such data to the Wettzell Seamless Auxiliary Data Archive (IVS, 2021a). At the same time, unexplained step changes in the HartRAO 26 m antenna's point source sensitivity (PSS) at 22 GHz were also detected. Observations at higher frequencies, such as 22 GHz, are particularly weather-sensitive. An opacity correction therefore has to be applied to the observations in the analysis for determining the antenna's PSS. The opacity correction is dependent on surface meteorological measurements recorded during the observations. The atmospheric refraction correction (not addressed in this study), which forms part of the antenna pointing model and is also dependent on surface meteorological measurements, came under review at this time as well. The aforesaid prompted an investigation of meteorological sensors and data at HartRAO.

4.1 WEATHER PARAMETERS FOR ASTROMETRIC AND GEODETIC VLBI

High-quality meteorological data are of great importance for astrometric and geodetic VLBI processing and analysis. Accurate and continuous meteorological data are required for accurate determination of troposphere delay and antenna thermal deformation. For

troposphere delay, surface measurements of barometric pressure are used to determine the *a priori* zenith hydrostatic delay (ZHD). A pressure change of 1 mbar corresponds to a path delay of ± 2.3 mm (Teke, Nilsson and Böhm, 2013). For sub-mm accuracy of the ZHD, an accuracy of 0.1 mbar in the measurement of surface pressure is required. An error in pressure of 3 mbar results in an error in estimated station height of ± 1 mm (J. Böhm, personal communication, 12 March 2021). For antenna thermal deformation, surface measurements of temperature are used to determine structural deformation of antennas due to variations in temperature. This causes variations in height of the VLBI reference point ranging from 4-6 mm (Nothnagel, 2009).

Meteorological sensors providing *in-situ* measurements of ambient temperature, relative humidity, barometric pressure as well as wind speed and direction for astrometric and geodetic VLBI (as well as for all other HartRAO 26 m and 15 m antenna observations) are listed in Table 4.1. During a geodetic/astrometric VLBI session, the temperature, pressure and relative humidity values are recorded in the station log file in response to the Field System (FS) '*wx*' command for each observation.

The state of the HartRAO meteorological sensors providing *in-situ* measurements for astrometric and geodetic VLBI, and the quality of historical and current meteorological data from the HartRAO sensors and its possible degradation over time were investigated.

4.1.1 Methodology

Once the HartRAO meteorological sensors (henceforth referred to as the *wx* sensors) had been located and their operational environment and condition had been inspected, the HartRAO antenna log books, IVS station log files and sensor technical data sheets were consulted to establish possible previous replacement or calibration of the *wx* sensors as well as performance and accuracy specifications. The HartRAO IVS station log files as well as ground survey reports assisted in determining *wx* sensor proximity to the 26 m and 15 m antennas respectively as well as *wx* sensor height above ground level and above or below the antenna reference points.

The quality of historical and current meteorological data from the *wx* sensors, and its possible degradation over time, were investigated by comparison with long-term meteorological data provided by the Paroscientific MET3 of the International GNSS Service (IGS) GNSS reference station HRAO. The HartRAO IGS station log file as well as ground survey reports were consulted to determine height above ground level, proximity to and height above the *wx* sensors as well as accuracy specifications. Data sets of the *wx* sensors and the MET3 were also compared to short-term data from a new Paroscientific MET4 test installation, used as a calibrator. The MET4 technical data sheets were consulted to determine the accuracy of its sensors.

4.1.2 Results and discussion

Investigation of HartRAO meteorological sensors:

HartRAO meteorological sensor characteristics are summarised in Table 4.1. The temperature and humidity sensors are enclosed in a Stevenson screen located on the lawn between the control room building and the 26 m antenna, the pressure sensor is located in the control room and the anemometer is located on the roof of the control room building (see Figure 4.1 and Figure 4.2). All sensors are located ~50 m from the 26 m antenna and ~100 m from the 15 m antenna. The *wx* sensors have not been calibrated or upgraded for the past 10 years. The temperature and humidity sensors were replaced and the pressure sensor was calibrated at the beginning of September 2011, just before the start of the CONT11 campaign.

Table 4.1 HartRAO meteorological sensors providing in-situ measurements for astrometric and geodetic VLBI.

Parameter	**Instrument**						
	Manufacturer	**Model**	**Sensor**	**Accuracy**	**Calibrated (c) / replaced (r)**	**Height above ground level**	**Height above (a) / below (b) antenna reference point**
Ambient temperature	Huato	HE400-EX	External	± 0.5 °C	2011-09-02 (r)	~1 m	15m: ~5.5 m (b) 26m: ~12 m (b)
Relative humidity				± 0.5%			
Barometric pressure	Setra	270	Variable capacitance	± 0.05% FS	2011-09-05 (c)	~3.5 m	15m: ~2.9 m (b) 26m: ~9.2 m (b)
Wind	RM Young Wind Monitor	05103L	Mechanical	Speed: ± 0.3 $m.s^{-1}$ Direction: ± 3°	Unknown	~10 m	15m: ~3.5 m (a) 26m: ~3 m (b)

Figure 4.1 The Stevenson screen on the lawn in the foreground houses the temperature and humidity sensors for astrometric and geodetic VLBI.

Figure 4.2 Location of HartRAO meteorological sensors and MET3 and MET4 units with respect to the 15 m and 26 m antennas.

Meteorological sensors and MET3 comparison:

The MET3 was installed in 2005 and is located on the roof of the facility's building at a height of ~6 m above ground level (see Figure 4.3). It is located ~2.5 m above the barometer in the control room and ~30 m away. It is located ~5 m above the temperature and pressure sensors in the Stevenson screen and ~50 m away. Accuracies of ± 0.5 °C, ± 0.1 mbar and ± 2% are quoted in the IGS station log file for temperature, pressure and relative humidity respectively.

Figure 4.3 The Paroscientific MET3 unit of the HRAO IGS GNSS station used in the comparison is located on the roof of the facility's building. The new MET4 is temporarily installed ~12 m behind the MET3 (obscured by MET3 in image).

The difference between the MET3 and HartRAO sensor values for both temperature and pressure displays a near-linear instrumental offset and drift for the period just before and shortly after replacement of the temperature sensor and calibration and re-installation of the pressure sensor at the end of August / beginning of September 2011 (see Figure 4.4 and Figure 4.5). For the pressure, a minimum resolution granularity due to data collection and storage – a resolution of 0.1 mBar for *wx* and also for GNSS Receiver INdependent EXchange (RINEX) format – is apparent. Some pressure sensors (*e.g.* MET3 and MET4) provide much higher resolution, and data resolution may have to be reviewed. The HartRAO relative humidity sensor persisted with an incorrect lower ceiling value, reaching a new low after sensor replacement in 2011, followed by a sudden rise in ceiling value in June of 2015 (see Figure 4.6). Sulphur from on-site diesel generators might be responsible for sensor contamination.The relative humidity sensor has never reached full-scale however. It needs to be investigated whether this is due to a wiring problem or a problem with the sensor itself. After the 2011 sensor replacement, a gap also appears in the data at ~70%, which could possibly be ascribed to electronic scaling and a faulty analogue-to-digital converter (ADC).

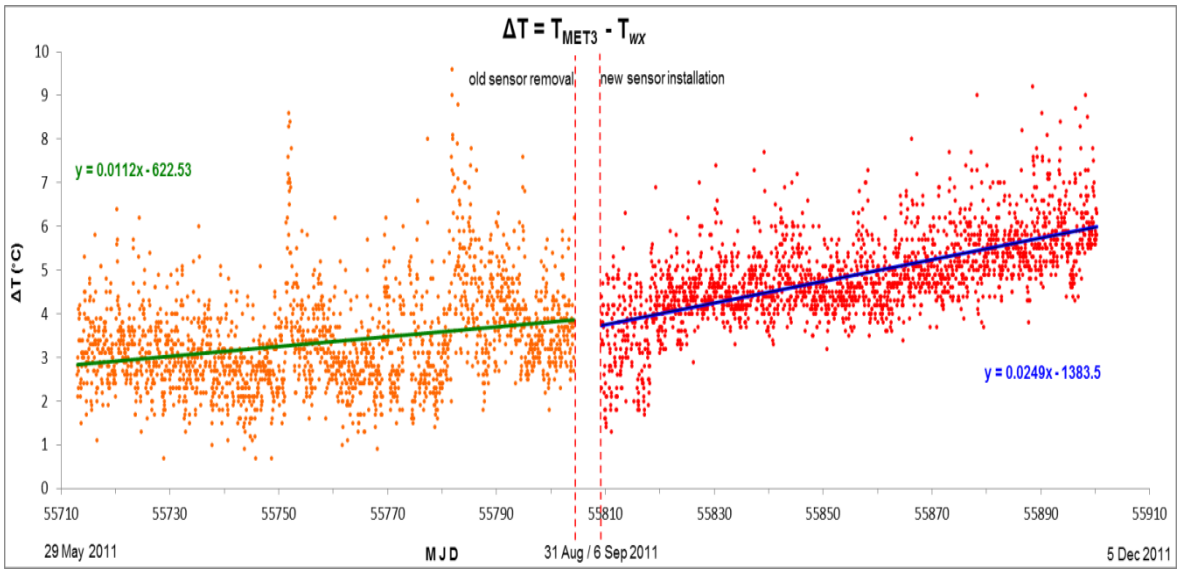

Figure 4.4 The temperature difference between the IGS GNSS MET3 and HartRAO on-site sensor (wx) displays a near-linear instrumental offset and drift for the period before and after sensor replacement in 2011.

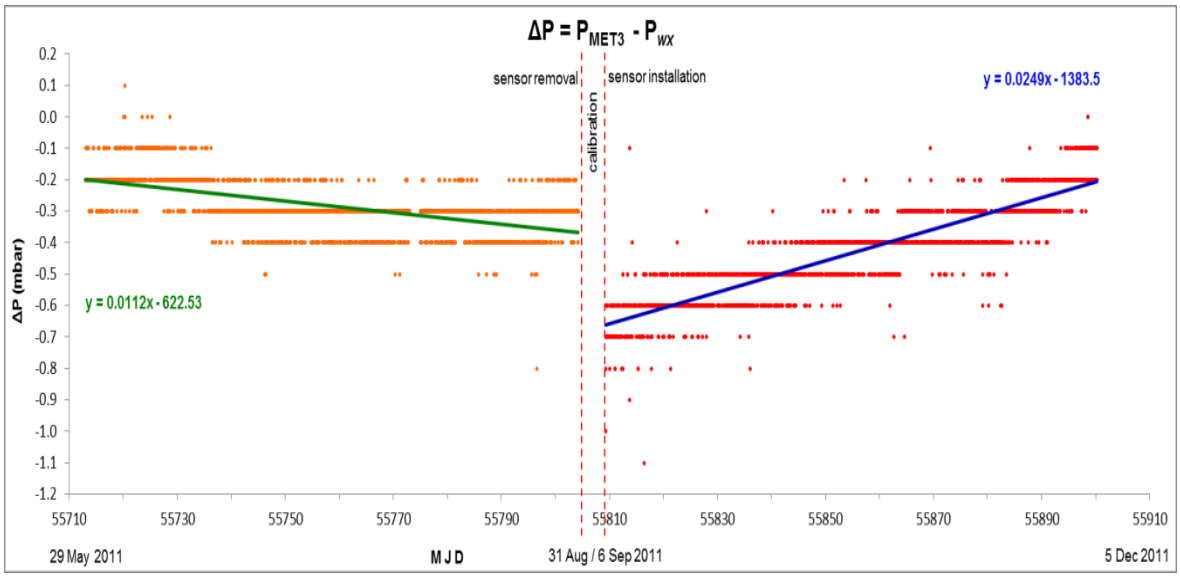

Figure 4.5 The pressure difference between the IGS GNSS MET3 and HartRAO on-site sensor (wx) also displays a near-linear instrumental offset and drift for the period before and after sensor calibration in 2011.

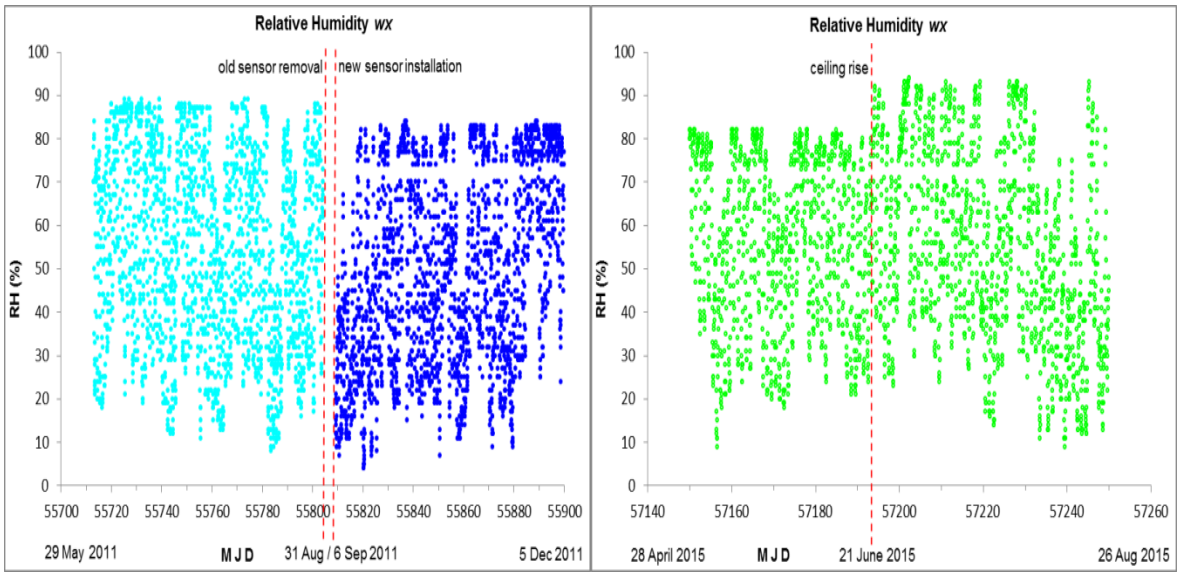

Figure 4.6 Left: The relative humidity from the on-site sensor (wx) displays an incorrect lower ceiling value before and after replacement in 2011 and also a gap in the data at ~70% after replacement. Right: During 2015, the persistent lower ceiling value increased to ~ 90%.

Meteorological sensors and MET4 comparison:

At the start of December 2020, the MET4 was installed on the roof of the facility in the vicinity of the MET3 (~12 m away) and at a height of ~5 m above ground level. Accuracies of ± 0.5 °C, ± 0.08 mbar and ± 1% are indicated for temperature, pressure and relative humidity respectively. The differential offsets in temperature between the HartRAO sensor and the MET4, as displayed in Figure 4.7, may be due to roof heating and radiation, caused by the temporary location of the MET4. The slight offset in pressure between the HartRAO sensor and the MET4 can be explained by the difference in height above ground level (~4 m). The HartRAO relative humidity sensor persisted in displaying a lower ceiling value, possibly due to a combination of effects (see Figure 4.8).

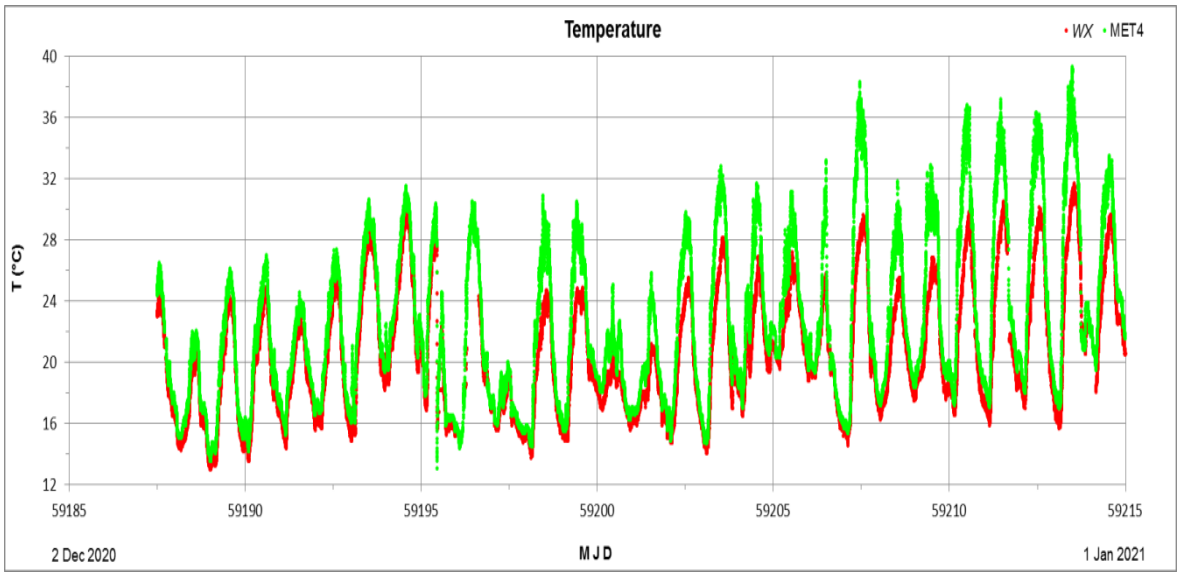

Figure 4.7 The non-linear temperature offset between the new MET4 unit and on-site sensor (wx) may be caused by heating and radiation due to the MET4's temporary location on the roof of the facility.

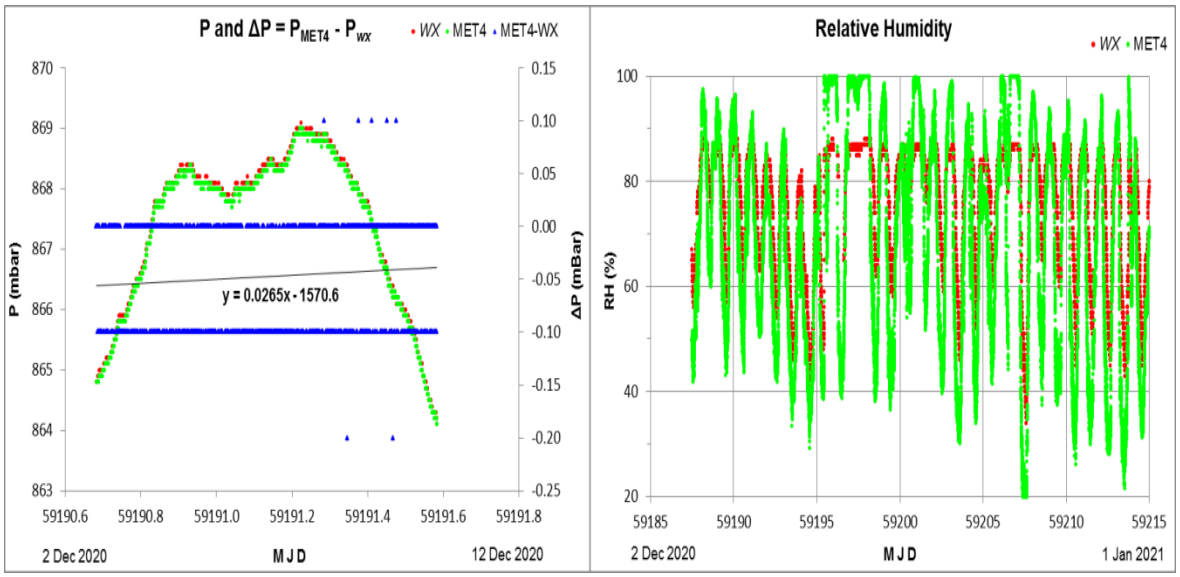

Figure 4.8 Left: The slight pressure difference between the MET4 and on-site sensor (wx) could be due to a difference in height between the two instruments. Right: Relative humidity readings from the on-site humidity sensor (wx) are clearly topping out when comparing it with readings from the new MET4 unit.

The investigation into HartRAO meteorological sensors/data revealed the need for calibration/upgrade/replacement. The installation of a full scientific-level meteorological sensor set and high-accuracy pressure sensors are being planned. Pressure laboratory standards will be acquired to enable in-house calibration of sensors.

Following advice of the scientific community, a further month-long comparison of the current HartRAO meteorological sensors with the new MET4 will be run in the interim. The MET4 unit is to be installed on a pole located next to the Stevenson screen at the height of the barometer in the control room. The MET4 will also be installed for a month next to the meteorological system of each of the collocated space geodetic techniques on-site (GNSS MET3, NASA and Roscosmos SLR MET4s) for further comparison. The exact position of each meteorological system will be determined for tropospheric ties to be applied in the comparison. Henceforth, all on-site meteorological data will be monitored and compared continuously.

Discussions are still underway deciding on the best location for the new MET4 unit. It will in all likelihood be installed at the reference height of the VGOS antenna with the Paroscientific pressure sensors being installed at the reference heights of 15 m and 26 m antennas (Heinkelmann, Böhm and Schuh, 2005). The current HartRAO meteorological sensor set used for astrometric/geodetic VLBI will be replaced/calibrated. It is also planned to include a Vaisala WXT533 rainfall and wind sensor as well as a Campbell Scientific CMP-3L Pyranometer to measure solar irradiance in the MET4 installation. The World Meteorological Organization (WMO) Commission for Instruments and Methods of Observation (CIMO) siting standards for siting and exposure of meteorological equipment (WMO, 2018) will be used as guidelines for the installations. A summary of pertinent guidelines appears in Table A.1 in Appendix A.

4.2 WEATHER PARAMETERS FOR SINGLE-DISH CALIBRATION

Accurate and continuous meteorological data are also required in order to apply accurate opacity corrections during calibration of the HartRAO 26 m antenna as well as to apply accurate elevation-dependent atmospheric refraction corrections for antenna pointing.

Single-dish calibration of the HartRAO 26 m antenna at 22 GHz is achieved by using Jupiter, for which the flux density is known, as calibrator source in order to determine the conversion factor or antenna PSS that should be used in converting from antenna temperature (Ta) in Kelvin (K) produced by an observed source to a source flux density in Jansky (Jy).

Observations at 22 GHz are extremely sensitive to the water vapour content of the atmosphere. An opacity / atmospheric absorption correction has to be applied in the analysis of 22 GHz gain calibration observations. Together with corrections for pointing inaccuracy and Jupiter's varying size as well as noise diode scaling factors, the atmospheric absorption correction allows for obtaining the corrected antenna temperature (Ta On corrected) produced by emission from Jupiter at the centre of the antenna's beam –

$$\text{Ta On corrected} = \text{Ta On} \times \text{atmospheric absorption correction} \times \text{other corrections [K]} \quad (4.1)$$

The antenna's point source sensitivity (PSS) in both the left and right circular polarisations (LCP and RCP) can then be determined from Jupiter's flux density and the corrected antenna temperature for Jupiter in the specific polarisation –

$$\text{PSS} = \text{Total planet flux density} / (2 \times \text{planet Ta On corrected}) \text{ [Jy/K/pol]} \quad (4.2)$$

The source flux density in each polarisation follows from the PSS as determined above and the corrected observed antenna temperature of the source for the specific polarisation –

$$S = \text{PSS} \times \text{source Ta On corrected [Jy]} \quad (4.3)$$

Surface meteorological measurements of temperature and humidity provided by the HartRAO *wx* sensors are recorded for each observation and used to determine the atmospheric absorption correction (ATM ABS COR) at the time of the observation as follows –

$$\text{ATM ABS COR} = e^{\text{TAU221} / \cos(\text{ZA} \times \pi / 180)} \quad (4.4)$$

where ZA is the zenith angle of the observation and TAU221 is the optical depth at 22.1 GHz –

$$TAU221 = 0.0140 + 0.00780 \times PWV \quad (4.5)$$

where PWV is the precipitable water vapour obtained from surface measurements of temperature (T) and relative humidity (RH) –

$$PWV = 4.39 \times RH / 100 / T \times e^{26.23-5416/T} \quad (4.6)$$

The faulty HartRAO relative humidity sensor could therefore conceivably lead to inaccurate atmospheric absorption corrections being applied to observations. This prompted an investigation of PWV values obtained from the HartRAO *wx* temperature and relative humidity sensor measurements, the derived atmospheric absorption corrections as well as the PSS obtained from the corrected antenna temperatures of the calibrator source used in the calibration of source observations and the impact on source flux density.

4.2.1 Methodology

The investigation consisted of comparing PWV and atmospheric absorption correction values calculated from temperature and relative humidity measurements by the HartRAO *wx* sensors over a year for the period 1 December 2019 to 30 November 2020 with PWV values calculated from temperature and relative humidity measurements by the MET3 sensors of the HRAO IGS GNSS station as well as with Global Positioning System (GPS) estimated PWV values for HRAO obtained from the SuomiNet GPS network for the corresponding time period. Suominet PWV is obtained by converting GPS signal delays caused by water vapour in the atmosphere to highly accurate integrated PWV estimates along the GPS ray path every 30 minutes (Ware *et al.*, 2000). In the comparison, an observation frequency of 30 minutes is thus used for all three sources of PWV. A zenith angle of 0° was employed to calculate the elevation-dependent atmospheric absorption correction.

Department of Geology, Geoinformatics and Meteorology
University of Pretoria

The investigation also consisted of comparing the PSS obtained from PWV and atmospheric absorption correction values from temperature and relative humidity measurements by HartRAO *wx* sensors during 22 GHz Jupiter gain calibration observations over the period 17 December 2017 to 2 April 2021 with the PSS obtained from Suominet PWV and atmospheric absorption correction values over the same time period. The maximum difference in PSS obtained from the two sources of PWV – observational *wx* and Suominet data – was used to establish the impact of applying an inaccurate PWV value for determining the atmospheric absorption correction, and thus the PSS used in the calibration of source observations, on the observed source flux density. The period 17 December 2017 to 2 April 2021 was chosen as it corresponds to the latest step change in the average PSS value for the 22 GHz Jupiter calibration data set stretching back to 2007. Although the PSS of the antenna is supposed to be a set value indicative of the antenna's aperture efficiency – Janskys of flux density required to produce an antenna temperature of 1 K in each polarisation – changes in the PSS do occur due to antenna hardware changes over the years. For the HartRAO 26 m antenna, two such steps in the average PSS are noticeable in the calibration data set – one starting on the 22nd of April 2014 when the ambient 22 GHz receiver was replaced by a cooled receiver and another caused by the removal of the 22 GHz receiver on the 12th of December 2017 for a holography campaign with reinstallation taking place on the 16th of December 2017.

4.2.2 Results and discussion

Comparison of precipitable water vapour and atmospheric absorption correction from wx sensor data and Suominet data:

In order to determine the effect of a suspected inaccurate humidity sensor reading from the HartRAO *wx* sensor on the determination of PWV and the atmospheric absorption correction applied in the calibration and analysis of 22 GHz observations, values derived from *wx* and MET3 sensor surface measurements of temperature and humidity as well as from Suominet PWV were compared for the period from 1 December 2019 to 30 November 2020.

The plots of yearly variation in the PWV and atmospheric absorption correction (see Figure 4.9) follow a similar seasonal pattern, as expected from the relation between these values, with maximum values occurring during the rainy summer months. The *wx* sensor and MET3 values are lower than the Suominet values in summer and higher during winter time. In comparison to the values derived from surface measurements of temperature and relative humidity for the *wx* and MET3 sensors, the Suominet PWV, being derived from GPS signal delays along the GPS ray path, provides a more accurate reflection of the water vapour content of the atmosphere above the antenna.

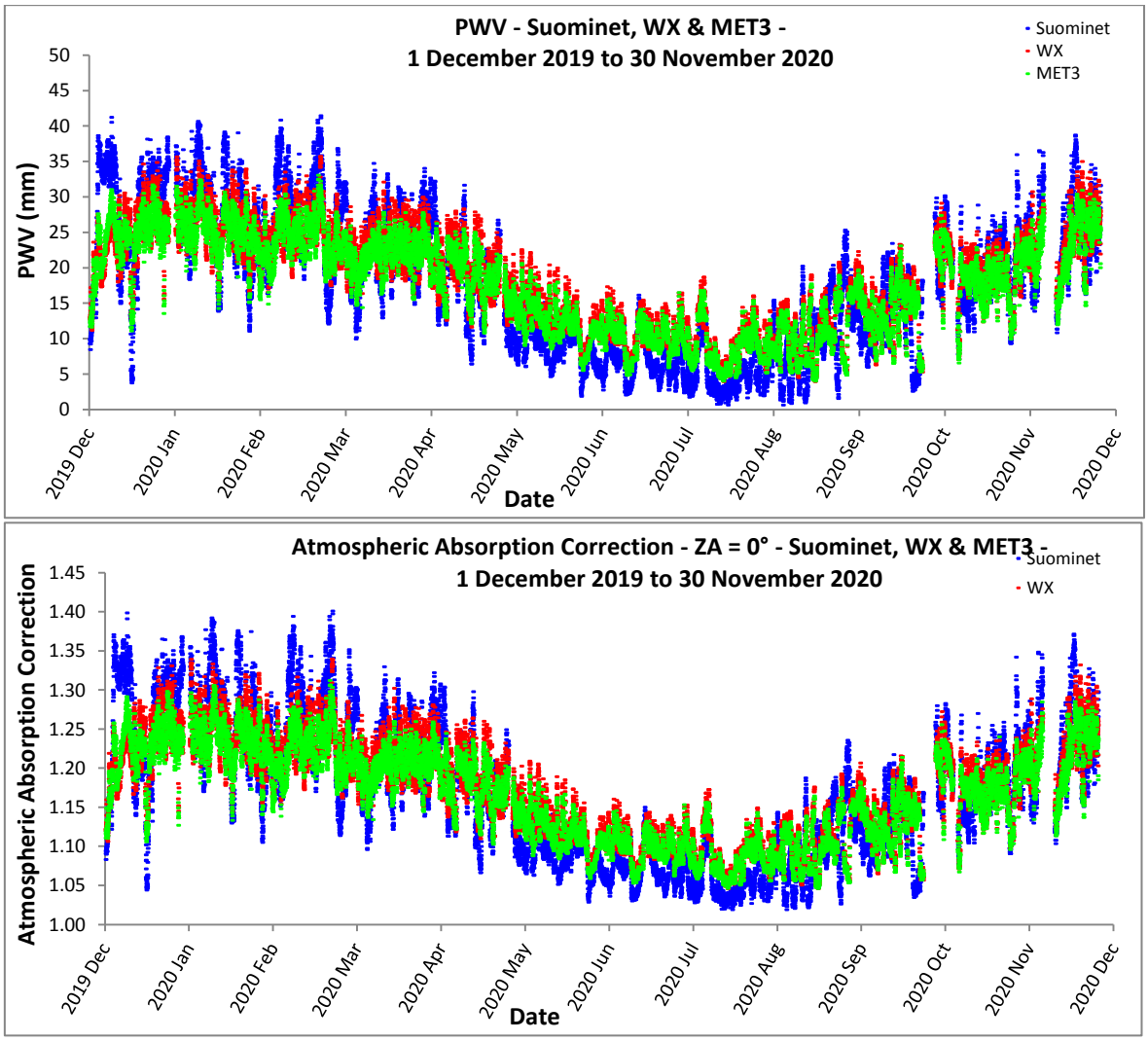

Figure 4.9 Yearly variation in precipitable water vapour (PWV, top) and atmospheric absorption correction (bottom) values from Suominet GPS-derived PWV data as well as from PWV calculated from wx and MET3 sensor surface temperature and humidity measurements for the period 1 December 2019 to 30 November 2020.

The plots of the difference in atmospheric absorption correction (and similar for the difference in PWV) between Suominet and the *wx* and MET3 sensors display a seasonal pattern of greater differences in the values for summer than for winter (see Figure 4.10) with the maximum difference occurring at the start of spring (see Table 4.2). A similar pattern exists for the difference between the *wx* and MET3 sensors but here the maximum difference occurs during autumn and is much lower. Suominet values seem slightly lower during the winter months compared to values from the *wx* and MET3 sensors. Again, the Suominet values from integrated PWV are considered to be more accurate.

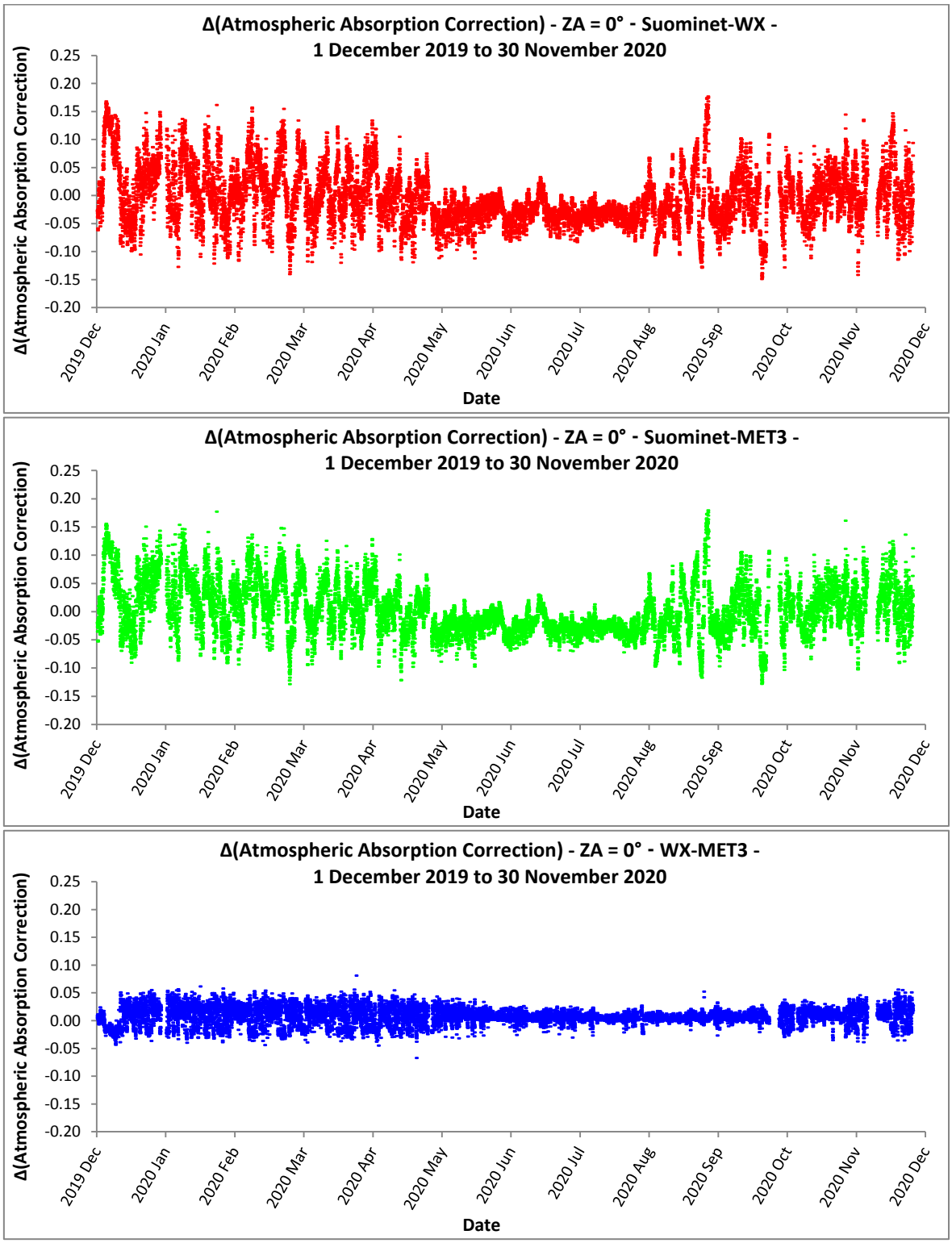

Figure 4.10 Difference in the atmospheric absorption correction between Suominet and wx sensors (top), Suominet and MET3 sensors (middle) as well as wx and MET3 sensors over the period 1 December 2019 to 30 November 2020.

Table 4.2 Maximum differences in precipitable water vapour (PWV) and the atmospheric absorption correction between Suominet and the wx and MET3 sensors as well as between the latter over a year.

	Maximum difference	
	ΔPWV (mm)	**ΔABSCOR**
Suominet-WX	+19.8 2020/08/31 02:15 UT	+0.18
Suominet-MET3	+20.1 2020/08/31 02:15 UT	+0.18
WX-MET3	+8.5 2020/03/26 06:15 UT	+0.08

Comparison of point source sensitivity and source flux density from wx sensor data and Suominet data:

In order to determine the effect of inaccurate PWV values, and therefore also inaccurate atmospheric absorption correction values, on the PSS used in the calibration of source flux densities at 22 GHz, PSS values derived from *wx* sensor surface measurements of temperature and humidity during 22 GHz Jupiter calibration observations over the period 17 December 2017 to 2 April 2021 were compared with PSS values derived from Suominet PWV at the corresponding time.

The plots for both PSS LCP and RCP show the PSS derived from Suominet PWV to lie slightly above that of the PWV from observational *wx* temperature and humidity sensor surface measurements over most of the time period (see Figure 4.11). The Suominet PWV values are therefore correspondingly lower than PWV values from the *wx* measurements during the observations. The slightly higher average PSS values in both LCP and RCP from Suominet PWV compared to that from PWV from *wx* surface measurements are indicated in

Table 4.3. The standard deviation, and thus the scatter, of the PSS in both LCP and RCP are similar for the two instances, indicating that using Suominet PWV would not necessarily offer an improvement in this regard. The maximum difference in PWV of 13.4 mm (with the *wx* PWV being the higher) for this time period would produce differences of 0.79 and 0.75 in PSS for LCP and RCP respectively. This lies within the respective errors for the average LCP and RCP PSS from *wx* PWV during the calibration observations. The maximum difference between PWV from the *wx* sensors and Suominet was used to predict the resulting difference in source flux density for sources with corrected antenna temperatures (Ta On corrected) in the range from 0.1 to 1 K. As displayed in the plot in Figure 4.12, should the *wx* PWV value be higher than the true value by 13.4 mm (with the Suominet PWV considered as truth here), it would cause the source flux density thus obtained to be lower than the true value by ~800 mJy for a 1 K source, which can be considered significant. The stronger the source, i.e. the higher the Ta On corrected, the greater the difference between the calculated and true value would be.

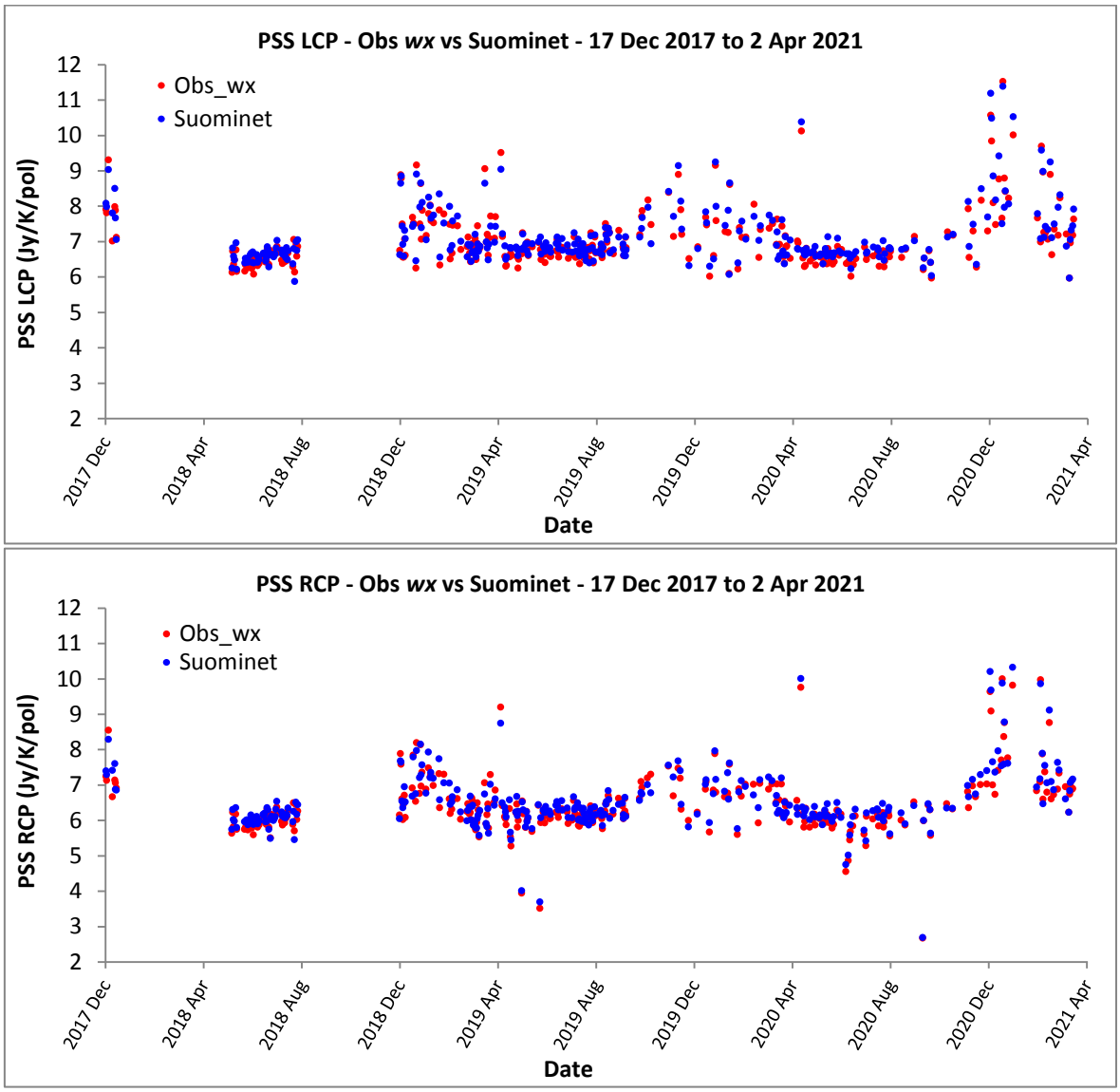

Figure 4.11 Point source sensitivity (PSS) left (top) and right (bottom) circular polarisation (LCP and RCP) derived from PWV calculated from wx sensor surface measurements of temperature and humidity during 22 GHz Jupiter calibration observations over the period 17 December 2017 to 2 April 2021 are compared with PSS LCP and RCP values derived from Suominet PWV at the corresponding time.

Table 4.3 Average point source sensitivity (PSS) left and right circular polarisation (LCP and RCP) values during latest step change in the average PSS value for the 22 GHz Jupiter calibration observations from 17 December 2017 to 2 April 2021, derived from PWV calculated from wx sensor surface measurements of temperature and humidity during calibration observations as well as from Suominet PWV. The differences in PSS in both LCP and RCP for the maximum difference in PWV during this time period are also indicated.

PSS (Jy/K/pol)	LCP	RCP
Average *wx*	7.02 ± 0.79	6.42 ± 0.82
Average Suominet	7.11 ± 0.8	6.51 ± 0.83
ΔPSS for maximum ΔPWV (= Suominet-Obs *wx* = -13.4 mm)	0.79	0.75

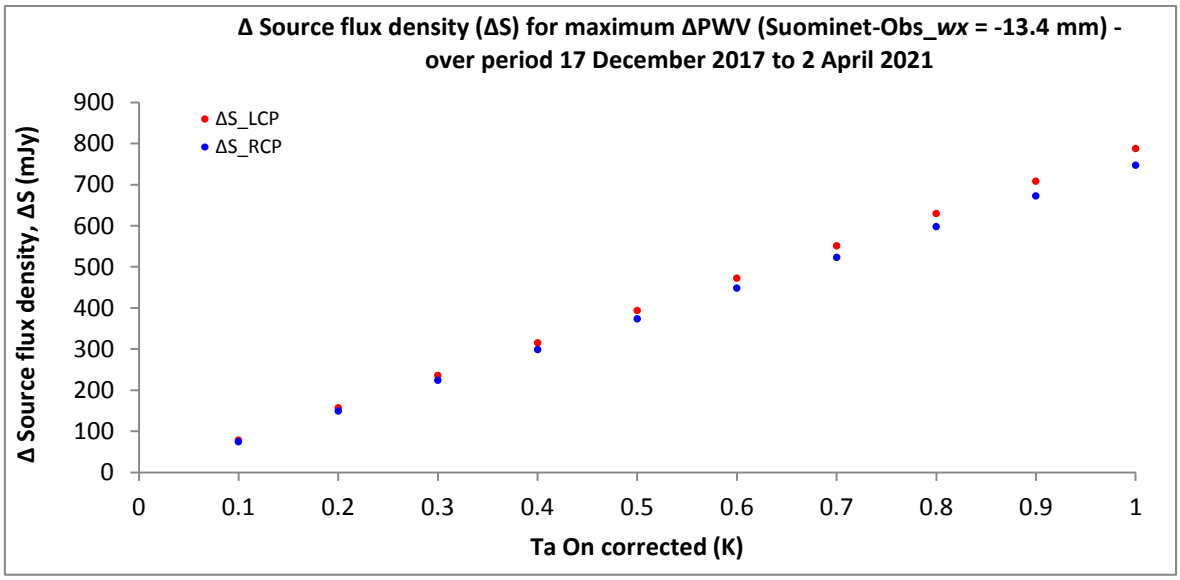

Figure 4.12 The difference in observed source flux density for a maximum difference in PWV of 13.4 mm between PWV from the wx sensors and from Suominet (with wx PWV higher) becomes significantly greater as the corrected antenna temperature (Ta On corrected) of the source increases.

It has been the norm to use the average PSS for both LCP and RCP over the entire Jupiter 22 GHz calibration data set, stretching back to 2007, to scale source flux densities at

22 GHz. However, such an approach does not take the step changes in PSS due to changes in hardware into account. A new approach is being considered in which monthly averages of PSS will rather be used for calibration purposes whilst being mindful of any possible step changes. The calibration accuracy can be further improved by making use of near real-time estimates of PWV over HartRAO (Combrink *et al*., 2004).

4.3 SUMMARY

Accurate and continuous meteorological data are required in geodetic VLBI for determining troposphere delay and antenna thermal deformation, and in astrometric VLBI for calculating the opacity correction. At HartRAO, surface meteorological data are provided by *in-situ* measurements from meteorological *wx* sensors during observations. Possible degradation of *wx* sensor data was investigated by comparison with Paroscientific MET3 and MET4 data. The investigation revealed offsets and drifts in the temperature and pressure data measured by the *wx* sensors compared to that measured by the MET3 and MET4, and also the existence of an incorrect lower ceiling value for the relative humidity *wx* sensor. The influence of the faulty humidity sensor on the opacity correction applied in determining the HartRAO 26 m antenna's PSS at 22 GHz was investigated by comparing PWV values calculated from *wx* sensor and MET3 temperature and relative humidity measurements, as well as GPS estimated PWV values from SuomiNet. The investigation revealed a seasonal difference between the *wx* sensor and Suominet values, with the latter, obtained from integrated PVW, considered to be the more accurate. In a further comparison of the 26 m antenna's PSS at 22 GHz derived from the *wx* sensor PWV and Suominet PWV, it was found that an inaccurate PWV value could lead to a significant difference between the calculated and true flux density of a source. The HartRAO meteorological sensor suite is in dire need of replacement.

CHAPTER 5 ANTENNA CALIBRATION AND POINTING

There are only a small number of antennas in the South that are astrometric and geodetic VLBI capable and able to contribute to ICRF development. Even fewer of these antennas participate in ICRF observations at K-band. Currently, only the HartRAO 26 m antenna and Hobart 26 m antenna in Australia regularly participate in Southern Hemisphere ICRF single-baseline observations at K-band (De Witt, 2014). HartRAO, and its 26 m antenna in particular, is therefore crucial in maintaining and densifying the ICRF in the South (Mayer *et al*., 2014). A K-band celestial reference frame (CRF) of more than 900 sources covering the full sky has been constructed using over 0.6 million observations from more than 70 observing sessions from the Very Long Baseline Array (VLBA) and the HartRAO-Hobart baseline. In the north, the VLBA is able to observe declinations of +90° to -40°. In the South, the HartRAO-Hobart baseline is currently the only baseline regularly observing the southern sky at K-band for CRF development, covering declinations from -90° to +0°.

The higher the observing frequency, the higher the demand placed on antenna pointing, as the beamwidth becomes progressively smaller at the increasingly shorter wavelengths. The 26 m antenna's pointing accuracy is therefore of paramount importance in observations at the higher 22 GHz frequency required for CRF work and for HartRAO to be able to contribute to CRF realisation. An unexpected low detection of sources in the K-band single-baseline sessions between the HartRAO and Hobart 26 m antennas as well as a significant declination (Dec) pointing offset detectable in 22 GHz pointing observations, prompted an investigation of the HartRAO 26 m antenna Dec pointing offsets and sub-reflector focus positions with a view to improving HartRAO performance at K-band. In this study, a first attempt is made to investigate the pointing problems experienced with the

HartRAO 26 m antenna at K-band. Gain calibration observations with Jupiter as calibrator source are analysed to determine the pointing correction and antenna gain at 22 GHz. A possible correlation between degraded Dec pointing and differential heating of the support structure is also explored.

5.1 JUPITER GAIN CALIBRATION AND FOCUS SETTING CURVES

In order to determine the pointing performance and gain of the 26 m antenna at 22 GHz, gain calibration observations were conducted with Jupiter as calibrator source.

5.1.1 Methodology

LINES data reduction procedure according to M. Gaylard (2011) and P. van Zyl (2016).

Gain calibration observations with the HartRAO 26 m antenna at 22 GHz consisted of measuring Jupiter's intensity with triple drift scans whereby the antenna's main beam drifts through Jupiter from its rising above the local horizon (east – hour angle, HA < 0°) through culmination (zenith – hour angle, HA = 0°) to its setting below the local horizon (west – hour angle, HA > 0°) due to the rotation of the Earth. A triple drift scan consists of a scan through the nominal source position (ON) and two scans at half of a half-power beamwidth (HPBW) north and south of the nominal source position, half-power North (HPN) and half-power South (HPS), with these two scans used in determining the pointing correction. Each of the three scans is observed in both left and right circular polarisation (LCP and RCP).

The observations were initially reduced and analysed with the LINES data reduction program. Plots of the raw data were produced for each of the six scans in the triple drift scan set. An example of a triple drift scan observed in RCP is shown in Figure 5.1 on the left with the ON scan displayed in black, the HPN scan in red and the HPS scan in green. The right ascension (RA) in degrees is displayed on the x-axis while the antenna temperature (Ta) in Kelvin (K) is displayed on the y-axis. The antenna temperature (Ta) represents the gain in the antenna system temperature (Tsys) due to the detection of the

Department of Geology, Geoinformatics and Meteorology
University of Pretoria

source signal. Each of the scans consists of a main beam in the centre with the first sidelobes visible on either side of the main beam.

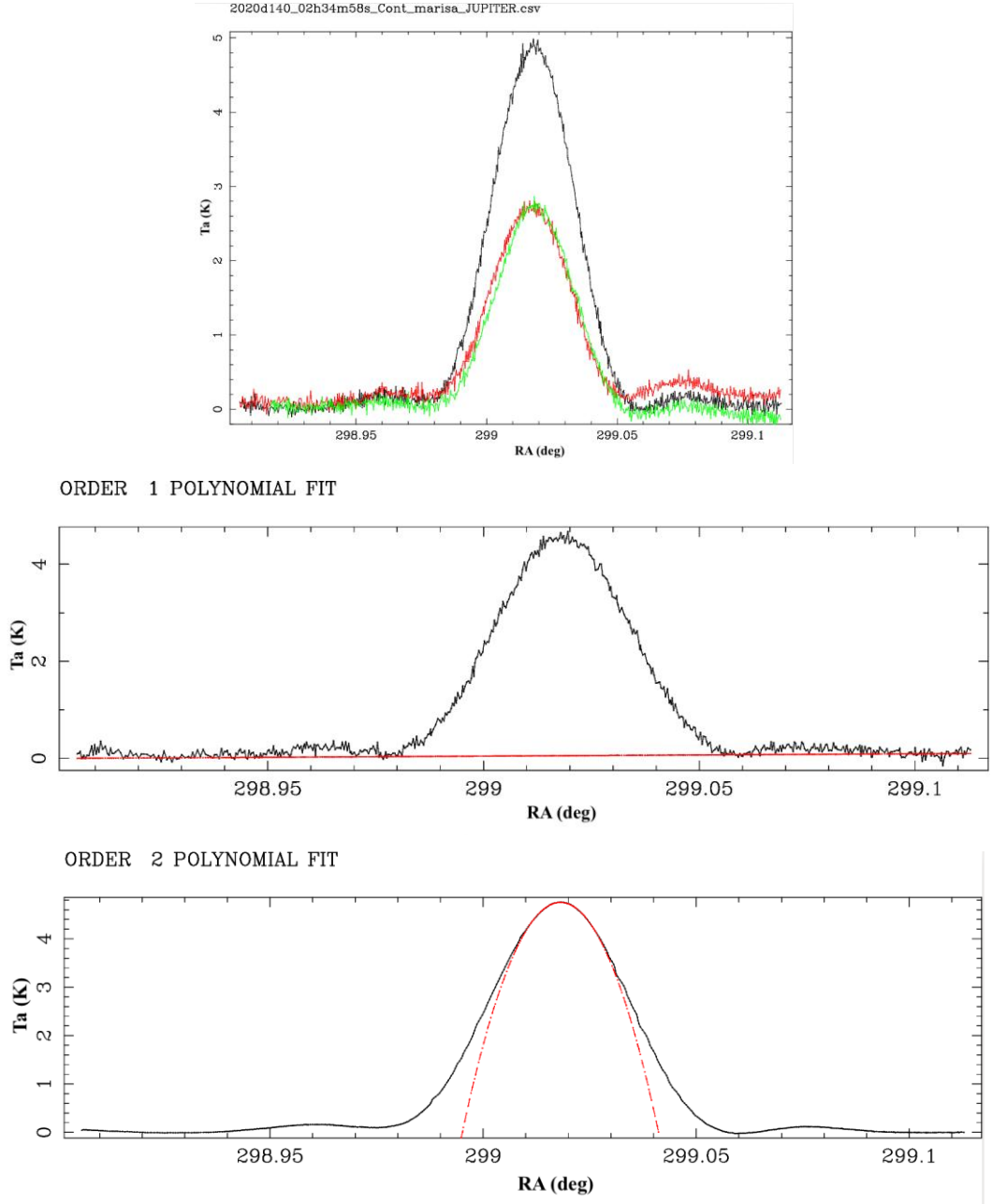

Figure 5.1 Top: Jupiter triple drift scan observed on the 19th of May 2020 with the HartRAO 26 m antenna at 22 GHz in right circular polarisation (RCP) for observations at ON (black), half-power North (HPN, red) and half-power South (HPS, green) positions. Middle: Baseline fitted through first null minima. Bottom: The main beam is approximated with a Gaussian profile to which a parabola is fitted to determine the peak antenna temperature (Ta) of the source.

In order to obtain an estimate of the peak antenna temperature (Ta), the user is required to firstly remove any slope in the baseline due to a slow drift in the signal level (conceivably from changing atmospheric conditions or a slow change in the gain of the receiver system). This is achieved by fitting the baseline through the minima or first nulls located between the main beam and first sidelobes on either side of the main beam (see Figure 5.1). A second order polynomial (parabola) is subsequently fitted to the top part of the Gaussian profile representing the main beam in order to estimate the centre of the main beam's peak amplitude above the baseline, and hence the peak antenna temperature (Ta) of the source for each of the ON, HPN and HPS scans in both LCP and RCP, i.e. Ta On LCP/RCP, Ta N LCP/RCP and Ta S LCP/RCP (see Figure 5.1). A pointing error results when the source does not pass through the centre of the main beam. The pointing correction can then be determined from Ta N + Ta S (for both HPN and HPS scans of good quality) or Ta On + Ta N (for unusable HPS scan) or Ta On + Ta S (for unusable HPN scan). The pointing correction is then applied to the uncorrected Ta On in both LCP and RCP to arrive at the true peak antenna temperature at the centre of the beam, the corrected Ta On in both LCP and RCP.

Initial Jupiter gain curve observations were conducted on the 9th of November 2019 (2019d313) and 11-12 April 2020 (2020d102-102) but the data were severely degraded due to inclement weather conditions. These observations were therefore followed up with gain curve observations on the 18th-19th of May 2020 (2020d139-140). Enlarged first sidelobes were detected in the triple drift scans of the 2020d139-140 gain curve observations. Such extended sidelobes, known as coma sidelobes, are due to astigmatism caused by gravitational deformation of the dish and prevent proper fitting of the baseline thereby contaminating the pointing correction determined from the half-power scans. This indicated that longer drift scan observations, extending data for baseline fitting beyond the coma sidelobes to the second nulls, might be required.

The 2020d139-140 observations were reduced with both the LINES data reduction program as well as with the Drift scan Reduction and ANalysis (DRAN) program which provides for fully automated data reduction based on LINES but with additional features, developed by HartRAO PhD candidate, Pfesesani van Zyl. A comparison of the results

produced by LINES and DRAN established that DRAN could be used for further data reduction. Plots of the raw triple drift scan observations output by DRAN were inspected to determine the effect of the coma sidelobes. Python plots of the Dec pointing correction and Ta On before and after correction were produced using results from the DRAN database to ascertain the influence of the coma sidelobes on the pointing correction, the behaviour of the latter over the range of hour angles (HAs) as well as the gain before and after the pointing correction was applied. Plots of Ta ratios were also produced in Python to determine that the correct HPBW was being used by the observing program and to detect possible pointing offsets to the north and south.

The Jupiter gain curve calibration observations were modified on the 11th-12th of August 2020 (2020d224-225) to observe at seven different sub-reflector focus settings in order to determine the impact of focussing on the coma sidelobes, pointing correction and the gain. The data were reduced with the automated software package, DRAN. Coma sidelobes again interfered with baseline fitting, requiring extension of the drift scan duration for subsequent focus curve observations. Follow-up focus curve observations were conducted on the 27th of April 2021 (2021d117) over a narrower range of more closely spaced focus settings with longer drift scan observations beyond the coma sidelobes in place and with a Dec pointing offset of 20 mdeg to the north as determined in test observations beforehand.

Follow-up Jupiter gain curve observations were conducted on the 14th-15th of May 2021 (2021d134) with longer drift scan observations to the second nulls and a Dec pointing offset of 10 mdeg to the north as determined in prior test observations. The data were reduced with the automated software package, DRAN. Similar to the 2021d117 focus curve observations, the data appeared degraded and with lowered gain. The longer drift scans seemed to have had improved the baseline fitting however, and it was decided to repeat the observations at an observing frequency of 12 GHz to ascertain the effect of frequency on the coma sidelobes. The 12 GHz gain curve observations were conducted on the 18th-19th of May 2021.

5.1.2 Results and discussions

First set of gain curve observations at 22 GHz – 2020d139-140 (18-19 May 2020):

In order to determine the pointing performance of the 26 m antenna at 22 GHz, triple drift scan observations of Jupiter from rising to setting with Jupiter at a declination of -21° were conducted between 20:35 UT and 07:37 UT on the 18/19th of May 2020.

The triple drift scan plots revealed the presence of a coma sidelobe, which switched sides in hour angle as Jupiter rose and set (see Figure 5.2). The sidelobe appeared less pronounced at culmination with the antenna at or close to zenith. Coma sidelobes appearing at low elevations and extreme hour angles are due to astigmatism caused by gravitational deformation of the dish from a circularly symmetric paraboloid (G. Nicolson, personal communication, 26 August 2020).

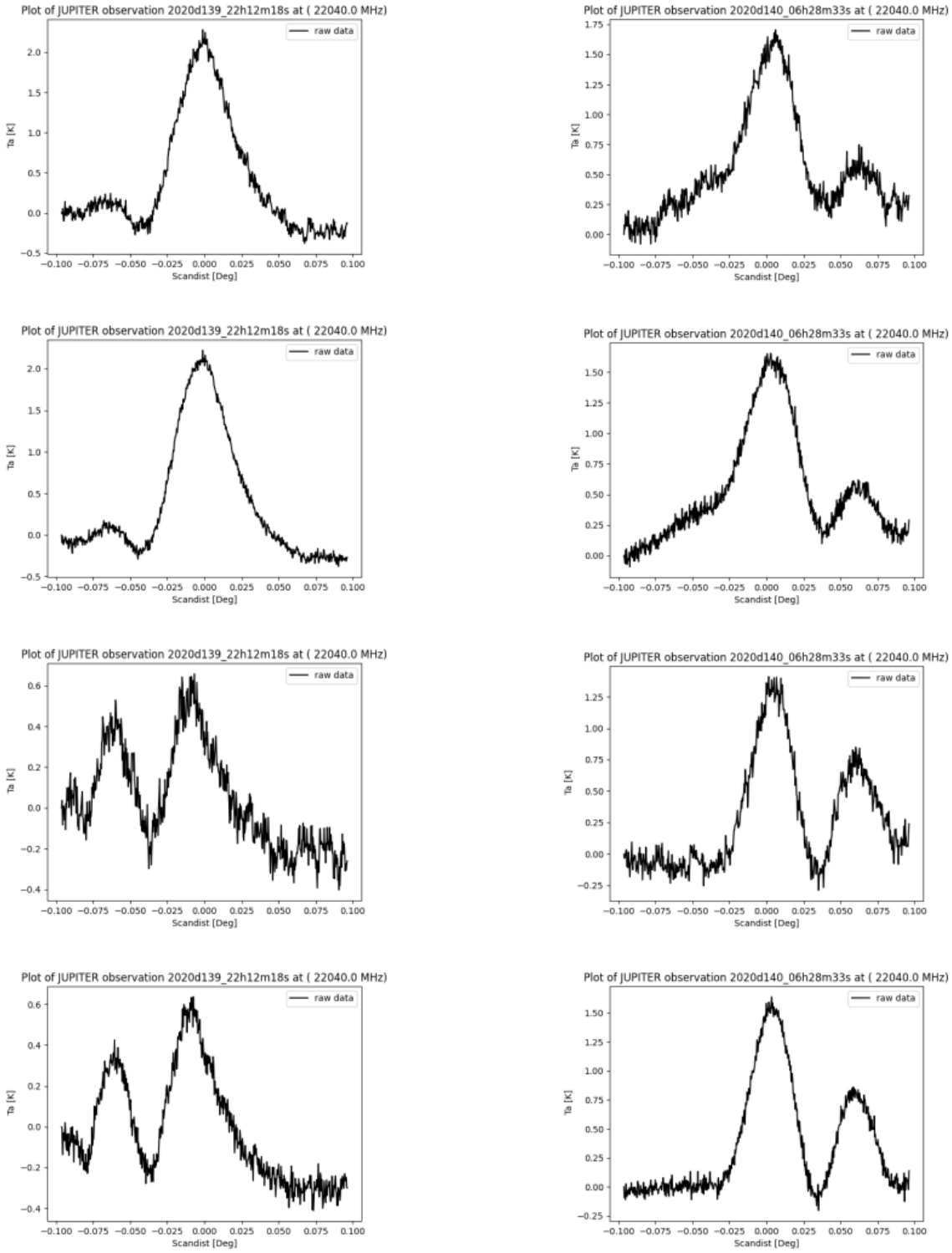

Figure 5.2 Raw plots – 2020d139-140 – scans at an elevation of 33° – left, top to bottom: HPN L&RCP and HPS L&RCP scans for Jupiter rising with coma sidelobes visible on left; right, top to bottom: HPN L&RCP and HPS L&RCP scans for Jupiter setting with coma sidelobes visible on right.

The coma sidelobes merge with the the main beam, preventing the baseline from being determined (see Figure 5.3). Inspection of the raw triple drift scan plots revealed the coma sidelobes to be stronger for the HPS scans, sometimes even exceeding the peak of the main beam. The stronger coma sidelobes in the HPS scans indicated that the sidelobes were typically positioned south of the main beam. The coma sidelobes also appeared stronger for Jupiter setting. There were numerous instances of the coma sidelobes blending into the main beam preventing a proper baseline fit. Strong coma sidelobes appeared even at high elevations where the gravitational distortion of the dish surface should be reduced.

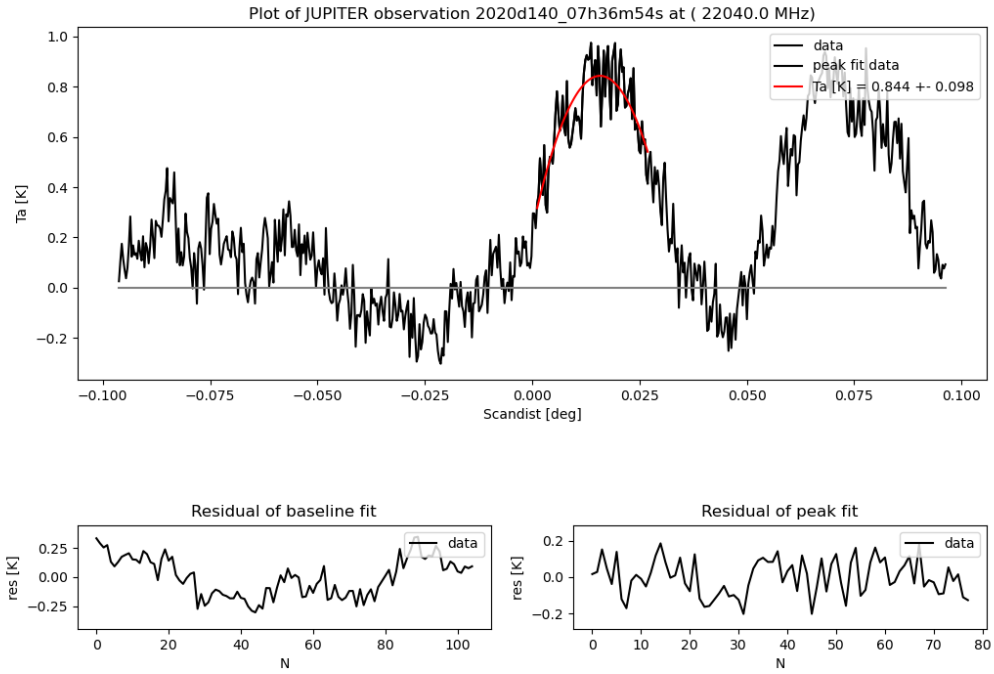

Figure 5.3 Fitted plots – 2020d139-140 – Jupiter rising – difficulty of fitting a baseline due to the coma sidelobes is displayed in this plot depicting the half-power South left circular polarisation (HPS LCP) scan of the final observation at an elevation angle of 18° with Jupiter setting in the west.

The influence of the coma sidelobes is also revealed in plots of the Dec pointing correction and antenna temperature for the on-source observations (Ta On), before and after the pointing correction had been applied, against hour angle (HA) for both LCP and RCP (see Figure 5.4). The pointing is expected to degrade at lower elevation angles but the pointing

correction is supposed to vary smoothly with elevation and to be similar in both polarisations. There is wide scatter in the pointing correction from -90° to -40° for Jupiter rising in the east. The pointing correction below HAs of 40° in the west and 30° in the east appears to be unreliable. The coma sidelobes prevent the baseline from being fitted properly or at all and thus contaminate the pointing correction at the lower elevations. It would seem as if better results can be obtained at 22 GHz without any pointing correction being applied. Longer drift scan observations would be required to eliminate the influence of the coma sidelobes on baseline fitting.

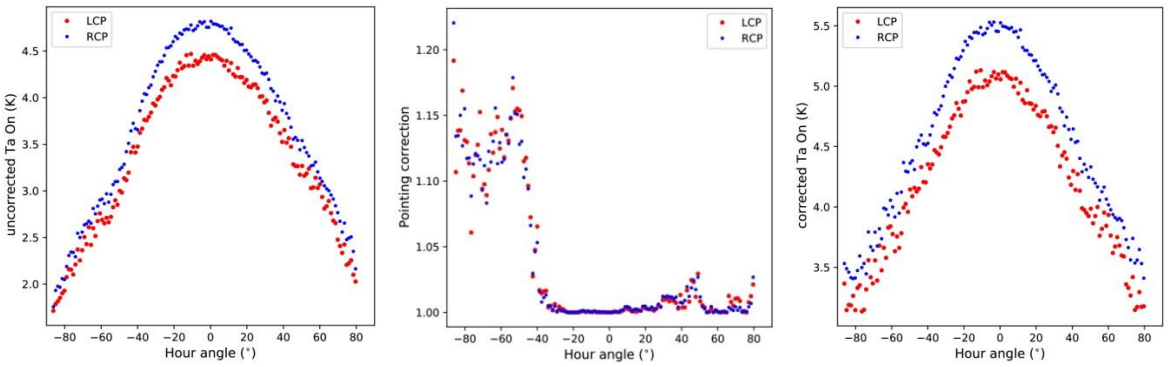

Figure 5.4 2020d139-140 – Plots of declination (Dec) pointing correction and antenna temperature for on-source scans (Ta On) before and after Dec pointing correction for LCP and RCP, against hour angle (HA).

The plots of the antenna temperature reflect the decrease in gain (Ta) as the gravitational deformation of the dish increases at the lower elevations. The plots also display a gain asymmetry, with the maximum being displaced from zenith to the east. Possible causes are a mis-set primary reflector or the sub-reflector not being central at meridian transit or being deformed or the feed not pointing directly at the centre of the sub-reflector (feed axis skew). Holography will be required to disentangle the various effects.

In order to determine whether the observing program was using the correct HPBW (assumed), the gain (Ta) ratio between the sum of antenna temperature for the HPN and HPS scans divided by the antenna temperature for the On scans in both LCP and RCP were plotted (see Figure 5.5 bottom). In the range where the pointing can be considered

reasonable, i.e. for HAs of between -40° and +20°, the plots of [(Ta N + Ta S) / Ta On] for both LCP and RCP (bottom plots) show this ratio to be ~1.05, which is close to the ideal ratio of 1 (actual). The HPBW used by the observing program at 22 GHz therefore seems to be correct. The gain ratio (Ta) of HPN to HPS scans is also close to 1 in the range of reasonable pointing as displayed in the antenna temperature ratio plots of Ta N L/RCP divided by Ta S L/RCP (see Figure 5.5 top) indicating that the pointing was not off to either the north or south.

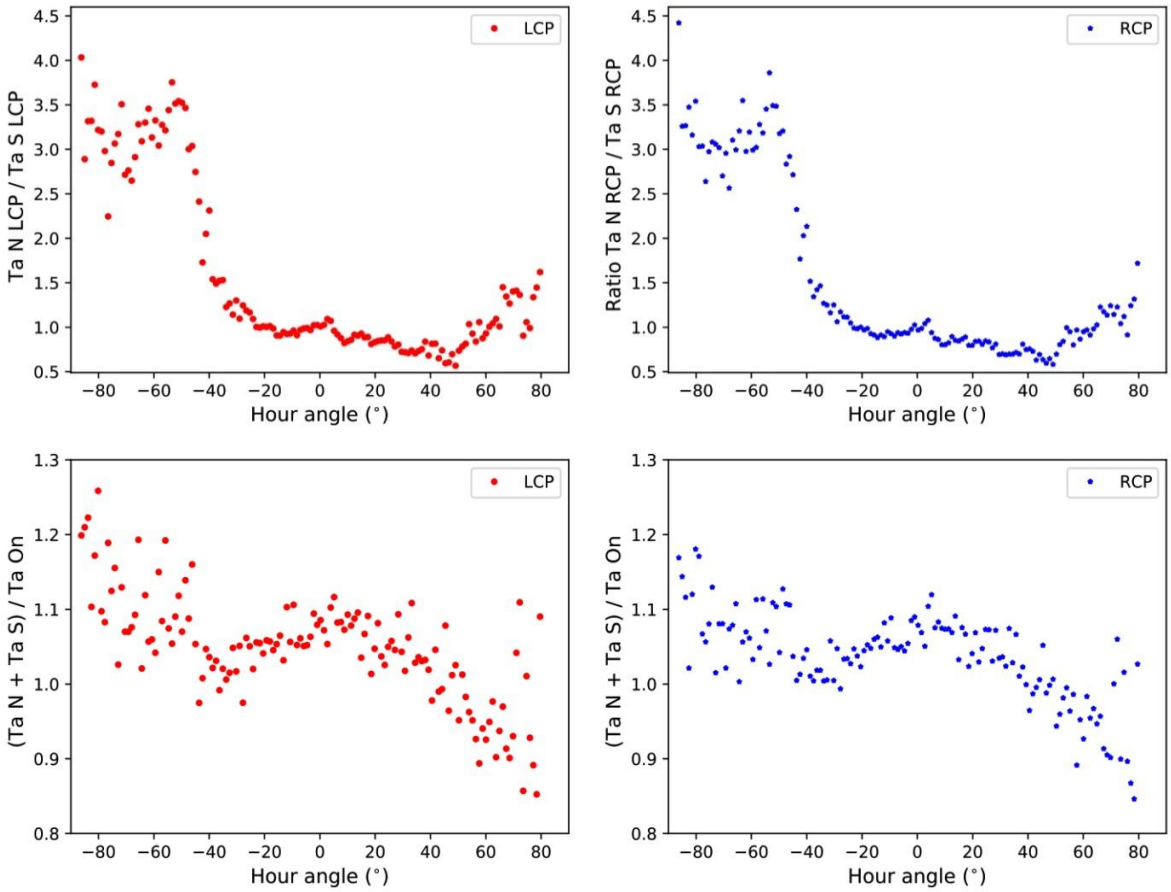

Figure 5.5 2020d139-140 – Plots of the antenna temperature (Ta) for North, South and On ratios in both LCP and RCP, against HA.

First set of sub-reflector focus offset gain curve observations at 22 GHz – 2020d224-225(11-12 August 2020):

As poor focussing could also be contributing to the coma sidelobes, the Jupiter gain curve observations were subsequently modified to cycle through seven different sub-reflector focus positions in order to investigate the impact of the focus settings on the sidelobes and to determine whether it would be possible to improve the gain by focussing.

In order to determine the pointing performance of the 26 m antenna at 22 GHz, triple drift scan observations of Jupiter from rising to setting and with Jupiter at a declination of -22° were conducted between 14:22:12 UT and 01:41:37 UT on the 11/12th of August 2020 at the default focus setting as well as at focus settings differing by an in/out linear movement of +0.5, +1.0 and +1.5 and -0.5, -1.0 and -1.5 cm from the default setting.

Raw plots of the triple drift scans for all focus settings displayed coma sidelobes for both Jupiter rising and setting and even at high elevations (see Figure 5.6 and Figure 5.7 for close to optimal focus settings and Figures A2.1a – e in Appendix A for other focus settings). The sidelobes were again stronger for Jupiter setting and for the HPS scans, with the sidelobes sometimes exceeding the height of the main beam peak. Coma sidelobes merging with the main beam prevented a proper baseline fit in many cases. Higher gain (Ta) at the default (+0.0) and +0.5 focus settings indicated these focus settings to be close to optimal.

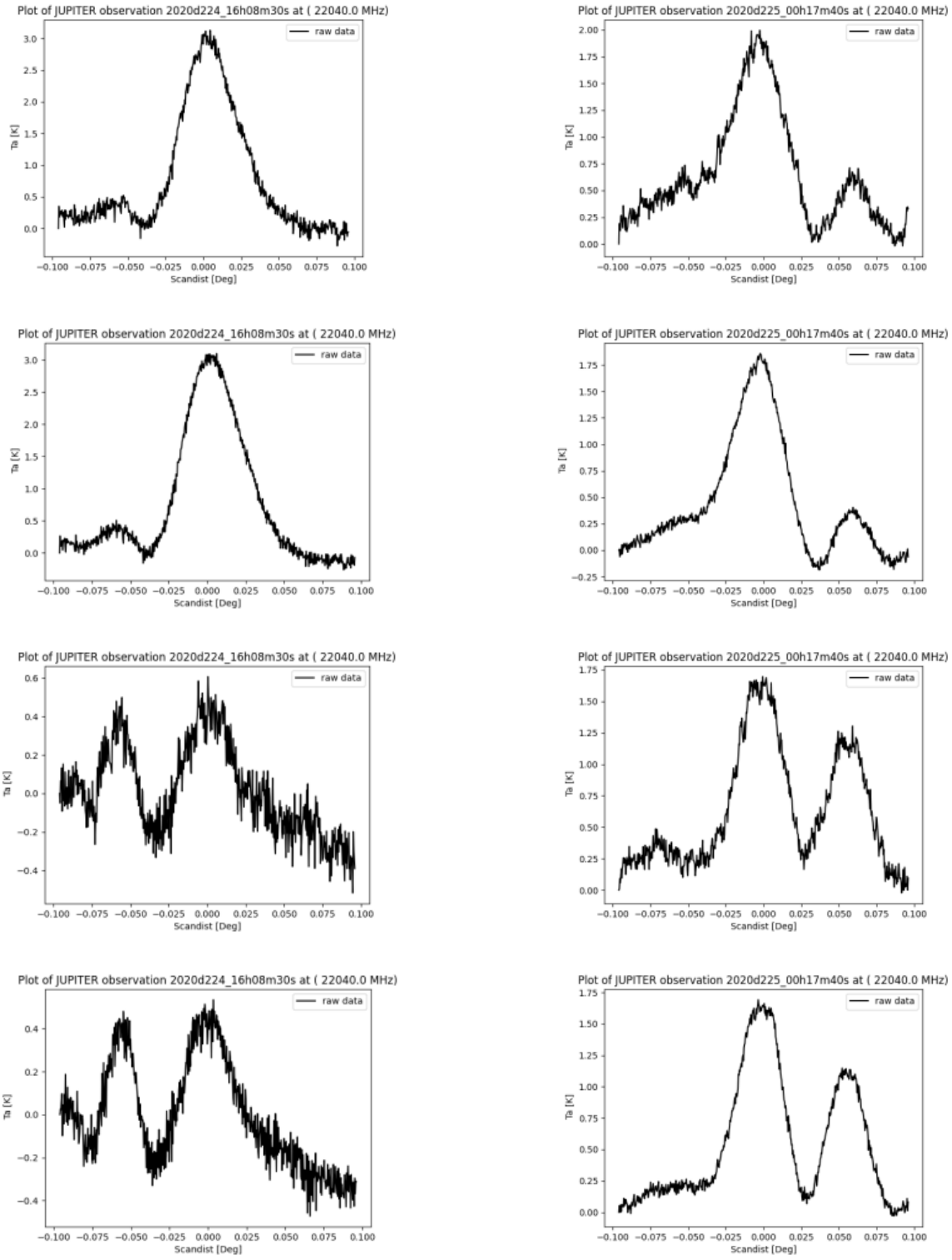

Figure 5.6 Raw plots – 2020d224-225 – focus setting = +0.0 – left, top to bottom: HPN L&RCP and HPS L&RCP scans at elevation of 35° with Jupiter rising; right, top to bottom: HPN L&RCP and HPS L&RCP scans at elevation of 34° with Jupiter setting.

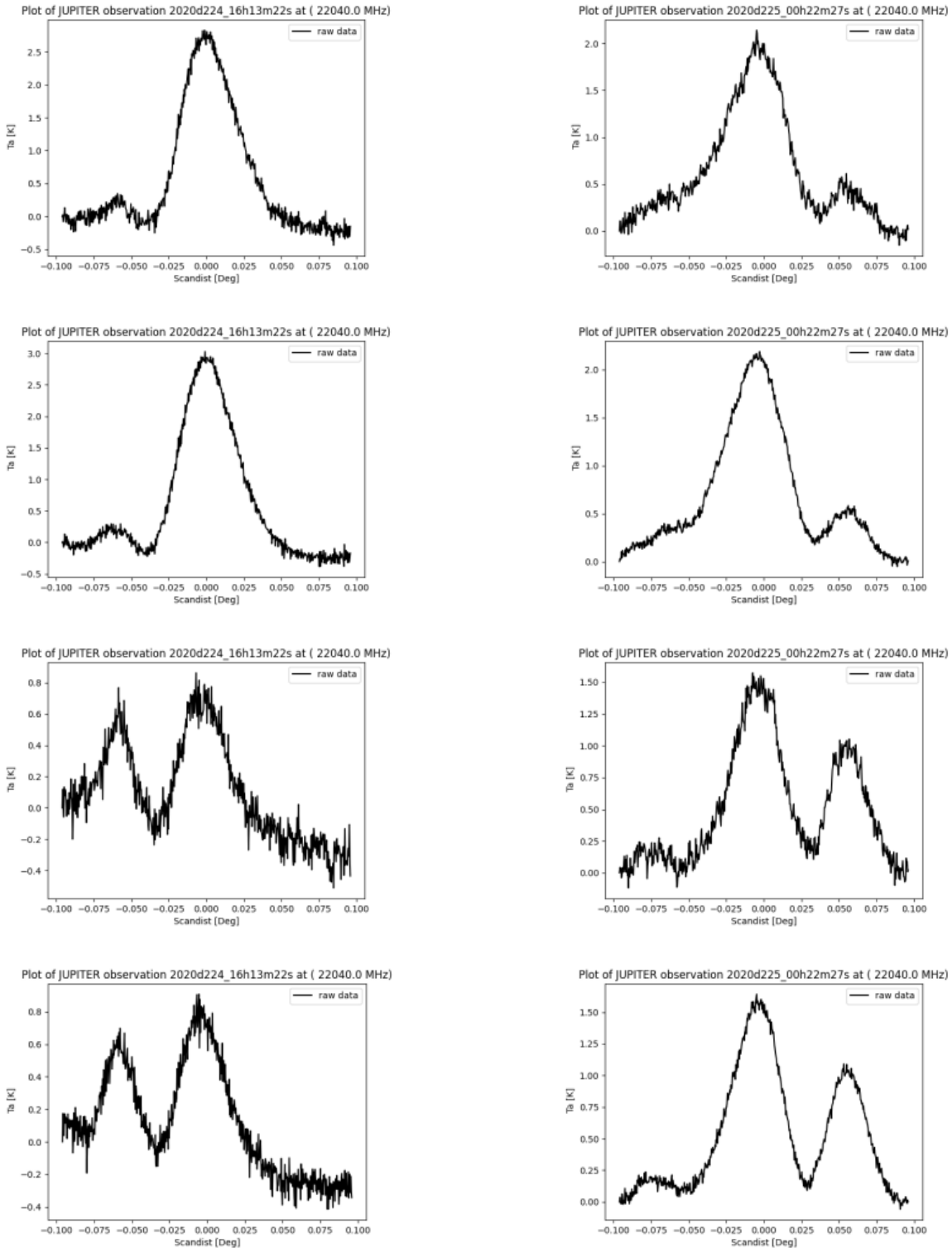

Figure 5.7 Raw plots – 2020d224-225 – focus setting = +0.5 – left, top to bottom: HPN L&RCP and HPS L&RCP scans at elevation of 36° with Jupiter rising; right, top to bottom: HPN L&RCP and HPS L&RCP scans at elevation of 33° with Jupiter setting.

Plots of the Dec pointing correction and antenna temperature of the on-source observations (Ta On), before and after the pointing correction had been applied, against HA for both LCP and RCP for the varying sub-reflector focus settings again revealed a contaminated pointing correction due to the coma sidelobes preventing a proper baseline fit (see Figure 5.8, Figure 5.9 and Figure 5.10). The plots of antenna temperature again show a higher gain for RCP compared to LCP and a pointing correction degrading the focus curves. There is wide scatter in the pointing correction below HAs of -40° in the west and +60° in the east. The pointing correction appears unreliable below 30° HA in both the west and east. Better results are achieved at 22 GHz with no pointing correction applied. A change in focus position does not seem to affect the pointing as the pointing correction remains similar to that obtained in the 2020d139-140 gain curve observations at the default focus setting.

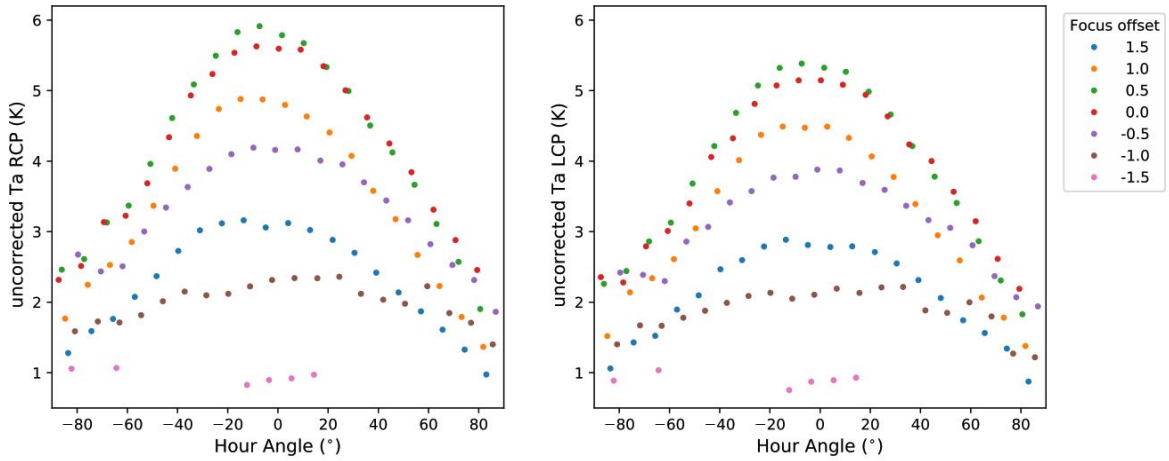

Figure 5.8 2020d224-225 – Plots of antenna temperature for on-source scans (Ta On) before Dec pointing correction for LCP and RCP, against HA, for the varying sub-reflector focus settings.

In the plots of the antenna temperature, the +0.5 sub-reflector focus offset provides for a higher maximum antenna temperature around zenith than the default +0.0 focus setting but drops below the default setting away from zenith. Most observations do not occur at zenith however, and the default +0.0 sub-reflector setting provides higher efficiency at other HAs and should be retained as a better average fixed value. Gain asymmetry was again apparent

in the antenna temperature plots. Longer drift scan observations would be required to eliminate the influence of the coma sidelobes on baseline fitting. Observations with a narrower range of more closely spaced focus settings and at another declination for Jupiter, i.e. a different time of year, would also be required.

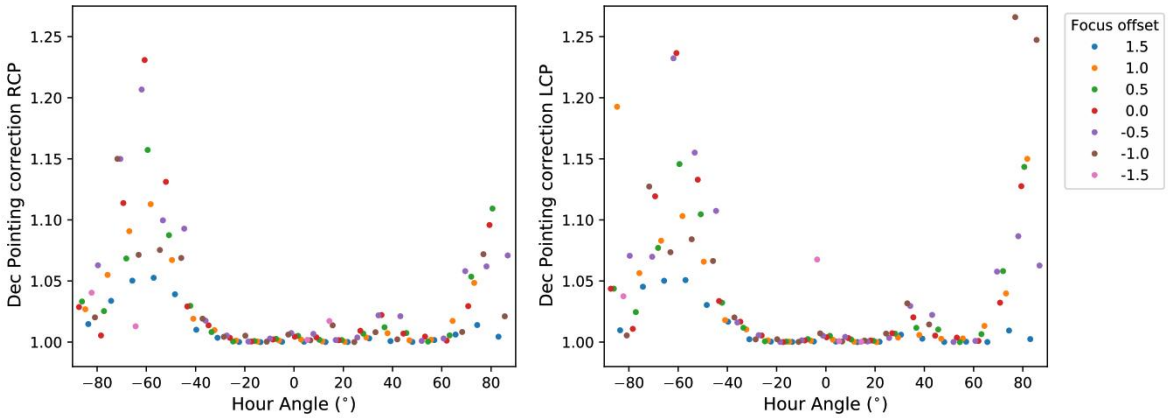

Figure 5.9 2020d224-225 – Plots of Dec pointing corrections for LCP and RCP, against HA, for the varying sub-reflector focus settings.

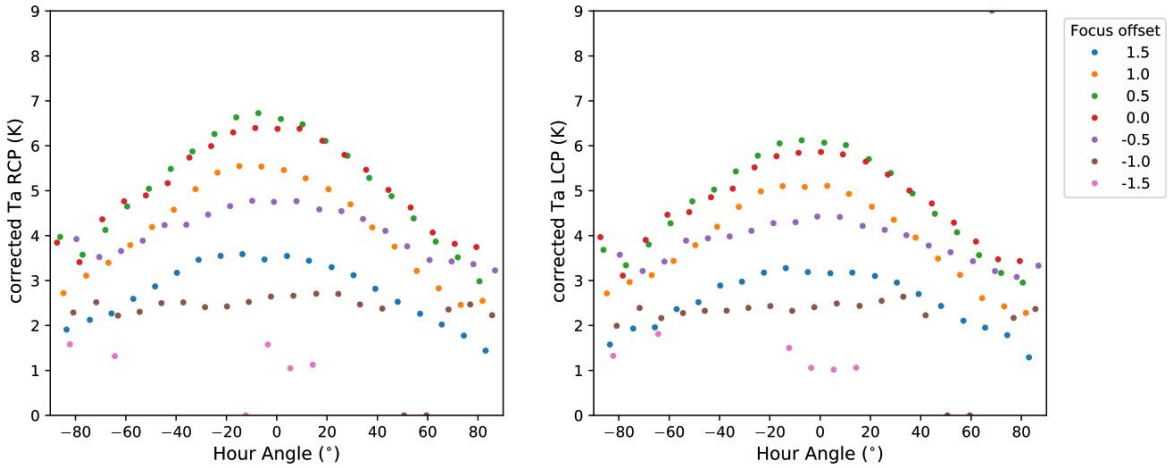

Figure 5.10 2020d224-225 – Plots of antenna temperature for on-source scans (Ta On) after the Dec pointing correction for LCP and RCP has been applied, against HA, for the varying sub-reflector focus settings.

Second set of sub-reflector focus offset gain curve observations at 22 GHz – 2021d117 (27 April 2021):

Test observations conducted prior to the focus curve observations revealed that the Dec pointing was off by more than half of the HPBW at 22 GHz, which precluded the peak flux from being estimated reliably. The triple drift scans were not straddling Jupiter – the central on-source scan was observing less of the source than the HPN scan, while the HPS scan was observing very little of the source. Several offsets were tested to eliminate the imbalance and optimise the straddling. The Dec pointing offset was subsequently adjusted by adding a 20 mdeg offset to the north.

The initial sub-reflector focus offset gain curve observations of 2020d224-225 were modified to incorporate longer drift scans to the second nulls with a 20 mdeg Dec pointing offset to the north and to cycle through a narrower range of seven more closely spaced sub-reflector focus positions with Jupiter at a different declination of -13° at this time of year. In order to determine the pointing performance of the 26 m antenna at 22 GHz, triple drift scan observations of Jupiter from rising to setting were conducted between 00:18:42 UT and 11:35:45 UT on the 27th of April 2021 at the default focus setting as well as at focus settings differing by an in/out linear movement of +0.25, +0.5, +0.75, and +1.0 cm and -0.25 and -0.5 cm from the default setting.

The raw plots of the triple drift scans revealed the data to be noisy with much lower gain than for the 2020d224-225 focus curve observations, which complicated fitting of the baseline and made it impossible to determine whether the longer drift scans led to any improvement in the baseline fitting (see Figure 5.11 and Figure 5.12 and Figures A.2.2a-e in Appendix A for other focus settings). It is suspected that the noisy observations could be the result of the 22 GHz receiver not performing optimally during the 2021d117 observations. The observations could also have been degraded by high water vapour content to which observations at 22 GHz are extremely sensitive. Precipitable water vapour (PWV) values calculated from ground surface measurements of temperature and humidity during the two observation runs indicate the PWV to have been similar during the two sets of observations – for 2020d224-225 observations, the PWV decreased from ~9.5 mm at the

start of observations (14:22 UT) to ~7.5 mm at sunrise and increased to ~10 mm at the end of observations (01:42 UT); for 2021d117 observations, the PWV decreased from ~11 mm at the start of observations (00:48 UT) to ~10.5 mm at sunrise and increased to ~13-15 mm towards the end of observations (11:18 UT). The PWV obtained from the surface measurements requires validation by comparison with GPS-derived PWV values however.

The raw plots of the triple drift scans for all focus settings displayed coma sidelobes for both Jupiter rising and setting. The coma sidelobes seemed relatively lower in HPS than for the 2020d224-225 observations and also with fewer instances of sidelobes approaching the height of the main beam peak. The coma sidelobes also only appeared at the higher elevations for Jupiter setting. Although difficult to determine due to the noisy data, the coma sidelobes seemingly remained higher for Jupiter on setting. Sidelobes merging with the main beam also remained prevalent. The HPS gain was higher than the HPN gain in both rising and setting, indicating that the average pointing was off towards the south. In further comparison with the 2020d224-225 observations, HPN gain for the 2021d117 observations seemed lower while HPS gain seemed higher, also indicative of the pointing difference between the two sets of observations. Due to the noisy data it was not possible to deduce an optimal focus setting for the 2021d117 observations.

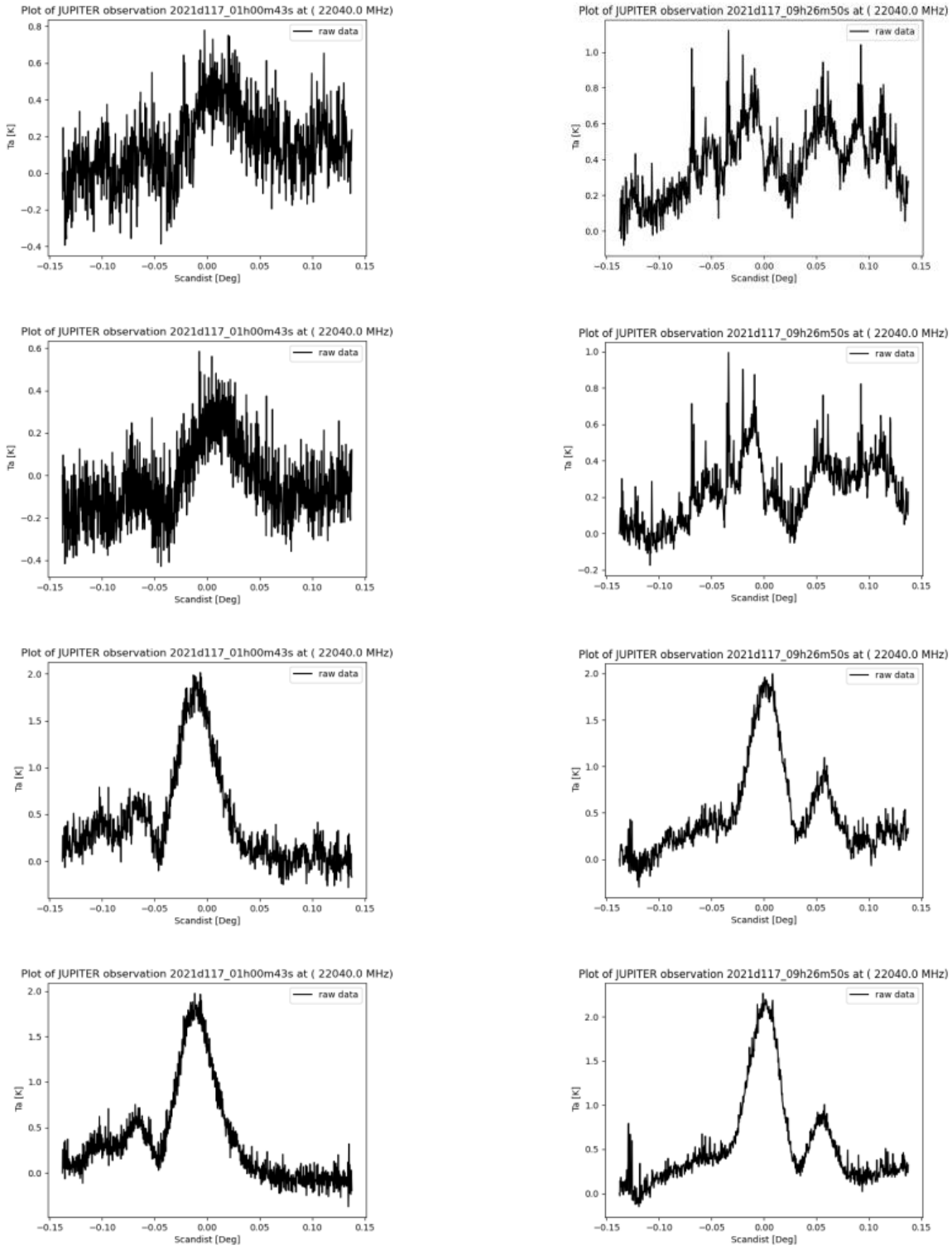

Figure 5.11 Raw plots – 2021d117 – focus setting = +0.0 – left, top to bottom: HPN L&RCP and HPS L&RCP scans at elevation of 21° with Jupiter rising; right, top to bottom: HPN L&RCP and HPS L&RCP scans at elevation of 38° with Jupiter setting.

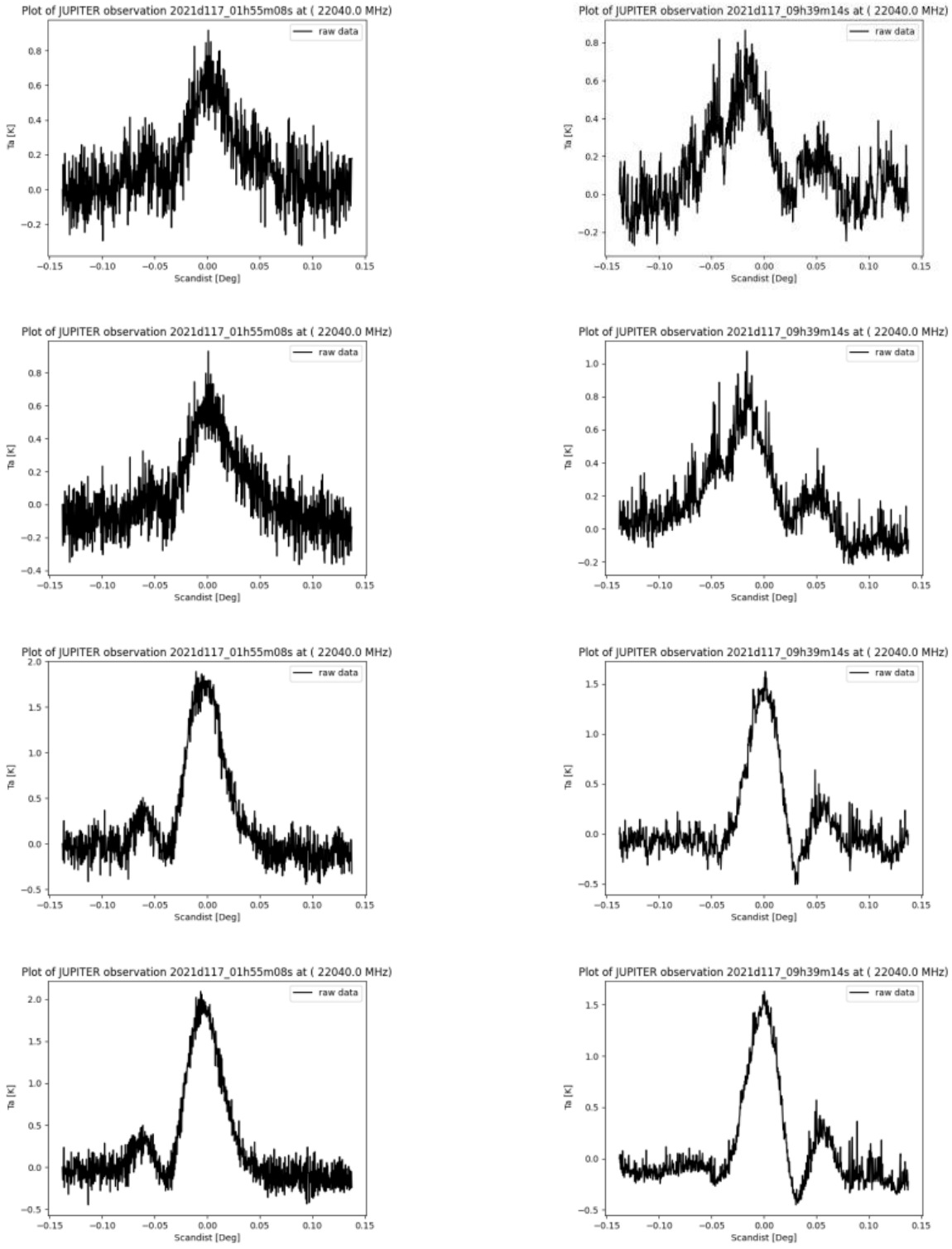

Figure 5.12 Raw plots – 2021d117 – focus setting = +0.5 – left, top to bottom: HPN L&RCP and HPS L&RCP scans at elevation of 33° with Jupiter rising; right, top to bottom: HPN L&RCP and HPS L&RCP scans at elevation of 35° with Jupiter setting.

Plots of the Dec pointing correction and antenna temperature for the on-source observations (Ta On), before and after the pointing correction had been applied, against HA for both LCP and RCP for the varying sub-reflector focus settings also showed the data to be poor (see Figure 5.13, Figure 5.14 and Figure 5.15). The pointing correction could be considered reliable only from HAs ~0° to +45°. It was therefore not possible to determine an optimal focus setting nor any possible gain asymmetry from the antenna temperature plots. It would be necessary to repeat this set of observations.

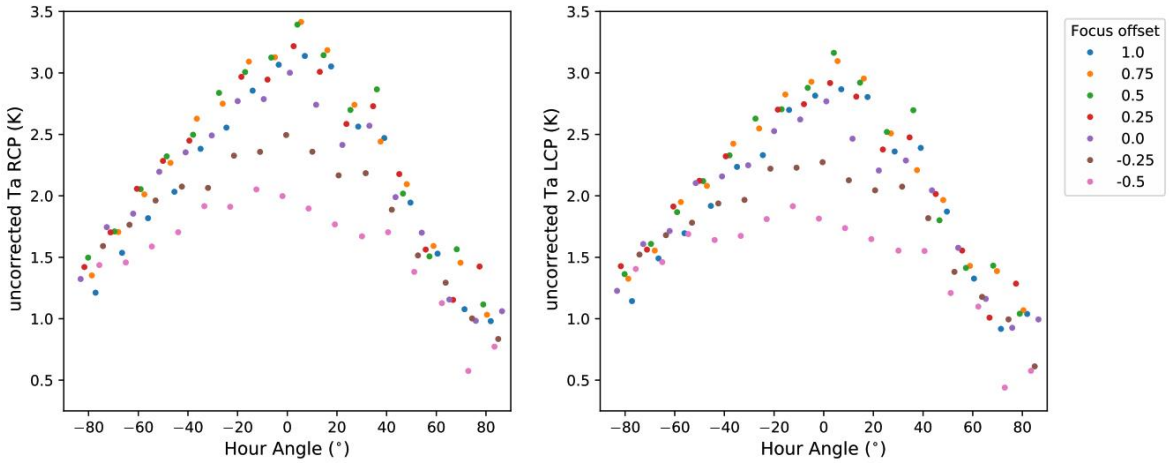

Figure 5.13 2021d117 – Plots of antenna temperature for on-source scans (Ta On) before Dec pointing correction for LCP and RCP, against HA, for the varying sub-reflector focus settings.

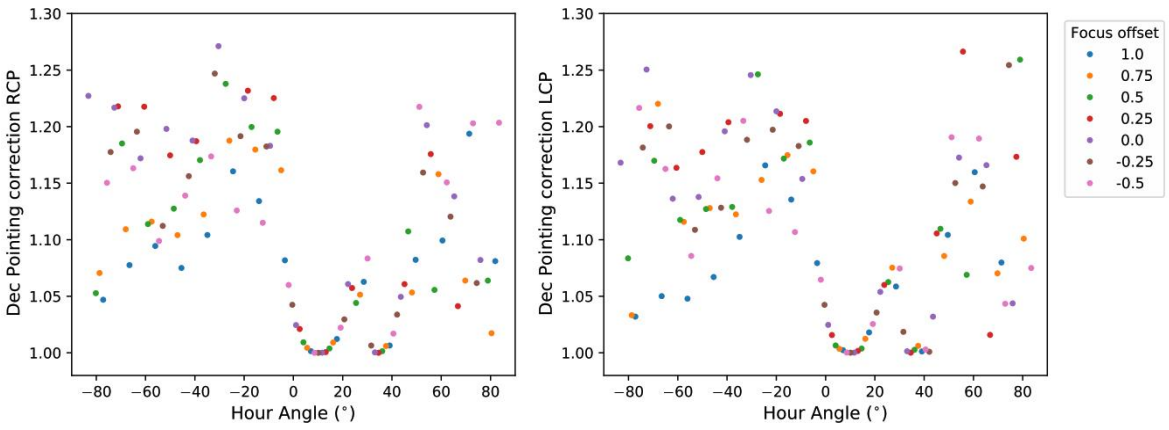

Figure 5.14 2021d117 – Plots of Dec pointing corrections for LCP and RCP, against HA, for the varying sub-reflector focus settings.

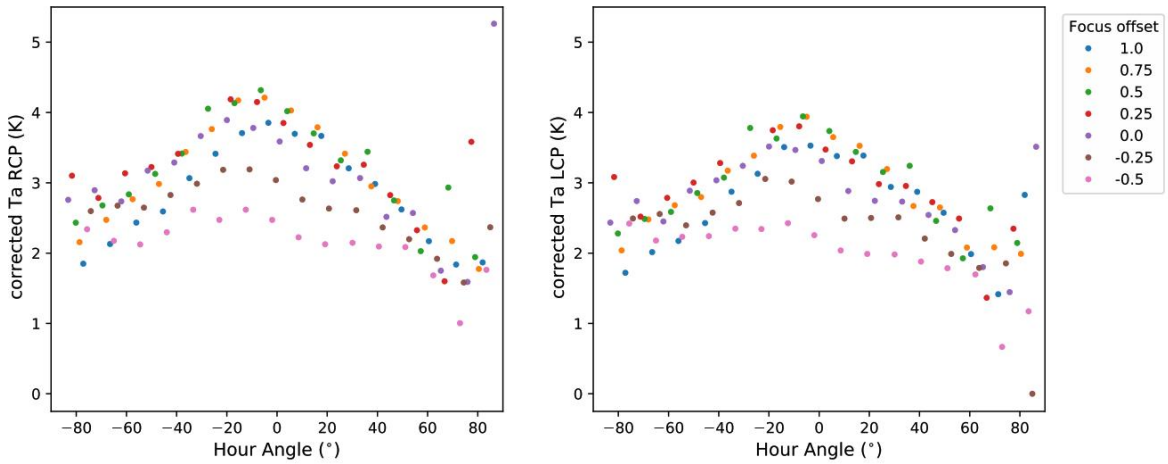

Figure 5.15 2021d117 – Plots of antenna temperature for on-source scans (Ta On) after the Dec pointing correction for LCP and RCP has been applied, against HA, for the varying sub-reflector focus settings.

Second set of gain curve observations at 22 GHz to second nulls with 10 mdeg declination pointing offset – 2021d134-135 (14-15 May 2021):

Prior to the second set of gain curve observations at 22 GHz, test observations revealed that the Dec pointing offset had changed once more and the offset was reduced to 10 mdeg north. Longer triple drift scan observations to the second nulls of Jupiter from rising to setting and with Jupiter at a declination of -12° were conducted between 08:31 UT and 10:33 UT on the 14/15th of May 2021.

Raw plots of the longer triple drift scans displayed coma sidelobes for both Jupiter rising and setting and also at high elevations (see Figure 5.16). The data were noisy again and, with the range of PWV values (11-17 mm) similar to that for the 2020d139-140 gain curve observations (11-13 mm), the suspicion is falling increasingly on a 22 GHz receiver not operating optimally since the focus curve observations of 2020d224-225 in November 2020. Coma sidelobes were again stronger for HPS, sometimes exceeding the height of the main beam peak. The HPS scans sometimes presented with two coma sidelobes. There were still several instances of sidelobes blending into the main beam,

preventing a proper baseline fit even with the longer drift scans. Strong coma sidelobes at high elevations persisted.

The plots of the Dec pointing correction and antenna temperature for the on-source observations (Ta On), before and after the pointing correction had been applied, against HA for both LCP and RCP seem to indicate that the longer drift scans have contributed to improving the baseline fit with significantly reduced scatter in the Dec pointing correction on rising in the east for HAs from -90° to -40° in comparison with that of the 2020d139-140 observations (see Figure 5.17). The scatter in the pointing correction in the west from approximately 10° to 50° in HA remains however. The Dec pointing correction in the west does not smooth out the elevation dependence but rather exacerbates it.

The plots of the antenna temperature again display a maximum gain east of meridian transit. A significant reduction in gain (Ta On) compared to the 2020d139-140 observations is of particular concern and might be due to a faulty receiver. The Dec pointing correction outliers in both the east and especially the west would require manual reprocessing to identify the cause and whether these outliers should be removed. It can then be decided whether even longer drift scans are required to further improve the baseline fitting. The longer drift scan observations should be repeated at 12 GHz with Jupiter at a similar declination in order to determine the effect of a change in observing frequency on the coma sidelobes.

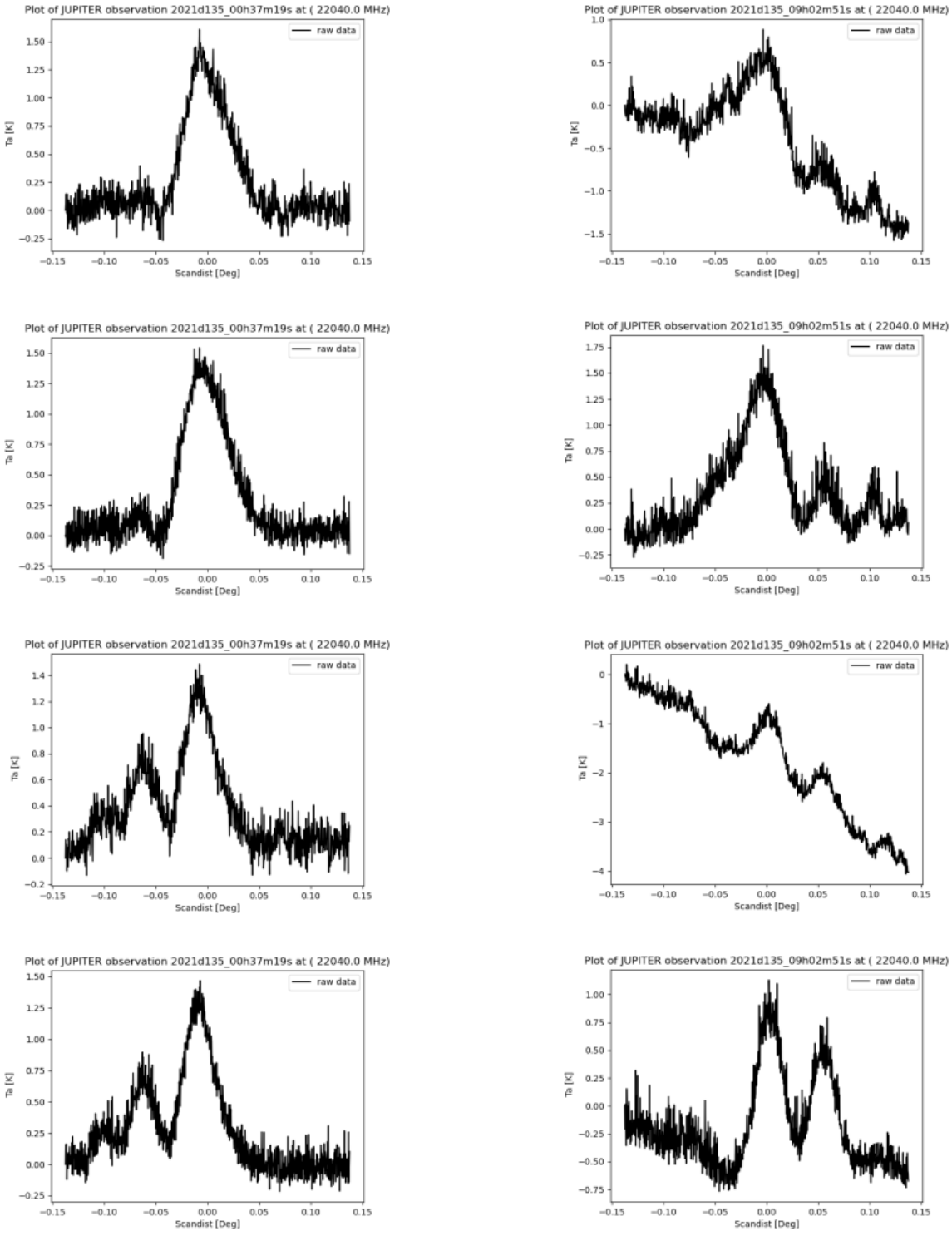

Figure 5.16 Raw plots – 2021d134-135 – scans at an elevation of 29°– left, top to bottom: HPN L&RCP and HPS L&RCP scans for Jupiter rising with coma sidelobes visible on left; right, top to bottom: HPN L&RCP and HPS L&RCP scans for Jupiter setting with coma sidelobes visible on right.

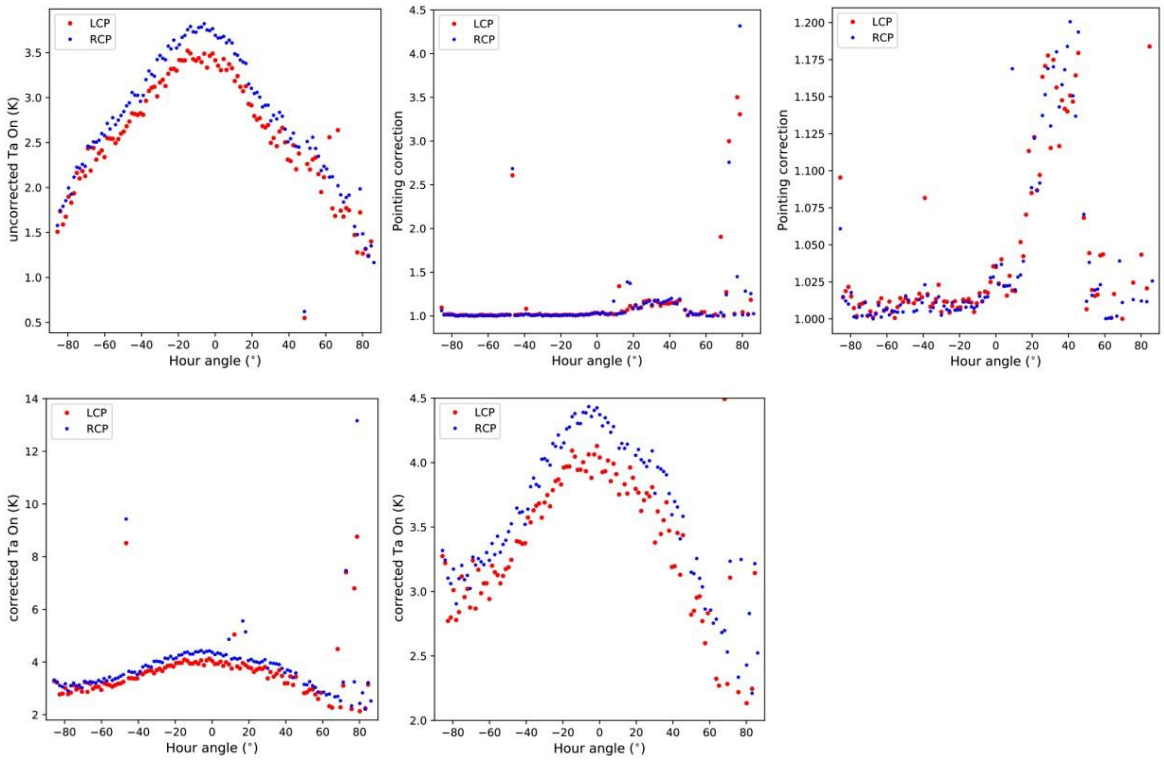

Figure 5.17 2021d134-135 – Plots of Dec pointing correction and antenna temperature for on-source scans (Ta On) before and after Dec pointing correction for LCP and RCP, against HA.

The use of the correct HPBW by the observing program for 22 GHz was confirmed by plots of the ratio (Ta N + Ta S) / Ta On for both LCP and RCP for the range of reasonable pointing, i.e. for HAs of between -90° and +10° (see Figure 5.18, bottom plots). Although the ratio is again ~1.05, more scatter appears than for the 2021d139-140 observations. The gain ratio (Ta) of HPN to HPS scans has also increased to ~1.5, which indicated average pointing to be off to the north (see Figure 5.18, top plots). Both the scatter and the imbalance in HPN and HPS gain could possibly be ascribed to the Dec pointing offset of +10 mdeg to the north applied at the start of observations.

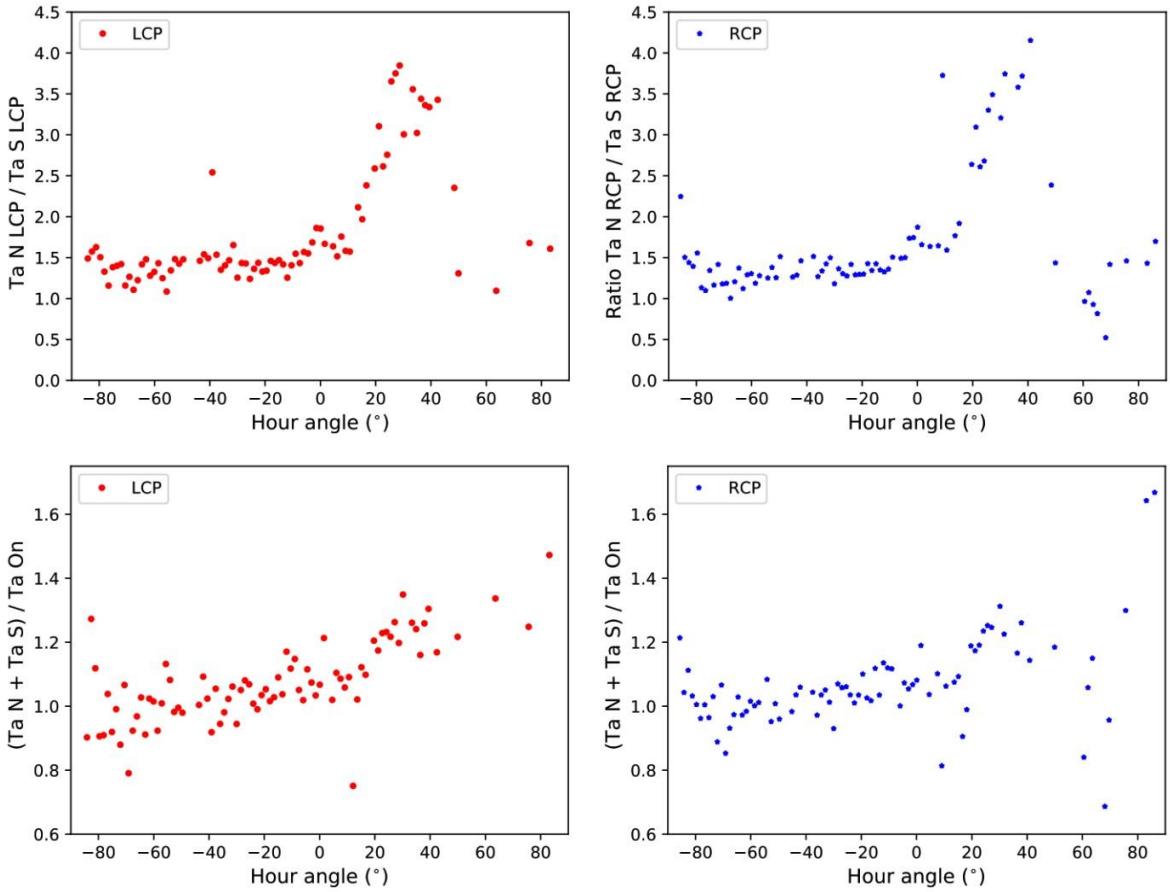

Figure 5.18 2021d134-135 – Plots of the antenna temperature (Ta) for North, South and On ratios in both LCP and RCP, against HA.

Third set of gain curve observations at 12 GHz to second nulls with 10 mdeg declination pointing offset – 2021d138-139 (18-19 May 2021):

Test observations conducted prior to the third set of gain curve observations at 12 GHz showed that the Dec pointing offset of +10 mdeg north should be retained. The longer triple drift scan observations with a Dec pointing offset of +10 mdeg and with Jupiter at a declination of -12° were repeated at 12 GHz a few days after the 2021d134-135 observations at 22 GHz. Observations at 12 GHz would allow for disentangling the various effects. With the larger beam and HPBW (0.059°) at 12 GHz, the coma sidelobes should be reduced and the pointing offset should be smaller than at 22 GHz with a HPBW of 0.031°. The 12 GHz observations to determine a comparative relative gain curve were conducted between 06:17 UT and 10:20 UT on the 18/19th of May 2021.

Raw plots of the longer triple drift scans displayed coma sidelobes for both Jupiter rising and setting reduced to the expected level for the sidelobes (see Figure 5.19). The reduced coma sidelobes remained stronger for HPS in both rising and setting, and for Jupiter setting in general, but with a much decreased height in comparison to the main peak. There were very few instances of sidelobes blending with the main beam and degrading the baseline or strong coma sidelobes at higher elevations. The gain (Ta) in HPS and HPN scans was again similar.

The plots of the Dec pointing correction and antenna temperature for the on-source observations (Ta On), before and after the pointing correction had been applied, against HA for both LCP and RCP, show the 12 GHz results to be similar to the corresponding 22 GHz results of 2021d134-135 but with a smaller and more smoothly varying Dec pointing correction due to the larger beam at 12 GHz (see Figure 5.20). There is still unexplained scatter in the Dec pointing correction in the west below an HA of approximately +40° and outliers requiring further investigation. The Dec pointing correction again does not improve the gain curve. The gain asymmetry remains, which, with the 12 GHz being a different feed, indicates feed axis skew to be an unlikely cause of the asymmetry.

Plots of the ratio (Ta N + Ta S) / Ta On for both LCP and RCP for the entire range show the ratio to be ~1.1, which would indicate that the HPBW assumed by the observing program is slightly too small at 12 GHz compared to the actual beam width (see Figure 5.21, bottom plots). As displayed in the antenna temperature ratio plots of Ta N L/RCP divided by Ta S L/RCP (top plots), the gain ratio (Ta) of HPN to HPS scans is close to 1, again indicating that the pointing was sound (see Figure 5.21, top plots).

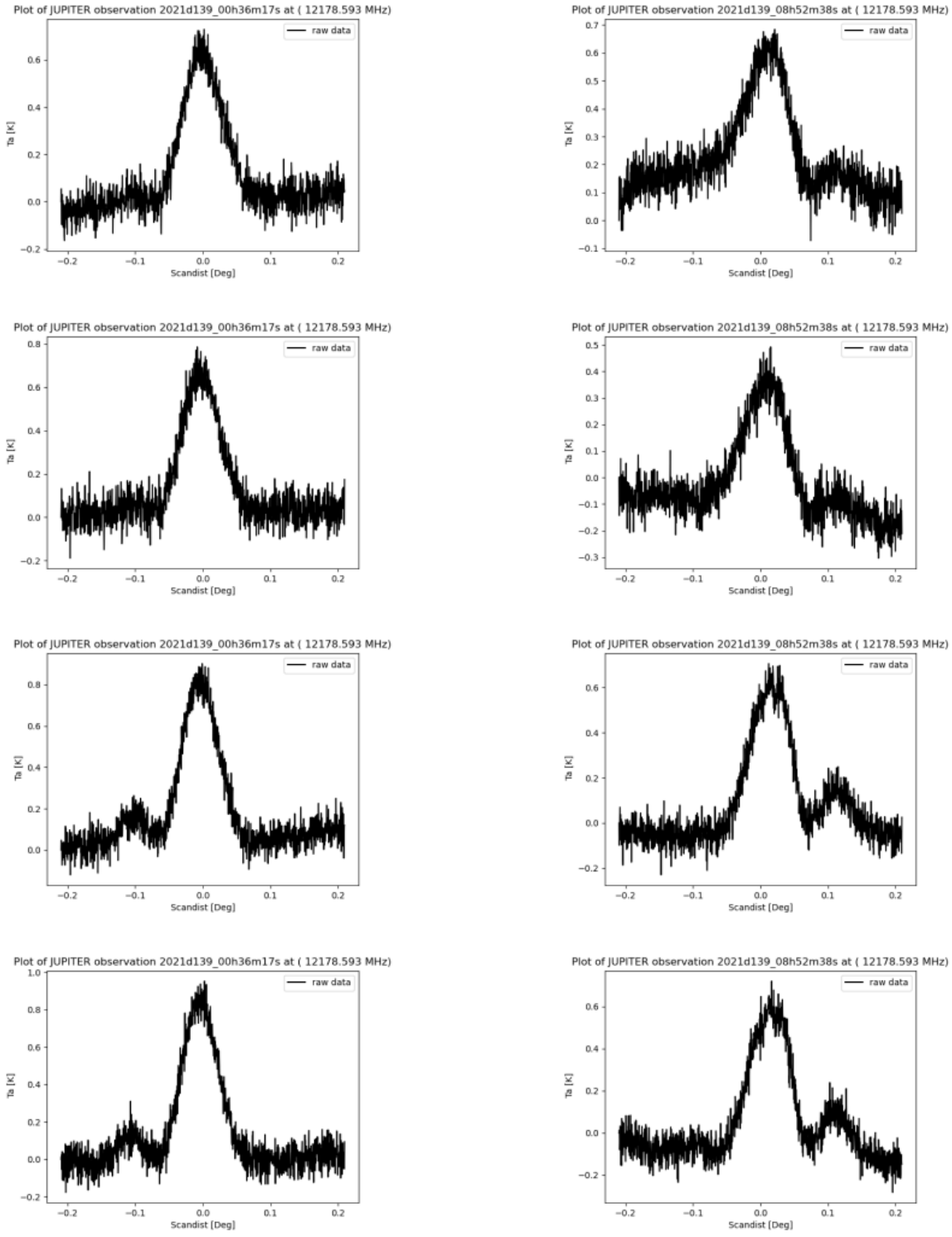

Figure 5.19 Raw plots – 2021d138-139 – left, top to bottom: HPN L&RCP and HPS L&RCP scans at an elevation of 32° for Jupiter rising with coma sidelobes visible on left; right, top to bottom: HPN L&RCP and HPS L&RCP scans at an elevation of 29° for Jupiter setting.

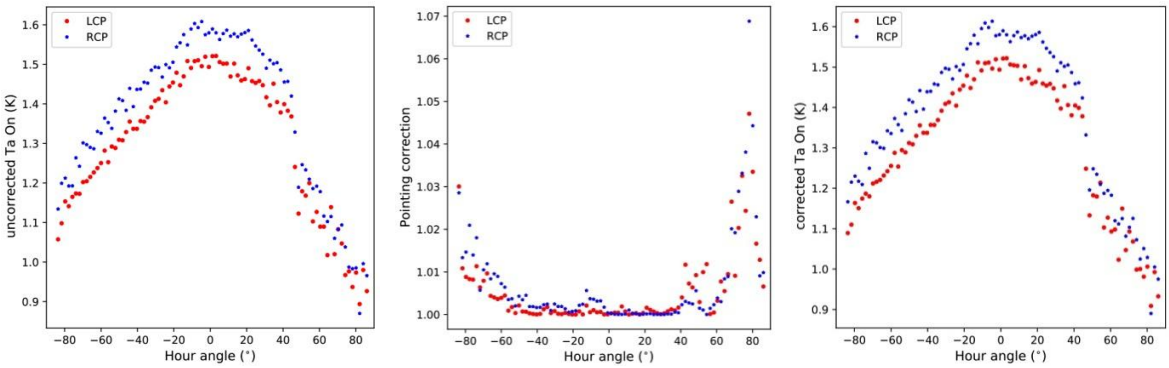

Figure 5.20 2021d138-139 – Plots of Dec pointing correction and antenna temperature for on-source scans (Ta On) before and after Dec pointing correction for LCP and RCP, against HA.

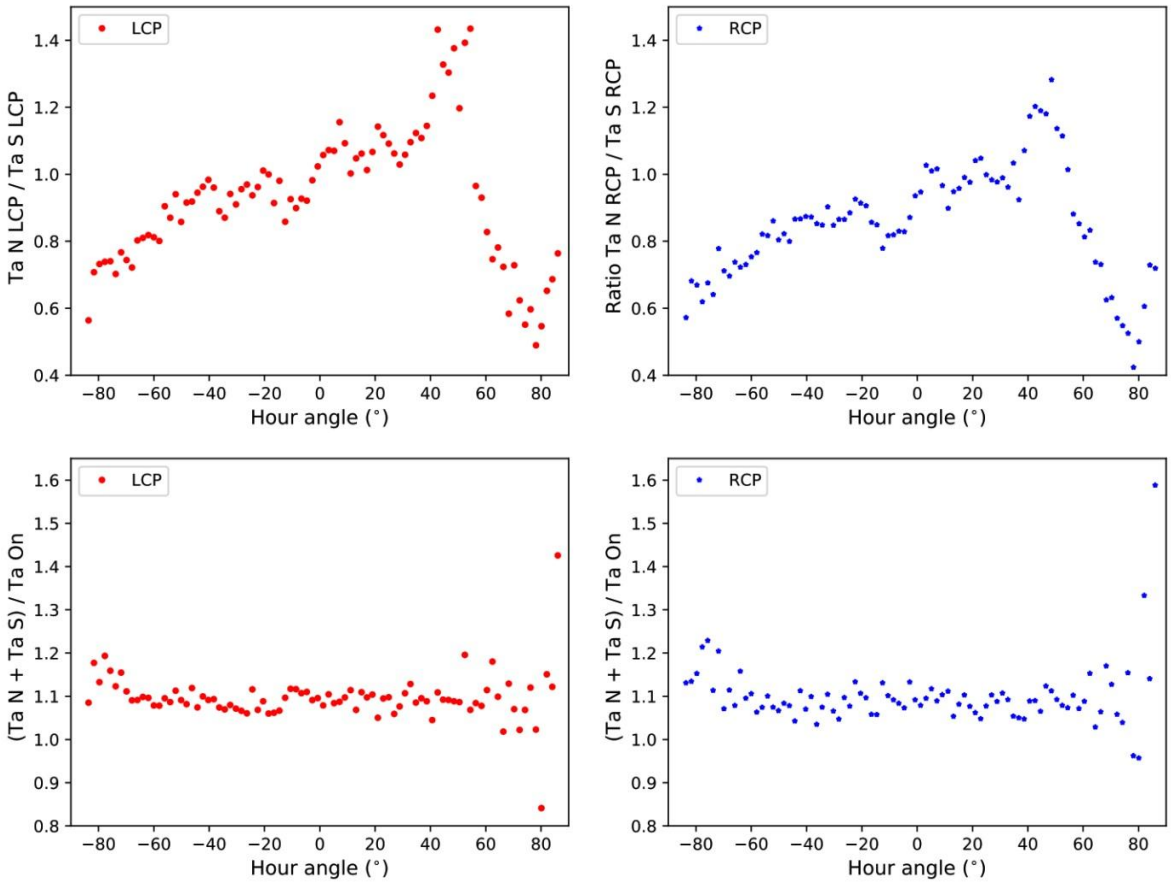

Figure 5.21 2021d138 139 – Plots of the antenna temperature (Ta) for North, South and On ratios in both LCP and RCP, against HA.

Gravitational distortion of the dish introduces dish surface errors which lead to frequency-dependent phase errors. The higher the observing frequency, the larger these phase errors. Dish surface accuracy therefore places an upper limit on observing frequency. The much reduced coma sidelobes at 12 GHz indicate the phase errors to be insignificant at the lower frequency. The strong coma sidelobes observed at 22 GHz are due to astigmatism caused by gravitational deformation of the dish from the circularly symmetric design paraboloid, which introduces large phase errors. Inability to achieve the required dish surface accuracy at 22 GHz is emphasized by the strong coma sidelobes appearing even at high elevations where gravitational distortion of the dish surface should be reduced and also by the appearance of a second coma sidelobe in the 2021d134-135 gain curve observations. Sub-reflector inaccuracy and misalignment of the primary reflector, sub-reflector and feed may all be contributory factors to the antenna's mediocre performance at 22 GHz and require holography to disentangle.

The reason for Dec pointing correction outliers and scatter should be investigated by manual inspection of the raw plots and examination of the results tables. Fitted plots should be inspected to ensure that all peaks and baselines have been fitted correctly. The results table should also be scrutinised for unusually low antenna temperature values for the HPN, HPS and On scans. Data should be flagged for instances where such values are missing from the results tables. Manual reprocessing would be required for scans where the fitting has failed. Noisy data and lowered gain during the 2021 observations are of concern and the 22 GHz receiver's performance requires further investigation, as do the influence of atmospheric attenuation and GPS-derived PWV values (as opposed to PWV derived from surface measurements). The appearance of a second coma sidelobe in the 2021d134-135 observations necessitates even longer drift scan gain curve observations at 22 GHz to ensure a proper fit of the baseline. The focus curve observations should also be repeated making use of longer drift scans. In order to further determine the frequency-dependence of the coma sidelobes, gain curve observations will be conducted at the top and bottom of the 22 GHz receiver band. Small-area beam maps at various HAs will also be produced to investigate remaining pointing problems. Further observations will be conducted when Jupiter is up all night and pointing is stable, as a possible correlation exists between the degraded pointing and sunrise (discussed in following section).

5.2 POINTING CORRECTION AND DIFFERENTIAL HEATING OF SUPPORT STRUCTURE

The polar-mounted 26 m antenna's steel support structure does not rotate from north to south and is thus subjected to strong temperature gradients. Temperature variation of different parts of the antenna structure influences pointing. A diurnal pointing variation, mainly in declination, is caused by diurnal temperature changes. In winter, a large day/night temperature change and the low angle of the sun, causing it to shine directly in under the dish, lead to significant differential heating of the support beams, causing Dec pointing to differ by 20 to 30 mdeg from night to day, with the Dec pointing offset at its maximum on clear sunny days in winter. A smaller day/night temperature change and indirect heating by air in summer lead to more even heating of the support beams with a correspondingly smaller Dec pointing offset. The diurnal effect on the HA pointing is smaller than for the Dec pointing.

The Dec pointing offset is caused by differential heating of four beams, two longer beams on the north side of the antenna and two shorter beams on the south side, supporting the Dec shaft bearing housings on the polar shaft bearing housings (see Figure 5.22). The platform to which the Dec shaft is fixed is suspected to tilt and the Dec shaft to rotate relative to the HA wheel due to the differential heating, which then introduces a false shift into the encoder. A smaller HA pointing offset is caused by differential heating of two beams on the south side of the antenna supporting the south polar shaft bearing housing, with one beam located towards the east side of the antenna and the other towards the west side (see Figure 5.22).

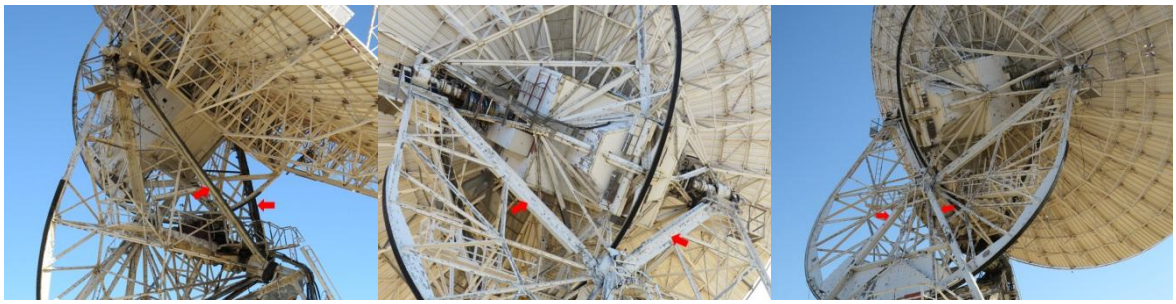

Figure 5.22 Left and middle: The two longer beams on the north and south sides supporting the Dec shaft. Right: The two beams on the east and west side supporting the south polar shaft.

A diurnal model, added as a separate day-of-year (DOY) dependent component of the pointing model, is applied to compensate for the false shift introduced into the encoder and the corresponding offset in the pointing. Separate diurnal models for Dec and HA pointing exist. For the Dec pointing it is necessary to distinguish between seasons, with a model for summer and winter and an interpolation between the summer and winter models used for autumn and spring. The diurnal model comprises a fixed list of built-in pointing diurnals in millidegree as a function of UT times for each of the hours 0-24 UT with interpolation between the hourly values of the curve, relevant for the particular DOY. The pointing offsets were determined in a pointing measurement campaign several years ago. Any pointing model observations have to be taken at night between the hours of 18 UT and 4 UT when the additive diurnal term is zero and therefore not applied.

The Dec pointing seasonal diurnal model applied during the May 2020 and May 2021 Jupiter gain curve observations would have been that for mid-winter, and with the varying times of sunrise/sunset, it is therefore possible that unsuitable Dec pointing offset diurnals had been applied during the gain curve observations at sunrise. It was decided to investigate a possible correlation between the degraded pointing in the Jupiter gain curve observations and preferential warming of the northern and eastern sides of the support structure with sunrise.

5.2.1 Methodology

Ten temperature sensors are mounted on the 26-m antenna's support structure to determine whether any correlation exists between structural temperature variations and observed diurnal pointing variations. Sensors AT1 to AT8 are mounted at the top and bottom of each of the four Dec bearing housing support beams to determine whether differential heating of these beams could be responsible for a significant diurnal offset in the Dec pointing. Sensors AT9 and ATA are mounted at the top of the two south polar bearing housing support beams to determine whether differential heating of these beams could be responsible for a smaller diurnal offset in the HA pointing.

Temperature sensor data during the 2020d139-140 gain curve observations were plotted in Python for each sensor individually to determine the temperature behaviour of the sensor, specifically at sunrise, and to compare it with that of the other sensors to detect possible differential heating of the support beams. Temperature sensor data during the 2020d139-140, 2021d134-135 and 2021d138-139 gain curve observations were subsequently investigated to determine a possible correlation between differential heating of the support beams and a degraded Dec pointing correction at sunrise. The difference in temperature of sensors mounted on the north beams and corresponding sensors mounted on the south beams was plotted in Python and differential heating of the north and south beams at sunrise was compared with the HA / time range over which there was an observable deterioration in the Dec pointing correction.

5.2.2 Results and discussion

Behaviour of individual temperature sensors on support structure:

The behaviour of each of the temperature sensors on the support structure during the 2020d139-140 gain curve observations (20:35 - 07:37 UT) was investigated and compared with a view to detecting differential heating effects at sunrise (04:42 UT).

Plots of each sensor's day/night temperature variation during the gain curve observations of the 18th and 19th of May 2020 show the temperature of the sensors to start increasing within an hour of sunrise on the 19th of May 2020, and at most within half an hour of an increase in the ambient temperature (see Figure 5.23 and Figure 5.24). The temperature of the sensor at the top of the north-east (NE) beam starts increasing at sunrise, half an hour before an increase in the ambient temperature. The temperature sensors display distinct differential heating effects, particularly under conditions of direct sunlight. It would seem as if the temperature increases for sensors on the north side before it increases for those on the south side and for sensors on the east side before it increases for those on the west side. The winter sun shining in low under the dish at sunrise is causing differential heating of the support beams. The temperature variation is largest for sensors mounted on the north side, and it is the longer north side beams which warm up more, possibly causing an even larger shift in Dec pointing due to differential heating.

In the plots of temperature sensors mounted on the west (AT9 / HA West) and east (ATA / HA East) sides of the south polar shaft support beams (see bottom of Figure 5.23), the AT9 sensor displays behaviour expected from a sensor mounted on the east side, with its temperature starting to increase at around sunrise compared to the increase in temperature for the ATA sensor starting at ~6 UT only. Initially it was suspected that readings from the HA West and HA East temperature sensors had been interchanged and that the spike in temperature appearing at ~6 UT for the AT9 sensor could possibly also be ascribed to a sudden increase in temperature due to the early morning sun, which would be behaviour expected from the HA East rather than HA West sensor. However, the physical location and wiring of all the temperature sensors have since been confirmed and do indeed correspond with their labelling. It still needs to be verified that none of the sensors have intermittent connections. The sensors should also be recalibrated.

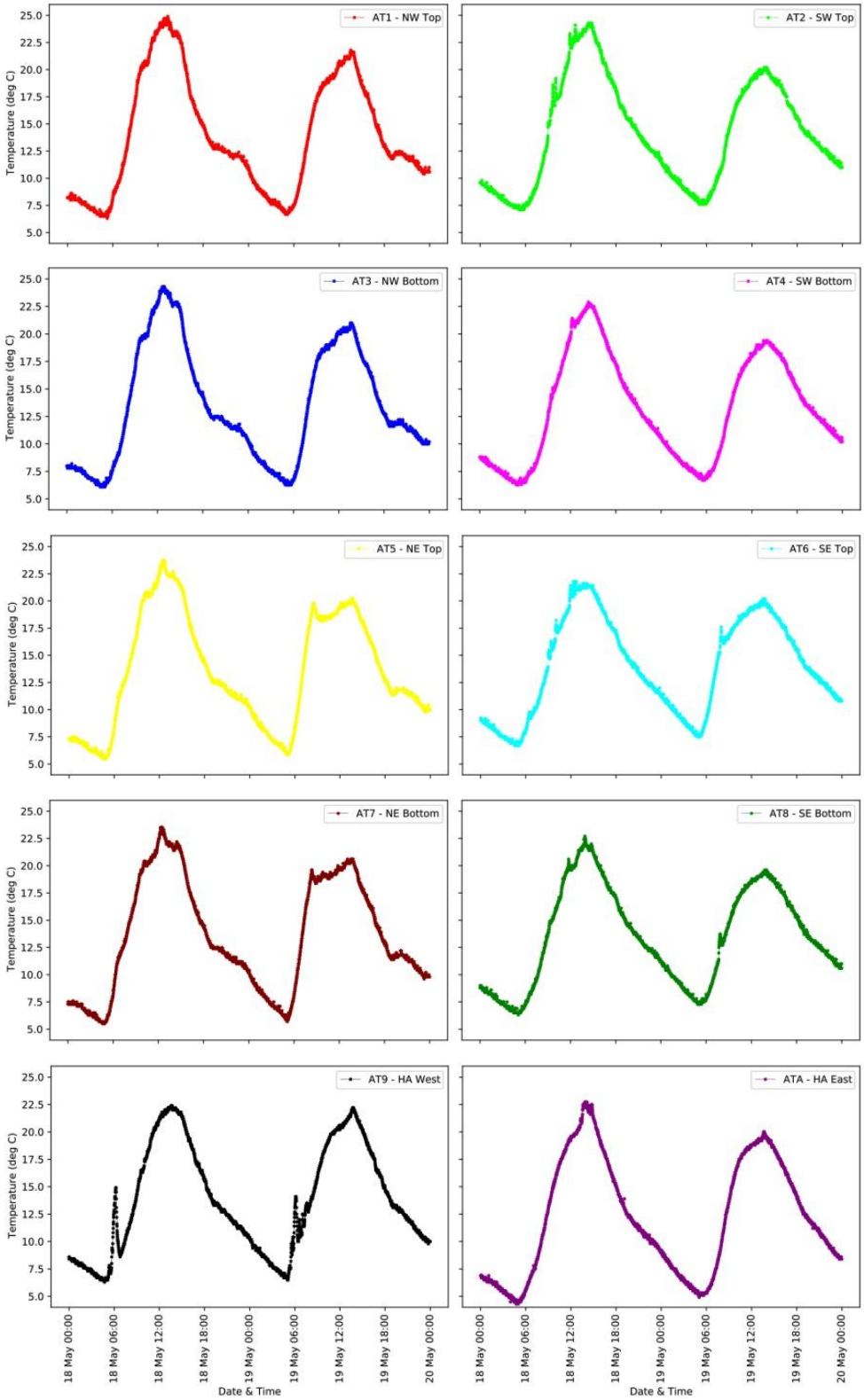

Figure 5.23 Plots of AT1-9 and ATA sensor day/night temperature behaviour during the 2020d139-140 gain curve observations (sunrise occurred at 04:42 UT on the 19th of May 2020).

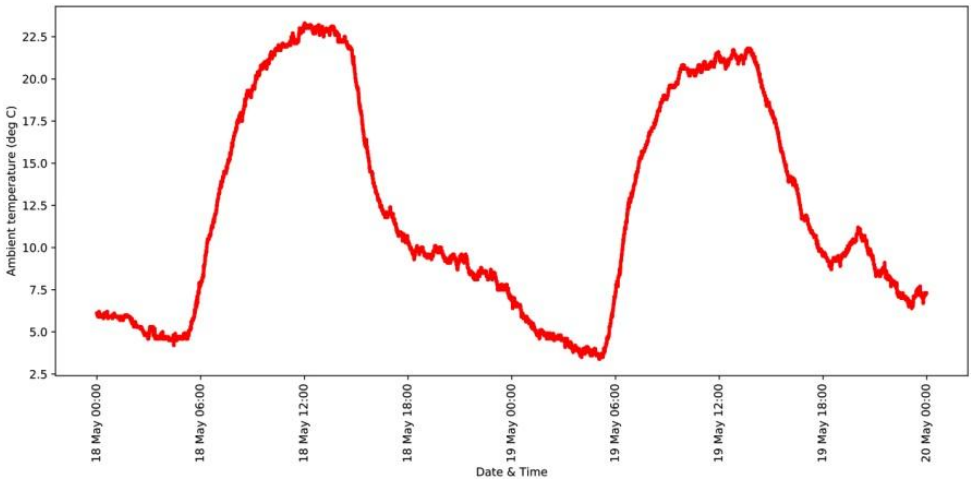

Figure 5.24 Plot of ambient temperature surface measurements during the 2020d139-140 gain curve observations (sunrise occurred at 04:42 UT on the 19th of May 2020).

Differential heating of the HA West and HA East beams is responsible for the HA pointing offset. The sinusoidal pattern of the HA diurnal pointing model does not agree with observed differential heating effects. In the model, the HA pointing offset is shifted to the west in the morning and to the east in the afternoon to allow for preferential heating of first the east side and then the west side of the antenna as the sun moves across the sky. The temperature sensors do not indicate such differential heating to take place however. The HA pointing offsets applied in the HA diurnal pointing model also do not agree with currently observed HA pointing offsets. Dec pointing offset diurnals also require re-evaluation, especially in cases where direct sunlight causes significant differential heating of the support beams. A thorough investigation of possible differential heating effects as indicated by the temperature sensors mounted on the antenna support structure should be conducted so that an appropriate model of a linear combination of the sensors can be developed that is able to reproduce the measured diurnal Dec pointing offset.

Differential heating at sunrise and declination pointing during the first set of gain curve observations at 22 GHz – 2020d139-140 (18-19 May 2020):

The 2020d139-140 triple drift scan gain curve observations extended from 20:35:21 UT on the 18th of May 2020 until the last scan was observed at 07:36:54 UT on the

19th of May 2020. Sunrise occurred at 04:42 UT on the 19th, corresponding to observations at an HA of +36°.

The increase in the Dec pointing correction between HAs of ~+25° to +55° occurred at ~4 to 6 UT (~0.5 h before to 1.5 h after sunrise) (see Figure 5.25). The smaller increase between HAs of ~+65° to +75° occurred at ~06:40 to 07:20 UT (~2 to 2.5 h after sunrise).

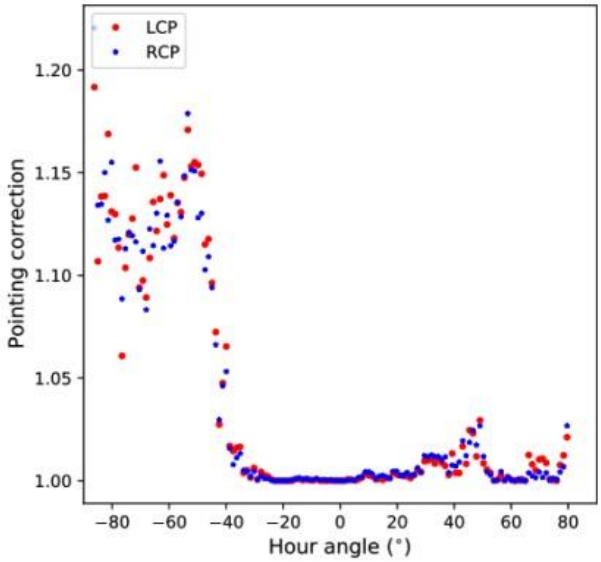

Figure 5.25 2020d139 140 – Plot of Dec pointing correction for LCP and RCP, against HA.

Plots of the differences between temperatures of sensors mounted on the north beams and that of sensors mounted on the south beams during the 2020d139-140 gain curve observations display diurnal variations (see Figure 5.26). Although, as indicated previously, the sensors may not be performing optimally and may require recalibration, especially of the zero reference, it is apparent that sensors mounted on the north beams display a higher temperature than sensors mounted on the south beams from about sunrise to sunset. Thereafter, the sensors on the north beams display a rapid decrease in temperature and, with the sensors on the south beams having closed the gap in temperature difference during the day, it is the latter that display a higher temperature from about sunset to sunrise. The accompanying differential heating of the support structure is responsible for the diurnal variation in the Dec pointing offset. As also indicated

previously, differential heating effects as suggested by the behaviour of the temperature sensors mounted on the west (AT9 / HA West) and east (ATA / HA East) sides of the south polar shaft support beams (see Figure 5.27, on left), do not support the sinusoidal pattern employed in the current HA pointing diurnal model.

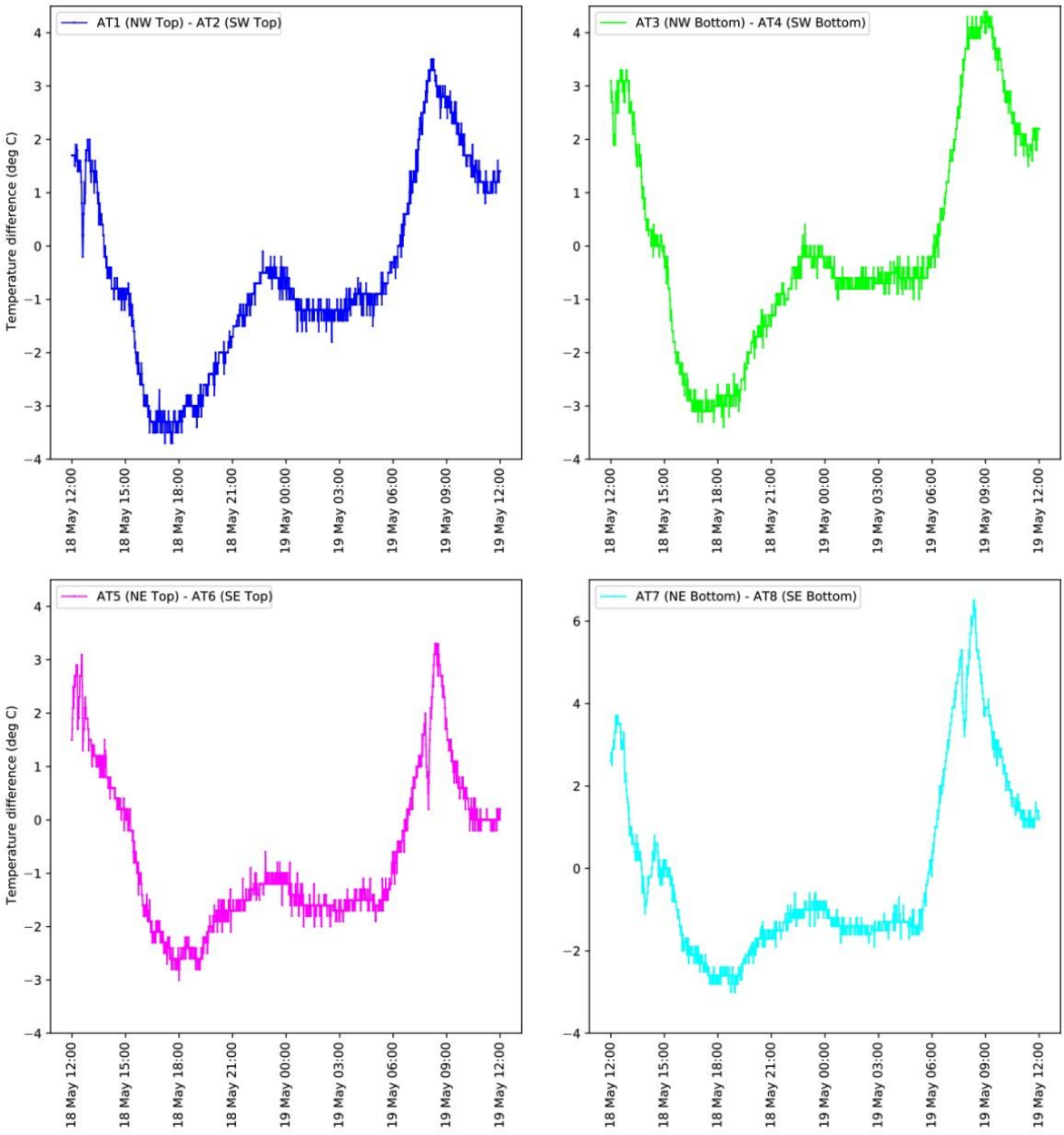

Figure 5.26 Plots of temperature differences between the temperature sensors on the north (AT1, AT3, AT5 and AT7) and south (AT2, AT4, AT6 and AT8) beams of the 26 m antenna during the 2020d139-140 Jupiter gain calibration observations.

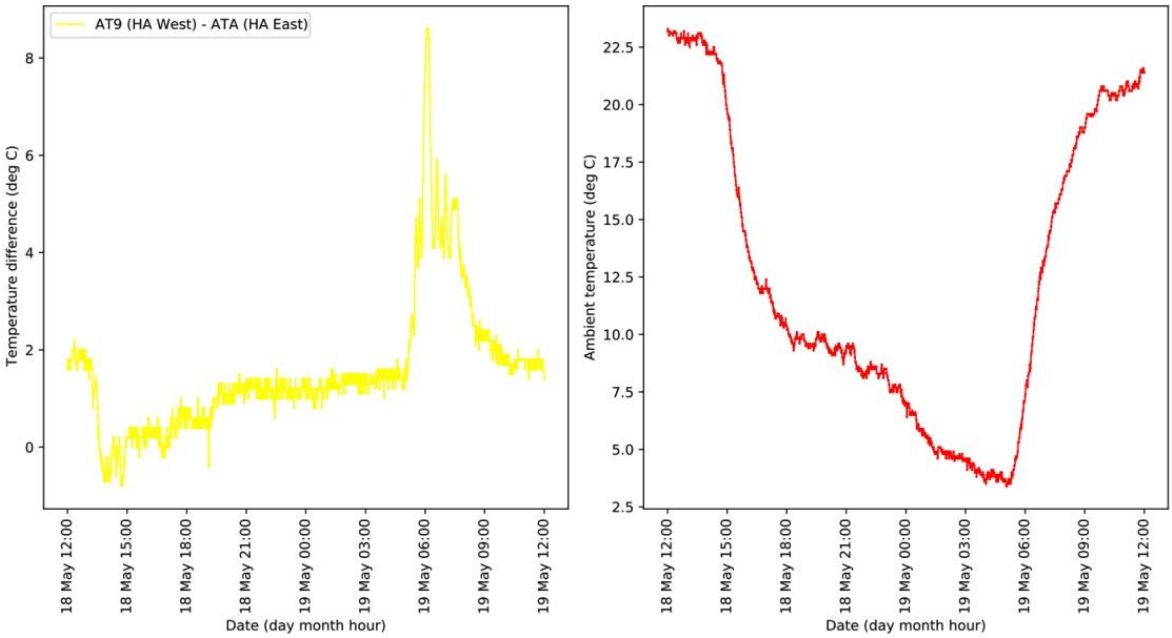

Figure 5.27 Plots of temperature differences between the temperature sensors on west (AT9) and east (ATA) beams of the 26 m antenna (on left) and ambient temperature surface measurements (on right) during the 2020d139-140 Jupiter gain calibration observations.

From the temperature sensor difference plots, it is apparent that the beams on the north side supporting the Dec shaft started warming up at around sunrise, between ~5 and 5:30 UT, corresponding to observations at HAs between ~+40° and +50° and reached a maximum after the end of observations between ~8 and 8:30 UT. The beam on the west side supporting the south polar shaft also started warming up at around sunrise at ~5 UT (HA = +41°) and spiked to a maximum at ~6:30 UT (HA = +62°), about 2 h after sunrise. The ambient temperature (see Figure 5.27 on right) started increasing shortly after sunrise at ~5 UT from ~3.5 °C to 16 °C at end of observations.

Differential heating and pointing during the second set of gain curve observations at 22 GHz – 2021d134-135 (14-15 May 2021):

The 2021d134-135 triple drift scan gain curve observations extended from 23:07:15 UT on the 14th of May 2021 until the last scan was observed at 10:32:48 UT on the

15th of May 2021. Sunrise occurred at 04:40 UT on the 15th, corresponding to observations at an HA of -3°.

The increase in the Dec pointing correction between HAs of ~+10° to +55° occurred at ~5:30 to 8:30 UT (~2 to 4 h after sunrise; see Figure 5.28).

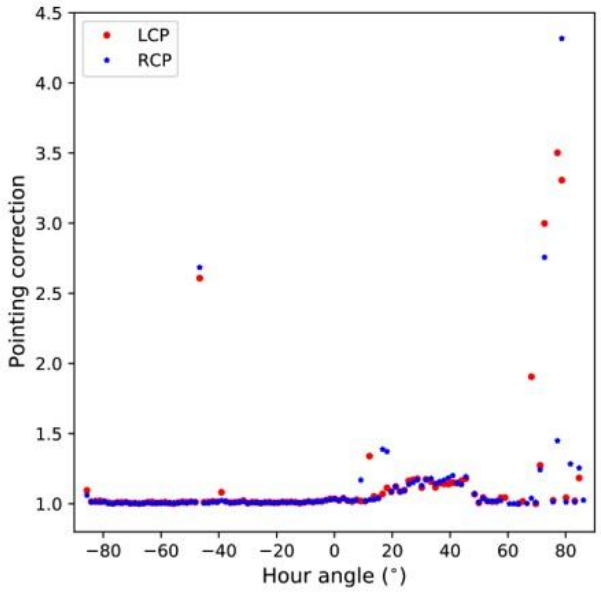

Figure 5.28 2021d134 135 – Plot of Dec pointing correction for LCP and RCP, against HA.

From the temperature sensor difference plots (see Figure 5.29), it is apparent that the beams on the north side supporting the Dec shaft started warming up at sunrise at ~5 UT (HA = -3°) and reached a maximum at ~7:30 UT (HA = +41°), about 3 h after sunrise. Thereafter the beams started cooling down, reaching a lower shoulder at ~9:00 to 9:30 UT (HA = +64° to +71°), about 4.5 h to 5 h after sunrise, with a slight peak at ~10:00 to 10:30 UT (HA = +79° to 86°) at end of observations. The beam on the west side supporting the south polar shaft (see Figure 5.30, on left) also started warming up at around sunrise at ~5 UT (HA = +3°) and spiked to a maximum at ~7:30 UT (HA = +41°), about 3 h after sunrise. Thereafter the beam rapidly cooled down and stabilised shortly after the end of observations. The ambient temperature (see Figure 5.30, on right) started increasing shortly after sunrise at ~5 UT from ~4 °C to 22 °C at end of observations.

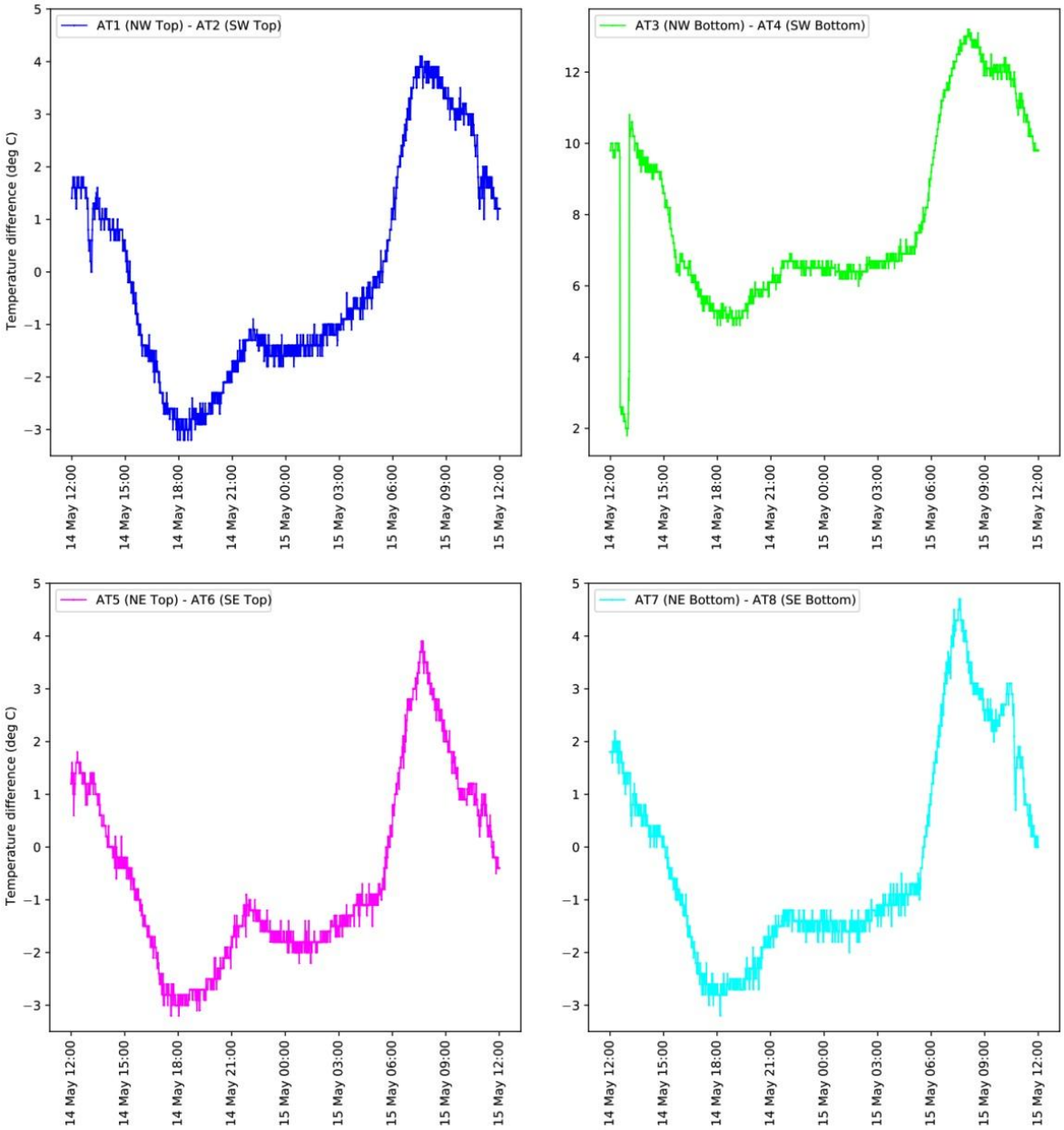

Figure 5.29 Plots of temperature differences between the temperature sensors on the north and south beams of the 26 m antenna during the 2021d134-135 Jupiter gain calibration observations.

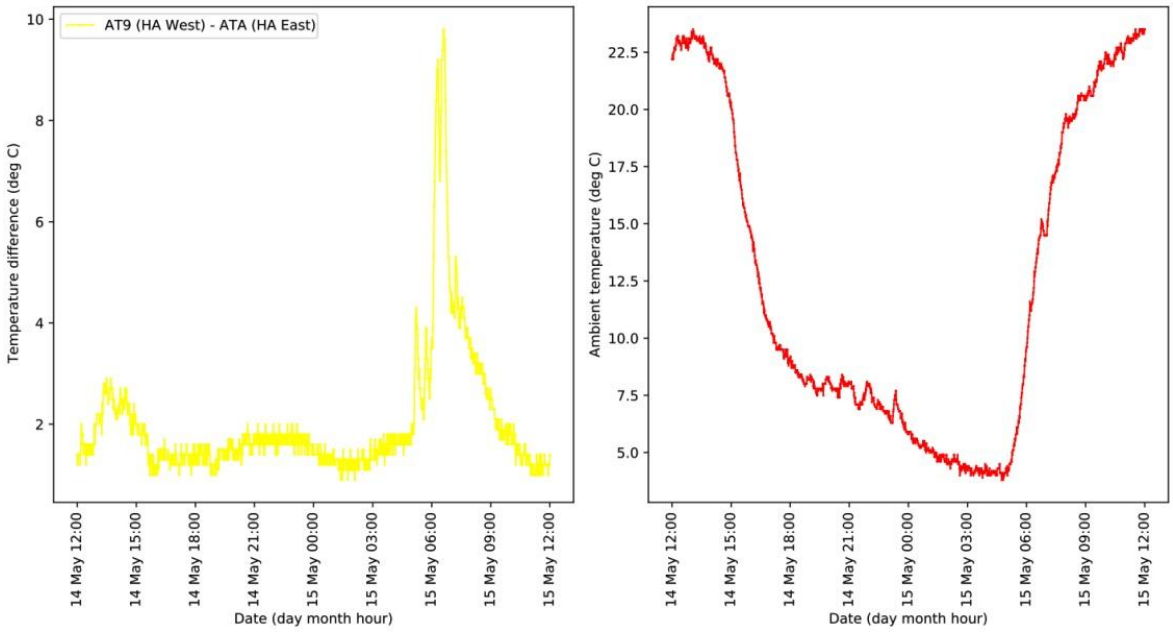

Figure 5.30 Plots of temperature differences between the temperature sensors on the west and east beams of the 26 m antenna (on left) and ambient temperature surface measurements (on right) during the 2021d134-135 Jupiter gain calibration observations.

Differential heating and pointing during the third set of gain curve observations at 12 GHz – 2021d138-139 (18-19 May 2021):

The 2021d138-139 triple drift scan gain curve observations extended from 23:02:05 UT on the 18th of May 2021 until the last scan was observed at 10:19:04 UT on the 19th of May 2021. Sunrise occurred at 04:42 UT on the 19th, corresponding to observations at an HA of +1°.

The slight increase in the Dec pointing correction between HAs of ~-20° to 0° occurred at ~3 to 4:30 UT (~1.5 h before sunrise to sunrise) (see Figure 5.31). Another slight increase occurred between HAs of ~+35° to +55° occurred at ~7 to 8 UT (~2.5 to 3.5 h after sunrise).

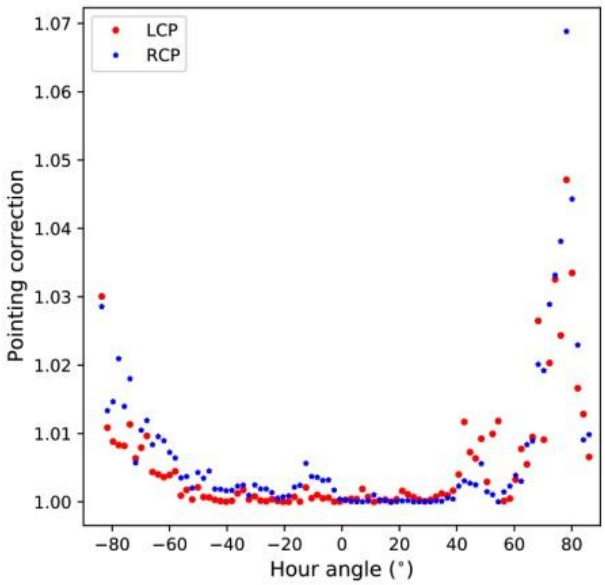

Figure 5.31 2021d138-139 – Plot of Dec pointing correction for LCP and RCP, against HA.

From the temperature sensor difference plots (see Figure 5.32), it is apparent that the beams on the north side supporting the Dec shaft started warming up at ~4:30 to 5:30 UT (HA = -1° to +13°), at about sunrise to an hour after sunrise, to reach a maximum at ~8 to 8:30 UT (HA = +52° to 58°), about 3.5 to 4 h after sunrise. The beam on the west side supporting the south polar shaft (see Figure 5.33, on left) started warming up at sunrise (HA = +1°) and spiked to a maximum at ~6 UT (HA = +21°), about 1.5 h after sunrise. Thereafter the beam cooled down rapidly to reach a first minimum at ~7 UT (HA = +37°), about 2.5 h after sunrise, then spiked to a lower maximum at ~7:30 UT (+45°), about 3 h after sunrise, then cooled again rapidly and stabilised shortly after the end of observations. The ambient temperature (see Figure 5.33, on right) started increasing shortly after sunrise at ~5:30 UT from ~3.5 °C to 20 °C at end of observations.

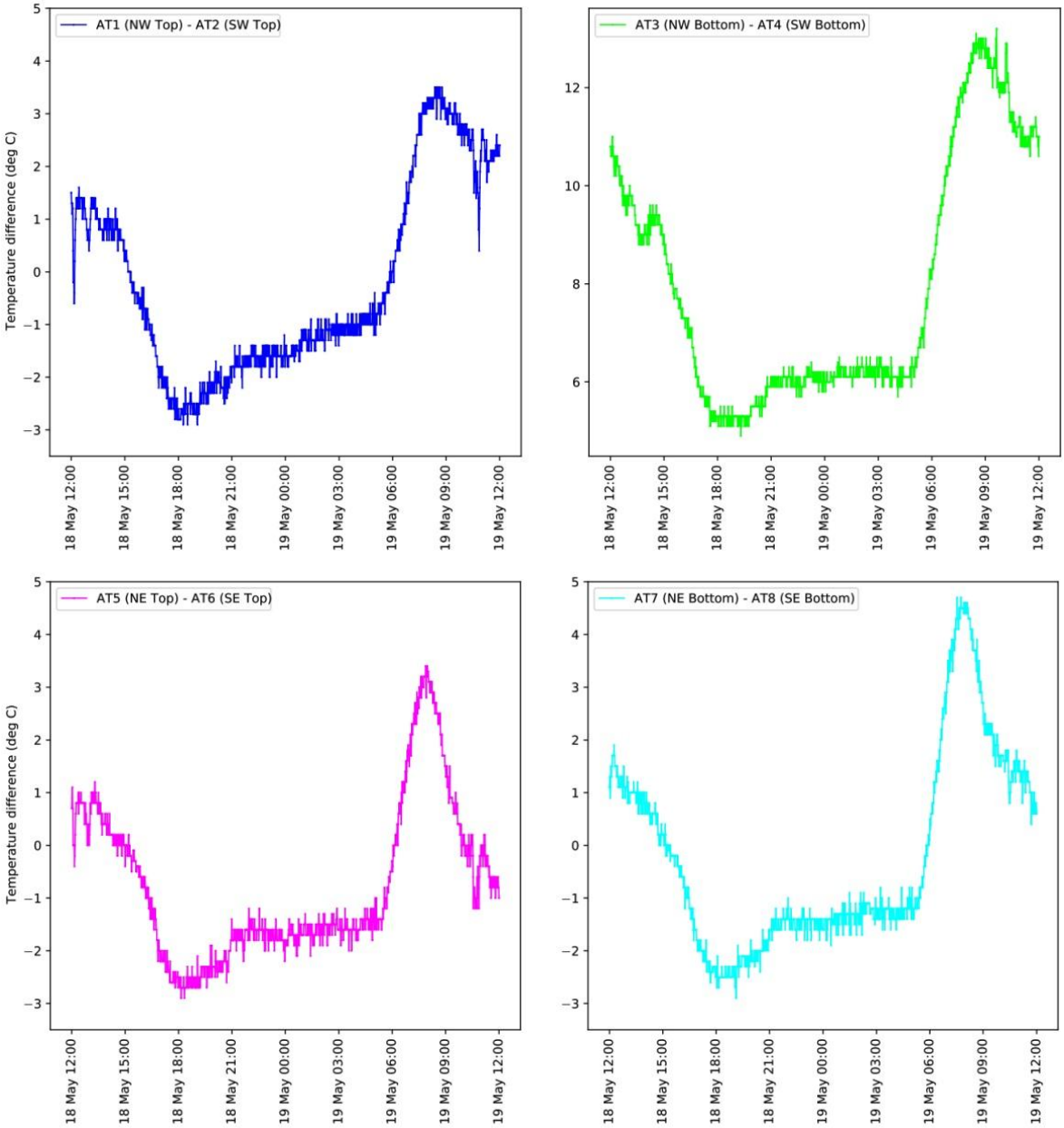

Figure 5.32 Plots of temperature differences between the temperature sensors on the north and south beams of the 26 m antenna during the 2021d138-139 Jupiter gain calibration observations.

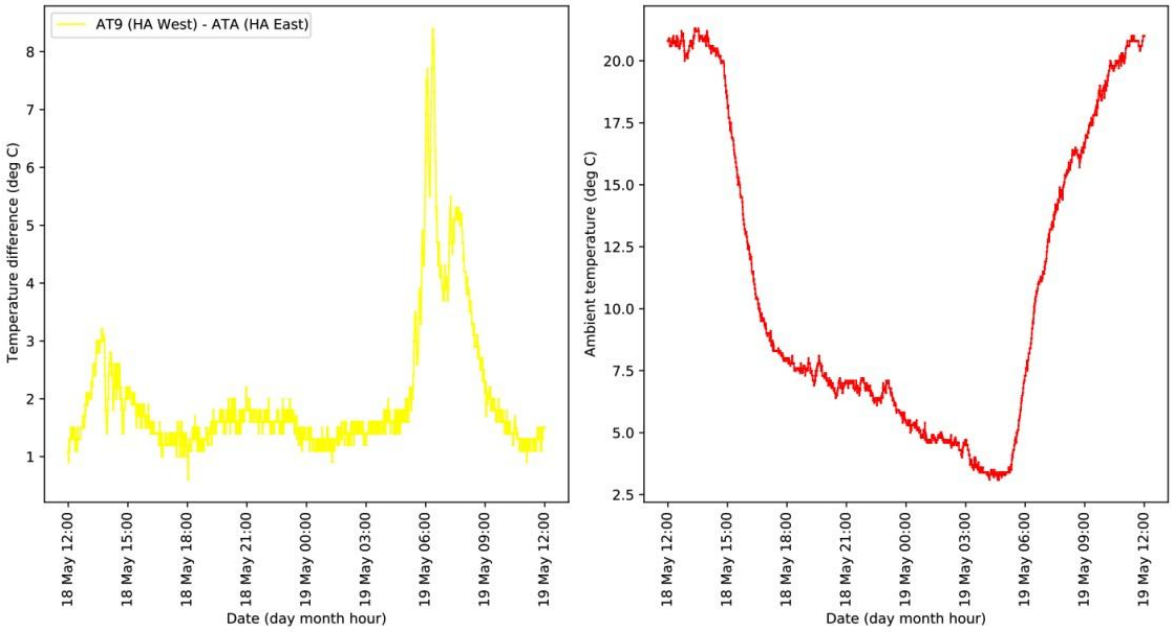

Figure 5.33 Plots of temperature differences between the temperature sensors on the west and east beams of the 26 m antenna (on left) and ambient temperature surface measurements (on right) during the 2021d138-139 Jupiter gain calibration observations.

The differential heating of beams on the north and south sides of the antenna supporting the Dec shaft, with the north side beams warming up before the south side beams at sunrise, could possibly have some influence on the Dec pointing degrading around sunrise, at least for the 2020d139-140 and 2021d138-139 observations (very slightly degrading for the latter). But for the 2021d134 observations, the Dec pointing degrades 2 to 4 hours after sunrise only. A similar lag in the Dec pointing degrading is observed for the smaller increases in the Dec pointing corrections of the 2020d139-140 and 2021d138-140 observations (again very slightly degrading for the latter), which occurred 2 to 2.5 h and 2.5 to 3.5 h after sunrise respectively. These smaller increases occurred just before the differential heating of the beams supporting the Dec shaft reached a maximum at ~3 to 4 hours after sunrise. An in-depth investigation of differential heating of the support structure as it relates to temperature sensor differentials and the angle of the sun is required to find more appropriate Dec and HA pointing diurnal models for all the seasons. Once the location and performance of the temperature sensors have been verified and additional sensors have been installed as required, an accurate temperature model based on data from

the temperature sensors can be constructed and included as part of the antenna's pointing model. Ultimately, it might be necessary to schedule the higher frequency 22 GHz observations to be performed only during the nighttime when pointing is stable.

The Dec pointing seems to degrade for similar HAs in the three sets of observations which could be due to an undiscovered pointing effect not related to differential heating at sunrise. Follow-up observations should be conducted with Jupiter up all night to determine whether the degraded pointing is indeed caused by differential heating or whether it is due to unrelated effects such as bearing failure, gravitational deformation and deflections, optical misalignment *etc*.

5.3 SUMMARY

Accurate pointing of the HartRAO 26 m antenna is required at K-band for contributing to CRF realisation. A low detection of sources in K-band observations and the existence of a significant pointing offset in K-band pointing observations prompted an investigation of the pointing performance of the HartRAO 26 m antenna at 22 GHz. Gain calibration observations with Jupiter as calibrator source were conducted to determine the pointing correction and antenna gain at 22 GHz. Coma sidelobes due to astigmatism caused by gravitational deformation of the dish were detected. Longer drift scan as well as 12 GHz observations were conducted in an attempt at reducing the influence of the coma sidelobes which contaminate the pointing correction. Coma sidelobes and scatter in the Dec pointing correction in the east (Jupiter rising) were diminished appreciably for 12 GHz observations only. An unexplained scatter in the Dec pointing correction in the west (Jupiter setting) and outliers remained. The Dec pointing corrections proved unreliable at lower elevations, not providing any improvement to the antenna gain curve. The antenna gain decreased sharply in the 2021 observations, which could possibly be due to a faulty 22 GHz receiver, but this requires further investigation. A gain asymmetry of unknown cause, prevalent from the start, persisted. The Jupiter gain curve calibration observations were modified subsequently to observe at seven different antenna sub-reflector focus positions in order to determine the impact of focussing on the coma sidelobes and antenna gain. Coma sidelobes appeared for all focus positions. Although the highest gain was achieved for the +0.5 focus position at

zenith, the +0.0 default focus position provided for higher gain at all other elevations and was therefore retained. In this study, it was found that the HartRAO 26 m antenna's pointing performance and gain at 22 GHz are indicative of an antenna no longer capable of meeting the stringent pointing accuracy requirements for ICRF realisation. As antenna pointing is impacted by temperature variations in the antenna structure, a possible correlation between the degraded pointing in the Jupiter gain curve observations and preferential warming of the northern and eastern sides of the HartRAO 26 m antenna's support structure with sunrise was investigated by comparing the behaviour of temperature sensors mounted on the structure and the Dec pointing correction at sunrise. It was found that differential heating of beams on the north and south sides of the antenna supporting the Dec shaft could possibly have some influence on the Dec pointing degrading around sunrise in some of the gain curve observation sets. The Dec pointing also seemed to degrade for similar HAs in the three sets of observations, apparently not caused by differential heating of the antenna support structure at sunrise, but possibly due to unrelated pointing effects. A rigorous study of differential heating of the support structure is required to improve the Dec as well as HA pointing diurnal models for all seasons.

CHAPTER 6 ANTENNA AXIS OFFSET

The VLBI reference point of an antenna, to which astrometric/geodetic VLBI observables are referred, is a point within the antenna which is fixed and invariant to the antenna's rotation. It is located at the intersection of the antenna's two rotation axes. In cases where the rotation axes do not physically intersect, such as for the HartRAO 26 m and 15 m antennas, the VLBI reference point is represented by the intersection of the antenna's fixed primary axis with the plane perpendicular to it containing the moving secondary axis, i.e. the point on the primary axis closest to the secondary axis (Combrinck and Merry, 1997). The antenna axis ofset (AO) is the distance between the VLBI reference point and the secondary axis, and it must be known with high accuracy if the VLBI reference point is to be determined accurately. The antenna AO causes geometric and dry tropospheric delays. As it contributes to the observed delay, it needs to be considered in the VLBI analysis. An antenna AO model is applied for antennas with non-intersecting rotation axes to correct for the additional delay caused by the antenna AO (Krásná, Nickola and Böhm, 2014).

An error in the value of the antenna AO would degrade the accuracy of station position estimates, displacing the VLBI reference point which defines the station's location. Nilsson *et al*. (2017) showed that antenna AO and station coordinates are highly correlated, with an error of 1 cm in the AO of an azimuth-elevation (az-el) mount antenna causing an error of ~1.3 cm in the estimated vertical station coordinate. At HartRAO, the 26 m legacy antenna's VLBI reference point serves as reference point for other co-located instruments, *e.g.* the 15 m antenna and a soon to become operational VGOS antenna. For accurate astrometric and geodetic VLBI results, the VLBI reference point, i.e. station coordinates of co-located antennas, and thus their AOs, have to be known with high accuracy. In order to reach the GGOS/VGOS goal of 1 mm accuracy in station coordinates, the AO needs to be known with sub-millimetre accuracy (Nilsson *et al*., 2017).

The *a priori* AO values recommended by the IVS for use in geodetic VLBI data analysis are taken from values measured in ground surveys where possible, as such values are more accurate than values obtained from the VLBI analysis itself. Stations are required to conduct terrestrial surveys to measure the AO accurately (IERS, 2005). Such surveys are, however, knowledge- and resource-intensive and are therefore not conducted on a regular basis. Ground survey AO values are thus available for only a few stations and, even then, the values might be from ground surveys conducted several years previously. It is therefore important to establish whether it is possible to estimate the AO in geodetic VLBI analysis with the required accuracy. In this study, the geodetic VLBI analysis software, VieVS (Böhm *et al*., 2018), was used to analyse data from global geodetic sessions in which the HartRAO 26 m and 15 m antennas participated in order to obtain an estimation of the AO for each of the antennas. The VieVS estimated antenna AO values were subsequently compared with values measured in ground surveys.

6.1 HARTRAO ANTENNA AXIS OFFSET

The rotation axes of the HartRAO 26 m equatorially mounted Cassegrain radio telescope do not intersect and an AO of 6.7 m exists. Its VLBI reference point is represented by the intersection of the fixed Hour Angle (HA) axis with the perpendicular plane containing the moving declination (Dec) axis (see Figure 6.1 (a)). For the equatorially mounted 26 m antenna, this AO produces a time delay, $\Delta\tau_{AO}$, dependent on the declination of the radio source, δ (Nothnagel, 2018) –

$$\Delta\tau_{AO} = \frac{1}{c} \cdot AO \cdot \cos\delta \tag{6.1}$$

The rotation axes of the HartRAO 15 m az-el mounted radio telescope also do not intersect and an AO of 1.5 m exists. Its VLBI reference point is represented by the intersection of the fixed azimuth axis with the perpendicular plane containing the moving elevation axis (see Figure 6.1 (b)). For the az-el mounted 15 m antenna, this AO produces a time delay, $\Delta\tau_{AO}$, dependent on the pointing elevation angle, ε (Nothnagel, 2018) –

$$\Delta\tau_{AO} = \frac{1}{c} \cdot AO \cdot \cos\varepsilon \tag{6.2}$$

Department of Geology, Geoinformatics and Meteorology
University of Pretoria

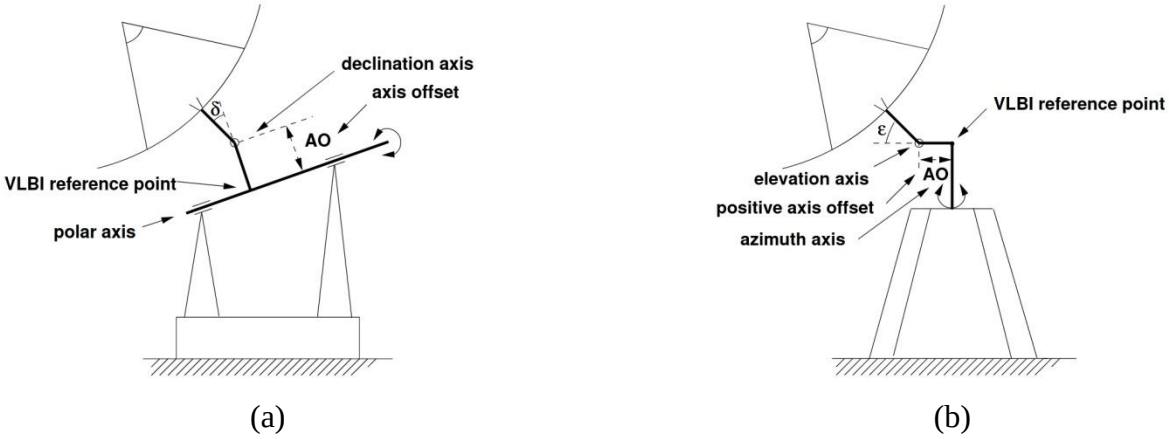

(a) (b)

Figure 6.1 (a) Equatorial (polar) mount (Nothnagel, 2018). (b) Azimuth elevation (az-el) telescope mount with positive axis offset (AO) (Nothnagel, 2018).

On the 3rd of October 2008, the HartRAO 26 m antenna suffered a critical failure of its south polar bearing. On the 11th of August 2010, the first post-repair geodetic VLBI session was run. Post-repair position time series solutions indicated no noticeable shift in position. Although the AO is considered to be fixed, major antenna repairs, such as a bearing replacement on the 26 m antenna in 2010, could conceivably cause a change in the AO (Kurdubov and Skurikhina, 2010; Nilsson *et al*., 2017). The failure and subsequent replacement of the 26 m antenna's south polar bearing therefore required that its AO after bearing replacement be investigated, as the *a priori* AO value used for the 26 m antenna in geodetic VLBI analysis originates from a 2003 ground survey, before bearing failure. The AO of the 15 m antenna also required investigation as the *a priori* value used in data analysis was determined in a preliminary Global Positioning System (GPS) survey only. For this investigation, data from geodetic VLBI sessions were analysed using VieVS to estimate the AOs of both the HartRAO 26 m and 15 m antennas. VieVS estimated AO values were compared with measurements from the latest ground survey conducted in 2014.

6.1.1 Methodology

The geodetic VLBI analysis software, VieVS, was used for data analysis (see Section 2.4). The software makes use of the VLBI delay observables to estimate the parameters of

interest in a least-squares adjustment. Geodetic VLBI data from 1482 sessions observed by 77 IVS network stations (Nothnagel *et al*., 2017) over the period 1986–2017, in which the HartRAO 26 m and/or 15 m antennas participated, were used in solutions of the combined geodetic VLBI sessions (global solutions) in VieVS.

Data analysis consisted of processing sessions individually with VieVS to remove clock breaks, set reference clocks, exclude defective stations, baselines, observations and/or station cable calibration and eliminate outliers where necessary. Normal equations, which serve as input to the global solutions, were generated with *a priori* modelling, in general following the IERS Conventions 2010 (IERS, 2010) and parametrisation as presented in Table 6.1. The normal equations of the single sessions were then combined to derive global solutions in which the antenna AO as well as station coordinates and velocities were estimated as global parameters for the period under investigation. The terrestrial datum was realised by applying no-net-translation (NNT) and no-net-rotation (NNR) constraints to coordinates of established stations. Position discontinuities were introduced where station coordinates had changed due to seismic events or relocation or repair of an antenna.

For the 26 m antenna, the AO value was estimated for the following sessions: (1) from the start of the 26 m antenna's operation in 1986 until the critical bearing failure in October 2008; (2) for sessions from after bearing replacement in August 2010 to the end of 2017; and (3) for the entire period from 1986 to 2017. For the 15 m antenna, the AO value was estimated for sessions from the start of the 15 m antenna's operation in October 2010 to the end of 2017. The *a priori* AO values used in the VLBI analysis are as recommended by the IVS. For the HartRAO 26 m antenna, the *a priori* AO value is based on the value determined in a 2003 co-location survey (IGN, 2005). For the HartRAO 15 m antenna, the *a priori* AO value is based on the value determined in a GPS survey in 2007 (HartRAO, n.d.).

Department of Geology, Geoinformatics and Meteorology
University of Pretoria

Table 6.1 Models applied and parameters estimated in single session analysis in VieVS.

VieVS3.2 Input parameters	
Models	
TRF	ITRF2020 (Altamimi *et al*., 2022)
CRF	ICRF3SX (Charlot *et al*., 2020)
Ephemerides	JPL 421 (Folkner *et al*., 2009)
ZHD and ZWD mapping function	VMF3 (Landskron and Böhm, 2018)
Solid Earth tides	IERS Conventions (IERS, 2010)
Tidal ocean loading	TPXO72 (Egbert and Erofeeva, 2002)
Tidal atmosphere loading	APL_VIENNA (Wijaya *et al*., 2013)
Non-tidal atmosphere loading	APL_VIENNA (Wijaya *et al*., 2013)
Pole tide	IERS Conventions (IERS, 2010)
Ocean pole tide	Desai (2002)
Thermal antenna deformation	Nothnagel (2009)
EOP	14C04 (IAU2000) (Bizouard *et al*., 2019)
Ocean tides	IERS Conventions (IERS, 2010)
Precession/nutation	IAU 2006/2000A (Capitaine *et al*., 2003, Mathews *et al*., 2002)
VieVS3.2 Estimated parameters	
Estimation – Least squares	
ZWD	interval = 0.5 h, constraints = 1.5 cm/h
Troposphere north and east gradients	interval = 3 h, constraints = 0.05 cm/6h, absolute constraints = 0.1 cm
Clock	interval = 1 h, constraints = 1.3 cm/h
EOP	interval = 1 day, constraints = 10^{-4} mas/day

To investigate the possibility of seasonal variations in antenna AO, sessions were divided into seasonal groupings – summer = DecJanFeb, autumn = MarAprMay, winter = JunJulAug, spring = SepOctNov – as well as into two six-month periods – autumn and winter months (Mar-Aug), spring and summer months (Sep-Feb) – for analysis. The AO was also estimated for IVS continuous (CONT) campaign sessions in which the

HartRAO antennas participated – CONT02, 05, 08 and 11 for the 26 m antenna and CONT14 and CONT17 for the 15 m antenna. These campaigns are conducted once every three years and each consists of 15 days of continuous VLBI sessions aimed at collecting the highest accuracy VLBI data possible. Given the limited 15-day time span of a CONT campaign, station velocities could not be estimated but were fixed to their ITRF2020 values.

The VieVS estimated antenna AO values from the various investigations were subsequently compared with AO values determined in: (1) the 2003 co-location survey for the 26 m; (2) the 2007 GPS survey for the 15 m antenna; and (3) a 2014 co-location survey (Muller, Pesce & Collilieux, 2020) for both the HartRAO antennas. Due to re-processing of the 2014 co-location survey data, the 2014 AO survey values for both the HartRAO antennas were not available for inclusion as *a priori* AO values for VLBI analysis in the ITRF2020 computation.

Antenna AO values for the HartRAO 26 m and 15 m antennas as determined by ground survey are displayed in Table 6.2. There is good agreement between the AO values determined for the 26 m antenna by: (1) conventional and GPS surveys well before the failure and replacement of the bearing in 2008–2010 (Combrinck and Merry, 1997); (2) a co-location survey in July and August of 2003 (IGN, 2005), five years before bearing failure; and (3) a co-location survey in February of 2014 (Muller, Pesce & Collilieux, 2020), less than four years after the bearing was replaced and operations on the 26 m antenna resumed in August of 2010. In contrast, the AO value determined for the 15 m antenna by GPS survey in 2007 (HartRAO, n.d.), well before the start of geodetic VLBI observations on the 15 m antenna in 2012, and that determined by the co-location survey of 2014 differ by ~5 mm.

In this study, three global solution tests were conducted in which the AO estimation was treated differently for stations other than HartRAO to determine which of the following approaches would produce VieVS estimated AO results for the HartRAO antennas closest to their 2014 co-location survey values:

(i) T1: global solution in which the AO was estimated for the two HartRAO antennas only

(ii) T2: global solution in which the AO was estimated for all participating stations except for those with *a priori* AO values based on ground survey values

(iii)T3: global solution in which the AO was estimated for all participating stations

Table 6.2 HartRAO 26 m and 15 m antenna axis offset (AO) values determined by ground surveys (26m a priori AO = 6695.3 mm; 15m a priori AO = 1495.0).

Survey method	**Determined by (year of survey)**	**AO (mm)**
26m before bearing failure:		
Conventional survey	M. Newling (1990)	6695 ± 3
HartRAO GPS	L. Combrinck (1995)	6695.6 ± 2.3
Local tie survey	IGN (2005)	6695 ± 2.5
26m after bearing replacement:		
Local tie survey	Muller, Pesce & Collilieux (2020)	6694.5 ± 0.7
15m:		
GPS survey	A. Combrinck (2007)	1495
Local tie survey	Muller, Pesce & Collilieux (2020)	1490.1 ± 1.3

A further test was conducted to investigate a possible change in the 26 m antenna's AO due to the bearing replacement during 2008–2010. Sessions from the entire period (1986–2017) in which the 26 m antenna participated were analysed in groupings of 30 consecutive sessions to avoid the artificial separation and comparison of older data from before bearing failure and later data after bearing replacement. The antenna AO was estimated in a global solution for each of the session groupings. Given the limited time span of an individual session grouping, station velocities could not be estimated but were fixed to their ITRF2020 values.

Department of Geology, Geoinformatics and Meteorology
University of Pretoria

6.1.2 Results and discussions

Comparison of VieVS estimated antenna axis offset values for the HartRAO 26 m and 15 m antennas with ground survey values:

In Table 6.3, the AO values estimated with VieVS for the 26 m and 15 m antennas in the current study are compared with ground survey values. For all the investigations, the test in which the antenna AO was estimated for all participating stations (T3) provides for the smallest difference between the VieVS estimated AO values for the 26 m and 15 m antennas and the AO values determined in the ground surveys. Henceforth results from T3 are thus used for comparison with the ground survey values.

For the 26 m antenna, the AO values estimated in the current study for the entire period (1986–2017) as well as for before bearing failure and after bearing replacement do not agree within the formal error with either the 2003 co-location survey value determined before bearing failure (the *a priori* AO value currently in use) or the 2014 co-location survey value determined after bearing replacement. The VieVS estimated AO values are larger than both ground survey values by several millimetres for the entire period (1986–2017) and after bearing replacement, and by a few millimetres for the period before bearing failure. The 26 m antenna's VieVS estimated AO values from before bearing failure and after bearing replacement differ by ~5 mm from each other. The particularly large difference in AO value for the 26 m antenna between the VieVS estimated AO value after bearing replacement and the 2003 co-location survey value before bearing failure (~7 mm) could be ascribed to a change in station position due to the bearing failure and replacement, propagating into the AO estimation. The 2003 co-location survey value is, however, corroborated by the 2014 co-location survey value determined after bearing replacement. The measurements of the AO during the co-location surveys before bearing failure in July and August of 2003 and after bearing replacement in February of 2014 indicate that no significant change occurred in the AO due to the failed bearing and its replacement. For the 15 m antenna, although the VieVS estimated AO value agrees within the formal error with the AO value determined by GPS survey in 2007 (and thus the *a priori* AO value currently in use), it does not agree within the formal error with the AO

value determined in the 2014 co-location survey and is several millimetres larger than this latest survey value.

Table 6.3 HartRAO 26 m and 15 m antenna AO values estimated with VieVS compared with ground survey values (26m a priori AO = 6695.3 mm; 15m a priori AO = 1495.0 mm).

	VieVS estimated AO and formal error (mm)		
	T1	**T2**	**T3**
26m:			
1986—2017	6700.22 ± 0.34	6700.82 ± 0.34	6699.11 ± 0.35
1986—2008	6698.59 ± 0.41	6699.66 ± 0.41	6697.12 ± 0.43
2010—2017	6703.10 ± 0.51	6703.07 ± 0.52	6702.47 ± 0.52
15m:			
2012—2017	1495.40 ± 0.46	1495.48 ± 0.46	1495.34 ± 0.46
	AO determined by ground survey		
	Survey type	**AO survey value (mm)**	
26m:			
2003 (*a priori*)	Co-location	6695.3	
2014	Co-location	6694.5	± 0.7
15m:			
2007 (*a priori*)	GPS	1495.0	
2014	Co-location	1490.1	± 1.3

Although the ground survey values are considered to be the more accurate, in the current study it is the VieVS estimated AO values which display the smaller formal errors, but this can be ascribed to unrealistic AO formal errors from the VLBI global solutions of the three tests (T1, T2 and T3), possibly due to variations of the difference between the estimated and *a priori* AO values propagating into other parameters in the global solution. The induced correlations between estimated parameters which are not properly accounted for in the least-square analysis lead to over-optimistic AO formal errors which are reflected by the estimated AO values for the three global solution tests not agreeing within the formal erors.

Comparison of VieVS estimated antenna axis offset values for the HartRAO 26 m antenna for 30-session groupings with the a priori value:

Differences between the 26 m antenna's VieVS estimated and *a priori* AO values for 35 groupings of 30 sessions for the entire period (1986–2017), to investigate the possibility of a change in the 26 m antenna's AO value due to the bearing replacement, are displayed in Figure 6.2. The variation of the differences between the groupings of 30 sessions is a good indicator for a more realistic error measure compared to the overoptimistic formal errors from the global solutions of the three tests as mentioned previously, for example the standard deviation of the differences (dAO) over the 26 groupings of 30 sessions before bearing repair is 4.77 mm. The data point indicated in blue represents the result for the session grouping which incorporates 9 sessions from August 2008, just before the bearing failure, as well as 21 sessions from August 2010 (when the 26 m antenna resumed operations after bearing replacement) until February 2011. This result—dAO = 5.72 mm ± 1.16—as well as those for session groupings just before and after, appear similar to the results for other session groupings and indeed show less of an excursion from the *a priori* AO value than results for some of the other session groupings. This would seemingly confirm the agreement between AO values for the 26 m antenna determined in the 2003 and 2014 co-location surveys, before bearing failure and after bearing replacement respectively.

Department of Geology, Geoinformatics and Meteorology
University of Pretoria

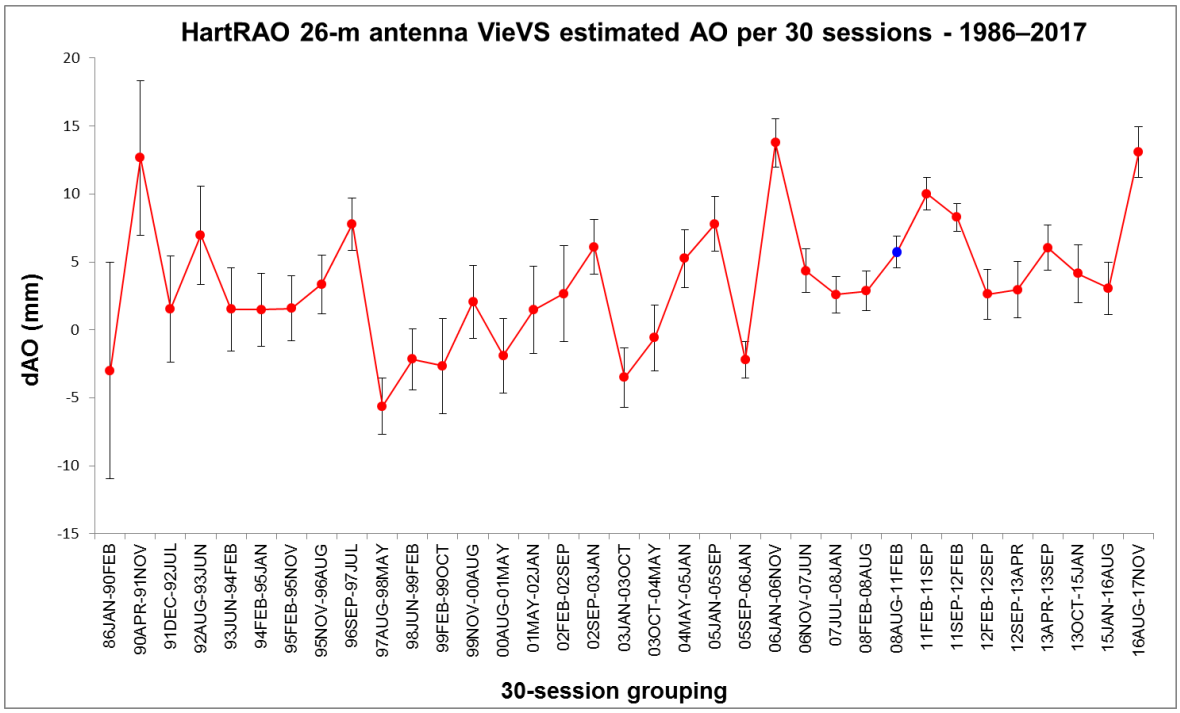

Figure 6.2 HartRAO 26 m antenna AO estimated with VieVS—differences (dAO) between the antenna AO estimated for 30-session groupings stretching over the entire period (1986–2017) and a priori AO value (26m a priori AO = 6695.3 mm).

Comparison of antenna axis offset estimated from continuous VLBI campaign data with ground survey values:

The VieVS estimated values of the AO for the CONT VLBI campaigns in which HartRAO participated (CONTnn, nn=year) are displayed in Table 6.4. The CONT02, CONT05 and CONT08 campaigns were all observed with the 26 m antenna before bearing failure, whilst CONT11 was observed after bearing replacement. CONT14 and CONT17 were observed with the 15 m antenna.

For the 26 m antenna, only VieVS estimated AO values for the CONT02 (before bearing failure) and CONT11 (after bearing replacement) campaigns agree within the formal error with each other. None of the VieVS estimated AO values for any of the CONT campaigns in which the 26 m antenna participated agree within the formal error with the value measured in the 2003 survey (before bearing failure and the 26 m antenna's *a priori* AO

value). Only the VieVS estimated AO value for the CONT05 campaign (before bearing failure) agrees within the formal error with the value measured in the 2014 survey (after bearing replacement). For the 15 m antenna, the VieVS estimated AO values for the CONT14 and CONT17 campaigns do not agree within the formal error with each other nor with the values measured in the 2007 GPS survey (and thus the *a priori* value) and 2014 co-location survey.

Table 6.4 VieVS estimated antenna AO values for the continuous (CONT) campaigns observed with the HartRAO 26 m or 15 m antennas (26m a priori AO = 6695.3 mm; 15 m a priori AO = 1495.0 mm).

Campaign	AO (mm)
26m:	
CONT02 (Oct 2002)	6705.62 ± 2.60
CONT05 (Sep 2005)	6693.82 ± 1.46
CONT08 (Aug 2008)	6700.44 ± 1.41
CONT11 (Sep 2011)	6703.90 ± 1.02
15m:	
CONT14 (May 2014)	1486.07 ± 2.36
CONT17 (Dec 2017)	1493.15 ± 1.71

Seasonal variation in HartRAO 26 m antenna axis offset:

In Table 6.5 and Table 6.6, the sessions in which the HartRAO 26 m antenna participated during various periods (before bearing failure, after bearing replacement, entire period)

were divided into seasonal groupings and into two six-month periods, respectively, to investigate the possibility of seasonal variations in antenna AO.

None of the seasonal VieVS estimated AO values for the 26 m antenna agree within the formal error with either the value measured in the 2003 survey (before bearing failure, and the 26 m antenna's *a priori* AO value) or the value measured in the 2014 survey (after bearing replacement). For the period before the bearing failure on the 26 m antenna, the seasonal deviation of the VieVS estimated AO value from both survey values appears to be larger for autumn and winter. For the period after the bearing replacement, the deviation from ground survey values is significantly larger (~1 cm) for all seasons except autumn, where the deviation is similar to that before bearing failure. Over the entire period, the deviation is similar for all the seasons and slightly larger than that before bearing failure.

Table 6.5 HartRAO 26 m antenna – VieVS estimated antenna AO value for specified months/seasons (a priori AO value = 6695.3 mm).

Month/Season	**Before bearing failure (1986.1-2008.9)**	**After bearing replacement (2010.8-2017.12)**	**All (1986.1-2017.12)**
Summer – DecJanFeb			
No. of sessions	239	65	304
AO (mm)	6697.33 ± 0.80	6703.91 ± 1.20	6699.85 ± 0.67
Autumn – MarAprMay			
No. of sessions	164	49	213
AO (mm)	6699.65 ± 0.94	6699.66 ± 1.42	6699.87 ± 0.78
Winter – JunJulAug			
No. of sessions	186	70	256
AO (mm)	6699.52 ± 0.81	6702.56 ± 1.15	6700.18 ± 0.65
Spring – SepOctNov			
No. of sessions	200	85	285
dAO (mm)	6697.25 ± 0.73	6703.56 ± 0.76	6700.61 ± 0.52

Table 6.6 HartRAO 26 m antenna – VieVS estimated antenna AO value for specified six-month period (a priori AO value = 6695.3 mm).

Month/Season	**Before bearing failure (1986.1-2008.9)**	**After bearing replacement (2010.8-2015.12)**	**All (1986.1-2015.12)**
Spring and summer – Sep - Feb			
No. of sessions	439	150	589
dAO (mm)	6697.53 ± 0.54	6703.75 ± 0.64	6700.51 ± 0.41
Autumn and winter – Mar - Aug			
No. of sessions	350	119	469
dAO (mm)	6699.88 ± 0.61	6701.49 ± 0.88	6700.33 ± 0.50

Seasonal variation in HartRAO 15 m antenna axis offset:

In Table 6.7 and
Table *6.8*, the sessions in which the HartRAO 15 m antenna participated were divided into seasonal groupings and into two six-month periods, respectively, to investigate the possibility of seasonal variations in antenna AO.

Neither of the six-month VieVS estimated AO values for the 15 m antenna agree within the formal error with either the 2007 GPS survey value (*a priori* AO value) or the 2014 survey value. For the 15 m antenna, the largest deviation of the VieVS estimated AO value from both survey values occurs during spring and summer (September to February).

Table 6.7 HartRAO 15 m antenna – VieVS estimated antenna AO value for specified months/seasons (a priori AO value = 1495.0 mm).

Month/Season	**No. of sessions**	**dAO (mm)**
Summer – DecJanFeb	123	1494.36 ± 0.92
Autumn – MarAprMay	89	1492.38 ± 1.18
Winter – JunJulAug	100	1493.60 ± 1.10
Spring – SepOctNov	134	1499.57 ± 0.91

Table 6.8 HartRAO 15 m antenna – VieVS estimated antenna AO value for specified six-month period (a priori AO value = 1495.0 mm).

Month/Season	No. of sessions	dAO (mm)
Spring and summer – Sep - Feb	257	1497.09 ± 0.65
Autumn and winter – Mar - Aug	189	1493.13 ± 0.81

The VieVS estimated antenna AO values for the HartRAO 26 m and 15 m antennas do not agree within the formal error with the values determined in a 2014 co-location survey. The sub-millimetre accuracy in AO, as required by the GGOS/VGOS goal of 1 mm accuracy in station coordinates, could not be achieved in the VLBI analysis. The antenna AO values show statistically significant differences between various data sets that are not well understood. For the VieVS estimated AO values of the 26 m antenna, there appear to be a significant change from before to after bearing replacement, but this is not reflected in the corresponding ground survey values. For both the 26 m and 15 m antennas, the AO estimated with VieVS differs considerably from the values measured during the 2014 co-location survey. Regarding possible seasonal variation in the estimated AO, it was not possible to establish any specific trend in AO variation across the seasons. As a construction value, the AO value is supposed to be fixed and should therefore remain constant over the entire year. If seasonal variations seem to occur, seasonal mismodelled and unmodelled effects, such as troposphere delay and atmosphere and hydrology loading, could possibly be propagating into the AO estimates in the VLBI analysis. Possible correlation of AO with station position, troposphere delay, clock parameters, structural

deformation, hydrology loading *etc*. requires further investigation. The effect of using a different tropospheric mapping function and erroneous pressure measurement on the estimated AO for a selection of stations, including the HartRAO 26 m antenna, was tested by Nilsson *et al*. (2015). Although a change in mapping function had a negligible effect on the estimated AO, an artificially introduced 10 hPa pressure error showed a significant effect on the estimated AO for az-el antennas.

6.2 ANTENNA AXIS OFFSET ALTITUDE CORRECTION

The antenna axis offset altitude correction (AOAC) implemented by Sovers, Fanselow, and Jacobs (1998) accounts for the effect of the orientation of equatorial and X-Y antennas on the tropospheric path delay. Zenith troposphere delays of 1-2 mm, increasing to 1-2 cm when mapped to low elevation angles, result for antennas with non-zero AOs where the secondary rotation axis (A in Figure 6.3) moves vertically with changing orientation, i.e. for antennas with equatorial and with X-Y mounts (Sovers, Fanselow, and Jacobs, 1998). A correction therefore has to be added to the zenith dry tropospheric delay (Z_d) for antennas with equatorial and X-Y mounts (Sovers, Fanselow, and Jacobs, 1998),

$$\delta Z_d = -Z_d (L/\Delta)\, \psi \tag{6.3}$$

where L is the antenna AO, Δ the troposphere scale height (≈ 8.6 km), and ψ is an angular factor that varies with the type of mount. For equatorial mounts, such as that of the HartRAO 26 m antenna,

$$\psi = \cos H \cos \phi_{gd} \tag{6.4}$$

where H is the local hour angle east of the meridian and ϕ_{gd} is the geodetic latitude. For north-south oriented X-Y mounts,

$$\psi = \sin E \,/\sqrt{1 - \cos^2\theta \cos^2 E} \tag{6.5}$$

while for east-west oriented X-Y mounts, such as that of the Hobart 26 m antenna,

$$\psi = \sin E \,/\sqrt{1 - \sin^2\theta \cos^2 E} \tag{6.6}$$

where E is the elevation angle and θ the azimuth.

Department of Geology, Geoinformatics and Meteorology
University of Pretoria

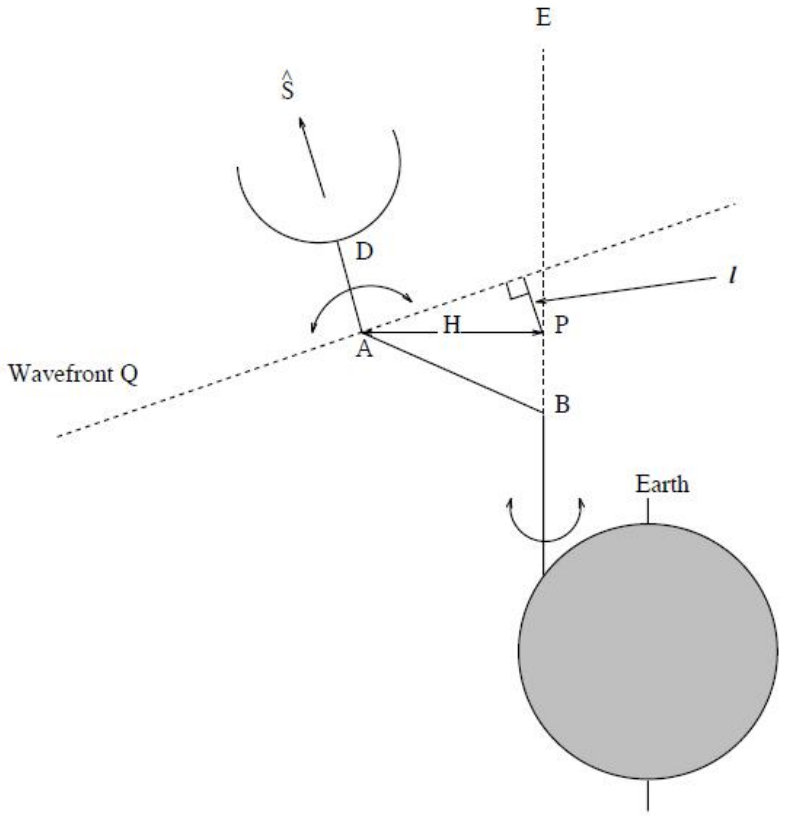

Figure 6.3 Geometry of two-station VLBI network with only one station shown. Declination (Dec) axis (end view represented by A) rotates in plane perpendicular to symmetry axis AD. Dec axis and polar axis (BE) are separated by distance H, the antenna axis offset. The VLBI reference point is represented by P (Combrinck and Merry, 1997).

6.2.1 Methodology

The AOAC was implemented in VieVS (Böhm *et al.*, 2018) according to Sovers, Fanselow, and Jacobs (1998) by Hana Krásná from the Technical University of Vienna (TUWIEN). It has bearing on the HartRAO 26 m antenna (HARTRAO, equatorial mount) and Hobart 26 m antenna (HOBART26, X-Y mount) only, as all other stations participating in sessions for the period under review (August 2010 to November 2014) have telescopes with az-el mounts to which the correction does not apply.

Simulation of HARTRAO antenna axis offset altitude correction:

The simulation tool in VieVS was used to simulate the effect of the AOAC on the estimated antenna AO and coordinates of the HartRAO 26 m (HARTRAO) antenna. The simulations were based on schedules from two different types of IVS sessions, R1663 (24 November 2014) and T2094 (17 December 2013), in which HARTRAO (but not HOBART26) participated, and for which the schedule and network geometry differed in the event that it influenced the propagation of the AOAC to the AO estimate. In the simulations, zero input observation files, in which the measured time delay was set equal to the theoretical time delay without the addition of any noise terms, were generated for these sessions. The AOAC was then applied during analysis of the simulated sessions for HARTRAO only. A simulation of the R1663 session with the altitude correction applied and with HARTRAO included in the datum – realised with the no-net-rotation (NNR) and no-net-translation (NNT) conditions on the antenna coordinates w.r.t. the *a priori* TRF – was also run in order to investigate the influence of the AOAC on the antenna coordinates of other stations participating in the session.

Session analysis to determine effect of antenna axis offset altitude correction on antenna axis offset and coordinates:

All IVS geodetic VLBI sessions (Nothnagel *et al*., 2017) in which the HartRAO 26 m antenna participated from August 2010 to November 2014 (totalling 176 sessions) were analysed with VieVS to investigate the effect of the AOAC on the estimated antenna AO and coordinates of the HartRAO 26 m (HARTRAO) and Hobart 26 m (HOBART26) antennas. The Hobart 26 m antenna participated in 32 of the 176 sessions. The sessions were processed with and without the AOAC applied and also with and without HARTRAO in the datum in order to investigate the influence of the AOAC on the antenna coordinates of other stations participating in the sessions, while HOBART26 was not included in the datum for any of the processing runs.

Department of Geology, Geoinformatics and Meteorology
University of Pretoria

6.2.2 Results and discussion

Simulation of HARTRAO antenna axis offset altitude correction:

The simulations showed the AOAC to have negligible effect on the HARTRAO AO estimate, being in the sub-millimetre region (see Table 6.9). The AOAC propagated to the HARTRAO antenna coordinates, also at the sub-millimetre level (see Figure 6.4). With HARTRAO in the datum, the antenna AO estimate remained the same but the AOAC propagated to the coordinates of other antennas as well. The difference in antenna coordinates was negligible however.

Table 6.9 Antenna axis offset altitude correction (AOAC) results from simulations showing the effect of applying the AOAC to HARTRAO only, on the estimated axis offset of the HartRAO 26 m antenna. The first column entries depict the simulation runs, SIM1 (based on R1663) and SIM2 (based on T2094). (dAO: difference between AO with and without AOAC applied; mAO: formal error; +Hh: AOAC applied with HARTRAO in datum).

Simulations	**Difference in HARTRAO AO: with AOAC – without AOAC**	
	dAO (cm)	**mAO (cm)**
SIM1: R1663	-0.041	0.001
SIM1: R1663 (+Hh)	-0.041	0.001
SIM2: T2094	-0.061	0.002

Department of Geology, Geoinformatics and Meteorology
University of Pretoria

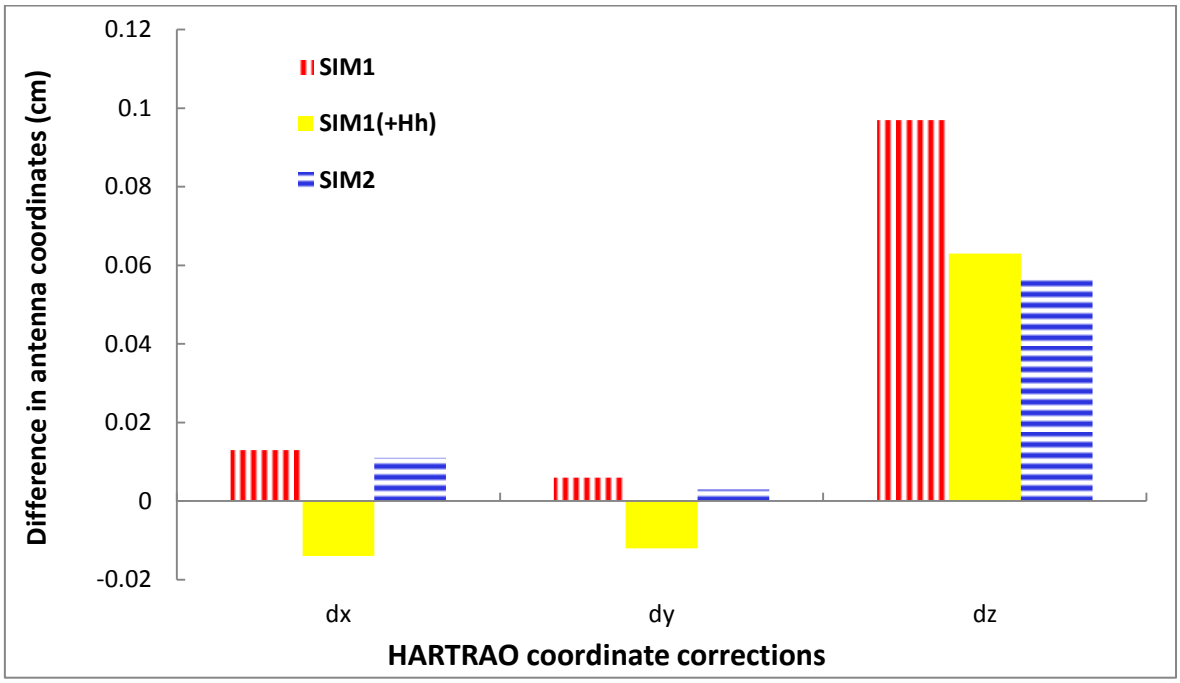

Figure 6.4 Simulations – antenna axis offset altitude correction (AOAC) results from simulations showing the effect of applying the AOAC to HARTRAO only on the estimated coordinates of the HartRAO 26 m antenna. SIM1 is based on R1663 and SIM2 is based on T2094. (dx, dy and dz: difference between antenna coordinates in the X, Y and Z directions with and without AOAC applied; +Hh: AOAC applied with HARTRAO in datum).

Session analysis to determine effect of antenna axis offset altitude correction on antenna axis offset and coordinates:

Results for the VieVS analysis of the 176 sessions HARTRAO participated in from August 2010 to November 2014 (inclusive of the 32 sessions which HOBART26 participated in) to investigate the effect of the AOAC on the estimated AO of the HartRAO and Hobart 26 m antennas are displayed in Table 6.10. Results for the investigation of the effect of the AOAC on antenna coordinates for only a selection of antennas (due to space constraints) that participated in 30 or more of these sessions (to ensure the inclusion of HOBART26), are depicted in Figure 6.5, Figure 6.6 and Figure 6.7.

Table 6.10 Antenna AOAC results from analysing 176 geodetic VLBI sessions between August 2010 and November 2014 with VieVS, showing the effect of applying the AOAC to HARTRAO and HOBART26 on the estimated axis offsets of the HartRAO and Hobart 26 m antennas.

Session analysis	dAO (cm)
Difference in HARTRAO AO: with AOAC – without AOAC	1.231 – 1.239 = 0.008
Difference in HOBART26 AO: with AOAC – without AOAC	0.222 – 0.216 = 0.006

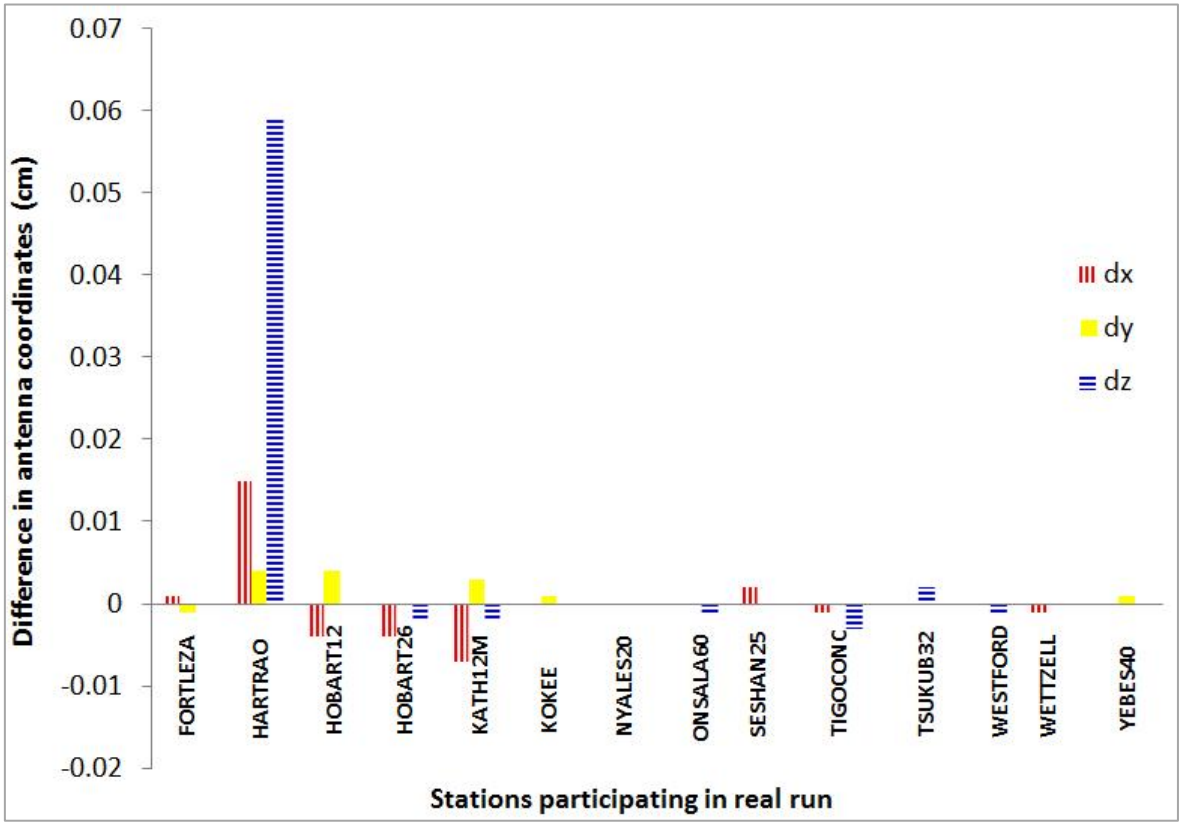

Figure 6.5 Run 1 – antenna AOAC results from analysing 176 geodetic VLBI sessions between August 2010 and November 2014 with VieVS, showing the effect of applying the AOAC to HARTRAO and HOBART26 on the estimated antenna coordinates of a selection of stations. The plot shows the difference in antenna coordinates (dx, dy and dz: difference between antenna coordinates in the X-, Y- and Z-directions) with and without the AOAC having been applied to HARTRAO and HOBART26 (neither station in datum).

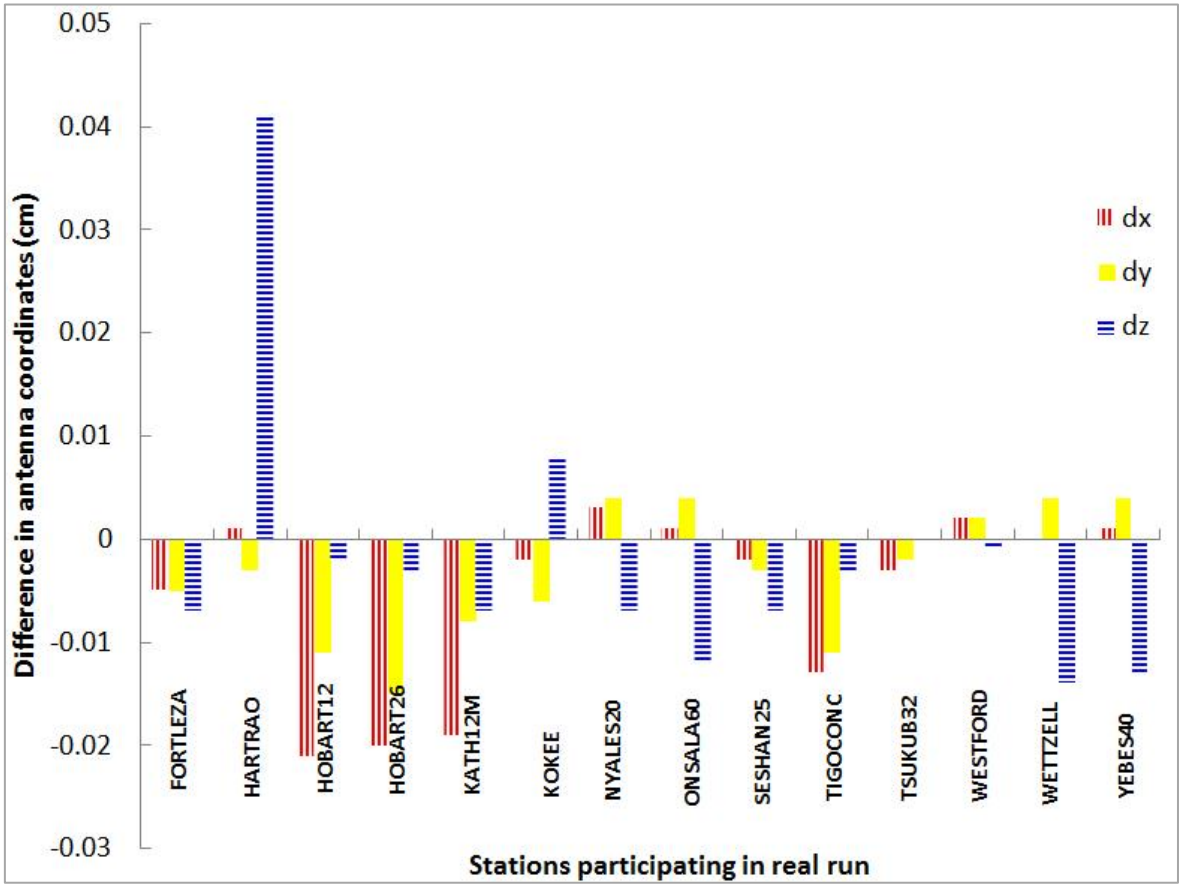

Figure 6.6 Run 2 – antenna AOAC results from analysing 176 geodetic VLBI sessions between August 2010 and November 2014 with VieVS, showing the effect of applying the AOAC to HARTRAO and HOBART26 on the estimated antenna coordinates of a selection of stations. The plot shows the difference in antenna coordinates (dx, dy and dz: difference between antenna coordinates in the X-, Y- and Z-directions) with and without the AOAC having been applied to HARTRAO and HOBART26 with HARTRAO in the datum.

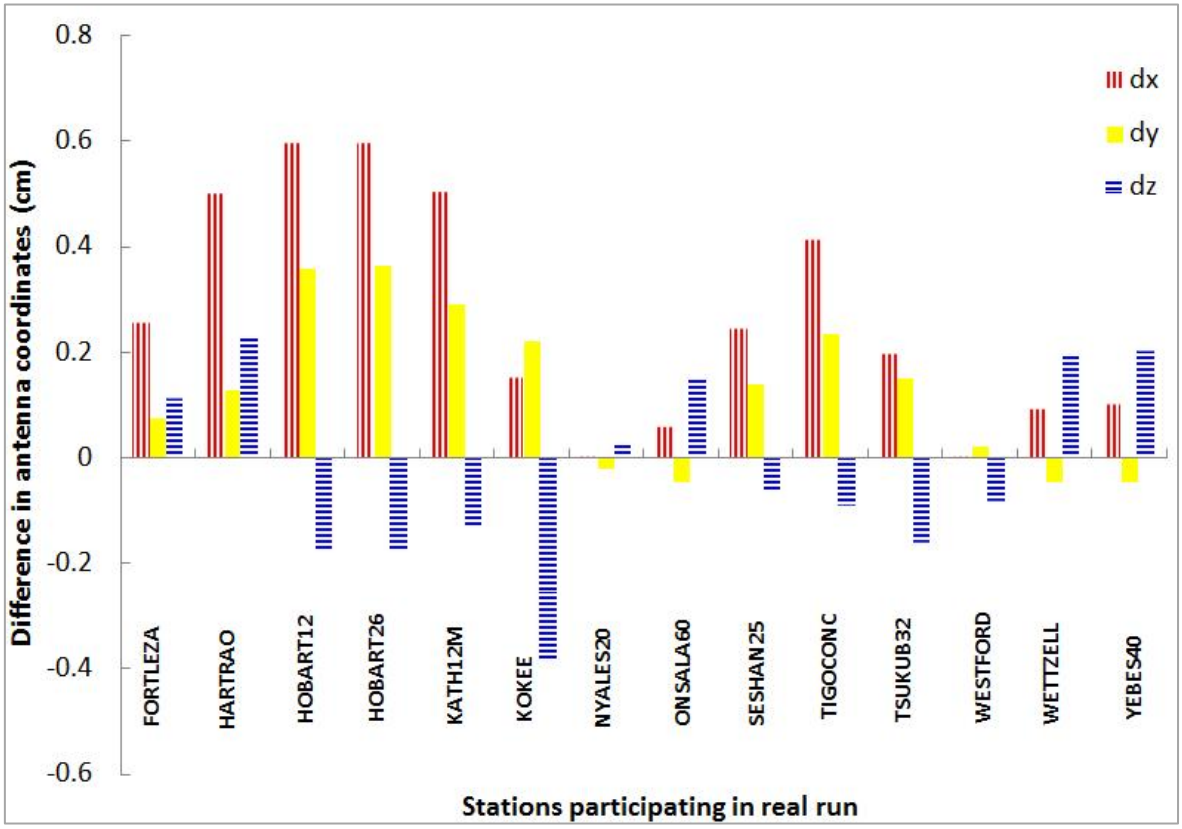

Figure 6.7 Run 3 – antenna AOAC results from analysing 176 geodetic VLBI sessions between August 2010 and November 2014 with VieVS, showing the effect of applying the AOAC to HARTRAO and HOBART26 on the estimated antenna coordinates of a selection of stations. The plot shows the difference in antenna coordinates (dx, dy and dz: difference between antenna coordinates in the X-, Y- and Z-directions) with the AOAC having been applied to HARTRAO and HOBART26 with and without HARTRAO in the datum.

Results from the session analysis are expected to be similar to simulation results. The difference in HARTRAO antenna coordinates for the session analysis is indeed similar to that for the simulation results (compare Figure 6.4 and Figure 6.5). However, the difference in the estimated antenna AO (with and without the AOAC applied) for the session analysis is smaller than that for the simulations, although also at sub-millimetre level (compare Table 6.9 and Table 6.10). This may be caused by the propagation of the correction to the coordinates of other antennas. A large correction to the antenna AO *a priori* value exists for HARTRAO in general (~1 cm) compared to that of HOBART26 (~1 mm) (see Table 6.10). The difference in antenna coordinates for stations where the

correction does not apply, should theoretically be zero as is seen in Figure 6.5. The minor influence of the AOAC on the antenna coordinates of HOBART26 is unexpected however. The presence of HARTRAO in the datum does not affect the antenna AO estimates, but coordinate corrections propagate to the coordinates of other antennas, albeit only at sub-millimetre level (see Figure 6.6 and Figure 6.7)

The results provide a smaller change in the estimated antenna coordinates than expected from the theoretical model of the AOAC, which predicts a change of 1-2 cm in the slant troposphere delay at low elevations. The AOAC changes HARTRAO and HOBART25 coordinates and AO by less than 1 mm. The smaller than expected shifts require further investigation. The VieVS results should be compared with results from the NASA Jet Propulsion Laboratory (JPL) VLBI modelling and estimation software ``MODEST'' (Sovers, Fanselow, and Jacobs, 1998) for a few observations to search for possible inconsistencies in the coding. The much larger correction to the antenna AO *a priori* value for HARTRAO compared to that of HOBART26 (~1 cm vs ~1 mm) and the negligible influence of the AOAC on the HOBART26 coordinates also require further investigation.

6.3 SUMMARY

An antenna AO exists for antennas with non-intersecting rotation axes, such as the HartRAO antennas. The AO contributes to the VLBI delay and has to be considered in the VLBI analysis. As the AO and station coordinates are highly correlated, the AO needs to be known with sub-millimetre accuracy to reach the GGOS/VGOS goal of 1 mm accuracy in station coordinates. The AO can be determined with high accuracy in ground surveys, but such surveys are conducted infrequently. In this investigation, the AO was estimated in VLBI analysis with the geodetic VLBI analysis software, VieVS, and compared with ground survey values, in order to establish whether the required accuracy could be achieved in VLBI analysis. The AO values estimated for the 26 m antenna did not agree within the formal error with the ground survey values. The estimated AO values from before bearing failure and after bearing replacement also differed by ~5 mm from each other. However, a change in AO due to the bearing repair could not be corroborated by either a comparison of AO values estimated for a 30-session grouping consisting of

sessions just before bearing failure and just after bearing replacement with 30-session groupings just before and after, nor by a comparison of the 2003 ground survey value from before bearing failure with the 2014 ground survey value after bearing replacement. The AO value estimated for the 15 m antenna agreed within the formal error with the AO value determined in the 2007 GPS survey but not with the 2014 ground survey value. The estimated AO and GPS survey values were several millimetres larger than the 2014 ground survey value. The AO values estimated from high-accuracy VLBI data collected during four CONT campaigns in which the 26 m antenna participated, showed very little agreement within the formal error amongst campaigns or with either of the ground survey values. The AO values estimated for the two CONT campaigns in which the 15 m antenna participated, failed to agree within the formal error with each other or with the values measured in the GPS and ground surveys. In the investigation into possible seasonal variation in the AO, none of the seasonal estimated AO values for the 26 m antenna agreed within the formal error with either of the ground survey values, and for the 15 m antenna, only the AO value estimated for summer agreed within the formal error with the 2007 GPS survey value only. It was not possible to detect any specific variation according to season.

The AOAC accounts for the effect of the orientation of an equatorial mount antenna, such as the HartRAO 26 m antenna, on the tropospheric path delay, and a 1-2 cm change in the slant troposphere delay at low elevations is predicted by the AOAC theoretical model. In the investigation into the effect of the AOAC on the estimated AO and coordinates of the HartRAO 26 m antenna, simulations and analysis of real sessions in VieVS showed the AOAC to have negligible effect on the AO and station coordinate estimates of the HartRAO 26 m antenna as well as on the coordinates of other antennas. The sub-millimetre difference in the estimated HartRAO 26 m antenna coordinates with and without the AOAC applied, is not in agreement with the theoretical model prediction, and requires further investigation. The AO estimated in VLBI analysis is not yet able to reach the sub-millimetre accuracy as required by GGOS/VGOS. Correlation of antenna AO with various station-based effects requires further investigation towards improvement of the AO model.

CHAPTER 7 BASELINE LENGTH AND LOCAL TIE

For accurate astrometric and geodetic VLBI results, the antenna coordinates (VLBI reference point) of, and baseline length (distance) between, co-located antennas have to be known with high accuracy. The VLBI reference points of newly built antennas, such as the VGOS antenna, need to be accurately tied to the VLBI reference points of legacy antennas with their long stable position time series. Stations are required to conduct terrestrial surveys to measure this local tie accurately. Such surveys are, however, knowledge- and resource-intensive and are therefore not conducted on a regular basis. Co-located antennas can be tied together by observing together and specifically by observing the same sources simultaneously (Plank, 2014). The accuracy of local ties estimated in geodetic VLBI analysis has to be established. In order to reach the VGOS goal of 1 mm accuracy in station coordinates and global baselines, it would be necessary to determine the baseline length with sub-millimetre accuracy.

At HartRAO, the 26 m legacy antenna's VLBI reference point serves as reference point for the co-location of the 15 m, and soon to become operational VGOS antennas. The 15 m antenna's VLBI reference point and, in the very near future, that of the VGOS antenna, need to be accurately tied to the VLBI reference point of the 26 m antenna. It is therefore necessary to determine, from VLBI analysis of sessions in which both the HartRAO 26 m and 15 m antennas participated, and, in particular, from short baseline (SBL) experiments between only these two antennas where the same sources are being observed simultaneously, whether the VGOS goal of 1 mm global baseline accuracy is achievable on such a short baseline at least. An automated total station for continuous monitoring of vector ties will soon become operational at HartRAO. This will allow for the measurement

of the local tie between the various on-site techniques but also for continuous comparison of VLBI determined antenna coordinates and baseline length with that measured by the total station (see Figure 7.1).

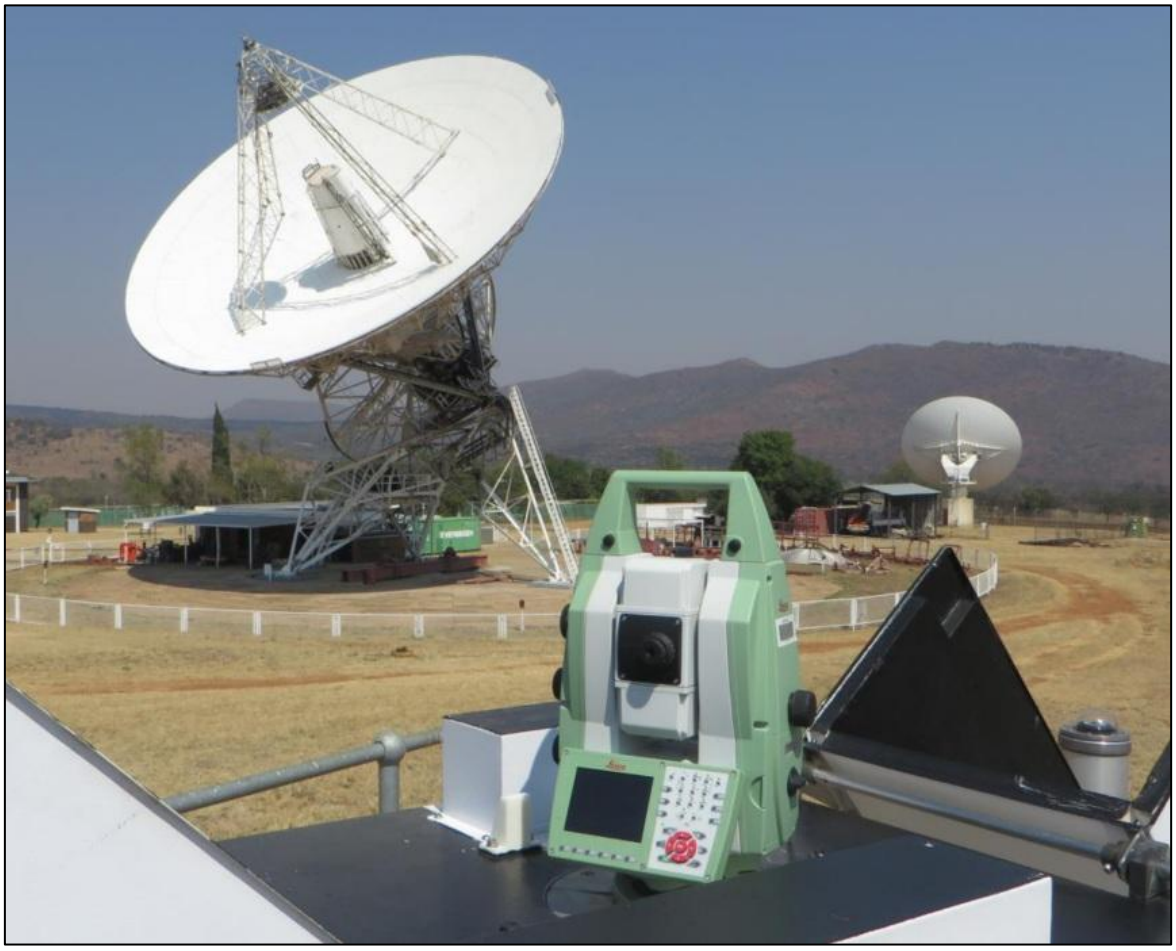

Figure 7.1 Short baseline of ~113 m between the HartRAO 26 m and 15 m antennas with the total station (Leica MS50 Multistation) under test in the foreground. Photo credit: R. Botha.

7.1 BASELINE LENGTH BETWEEN HARTRAO ANTENNAS FROM GLOBAL ASTROMETRIC/GEODETIC VLBI SESSIONS

The baseline length between the co-located HartRAO antennas is the three-dimensional (3D) distance between the 26 m and 15 m antennas. It is calculated from the difference

Department of Geology, Geoinformatics and Meteorology
University of Pretoria

between the geocentric Cartesian coordinates of the antennas' VLBI reference points (antenna XYZ coordinates at the specific epoch), as follows:

$$BL_{Hh-Ht} = \sqrt{(X_{Hh} - X_{Ht})^2 + (Y_{Hh} - Y_{Ht})^2 + (Z_{Hh} - Z_{Ht})^2} \quad (7.1)$$

For this investigation, data from global geodetic VLBI sessions in which both the HartRAO 26 m and 15 m antennas participated, were analysed using the geodetic VLBI analysis software, Vienna VLBI and Satellite Software (VieVS, Böhm *et al*., 2018, see Section 2.4), to estimate the baseline length (local tie) between the two HartRAO antennas. The VieVS estimated baseline lengths from these dual global sessions were compared with the *a priori* value, the value determined from the most recent ground survey measurements conducted from 13 February to 5 March 2014 (Muller, Pesce & Collilieux, 2020) as well as with corresponding IVS Combination Centre (IVSCC) values. The *a priori* and estimated baseline lengths are calculated in VieVS from the *a priori* and estimated antenna coordinates, respectively. Possible seasonal variations in baseline length were also investigated.

The IVS global sessions comprise experiments on intercontinental baselines, with different network configurations and observing strategies to achieve specific science goals. The 29 dual global IVS sessions in which both the HartRAO antennas participated during 2013-2017 consisted of:

- nineteen R1 sessions for providing rapid EOP results with 7-12 participating stations located on the African plate (HartRAO) and on, from amongst, the Eurasian, Indo-Australian, North American, Pacific and South American plates;
- five AUSTRAL sessions for improved CRF/TRF determination in the southern hemisphere with 6-7 participating stations located on the African (HartRAO) and Australian-Indian plates;
- four T2 sessions for monitoring the TRF with 14-20 participating stations located on the African plate (HartRAO) and on, from amongst, the African (Noto – Sicily, Italy), Antarctic, Eurasian, Indo-Australian, North American, Pacific and South American plates; and

- one R&D session for determining Gaia source positions with 6 participating stations on the African (HartRAO), Eurasian, Indo-Australian, Pacific and South American plates.

Separate hydrogen maser reference clocks were used on the two HartRAO antennas for all these dual global sessions – the 26 m antenna was being run off the iMaser72 clock while the 15 m antenna was run off the EFOS-28 clock. For most of the sessions, the EFOS-28 clock on the 15 m antenna had to be offset in frequency from the iMaser72 clock on the 26 m antenna to prevent phase-cal cross-correlation, while phase-cal was usually turned off on the 15 m antenna for the astrometric AUSTRAL sessions.

7.1.1 Methodology

The geodetic VLBI analysis software, VieVS (Böhm *et al*., 2018), was used for data analysis. Geodetic VLBI data (Nothnagel, 2017) from global sessions observed by IVS network stations in which both the HartRAO 26 m and 15 m antennas participated from the start of 2013 to the end of 2017 were used to estimate the baseline length between the two HartRAO antennas for each of these sessions, in order to determine the local tie between the two antennas.

Data analysis consisted of single session analysis with VieVS. Sessions were processed individually to remove clock breaks, set reference clocks, exclude defective stations, baselines, observations and/or station cable cal and eliminate outliers where necessary. Normal equations were generated with *a priori* modelling in general following the IERS Conventions 2010 (IERS, 2010) and parametrisation as presented in

Table *7.1*. Radio source positions were fixed to their ICRF-3 coordinates (Charlot et al., 2020). The *a priori* antenna coordinates and station velocities were obtained from the ITRF2014 (Altamimi et al., 2016) solution. Antenna coordinates were estimated by applying no-net-translation (NNT) and no-net-rotation (NNR) constraints to coordinates of all stations in this TRF.

Table 7.1 Models applied and parameters estimated in the single session analysis of the dual global sessions in VieVS.

VieVS3.2 Input parameters	
Models	
TRF	ITRF2014 (Altamimi *et al*., 2016)
CRF	ICRF3SX (Charlot *et al*., 2020)
Ephemerides	JPL 421 (Folkner *et al*., 2009)
ZHD and ZWD mapping function	VMF3 (Landskron and Böhm, 2018)
Solid Earth tides	IERS Conventions (IERS, 2010)
Tidal ocean loading	FES2004 (Lyard *et al*., 2006)
Tidal atmosphere loading	APL_VIENNA (Wijaya *et al*., 2013)
Non-tidal atmosphere loading	APL_VIENNA (Wijaya *et al*., 2013)
Pole tide	IERS Conventions (IERS, 2010)
Ocean pole tide	Desai (2002)
Thermal antenna deformation	Nothnagel (2009)
EOP	14C04 (IAU2000) (Bizouard *et al*., 2019)
Ocean tides	IERS Conventions (IERS, 2010)
Precession/nutation	IAU 2006/2000A (Captaine *et al*., 2003, Mathews *et al*., 2002)
VieVS3.2 Estimated parameters	
Estimation – Least squares	
ZWD	interval = 0.5 h, constraints = 1.5 cm/h
Troposphere north and east gradients	interval = 3 h, relative constraints = 0.05 cm/6h, absolute constraints = 0.1 cm
Clock	interval = 1 h, constraints = 1.3 cm/h

EOP	interval = 1 day, constraints = 10^{-4} mas/day

The VieVS estimated baseline length for each of the dual global sessions was compared with the *a priori* value as well as with the value determined from measurements made during the February 2014 co-location survey (Muller, Pesce & Collilieux, 2020). The VieVS estimated baseline lengths were also compared with the corresponding dual global sessions' values as provided by the IVS Combination Centre's (IVSCC) Time Series of Baseline Lengths product, hosted by Germany's Federal Agency for Cartography and Geodesy (BKG)/German Geodetic Research Institute (DGFI) – https://www.ccivs.bkg.bund.de/index.php?uri=quarterly/baseline. The BKG/DGFI COMBI product, comprising the combination of session-based intermediate results submitted by six participating IVS Analysis Centres – BKG, Goddard Space Flight Center (GSFC), DGFI, Norwegian Mapping Authority (NMA), Agenzia Spaziale Italiana / Centro di Geodesia Spaziale (ASI) and Onsala Space Observatory (OSO, Sweden) – into a final combined solution, was used in the comparison. The dual global sessions were also divided into seasonal groupings – summer = DecJanFeb, autumn = MarAprMay, winter = JunJulAug, spring = SepOctNov – in the analysis with VieVS to investigate the possibility of seasonal variation in the baseline length between the HartRAO 26 m and 15 m antennas. Seasonal averages of the VieVS estimated baseline lengths were compared with the *a priori* and 2014 ground survey values.

7.1.2 Results and discussion

Comparison of VieVS estimated HARTRAO-HART15M baseline length from dual global sessions with a priori and ground survey values:

Values for the baseline length between the HartRAO 26 m and 15 m antennas as estimated with VieVS for 29 dual global sessions observed during 2013 to 2017 are displayed in Figure 7.2 and

Table 7.2. Also displayed in Figure 7.2 is the difference between the *a priori* baseline length and the VieVS estimated baseline length for each of the 29 dual sessions as well as the difference between the baseline length determined during the 2014 co-location survey and the VieVS estimated baseline length for each of the 29 dual sessions.

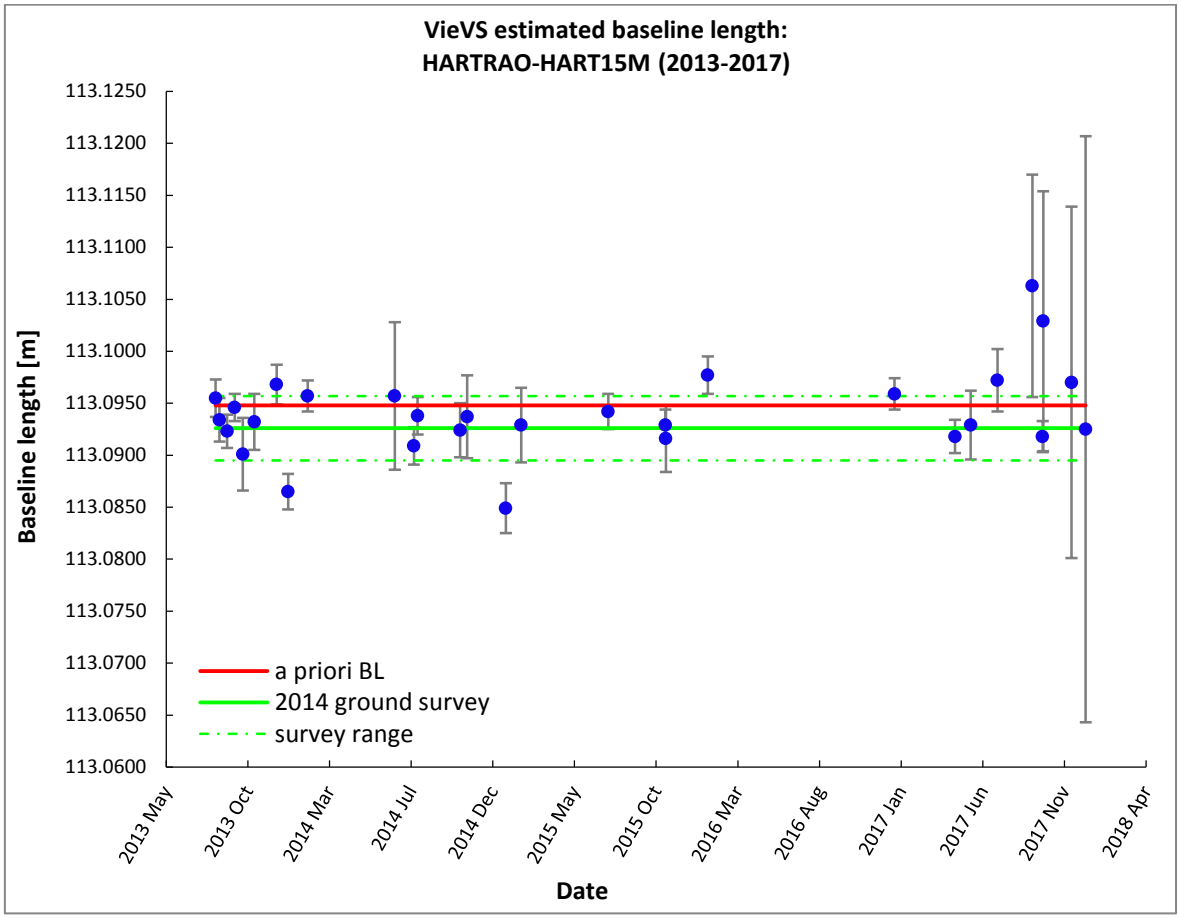

Figure 7.2 Baseline lengths between the HartRAO 26 m and 15 m antennas estimated with VieVS for 29 dual global sessions during 2013 to 2017 compared to a priori (= 113.0948 m) and 2014 ground survey (= 113.0926 ± 0.0031 m) values.

Table 7.2 Offset (Δ) of HARTRAO-HART15M baseline length (BL) estimated with VieVS for 29 dual global session during 2013 to 2017 from a priori (= 113.0948 m) as well as 2014 ground survey (113.0926 ± 0.0031 m) values.

Date	Session	VieVS estimated dual BL [m]	Δ (*a priori* – estimated dual) BL [m]	Δ (ground survey – estimated dual) BL [m]
2013/08/05	R1597	113.0955 ± 0.0018	-0.0007	-0.0029 ± 0.0036
2013/08/12	R1598	113.0934 ± 0.0021	0.0014	-0.0008 ± 0.0037
2013/08/26	R1600	113.0923 ± 0.0016	**0.0025**	0.0003 ± 0.0035
2013/09/09	R1602	113.0946 ± 0.0013	0.0002	-0.0020 ± 0.0034
2013/09/24	R1604	113.0901 ± 0.0035	**0.0047**	0.0025 ± 0.0047
2013/10/15	R1607	113.0932 ± 0.0027	0.0016	-0.0006 ± 0.0041
2013/11/25	R1613	113.0968 ± 0.0019	**-0.0020**	-0.0042 ± 0.0036
2013/12/16	R1616	113.0865 ± 0.0017	**0.0083**	**0.0061 ± 0.0035**
2014/01/21	R1621	113.0957 ± 0.0015	-0.0009	-0.0031 ± 0.0034
2014/06/30	AUST29	113.0957 ± 0.0071	-0.0009	-0.0031 ± 0.0077
2014/08/04	R1647	113.0909 ± 0.0018	**0.0039**	0.0017 ± 0.0036
2014/08/11	R1648	113.0938 ± 0.0018	0.0010	-0.0012 ± 0.0036
2014/10/28	RD1410	113.0924 ± 0.0026	0.0024	0.0002 ± 0.0040
2014/11/10	R1661	113.0937 ± 0.0040	0.0011	-0.0011 ± 0.0051
2015/01/20	R1671	113.0849 ± 0.0024	**0.0099**	**0.0077 ± 0.0039**
2015/02/17	T2102	113.0929 ± 0.0036	0.0019	-0.0003 ± 0.0048
2015/07/27	R1698	113.0942 ± 0.0017	0.0006	-0.0016 ± 0.0035

2015/11/09	R1713	113.0929 ± 0.0015	**0.0019**	-0.0003 ± 0.0034
2015/11/10	T2107	113.0916 ± 0.0032	0.0032	0.0010 ± 0.0045
2016/01/26	R1724	113.0977 ± 0.0018	**-0.0029**	**-0.0051 ± 0.0036**
2017/01/03	R1773	113.0959 ± 0.0015	-0.0011	-0.0033 ± 0.0034
2017/04/24	R1789	113.0918 ± 0.0016	**0.0030**	0.0008 ± 0.0035
2017/05/23	T2118	113.0929 ± 0.0033	0.0019	-0.0003 ± 0.0045
2017/07/11	T2119	113.0972 ± 0.0030	-0.0024	-0.0046 ± 0.0043
2017/09/13	AUA026	113.1063 ± 0.0107	**-0.0115**	-0.0137 ± 0.0111
2017/10/02	R1812	113.0918 ± 0.0015	**0.0030**	0.0008 ± 0.0034
2017/10/03	AUA028	113.1029 ± 0.0125	-0.0081	-0.0103 ± 0.0129
2017/11/24	AUA032	113.0970 ± 0.0169	-0.0022	-0.0044 ± 0.0172
2017/12/20	AUA034	113.0925 ± 0.0282	0.0023	0.0001 ± 0.0284

For 11 of these dual global sessions (indicated in bold in the fourth column of Table 7.2), the VieVS estimated baseline length does not agree within the formal error with the a priori *value and for three of the sessions the difference is close to 1 cm. For three of the dual global sessions (indicated in bold in the fifth column of*

Table 7.2), the VieVS estimated baseline length does not agree within the formal error with the ground survey value. The average value of the 29 dual sessions' baseline lengths estimated with VieVS (= 113.0940 ± 0.0041 m) does however agree within the formal error with both the *a priori* and ground survey values.

Comparison of VieVS estimated HARTRAO-HART15M baseline length from dual global sessions with corresponding IVS Combination Centre values:

Values for the baseline length between the HartRAO 26 m and 15 m antennas as estimated with VieVS for the 29 dual global sessions observed during 2013 to 2017 were also compared with corresponding values provided by the IVSCC for the sessions as displayed in Table 7.3 and Figure 7.3.

The VieVS estimated baseline length does not agree within the formal error with the IVSCC value for two of the dual global sessions (indicated in bold in the fifth column of Table 7.3). The average value of the 29 dual sessions' baseline lengths estimated with VieVS (= 113.0940 ± 0.0041 m) does agree within the formal error with the average value provided by the IVSCC for the 29 sessions' baseline length (= 113.095 ± 0.005 m).

Department of Geology, Geoinformatics and Meteorology
University of Pretoria

Table 7.3 Offset (Δ) of HARTRAO-HART15M baseline length (BL) estimated with VieVS for 29 dual global session during 2013 to 2017 from corresponding IVS Combination Centre (IVSCC) values for each of the sessions.

Date	Session	VieVS estimated dual BL [m]	IVS Combination Centre dual BL [m]	Δ (IVS Combi dual – estimated dual) BL [m]
2013/08/05	R1597	113.0955 ± 0.0018	113.095 ± 0.002	-0.001 ± 0.028
2013/08/12	R1598	113.0934 ± 0.0021	113.092 ± 0.002	-0.001 ± 0.003
2013/08/26	R1600	113.0923 ± 0.0016	113.093 ± 0.002	0.001 ± 0.003
2013/09/09	R1602	113.0946 ± 0.0013	113.094 ± 0.001	-0.001 ± 0.002
2013/09/24	R1604	113.0901 ± 0.0035	113.092 ± 0.006	0.002 ± 0.007
2013/10/15	R1607	113.0932 ± 0.0027	113.094 ± 0.002	0.001 ± 0.003
2013/11/25	R1613	113.0968 ± 0.0019	113.096 ± 0.002	-0.001 ± 0.003
2013/12/16	R1616	113.0865 ± 0.0017	113.090 ± 0.001	**0.004 ± 0.002**
2014/01/21	R1621	113.0957 ± 0.0015	113.096 ± 0.002	0.000 ± 0.002
2014/06/30	AUST29	113.0957 ± 0.0071	113.090 ± 0.004	-0.006 ± 0.008
2014/08/04	R1647	113.0909 ± 0.0018	113.091 ± 0.002	0.000 ± 0.003
2014/08/11	R1648	113.0938 ± 0.0018	113.094 ± 0.005	0.000 ± 0.005
2014/10/28	RD1410	113.0924 ± 0.0026	113.093 ± 0.002	0.001 ± 0.007
2014/11/10	R1661	113.0937 ± 0.0040	113.095 ± 0.003	0.001 ± 0.005
2015/01/20	R1671	113.0849 ± 0.0024	113.087 ± 0.001	0.002 ± 0.003
2015/02/17	T2102	113.0929 ± 0.0036	113.087 ± 0.009	-0.006 ± 0.010
2015/07/27	R1698	113.0942 ± 0.0017	113.096 ± 0.003	0.002 ± 0.003
2015/11/09	R1713	113.0929 ± 0.0015	113.092 ± 0.002	-0.001 ± 0.002
2015/11/10	T2107	113.0916 ± 0.0032	113.095 ± 0.003	0.003 ± 0.004
2016/01/26	R1724	113.0977 ± 0.0018	113.097 ± 0.001	-0.001 ± 0.002
2017/01/03	R1773	113.0959 ± 0.0015	113.094 ± 0.001	-0.002 ± 0.002
2017/04/24	R1789	113.0918 ± 0.0016	113.093 ± 0.001	0.001 ± 0.002
2017/05/23	T2118	113.0929 ± 0.0033	113.095 ± 0.005	0.002 ± 0.006
2017/07/11	T2119	113.0972 ± 0.0030	113.105 ± 0.003	**0.008 ± 0.004**
2017/09/13	AUA026	113.1063 ± 0.0107	113.109 ± 0.036	0.003 ± 0.038
2017/10/02	R1812	113.0918 ± 0.0015	113.093 ± 0.001	0.001 ± 0.002
2017/10/03	AUA028	113.1029 ± 0.0125	113.098 ± 0.016	-0.005 ± 0.020
2017/11/24	AUA032	113.0970 ± 0.0169	113.100 ± 0.035	0.003 ± 0.039

2017/12/20	AUA034	113.0925 ± 0.0282	113.1030 ± 0.019	0.010 ± 0.034

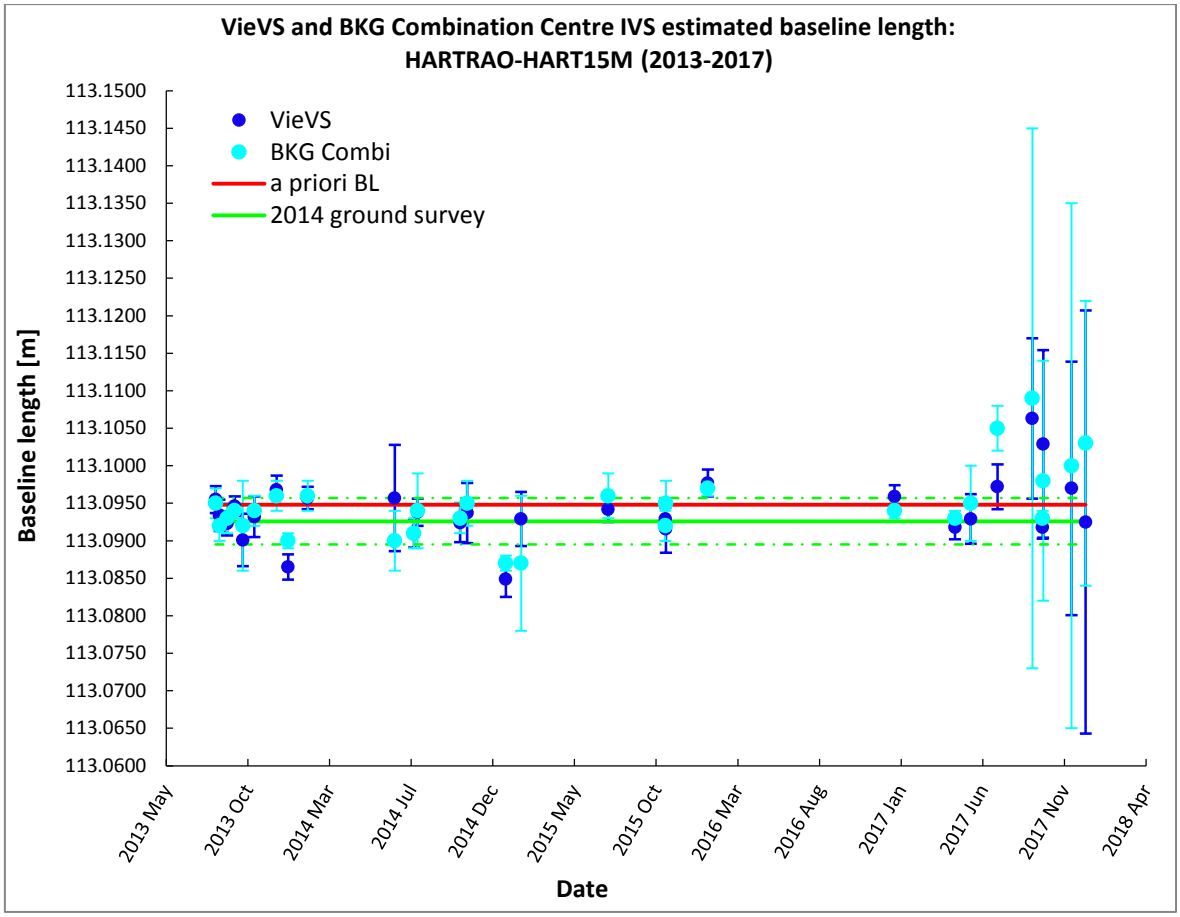

Figure 7.3 Baseline lengths between the HartRAO 26 m and 15 m antennas estimated with VieVS for 29 dual global sessions during 2013 to 2017 compared with corresponding IVS Combination Centre (IVSCC) as well as a priori (= 113.0948 m) and 2014 ground survey (= 113.0926 ± 0.0031 m) values.

Seasonal variation in VieVS estimated HARTRAO-HART15M baseline length from dual global sessions:

Figure 7.4 displays the 29 dual global sessions divided into seasonal groupings to investigate the possibility of seasonal variations in the HARTRAO-HART15M baseline length. The average value of the VieVS estimated baseline lengths for each of these seasonal groupings as well as offsets from the *a priori* and ground survey values are

displayed in

Table 7.4.

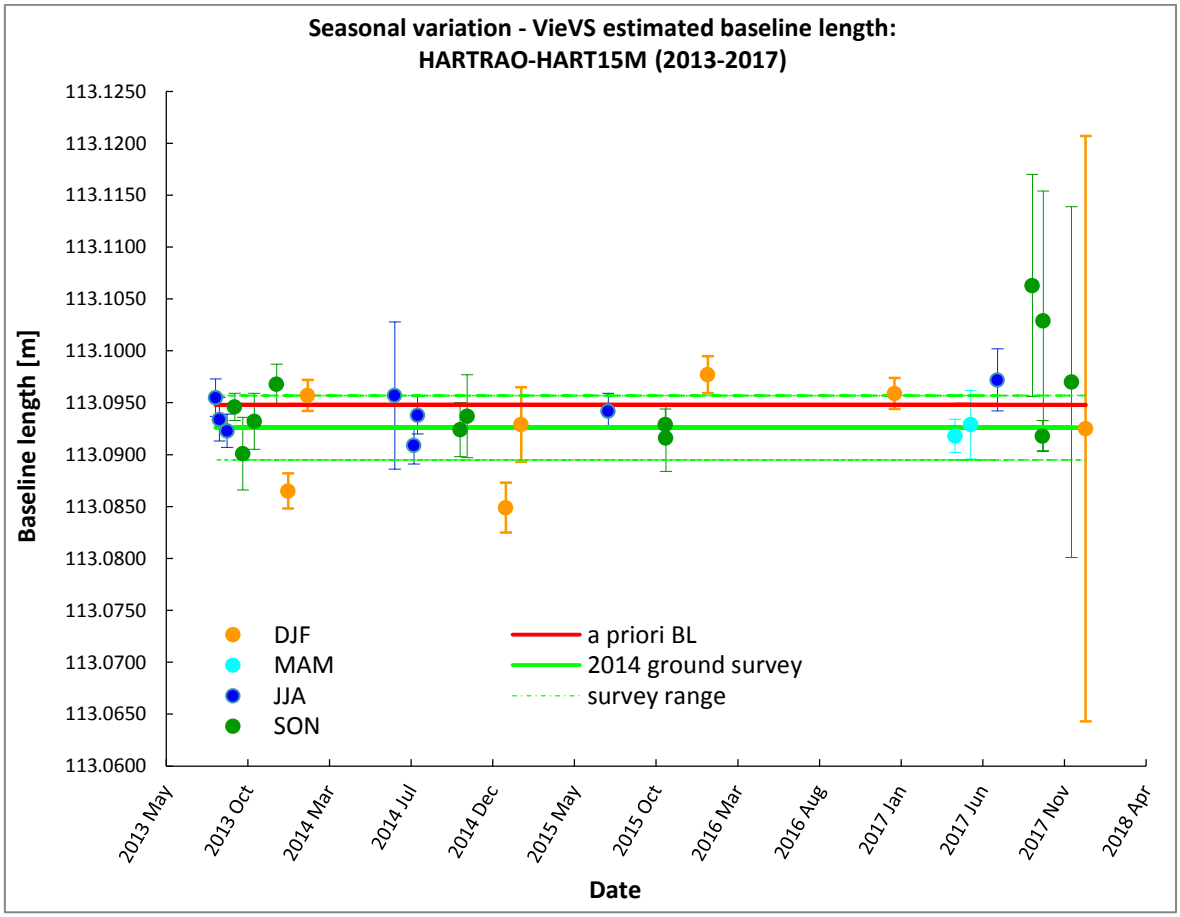

Figure 7.4 Baseline lengths between the HartRAO 26 m and 15 m antennas estimated with

VieVS for 29 dual global sessions during 2013 to 2017 divided into seasonal groupings (DJF = summer, MAM = autumn, JJA = winter, SON = spring).

Table 7.4 Offset (Δ) of seasonal average of HARTRAO-HART15M baseline lengths (BL) estimated with VieVS from 29 dual global session observed during 2013 to 2017 from a priori (= 113.0948 m) as well as 2014 ground survey (= 113.0926 ± 0.0031 m) values.

Season	**Seasonal average (VieVS estimated dual) [m]**	**Δ (*a priori* – estimated dual) BL [m]**	**Δ (ground survey – estimated dual) BL [m]**
Summer – DecJanFeb (DJF)	113.0923 ± 0.0049 (7 sessions)	0.0025	0.0003 ± 0.0058
Autumn – MarAprMay (MAM)	113.0924 ± 0.0008 (2 sessions)	**0.0025**	0.0002 ± 0.0032
Winter – JunJulAug (JJA)	113.0941 ± 0.0020 (8 sessions)	0.0007	-0.0015 ± 0.0037
Spring – SepOctNov (SON)	113.0953 ± 0.0048 (12 sessions)	-0.0005	-0.0027 ± 0.0057

Only one of the seasonal averages of the 29 dual global sessions' baseline lengths estimated with VieVS, that of autumn (indicated in bold in the third column of

Table 7.4), does not agree within the formal error with the *a priori* value. Seasonal averages for summer and autumn are closer to that of the ground survey value, while those for winter and spring appear closer to the *a priori* value.

7.2 BASELINE LENGTH BETWEEN HARTRAO ANTENNAS FROM LOCAL SHORT BASELINE EXPERIMENTS

In preparation for upcoming VGOS operations at HartRAO, with the accompanying requirement of 1 mm accuracy in station coordinates and global baselines, short baseline (SBL) VLBI experiments between the HartRAO 26 m legacy and co-located 15 m antennas were conducted with a view to testing this accuracy. If the VGOS goal of 1 mm accuracy is to be achieved on global baselines, it must be possible to at least reach this goal for the short baseline of ~113 m between the HartRAO antennas.

These SBL experiments should allow for more accurate estimation of the baseline length and local tie than is possible with the dual global sessions. Dedicated observations can be scheduled: (1) at night, to minimise thermal gradients; and (2) to optimise sky coverage and cable wrap for the two antennas. On such a short baseline, it is not necessary to apply source structure corrections. These experiments also need not be observed in dual-frequency mode, as is the case for the global sessions where observations at both X- and S-band are required to account for the dispersive effect of the ionosphere. The SBL sessions can be observed at X-band only as the ionospheric effect is expected to be negligible on such a short baseline with the antennas observing the same part of the sky. Observations at X-band only, provide the added advantage of being able to exclude S-band

Department of Geology, Geoinformatics and Meteorology
University of Pretoria

observations contaminated strongly by radio-frequency interference (RFI). Most atmospheric and geophysical error sources cancel out – the antennas point in the same direction and observe through nearly the same atmosphere and are therefore similarly affected by the troposphere; the antennas are supposed to be located on the same bedrock which should preclude differential motion. Clock variations can be eliminated by running the antennas off the same hydrogen maser clock.

The EFOS-28 hydrogen maser, previously employed for VLBI on the 15 m antenna, developed an internal heater fault and was taken out of service in September 2018. The iMaser72 hydrogen maser was used as reference clock for both 26 m and 15 m antennas in the SBL sessions, except for in the first/test session, SBL500 (11 May 2018). In order to prevent cross-correlation of the two antennas' phase calibration signals from drowning out the astronomical signal, phase-calibration was turned off on the more stable 26 m antenna and manual phase-cal was applied instead in all of the SBL sessions.

For this investigation, SBL experiments in which only the HartRAO 26 m and 15 m antennas participated, therefore observing the same sources simultaneously, were scheduled and analysed with VieVS in order to estimate the local tie vector between the antennas more accurately. Baseline length was calculated as indicated in Section 7.1 according to Equation 7.1. The results for baseline components and baseline length were compared with the corresponding results from the 2014 co-location survey. The average value of VieVS estimated baseline lengths from the SBL sessions were also compared with *a priori* and ground survey values as well as with the VieVS estimated and IVSCC average values for the dual global sessions. The *a priori* and estimated baseline lengths are calculated in VieVS from the *a priori* and estimated antenna coordinates, respectively. Possible seasonal variations in baseline length were also investigated.

7.2.1 Methodology

A first SBL test experiment between the HartRAO 26 m and 15 m antennas, SBL500, was conducted on the 11th of May 2018. Thereafter, regular SBL experiments were conducted monthly from December 2019 until June 2021 (SBL501-519). It was hoped to establish

some seasonal overlap, but unfortunately only the first ten of these regular sessions (December 2019, SBL501 to September 2020, SBL510) have been correlated thus far and could be included in this investigation together with the test session SBL500. The methodology for determining the baseline length between the HartRAO antennas from SBL sessions is described in terms of this first SBL test experiment, which served as template for the SBL sessions that followed. From SBL502 onwards, it was possible to include ICRF-3 defining sources in the source catalogue used for scheduling observations. It was not possible to run the antennas off the same clock for the first SBL test experiment, SBL500, but co-location ensured common local geophysics and atmosphere at least.

Scheduling of the first short baseline experiment, test session SBL500 (11 May 2018):

The SBL500 session was scheduled with VieVS (Böhm *et al*., 2018) to observe the same ICRF-2 defining sources simultaneously with the HartRAO 26 m and 15 m antennas at X-band using a data rate of 2 Gbps per antenna. Phase-cal was turned off for the 26 m antenna, which carries less cable length from receiver to backend, in order to avoid corrupting the cross-correlation. The 4-hour session ran from 22:00 UT on the 11th of May until 02:00 UT on the 12th of May 2018, well away from sunset and sunrise to ensure temperature stability. This was necessary to minimise thermally induced changes in cables, low-noise amplifiers (LNAs) and downconverters as well as thermal expansion of the antennas.

By observing the same sources with the two antennas simultaneously, measurements were made through a similar troposphere, and the the local tie vector could thus be estimated more accurately. Scans were scheduled to cover the full range of azimuth, elevation and cable wrap. Sweeping the full range of azimuth allowed for determining east and north baseline components, while sweeping the full range of elevation allowed for reducing the correlation between the vertical component of the baseline and the troposphere. Scans were scheduled so that the antennas would nod up and down in elevation in 15° steps (from 10° to 70°) as they swept in azimuth in 30° steps (see Figure 7.5). Following this approach, the older 26 m legacy antenna did not waste much time on long slews. The first scan was scheduled at a higher elevation of 55° for calibration purposes, and at an azimuth of 115°.

Department of Geology, Geoinformatics and Meteorology
University of Pretoria

Scans were scheduled over the full range of mutual visibility for the hour angle-declination (HA-Dec) mounted 26 m antenna and azimuth-elevation (az-el) mounted 15 m antenna. Due to the 26 m antenna's polar mount, it was not possible to observe many soures at low elevations for southerly azimuths.

The 15 m antenna with its faster slew rate (az = 2/s, el = 1/s) had to wait for the slower 26 m legacy antenna (slew rate: HA = 0:5/s, Dec = 0:5/s) for a considerable amount of time (see Figure 7.6). The only idle time experienced by the 26 m antenna was whilst waiting for the 15 m az-el antenna to complete two cable wrap slews, lasting 211 and 220 seconds, respectively. Pre-observation time of 10 seconds, to allow for settling time and calibration, and observation time of 30 seconds per scan were scheduled. The schedule produced 95 scans and 880 GB of data per antenna.

Correlation and post-processing of the first short baseline experiment, test session SBL500 (11 May 2018):

The SBL500 session was subsequently correlated at the Vienna correlator (Gruber *et al*., 2021) with the distributed FX-architecture (DiFX) software VLBI correlation package, using a spectral resolution of 0.2 MHz and applying local oscillator (LO) frequency offsets of 9999.9 Hz to HARTRAO (the 26 m antenna). Fringe-fitting and post-processing were also performed at the Vienna correlator making use of the Haystack Observatory Postprocessing System (HOPS) software package. An example of the fringe plot produced by the *fourfit* program in HOPS for scan no0057 of SBL500 on the radio source 1921-293 is shown in Figure 7.7. The SBL500 correlator output was made available as VGOS database (vgosDB) files.

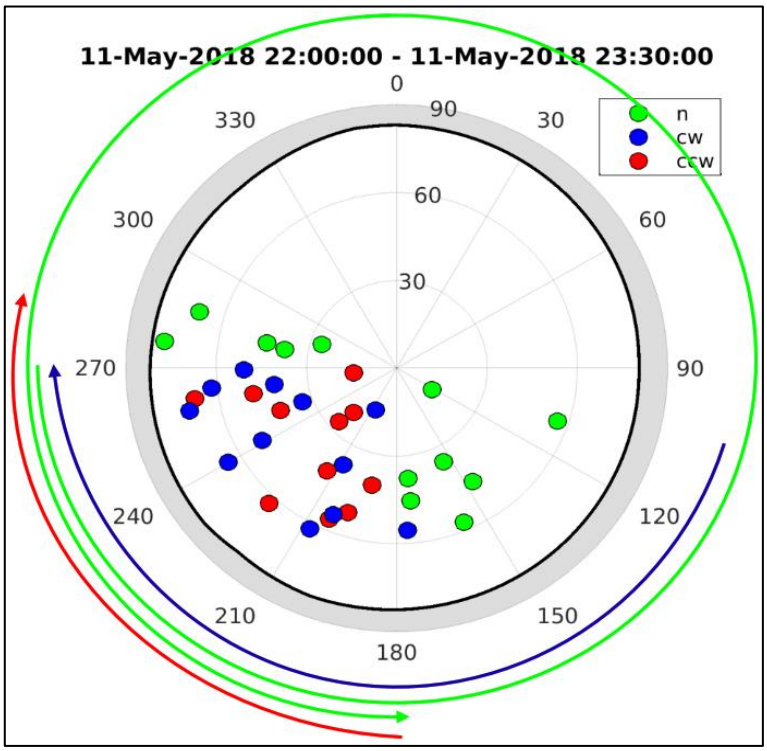

Figure 7.5 Slew plot and scans/observations for the HartRAO 26 m and 15 m antennas during the first 90 minutes of the first 4-hour short baseline (SBL) experiment, test session SBL500. Credit: M. Schartner.

statistics	mean	std	HART15M	HARTRAO
Scan Time	23.82 %	0.00 %	23.82 %	23.82 %
Slew Time	41.35 %	33.06 %	17.97 %	64.73 %
Idle Time	24.41 %	33.06 %	47.79 %	1.03 %
Calibration Time	10.42 %	0.00 %	10.42 %	10.42 %
Number of Scans	95.0	0.0	95	95
Scans per hour	23.7	0.0	23.7	23.7

Figure 7.6 Statistics for the SBL500 observing schedule of the HartRAO 26 m and 15 m antennas. Credit: M. Schartner.

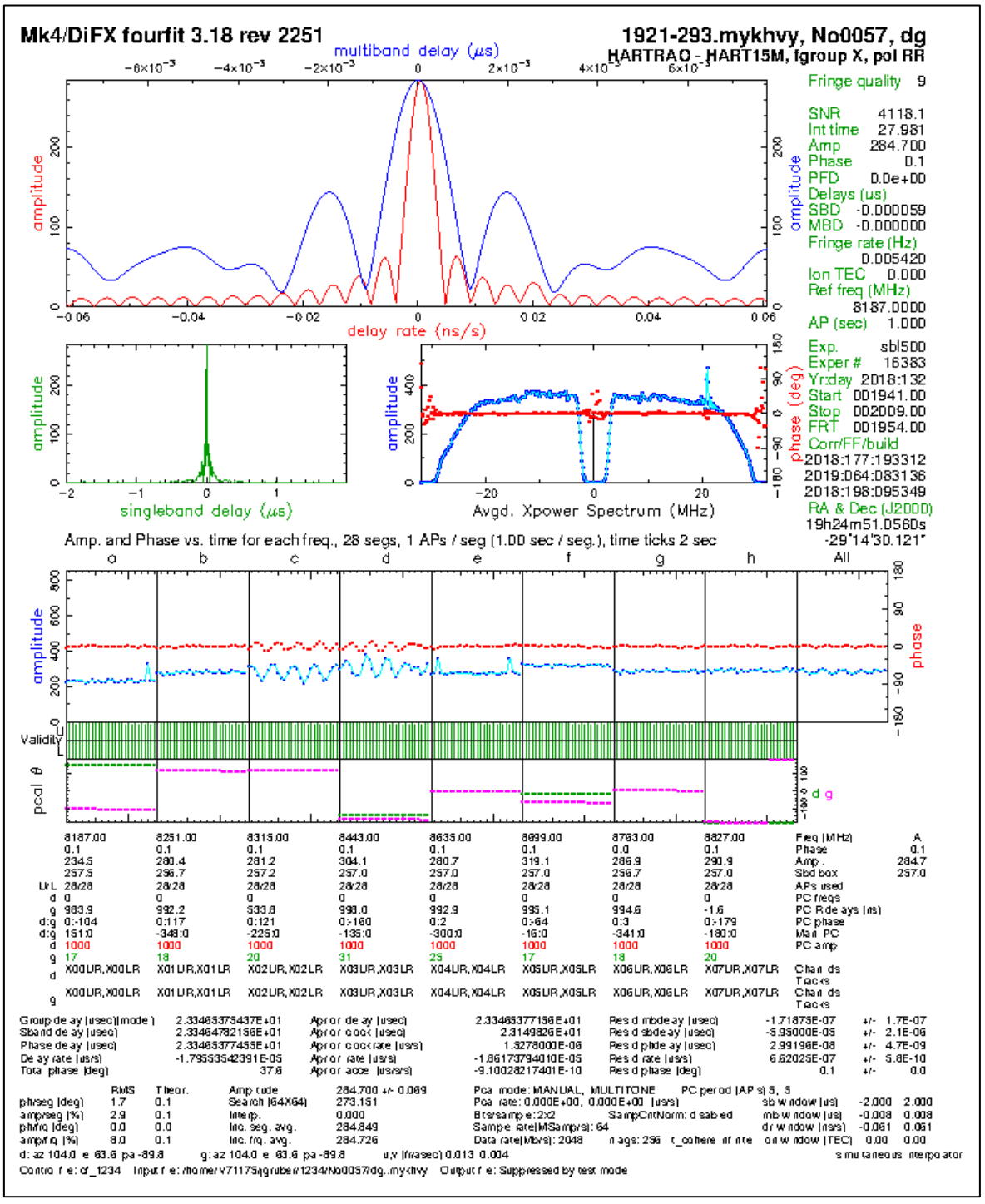

Figure 7.7 Fringe plot of HARTRAO-HART15M cross-correlation of SBL500 scan no0057 for the radio source 1921-293. Credit: J. Gruber.

Data analysis of short baseline experiments, SBL500-510:

The geodetic VLBI analysis software, VieVS (Böhm *et al*., 2018), was used for data analysis. Geodetic VLBI data from local SBL experiments in which only the HartRAO 26 m and 15 m antennas participated during May 2018 (test experiment, SBL500) and then monthly from December 2019 to September 2020 (SBL501-510) were analysed to estimate the baseline length between the HartRAO 26 m and 15 m antennas for each of these sessions, in order to determine the local tie between the two antennas.

The data analysis procedure followed was the same as that for the global dual sessions (as discussed in the second paragraph of Section 7.7.1) with *a priori* modelling in general following the IERS Conventions 2010 (IERS, 2010) and parametrisation as presented in

Table *7.1*. The EOP were, however, not estimated in the analysis of these single baseline experiments but rather fixed to the IERS 14 C04 (Bizouard et al., 2019) time series.

The VieVS estimated XYZ-components and 3D-distance (baseline length) of the baseline between the HartRAO 26 m and 15 m antennas for each of the SBL experiments were compared with corresponding results from IGN measurements made during the February 2014 co-location survey (Muller, Pesce & Collilieux, 2020). The average value of VieVS estimated baseline lengths from the SBL sessions were compared with the *a priori* and ground survey values as well as with the VieVS estimated and IVSCC average values for the dual global sessions. The SBL sessions were also divided into seasonal groupings – summer = DecJanFeb, autumn = MarAprMay, winter = JunJulAug, spring = SepOctNov – to investigate the possibility of seasonal variation in the XYZ-components and 3D-distance (baseline length). Seasonal averages of the VieVS estimated SBL XYZ-components and 3D-distance (baseline length) were compared with corresponding 2014 ground survey values.

Department of Geology, Geoinformatics and Meteorology
University of Pretoria

7.2.2 Results and discussion

Comparison of VieVS estimated HARTRAO-HART15M baseline components and baseline length from short baseline experiments with corresponding values from ground survey:

In Table 7.5 and Figure 7.8 to Figure 7.8, results for baseline XYZ-components and baseline length (3D-distance) estimated with VieVS in VLBI analysis of the SBL experiments, SBL500 (11 May 2018, test session) and SBL501-510 (December 2019 to September 2020) are compared with the corresponding results from IGN measurements as determined during the February 2014 co-location survey (Muller, Pesce & Collilieux, 2020).

The VieVS estimated baseline length does not agree within the formal error with the ground survey baseline length for only two of the SBL experiments, SBL500 (11 May 2018, test session) and SBL504 (15 May 2020) (indicated in bold in the last column of Table 7.5), due to a significant offset in the baseline Y-component for the former (indicated in bold in the sixth column of Table 7.5), and in the baseline X-component for the latter session (indicated in bold in the fourth column of Table 7.5).

Table 7.5 VieVS estimated values for HARTRAO-HART15M baseline XYZ-components and baseline length (3D-distance) from the short baseline (SBL) experiments, SBL500-510, and offset from corresponding baseline values measured during the 2014 local tie survey (X-component = -48.0338 ± 0.0028 m, Y-component = 102.3019 ± 0.0032 m, Z-component = -4.1239 ± 0.0077 m, baseline length (3D-distance) = 113.0926 ± 0.0031 m).

Date	Session	Baseline X-component [m]	X-offset [mm]	Baseline Y-component [m]	Y-offset [mm]	Baseline Z-component [m]	Z-offset [mm]	Baseline 3D-distance [m]	3D-offset [mm]
2018/05/11	SBL500	-48.0325 ± 0.0020	-1.3 ± 3.4	102.2929 ± 0.0030	**9.0 ± 4.4**	-4.1284 ± 0.0014	4.5 ± 7.8	113.0841 ± 0.0029	**8.5 ± 4.2**
2019/12/06	SBL501	-48.0369 ± 0.0021	3.1 ± 3.5	102.3024 ± 0.0032	-0.5 ± 4.5	-4.1288 ± 0.0015	4.9 ± 7.8	113.0945 ± 0.0030	-1.9 ± 4.3
2020/01/06	SBL502	-48.0368 ± 0.0017	3.0 ± 3.3	102.3022 ± 0.0018	-0.3 ± 3.7	-4.1288 ± 0.0015	4.9 ± 7.8	113.0943 ± 0.0018	-1.7 ± 3.6
2020/02/07	SBL503	-48.0365 ± 0.0024	2.7 ± 3.7	102.3015 ± 0.0041	0.4 ± 5.2	-4.1287 ± 0.0015	4.8 ± 7.8	113.0935 ± 0.0038	-0.9 ± 4.9
2020/03/15	SBL504	-48.0389 ± 0.0022	**5.1 ± 4.2**	102.3067 ± 0.0032	-4.8 ± 4.5	-4.1289 ± 0.0015	5.0 ± 7.8	113.0993 ± 0.0031	**-6.7 ± 4.4**
2020/04/19	SBL505	-48.0364 ± 0.0023	2.6 ± 3.6	102.3013 ± 0.0036	0.6 ± 4.8	-4.1287 ± 0.0015	4.8 ± 7.8	113.0933 ± 0.0034	-0.7 ± 4.6
2020/05/17	SBL506	-48.0356 ± 0.0025	1.8 ± 3.8	102.2997 ± 0.0041	2.2 ± 5.2	-4.1287 ± 0.0015	4.8 ± 7.8	113.0915 ± 0.0039	1.1 ± 5.0
2020/06/19	SBL507	-48.0357 ± 0.0028	1.9 ± 4.0	102.2998 ± 0.0051	2.1 ± 6.0	-4.1287 ± 0.0015	4.8 ± 7.8	113.0916 ± 0.0047	1.0 ± 5.6
2020/07/18	SBL508	-48.0385 ± 0.0028	4.7 ± 4.0	102.3057 ± 0.0051	-3.8 ± 6.0	-4.1289 ± 0.0015	5.0 ± 7.8	113.0982 ± 0.0048	-5.6 ± 5.7
2020/08/14	SBL509	-48.0375 ± 0.0022	3.7 ± 3.6	102.3037 ± 0.0034	-1.8 ± 4.7	-4.1288 ± 0.0015	4.9 ± 7.8	113.0960 ± 0.0032	-3.4 ± 4.5
2020/09/20	SBL510	-48.0356 ± 0.0028	1.8 ± 4.0	102.2997 ± 0.0051	2.2 ± 6.0	-4.1287 ± 0.0016	4.8 ± 7.9	113.0915 ± 0.0048	1.1 ± 5.7

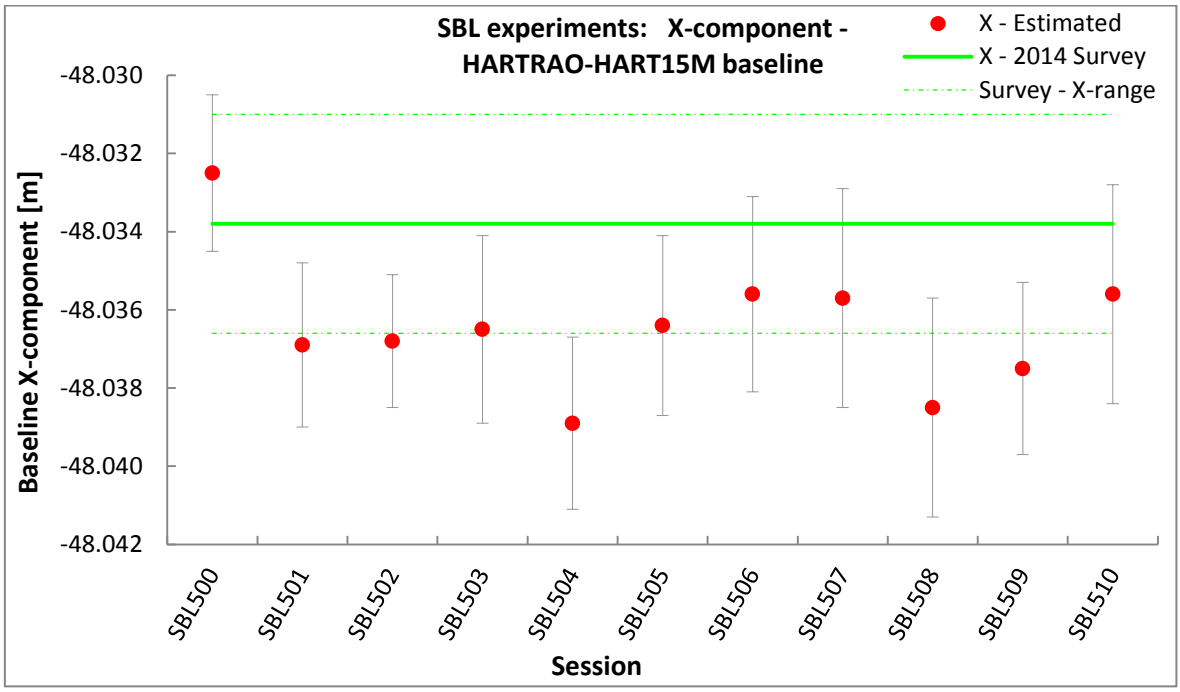

Figure 7.8 VieVS estimated SBL500-510 HARTRAO-HART15M baseline X-components compared with value measured in ground survey (= 48.0338 ± 0.0028 m).

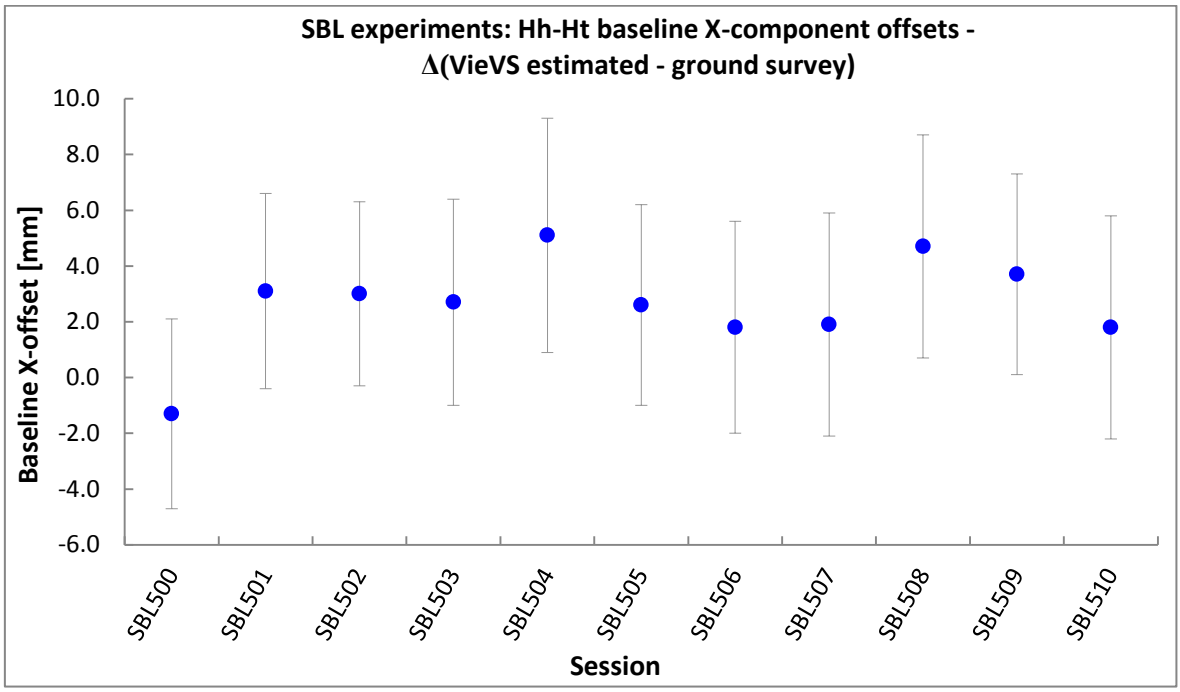

Figure 7.9 Offset between VieVS estimated SBL500-510 HARTRAO-HART15M baseline X-components and ground survey value (= 48.0338 ± 0.0028 m).

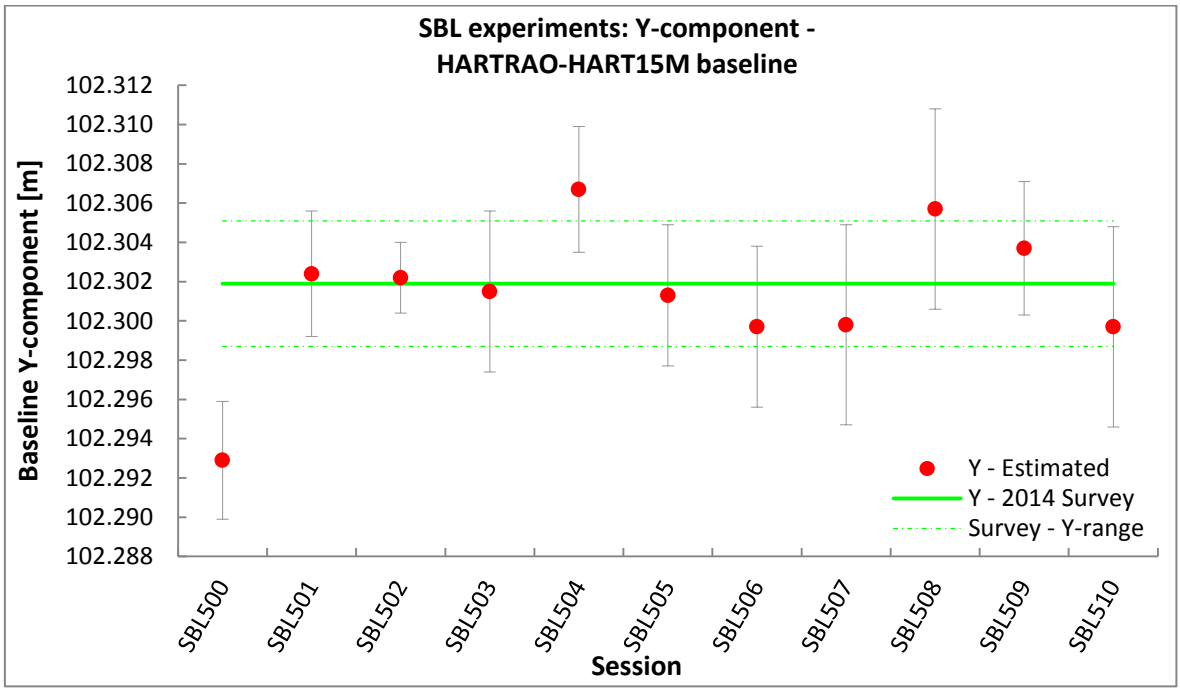

Figure 7.10 VieVS estimated SBL500-510 HARTRAO-HART15M baseline Y-components compared with value measured in ground survey (= 102.3019 ± 0.0032 m).

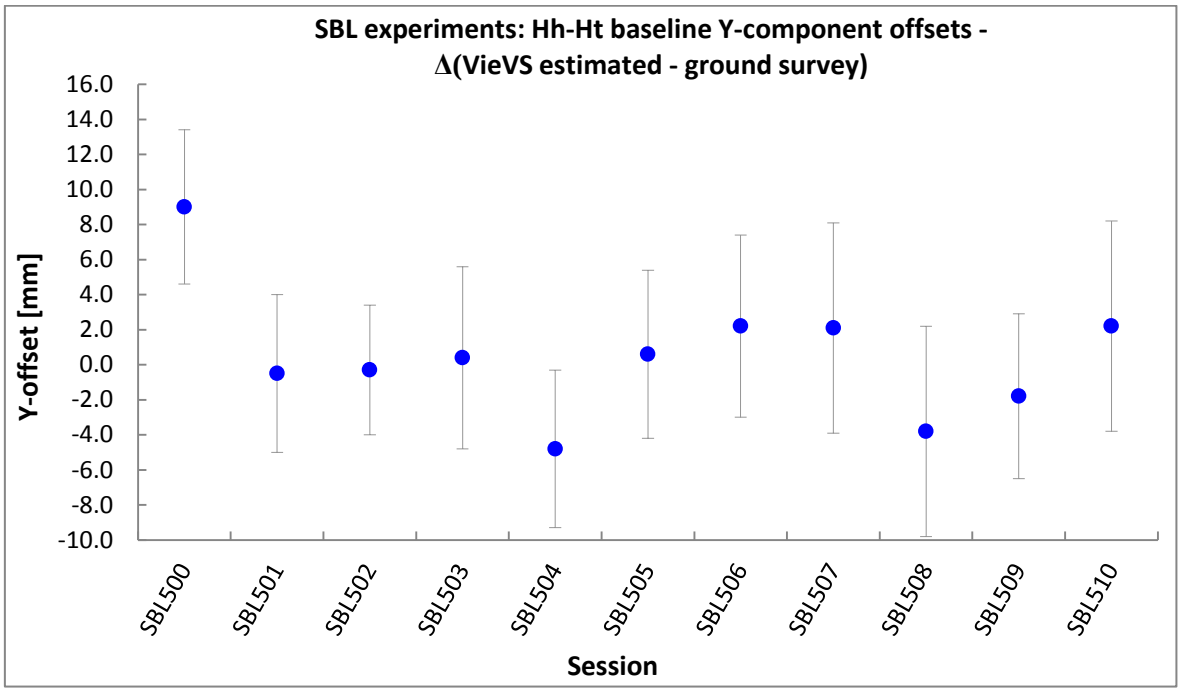

Figure 7.11 Offset between VieVS estimated SBL500-510 HARTRAO-HART15M baseline Y-components and ground survey value (= 102.3019 ± 0.0032 m).

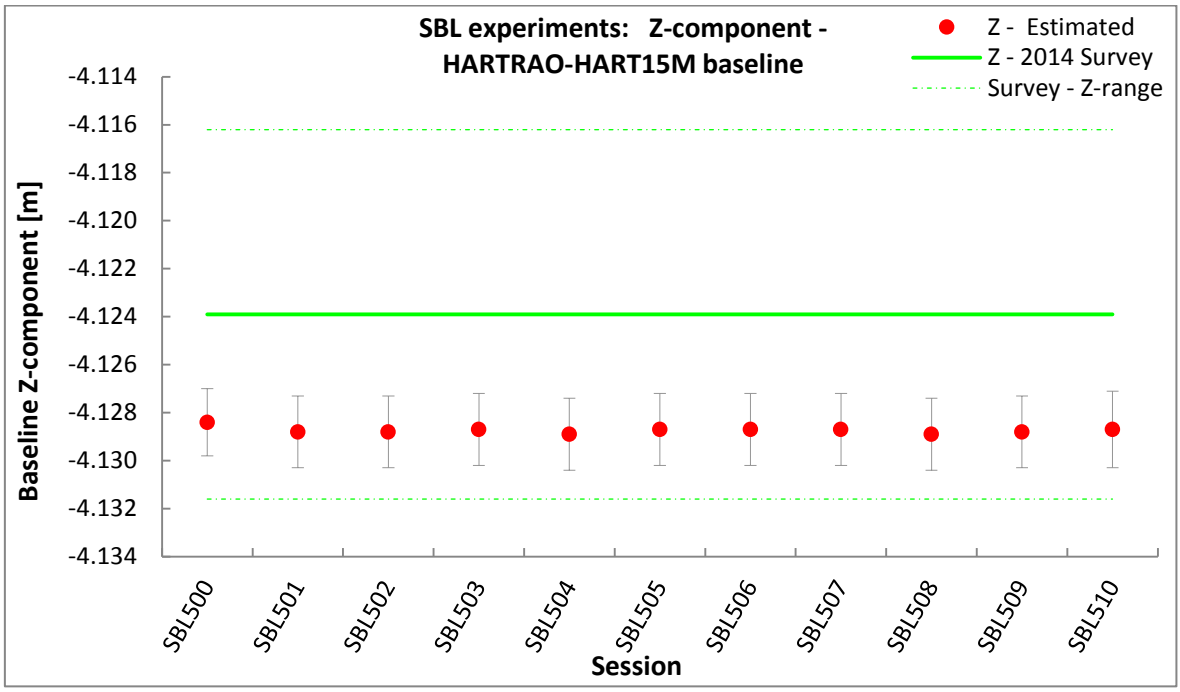

Figure 7.12 VieVS estimated SBL500-510 HARTRAO-HART15M baseline Z-components compared with value measured in ground survey (= 4.1239 ± 0.0077 m).

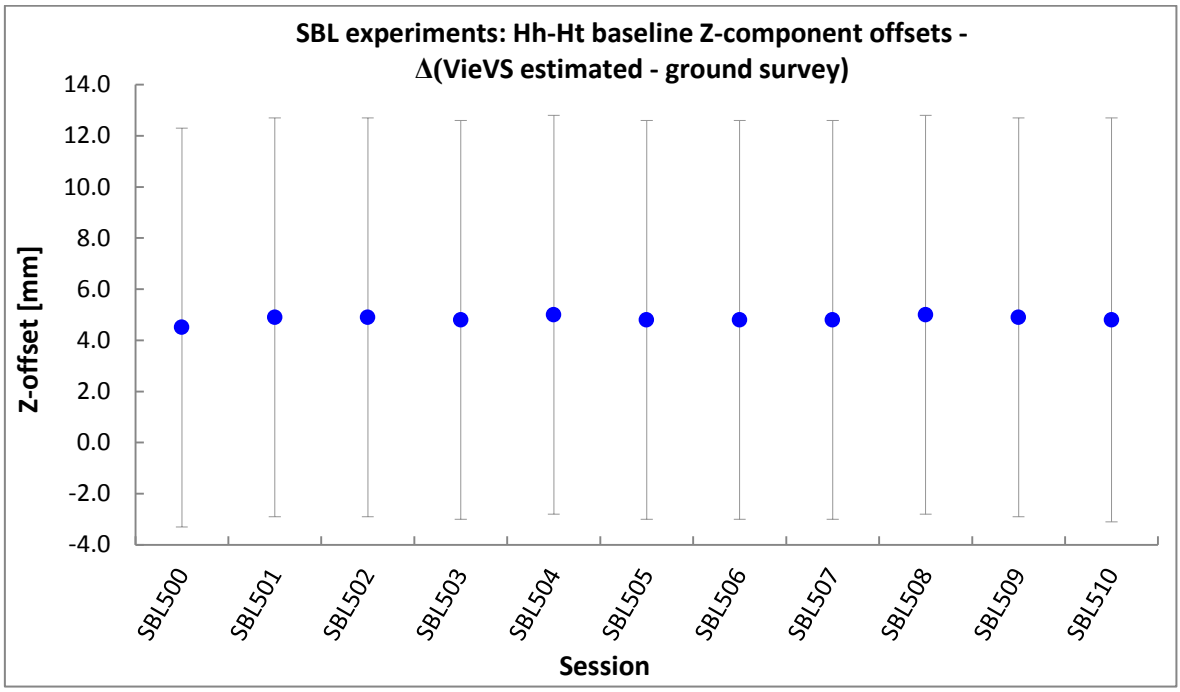

Figure 7.13 Offset between VieVS estimated SBL500-510 HARTRAO-HART15M baseline Z-components and ground survey value (= 4.1239 ± 0.0077 m).

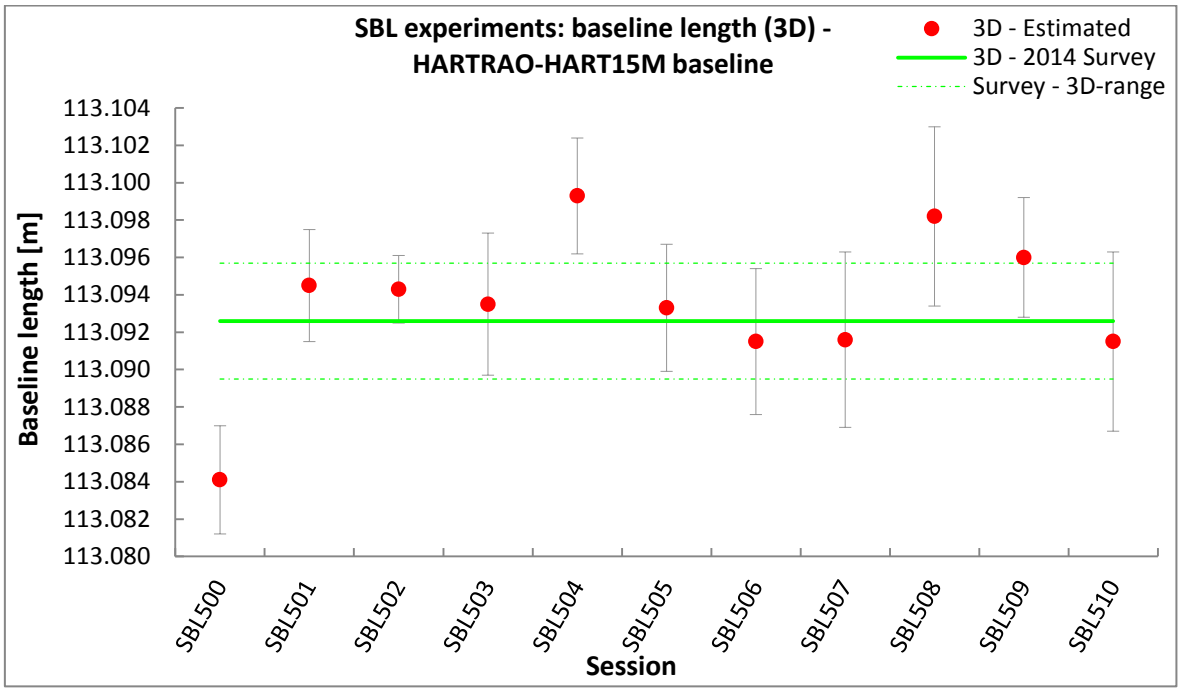

Figure 7.74 VieVS estimated SBL500-510 HARTRAO-HART15M baseline length compared with value determined in ground survey (= 113.0926 ± 0.0031 m).

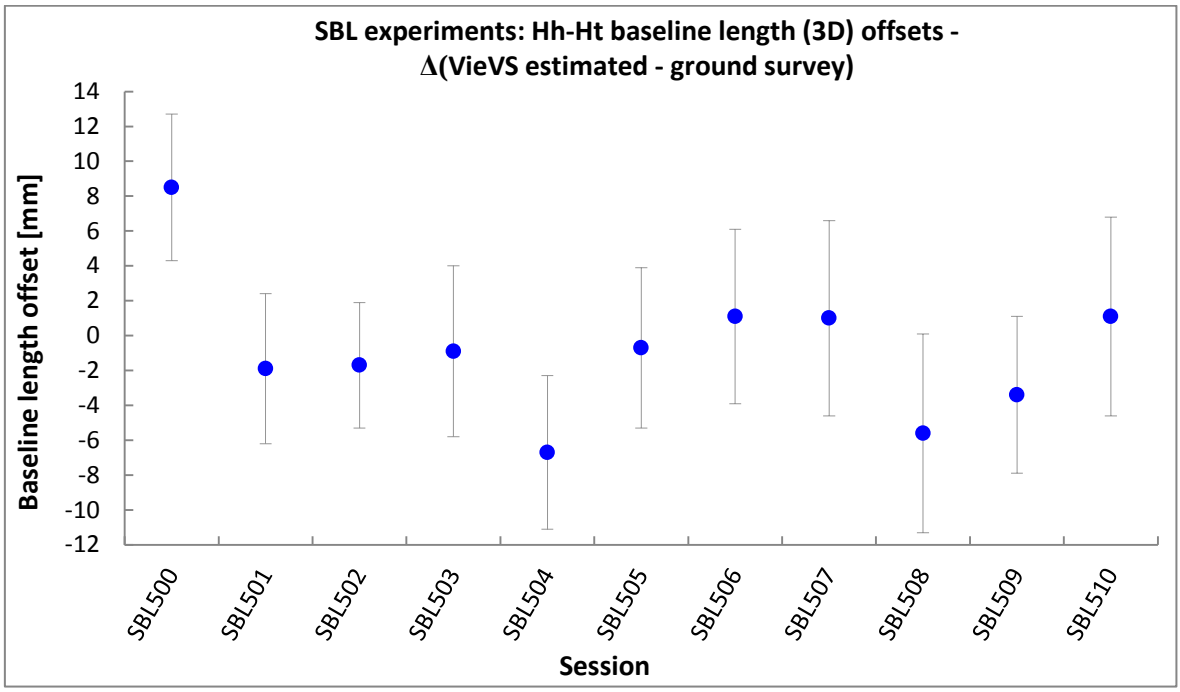

Figure 7.8 Offset between VieVS estimated SBL500-510 HARTRAO-HART15M baseline length and value determined in ground survey (= 113.0926 ± 0.0031 m).

Comparison of VieVS estimated HARTRAO-HART15M baseline length from short baseline experiments with a priori, ground survey and dual global session values:

The average value of the baseline length between the HartRAO 26 m and 15 m antennas estimated with VieVS from the SBL experiments (both including and excluding the test session, SBL500) is displayed in Table 7.6, together with the *a priori* value used in VLBI analysis, the value determined during the 2014 co-location survey as well as average baseline length values from VieVS estimation of the dual global sessions and that provided by the IVSCC for corresponding dual global sessions. As suggested by the previous investigation, the X- and Y-components as well as baseline length of the test session, SBL500, could very well be treated as outliers. This session was therefore both included and excluded in the comparison here.

Table 7.6 Comparison of HARTRAO-HART15M average baseline length as estimated with VieVS from the SBL experiments (also excluding the test session, SBL500) with the a priori value used in VLBI analysis, with the value determined by ground survey, with the average value of the dual global sessions' baseline lengths estimated with VieVS and with the average value provided by the IVSCC for these dual global sessions.

Baseline length from	**Sessions / Date**	**Average baseline length [m]**
SBL experiments	SBL500-510 / May 2018, Dec 2019 – Sep 2020	113.0934 ± 0.0039
SBL (excl. SBL500)	SBL501-510 / Dec 2019 – Sep 2020	113.0944 ± 0.0027
a priori value	IVS	113.0948
Co-location survey	February 2014	113.0926 ± 0.0031
VieVS estimated	Dual global sessions / 2013-2017	113.0940 ± 0.0041
IVS Combination Centre	Dual global sessions / 2013-2017	113.0948 ± 0.0048

The average HARTRAO-HART15M baseline length estimated with VieVS from the SBL sessions, both excluding and including the test session, SBL500, agrees within the formal error with values determined in all the various investigations as well as with the *a priori* value used in the VLBI analysis, and all these investigations' values also agree within the formal error with each other.

Seasonal variation in VieVS estimated HartRAO baseline length from short baseline esperiments:

Figure 7.9 to Figure 7.12 display the SBL experiments, SBL500-SBL510, divided into seasonal groupings to investigate the possibility of seasonal variations in the XYZ-components and 3D-distance of the HARTRAO-HART15M baseline. The average value of the VieVS estimated XYZ-components and 3D-distance for each of these seasonal groupings, both excluding and including the test session, SBL500, as well as offsets from the February 2014 co-location survey values are displayed in Table 7.7.

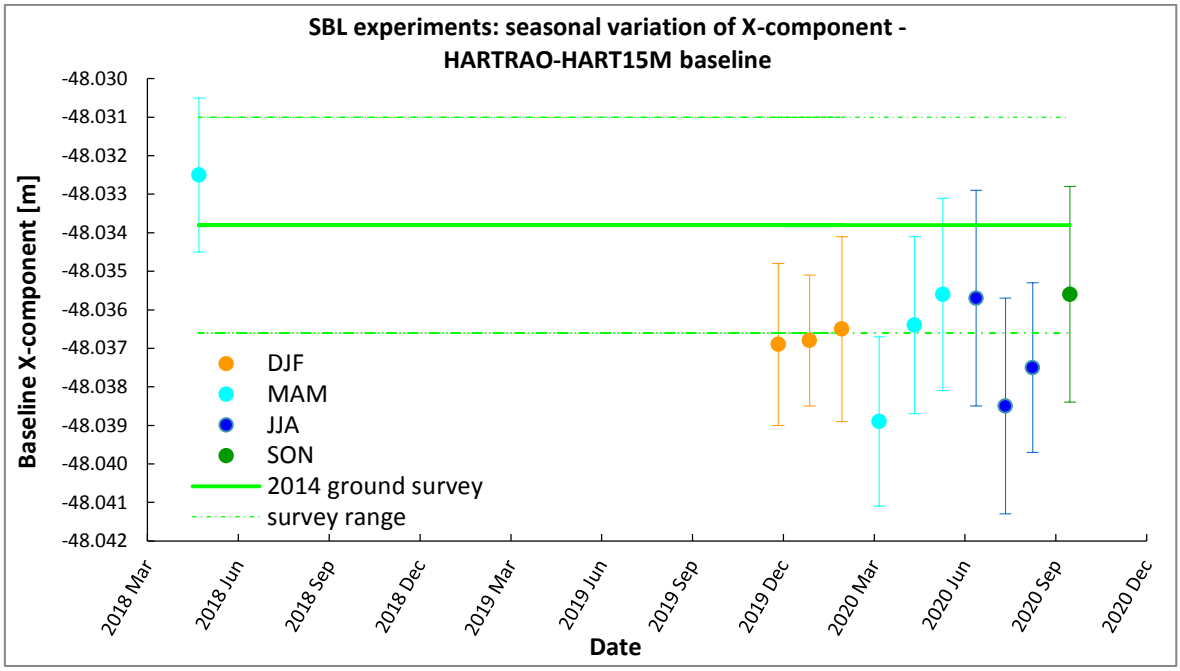

Figure 7.9 VieVS estimated SBL500-510 HARTRAO-HART15M baseline X-components, divided into seasonal groupings (DJF = summer, MAM = autumn, JJA = winter, SON = spring), compared with value measured in ground survey (= 48.0338 ± 0.0028 m).

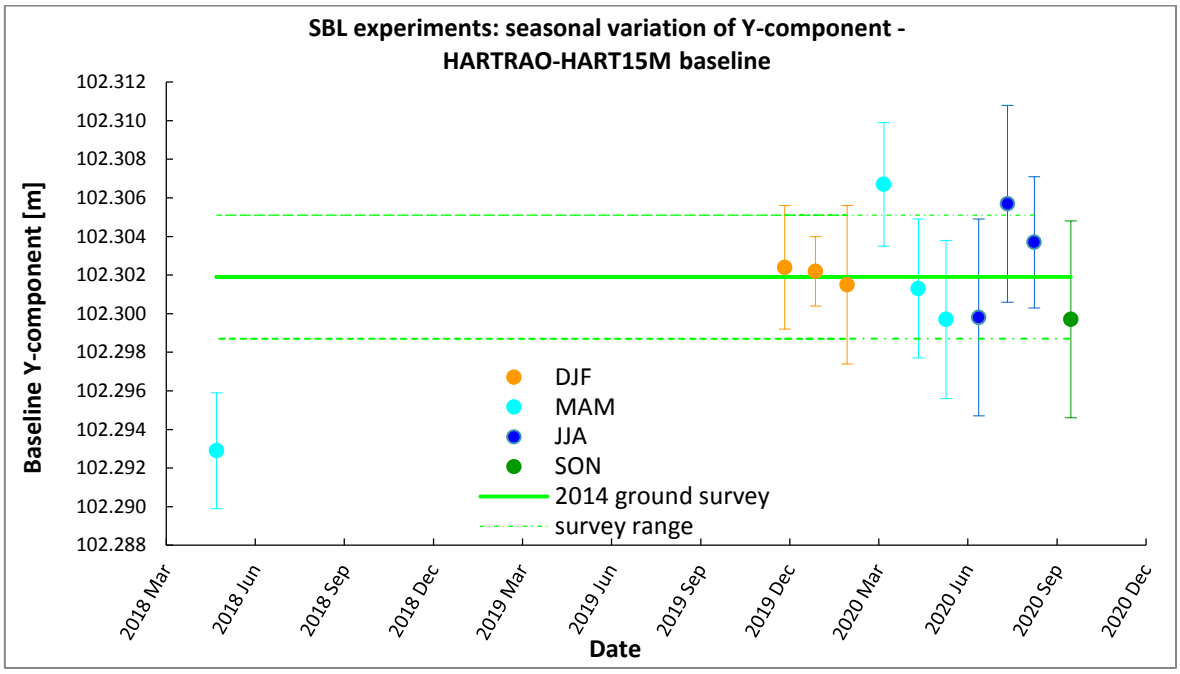

Figure 7.10 VieVS estimated SBL500-510 HARTRAO-HART15M baseline Y-components, divided into seasonal groupings (DJF = summer, MAM = autumn, JJA = winter, SON = spring), compared with value measured in ground survey (= 102.3019 ± 0.0032 m).

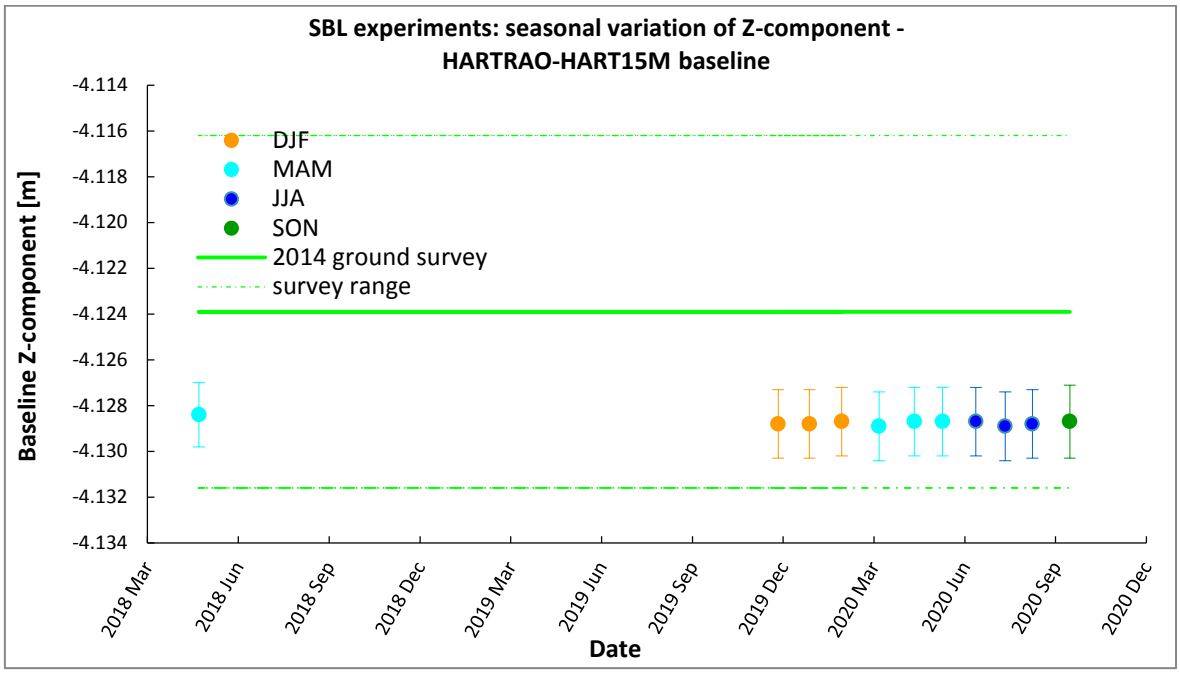

Figure 7.11 VieVS estimated SBL500-510 HARTRAO-HART15M baseline Z-components, divided into seasonal groupings (DJF = summer, MAM = autumn, JJA = winter, SON = spring), compared with value measured in ground survey (= 4.1239 ± 0.0077 m).

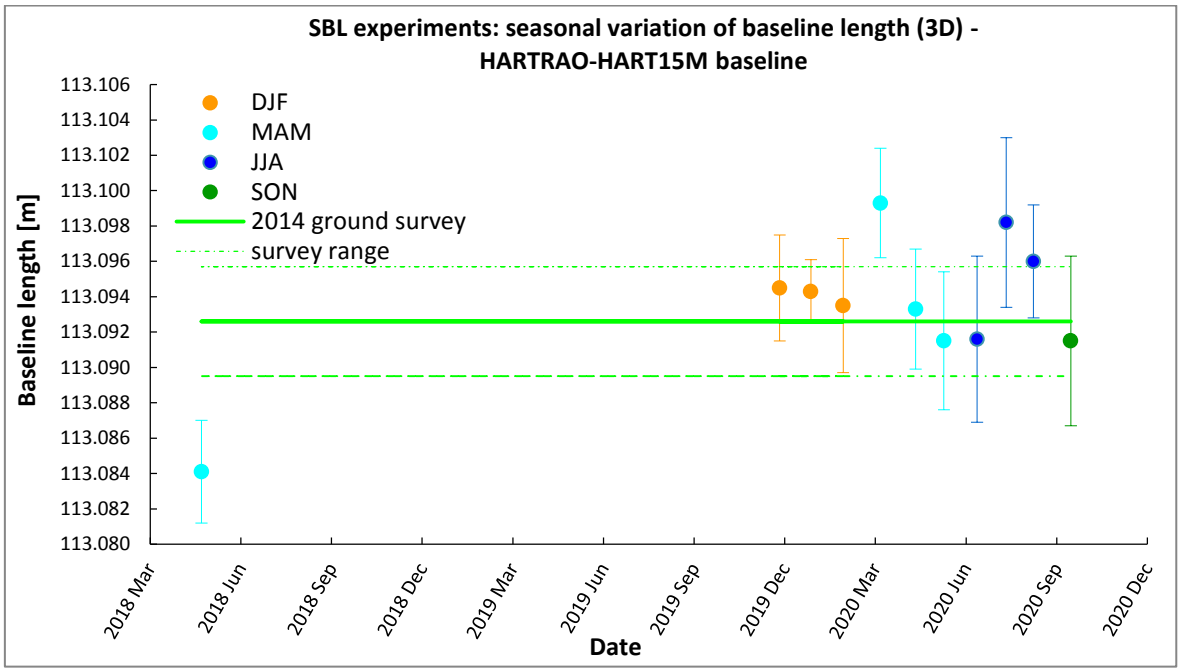

Figure 7.12 VieVS estimated SBL500-510 HARTRAO-HART15M baseline length, divided into seasonal groupings (DJF = summer, MAM = autumn, JJA = winter, SON = spring), compared with value measured in ground survey (= 113.0926 ± 0.0031 m).

Table 7.7 Offset (Δ) of seasonal average of HARTRAO-HART15M baseline XYZ-components and baseline length (3D-distance), estimated with VieVS from the SBL experiments, SBL500-510, from corresponding baseline values measured during the 2014 local tie survey (X-component = -48.0338 ± 0.0028 m, Y-component = 102.3019 ± 0.0032 m, Z-component = -4.1239 ± 0.0077 m, baseline length (3D-distance) = 113.0926 ± 0.0031 m). Autumn (MAM) values are provided for both SBL500 (11 May 2018, test session) excluded (top values) and included (bottom values).

Season	**Seasonal average (VieVS estimated SBL) [m]**				**Δ (ground survey – estimated SBL) BL [m]**			
	Baseline X-component [m]	**Baseline Y-component [m]**	**Baseline Z-component [m]**	**Baseline 3D-distance [m]**	**X-offset [mm]**	**Y-offset [mm]**	**Z-offset [mm]**	**3D-offset [mm]**
Summer – DJF (3 sessions)	-48.0367 ± 0.0002	102.3020 ± 0.0005	-4.1288 ± 0.0001	113.0941 ± 0.0005	2.9 ± 2.8	0.0 ± 3.2	4.9 ± 7.7	-1.5 ± 3.1
Autumn – MAM (3/4 sessions)	-48.0370 ± 0.0017 -48.0359 ± 0.0026	102.3026 ± 0.0005 102.3002 ± 0.0005	-4.1288 ± 0.0000 -4.1287 ± 0.0001	113.0947 ± 0.0041 113.0921 ± 0.0063	3.2 ± 3.3 2.1 ± 3.8	-0.7 ± 3.2 1.7 ± 3.2	4.9 ± 7.7 4.8 ± 7.7	-2.1 ± 5.1 0.5 ± 7.0
Winter – JJA (3 sessions)	-48.0372 ± 0.0014	102.3031 ± 0.0030	-4.1288 ± 0.0001	113.0953 ± 0.0034	3.4 ± 3.1	-1.2 ± 4.4	4.9 ± 7.7	-2.7 ± 4.6
Spring – SON (1 session)	-48.0356 ± 0.0028	102.2997 ± 0.0051	-4.1287 ± 0.0016	113.0915 ± 0.0048	1.8 ± 4.0	2.2 ± 6.0	4.8 ± 7.9	1.1 ± 5.7

All seasonal averages of the SBL experiments' XYZ-components and 3D-distance estimated with VieVS agree within the formal error with the ground survey values. Overall, averages for SBL baseline components in summer appear closest to that of the ground survey values, as would be expected as the co-location survey was conducted in February of 2014. In general it is the average baseline lengths for SBL sessions conducted in autumn (including SBL500) and spring that appear closest to the ground survey value, while average baseline lengths for SBL sessions conducted in summer, autumn (excluding SBL500) and winter appear closer to the *a priori* value.

In general, in comparing the baseline length estimated in VLBI analysis with that determined from local tie ground survey measurements, which are taken to be the more accurate, the sub-millimetre accuracy required from VLBI analysis of the SBL experiments between the HartRAO 26 m and 15 m antennas with a view to reaching the VGOS goal of 1 mm accuracy in global baselines, could not be attained. Baseline length results obtained from VLBI analysis of IVS global sessions mostly agree at sub-centimetre level with the *a priori* value and local tie survey results, and for a few of the sessions the difference is actually close to or in excess of 1 cm. VieVS estimated values also mostly agree with IVSCC values at sub-centimetre level. Except for the SBL test session, SBL500, and SBL504, there is also sub-centimetre level agreement between the baseline length results obtained from VLBI analysis of the SBL sessions and the local tie survey results. The average value for the SBL sessions' baseline lengths also agrees with that for IVS global sessions (for both VieVS estimated and IVSCC) as well as with the *a priori* value at the sub-centimetre level. It was difficult to determine whether any seasonal trend in baseline length exists due to the dearth of dual IVS global sessions, especially for autumn, and no seasonal overlap for the SBL sessions due to the correlation backlog. In fact, no correlated SBL sessions were available for analysis for the months of October and November.

7.3 PLANS FOR AUTOMATED LOCAL TIE GROUND SURVEY

The ITRF is realised through the combination of solutions from co-located space geodetic techniques, and depends on highly accurate local tie vectors between the reference points

of the instruments. In the past, local tie vectors between the reference points of the co-located VLBI, GNSS, S/LLR and DORIS equipment at HartRAO had been determined by terrestrial or GPS surveys from time to time, with the last full co-location survey being conducted in February of 2014 with an accuracy at the millimetre level. With a view to new GGOS requirements for the local tie being performed "with 0.1 mm accuracy, in a fully automated way and on an almost continuous basis" (Rothacher *et al.*, 2009), a local automated site tie system for continuous monitoring of vector ties is currently being implemented and tested at HartRAO. This will contribute significantly to improving the local ties between the various techniques on site.

The planned measurement system is to consist of one Leica MS50 Multistation mounted on a permanent reference pier (currently under test, see Figure 7.1) as well as an additional Leica MS50 Multistation to be installed on the roof of the HartRAO control room. The planned reference network is to consist of the on-site GNSS stations – HRAO IGS GNSS reference station as well as the European Space Agency (ESA), German Aerospace Centre (DLR) and Russian GNSS stations being hosted at HartRAO – to tie the measurement system in with GNSS observations to link it to the ITRF (see Figure 7.20). Measurements to these GNSS reference stations, the HartRAO antennas, the NASA and Roscosmos SLRs as well as to various reference piers will be performed on a regular basis towards fully automating the system.

Figure 7.20 Planned VLBI local tie observing system at HartRAO – components of measurement and reference network. Photo credit: R. Botha.

The HartRAO 26 m, 15 m and VGOS antennas will form part of these local tie measurements in due course. Measurements are to be made to prisms installed on the HartRAO 26 m and 15 m antennas and reference network first. It is intended to mount the targets on both the 26 m and 15 m antennas on-axis where possible. Targets on the 26 m antenna are to consist of prisms mounted on each of the east and west ends of the declination shaft as well as at the south end of the polar shaft (see Figure 7.13 and Figure 7.22 (a)). The north end of the polar shaft is obscured by the bearing housing, requiring the design of special adapters to mount prisms at this end. On the 15 m antenna, it is possible to mount a prism at the west end of the elevation shaft. The east end of the elevation shaft is obscured by the elevation cable wrap. Again, either special adapters will have to be designed to mount the prisms, or prisms will have to be mounted off-axis at this end (Figure 7.22 (b)). Similarly for the 15 m antenna's azimuth axis, which is not accessible for the placement of on-axis prisms. Any existing targets on the antenna's structure will also be employed. Targets will be measured by the two total stations, simultaneously, for various positions of the primary and secondary axes respectively. For antennas with intersecting rotation axes, it is relatively straightforward to determine the VLBI reference point. However, the rotation axes of the HartRAO 26 m polar-mount and 15 m az-el mount antennas do not intersect but an antenna axis offset (AO) exists for each of the antennas. For the 26 m antenna, the VLBI reference point is represented by the intersection of the fixed HA axis with the perpendicular plane containing the moving Dec axis. For the 15 m antenna, the VLBI reference point is represented by the intersection of the fixed azimuth axis with the perpendicular plane containing the moving elevation axis.

Department of Geology, Geoinformatics and Meteorology
University of Pretoria

(a) (b)

Figure 7.13 (a) Targets consisting of a combination of Leica prisms and custom-made adapters. (b) Prism combination mounted at south end of 26 m polar shaft acquired by the Leica MS50 Multistation. Photo credit: R. Botha.

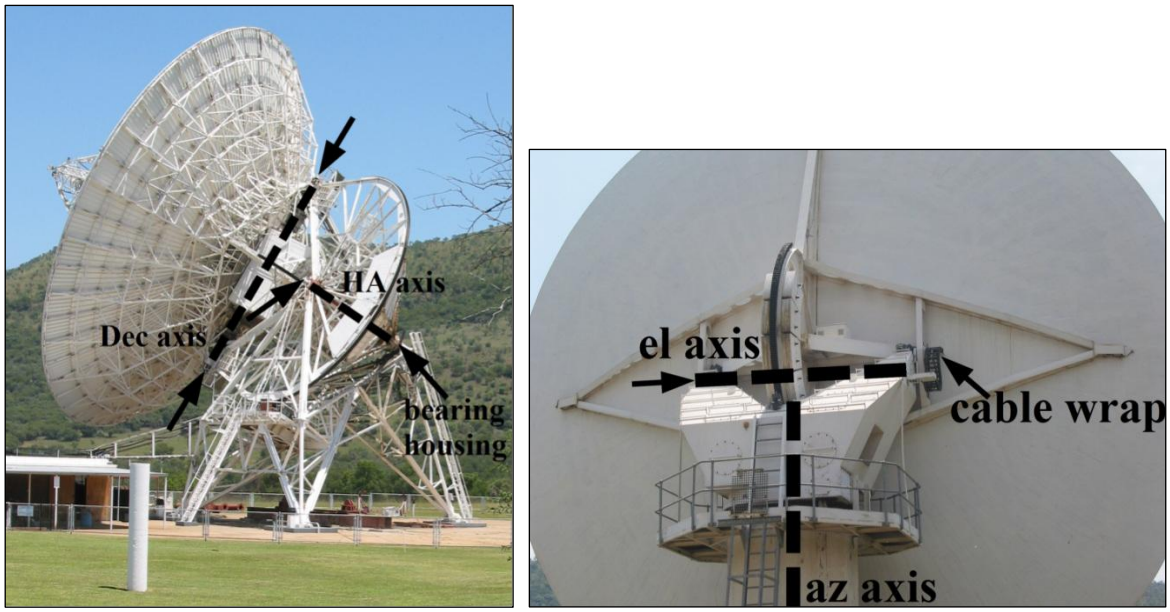

(a) (b)

Figure 7.22 (a) HartRAO 26 m polar mount antenna – rotation axes and on-axis prism mounting points on declination (Dec) shaft (top and bottom arrows) and at south end of polar shaft (arrow in middle). The north end of the polar shaft is obscured by the bearing housing (arrow on right). (b) HartRAO 15 m azimuth-elevation (az-el) mount antenna – rotation axes and on-axis prism mounting point at west end of elevation shaft (arrow on left). The east end of the elevation shaft is obscured by the cable wrap (arrow on right).

In addition to the daily measurement of various targets in the measurement and reference network by the automated total station, which will include the continuous measurement of the VLBI reference points of all the HartRAO antennas, it is envisaged that the local tie and SBL experiments will be conducted on a monthly basis. Measurement of VLBI reference points / station coordinates, baseline lengths and antenna Aos, obtained by conventional survey with the total station, will be compared with VLBI determined values from the SBL sessions. An error budget will be drawn up for the short baseline ties. Station-specific errors will be investigated with a view to eliminating or reducing these errors in order to improve the accuracy of VLBI results. The automated total station could additionally be used to investigate deformation of the HartRAO antennas.

7.4 SUMMARY

In order to meet the GGOS/VGOS goal of 1 mm accuracy on global baselines, the baseline length between co-located antennas have to be known with sub-millimetre accuracy. The VLBI reference points of the HartRAO 15 m antenna and soon to become operational VGOS antenna need to be tied accurately to that of the HartRAO 26 m legacy antenna. The most accurate method of determining the local tie is by terrestrial survey, but as such surveys are conducted infrequently, it is important to establish whether the local tie vector can be determined with the required accuracy in VLBI analysis. To this end, SBL experiments were conducted, in which the same sources were observed simultaneously by the HartRAO 26 m and 15- antennas, in order to ascertain whether the global baseline length accuracy requirements of GGOS/VGOS could be achieved on such a short baseline at least. The SBL sessions were scheduled and analysed with VieVS and the estimated baseline components and baseline lengths were compared with corresponding values determined in the 2014 co-location survey as well as with the *a priori* baseline length value and with VieVS estimated and IVSCC baseline length values for dual global sessions in which both the HartRAO antennas participated. In the comparison of the average values of the VieVS estimated HARTRAO-HART15M baseline length from the dual global sessions and SBL experiments with *a priori* and ground survey baseline length values as well as with the average value provided by the IVSCC for the dual global sessions' baseline lengths, all these investigations' values agreed within the formal error with each other.

Regarding seasonal variation in the HARTRAO-HART15M baseline length, average values of the VieVS estimated baseline lengths for corresponding seasonal groupings of the dual global sessions and SBL experiments agreed within the formal error with each other and with all other investigations' values, except for the average value of the VieVS estimated baseline length for the dual global sessions of autumn, which failed to agree within the formal error with the *a priori* value. It was not possible to discern any specific trend in the variation of the HARTRAO-HART15M baseline length according to season. The VieVS estimated baseline length values for the SBL experiments and the dual global sessions agreed with the ground survey value (taken as the more accurate) at sub-centimetre level. The required sub-millimetre accuracy could therefore not be reached in the VLBI analysis, even for the short baseline. The implementation of an automated site tie system at HartRAO should improve the local tie significantly. It will allow for continuous measurement of the HartRAO antennas' VLBI reference points and also for continuous and simultaneous comparison of results from SBL sessions with the ground survey results.

CHAPTER 8 CONCLUSIONS AND RECOMMENDATIONS

In this study, error sources specific to the HartRAO site were identified, and their effect on the accuracy of HartRAO 26 m and 15 m antenna parameters and the local tie between the antennas, and thus on the accuracy of astrometric and geodetic VLBI results used in the realisation of the ICRF and determination of the ITRF, was investigated. The quality of HartRAO surface meteorological data used for astrometric and geodetic VLBI and single-dish calibration purposes was assessed. The HartRAO 26 m antenna's pointing performance and gain at 22 GHz were investigated. The antenna axis offset (AO) of the HartRAO antennas and baseline length between the antennas were estimated in VLBI analysis and compared with ground survey values, in order to determine whether GGOS/VGOS accuracy requirements could be met in the VLBI analysis. The findings, recommendations and conclusions of these investigations are as follows:

8.1 ANSWERING RESEARCH QUESTIONS AND ACHIEVEMENT OF AIMS

- ***Research question 1 – HartRAO error sources:***
  a) Which station-specific error sources are possibly corrupting the VLBI delay observable at HartRAO?
  b) What course of action is required to reduce the size of the errors involved?

Several possible sources of error were identified by consulting with HartRAO Engineering, Operations and astronomers as well as by taking IVS requirements into consideration. Sources of error related to HartRAO meteorological data, antenna calibration and pointing, antenna AO and the local tie between the 26 m and 15 m antennas

were addressed in this study and possible courses of action to mitigate these sources of error were suggested (see individual chapters and Section 8.3 Recommendations). *Research question 1* was therefore answered and *Objective 1* achieved.

- ***Research question 2 – HartRAO weather data:***
  a) What is the state of HartRAO's *in situ* meteorological surface sensors?
  b) What is the quality of meteorological data used in astrometric/geodetic VLBI and single-dish calibration?

It was found that the HartRAO meteorological (*wx*) sensors have not been calibrated or upgraded for the past 10 years and are providing inaccurate measurements of ambient temperature, barometric pressure and relative humidity. For geodetic VLBI observations, errors in the surface measurements of barometric pressure for determining troposphere delay, and ambient temperature for determining antenna thermal deformation, result in errors in the estimated station height and variation in the VLBI reference point, respectively. For astrometric VLBI observations, errors in the surface measurements of relative humidity and temperature additionally result in errors in the opacity correction applied in gain calibration observations at 22 GHz on the HartRAO 26 m antenna, and thus to incorrect antenna gain and point source sensitivity (PSS) and, ultimately, incorrect source flux density. Degraded meteorological surface data could therefore be considered as a station-specific error source at HartRAO. *Research question 2* was thereby answered and *Objective 2* achieved.

- ***Research question 3 – Antenna calibration and pointing:***
  a) What is the HartRAO 26 m antenna's pointing performance and gain at 22 GHz?
  b) Could there be a correlation between degraded declination pointing and differential heating of the support structure?

It was found that the 26 m antenna is not able to attain the pointing accuracy required for southern CRF realisation. In the gain calibration observations, strong coma sidelobes, caused by gravitational deformation of the dish, appeared even at high elevations where gravitational distortion of the dish surface should be reduced. Second coma sidelobes also

appeared in one of the observation sets. This is indicative of the 26 m antenna not being able to attain the required dish surface accuracy at 22 GHz. The Dec pointing correction proved unreliable at lower elevations and unable to provide an improvement to the gain curve. The gain curve displayed asymmetry. The antenna gain was much reduced in the 2021 observations which could possibly be ascribed to a faulty 22 GHz receiver. The investigation into a possible correlation between the degraded Dec pointing and differential heating of the antenna support structure, as determined from temperature measurements by sensors mounted on the structure, revealed a possible correlation between the Dec pointing degrading at sunrise and differential heating of beams on the north and south sides of the antenna. Degraded declination pointing and differential heating of the support structure could be contributing to the 26 m antenna's poor pointing accuracy and could therefore be considered as station-specific error sources at HartRAO. *Research question 3* was thereby answered and *Objective 3* achieved.

- ***Research question 4 – Antenna axis offset:***
  a) What are the values estimated in VLBI analysis for the AO of the HartRAO 26 m antenna, before bearing failure and after bearing replacement, as well as for the 15 m antenna?
  b) How do these estimated values compare with values measured in the most recent ground survey?
  c) Are GGOS accuracy goals achievable with the estimation of AO in VLBI analysis?
  d) Is there any seasonal variation in AO?
  e) What is the effect of the axis offset altitude correction (AOAC) on the estimated AO of the HartRAO 26- antenna?

It was established that the VLBI estimated values do not agree within the formal error with ground survey values, and the sub-millimetre accuracy in AO required for meeting the GGOS/VGOS goal of 1 mm accuracy in station coordinates could therefore not be reached. The antenna AO values estimated with VieVS for the HartRAO 26 m and 15 m antennas did not agree within the formal error with the values determined in a 2014 co-location survey. Although there was close agreement between the *a priori* AO value (2003 ground survey value) and the 2014 ground survey value for the 26 m antenna, the *a priori* AO

value (2007 GPS survey value) for the 15 m antenna and the 2014 ground survey value differed by ~5 mm. For the VieVS estimated AO values of 26 m antenna, there appeared to be a significant change from before bearing failure to after bearing replacement, but this was not reflected in the corresponding ground survey values nor in the AO estimated in the 30-session groupings before bearing failure and after bearing replacement. For the 15 m antenna, although the estimated AO value agreed within the formal error with the value determined in a 2007 GPS survey, it differed by ~5 mm from the value determined in the 2014 co-location survey. The formal error of the AO value measured in the GPS survey is unknown, but it should be at the several millimetre level (~2–3 mm), therefore the VieVS estimated AO value could ultimately be in agreement with the 2014 co-location survey AO value within the formal error. Regarding possible seasonal variation in the estimated AO, although the AO differed between the various seasonal groupings, it also differed in a contradictory manner between corresponding seasons in the various session groupings and between corresponding seasons for the 26 m and 15 m antennas. No trend could thus be detected in AO variation according to season. The AOAC had a negligible effect on the estimated AO and station coordinates of the HartRAO 26 m antenna as well as on the coordinates of other antennas. This is not what was expected as the theoretical model predicts a change of 1-2 cm in the slant troposphere delay. *Research question 4* was thereby answered and *Objective 4* achieved.

- ***Research question 5 – Baseline length and local tie:***
  a) What is the value estimated in VLBI analysis for the baseline length between the HartRAO 26 m and 15 m antennas?
  b) How does the estimated value compare with the value measured in the most recent ground survey?
  c) Are GGOS accuracy goals achievable with the estimation of the local tie and baseline length in VLBI analysis?
  d) Is there any seasonal variation detectable in baseline length?

It was established that the VLBI estimated values agree within the formal error with the ground survey value but at sub-centimetre level only. The required sub-millimetre accuracy in baseline length required for meeting the GGOS/VGOS goal of 1 mm accuracy

on global baselines could therefore not be reached, not even on the short ~113 m baseline between the two HartRAO antennas. Several station-specific error sources could have affected the accuracy of the results obtained in the VLBI analysis. Gravitational deformation models do not exist for either of the HartRAO antennas and could thus not be applied in the VLBI analysis. Degraded *in situ* meteorological data and the lack of an accurate tropospheric tie between the antennas would have an impact on the tropospheric delay and thermal deformation models applied in the VLBI analysis. Differential local motions due to possible groundwater seepage at the 15 m antenna foundation, for example, would have affected the *a priori* station coordinates used in the VLBI analysis. Uncalibrated instrumental delay variations due to manual phase calibration having been applied for the 26 m antenna, a lack of a cable calibration system on 15 m antenna and possible dependence of delay on antenna orientation, would have an effect on the instrumental calibration corrections applied in the VLBI analysis. Thermal deformation and a common reference temperature were applied in the local tie survey. Regarding possible seasonal variation in the estimated baseline length, with the small number of both dual and short baseline (SBL) sessions per seasonal grouping and the want of seasonal overlap for the SBL sessions, no seasonal trend could be detected in baseline length variation in comparison of the SBL and dual global sessions' seasonal groupings. *Research question 5* was thereby answered and *Objective 5* achieved.

In answering the *Research questions* and achieving the *Objectives* set for this study, the *aims* of this study – (1) to identify HartRAO station-specific error sources degrading astrometric and geodetic VLBI results, and to suggest a course of action to mitigate these sources of error towards meeting GGOS accuracy requirements and improving ITRF and ICRF realisation; and (2) to determine whether the AO of the HartRAO 26 m and 15 m antennas as well as the local tie between the two antennas could be estimated in VLBI analysis in accordance with GGOS accuracy requirements – were met.

8.2 RECOMMENDATIONS AND FUTURE RESEARCH

- ***HartRAO weather data*:**

It is imperative that the current HartRAO meteorological (*wx*) sensors be calibrated and/or upgraded or replaced. In the interim, a comparison campaign will be conducted in which data from the new Paroscientific MET4 unit will be compared with *wx* sensor data for an extended period of time, as well as with data from the meteorological systems of the co-located space geodetic techniques on-site. The MET4 unit will be installed next to each of the meteorological systems at barometer height. The MET4 unit will eventually be installed at the VLBI reference height of the VGOS antenna in combination with rainfall and wind sensors as well as a pyranometer. High-accuracy pressure sensors will be installed as close to the VLBI reference heights of the 26 m and 15 m antennas as possible. Installation of meteorological systems will be carried out in accordance with WMO CIMO guidelines, and tropospheric ties will be performed for all meteorological systems on-site.

- ***Antenna calibration and pointing*:**

The coma sidelobes, widely scattered Dec pointing correction at lower elevations as well as the asymmetry displayed in the antenna gain curve, all require further investigation. Even longer drift scan observations, beyond the second nulls, should be conducted to ensure a proper baseline fit. The frequency-dependence of the coma sidelobes will be further explored by conducting gain curve observations at the top and bottom of the 22 GHz receiver band. A comprehensive amplitude calibration of the HartRAO 26 m antenna must be conducted to assess whether the 22 GHz receiver is performing optimally and to identify required improvements. This would entail calibration of noise diodes and measurement of noise diode calibration temperatures (Tcal), measurement of total power integration (TPI), measurement of degrees-per-flux-unit (DPFU) and gain as well as measurement of system temperature (Tsys) and system-equivalent flux density (SEFD). The possible correlation between degraded pointing and sunrise requires future 22 GHz gain curve observations to be conducted at night when the pointing is stable. It would then be possible to determine whether the degraded pointing is indeed caused by differential heating of the antenna structure or rather by unrelated effects. The HartRAO 26 m antenna

pointing accuracy is affected by various error budget contributors. Pointing accuracy is affected by the surface accuracy of the primary reflector and sub-reflector as well as positioning and alignment of the reflectors, quadrupod, feed and antenna axes. Distortions, deformations and deflections of the reflectors, quadrupod, feed and antenna structure caused by thermal/gravitational deformation degrade pointing accuracy. A holography campaign is required to determine the 26 m antenna's surface accuracy and to probe suspected panel as well as primary reflector, sub-reflector and feed misalignments. A suspected gravitational deflection of the sub-reflector relative to the primary reflector and its focus requires further examination, possibly by making use of a camera/laser setup. Thermal deformation of the antenna needs to be analysed and a gravitational deformation survey should be conducted in order that the appropriate models may be constructed. The failed bearing on the 26 m antenna's declination shaft is not only prohibiting installation of higher resolution encoders, but its movement may also be contributing to pointing errors. The current encoders provide insufficient resolution to reach K-band pointing tolerance, delivering a pointing resolution of 5 arcsec compared to the 0.15 arcsec that would be possible with the new encoders. Spot calibrator measurements indicate that K-band pointing may sometimes be off by up to a quarter of a half-power beamwidth (J. Quick, personal communication, 27 August 2019). One of the highest priorities for the HartRAO 26 m antenna, is to update the current pointing model. The pointing model can however only be updated once the bearing has been replaced and the new encoders have been installed. Atmospheric refraction correction as well as seasonal Dec and HA diurnal pointing offset models, incorporated into the antenna's pointing model, are currently also under review. Due to the presence of the water vapour line at 22 GHz, system (noise) temperatures show an increase at K-band, and observations become more susceptible to degradation from inclement weather. The opacity corrections applied to the observations can be improved by making use of near real-time estimates of PWV over HartRAO.

- ***Antenna axis offset:***

An automated Total Station is currently being implemented at HartRAO. It will support continuous measurement of the AOs and VLBI reference points of the HartRAO antennas, and should contribute significantly to investigation of the possible correlation of antenna

AO with station position, tropospheric delay, clock parameters, structural deformation, hydrology loading *etc*. In a synthesis network, containing both VLBI and continuous automated Total Station measurements, one should be able to identify technique dependent parameters that adversely affect the accuracy of either VLBI or Total Station measurements. It is intended to repeat the tests for the AOAC in the NASA JPL VLBI modelling and analysis software "MODEST" (Sovers, Fanselow, and Jacobs, 1998) for comparison with the VieVS results. It is clear that the VLBI technique has the potential to solve for AO to a high degree of accuracy, however it is also clear that there is room for improvement, further work should therefore be done on improving AO modelling within VieVS (L. Combrinck, personal communication, 21 July 2022).

- ***Baseline length and local tie*:**

The SBL experiments provide an opportunity to build an error budget for short baseline ties between the HartRAO antennas (including the newly built VGOS antenna in future) and to improve our understanding of the HartRAO complex. Running off the same clock under the same atmosphere from the same location allows most geophysical and atmospheric effects to mostly cancel in common mode on the short baseline. These experiments thus provide a laboratory for investigating VLBI instrumental effects, antenna structure, local ground motions and tropospheric effects, thereby allowing for the discovery of station-specific errors (Plank, 2014). Conducting these SBL experiments on a regular basis would allow for discovering any seasonal effects. It should also be possible to determine if there are any changes in AO, VLBI reference point and antenna position due to the failing bearing on the 26 m antenna by running the local tie sessions between the 26 m and 15 m antennas before and after bearing replacement. The newly built VGOS antenna also needs to be accurately tied to the aging 26 m and 15 m antennas as soon as possible. Once it has been furnished with receivers and become operational, it will be included in the SBL sessions. Together with the automated total station being implemented for continuous monitoring of vector ties at HartRAO, it should then be possible to isolate issues to a specific antenna in this local three-antenna network and improve the accuracy of the SBL experiments for local tie measurement.

8.3 CONCLUSION

It is apparent that site-specific error sources are adversely affecting HartRAO's ability to meet the more demanding GGOS/VGOS accuracy requirements and continued contribution to ICRF realisation and ITRF determination. It is also evident that the antenna AO and local tie cannot be determined in VLBI analysis with the same high accuracy as that achievable by ground survey measurements, yet. The implementation of an automated total station for continuous measurement of the VLBI reference points, AO and local tie is therefore of paramount importance, especially with a view to imminent VGOS operations at HartRAO, but also to investigate correlation of AO with various station-based effects towards improvement of the AO model used in the VLBI analysis. The operation of the automated Total Station, together with ground surveys, meteorological monitoring and VLBI solutions, will continue at HartRAO to build up a time series of data that will allow site-specific errors to be minimised or eliminated over time. Temporal studies of site-specific error sources, such as ground subsidence, antenna deformation, tropospheric and ionospheric delay and station clock bias, will contribute to more accurate VLBI results able to meet GGOS accuracy demands. The next step is to draw up a comprehensive error budget and plan of action in consultation with HartRAO Science, Engineering and Operations and the wider IVS community towards disentangling the various effects, identifying all possible error budget contributors, and prioritising their investigation and mitigation according to their contribution to the error budget where practically possible.

REFERENCES

Altamimi, Z., P. Rebischung, L. Metivier & Collilieux, X. (2016). ITRF2014: A new release of the International Terrestrial Reference Frame modeling nonlinear station motions. *Journal of Geophysical Research (Solid Earth)*, **121**:6109-6131 pp. DOI:10.1002/2016JB013098

Altamimi, Z., Rebischung, P., Collilieux, X., Metivier, L. & Chanard, K. (2022). ITRF2020: main results and key performance indicators. *EGU General Assembly 2022*. Vienna, May 2022. EGU22-3958. DOI:10.5194/egusphere-egu22-3958

Angermann, D., Seitz, M. & Drewes, H. (2013). Global terrestrial reference systems and their realizations. *Sciences of Geodesy II, Innovations and Future Developments*. Heidelberg: Springer-Verlag. 97–132 pp. G, Xu. (ed.). DOI: 10.1007/978-3-642-28000-9_3

Artz, T., Springer, A & Nothnagel A. (2014). A complete VLBI delay model for deforming radio telescopes: the Effelsberg case. *Journal of Geodesy*, **88**(12):1145–1161 pp. DOI: 10.1007/s00190-014-0749-1

Behrend, D., Thomas, C., Gipson, J., Himwich, E. & Le Bail, K. (2020). On the organization of CONT17. *Journal of Geodesy*, **94**. 100 p. DOI: 10.1007/s00190-020-01436-x

Behrend, D. (2021). VGOS Observing in 2022. *IVS Newsletter*, 61. December 2021. https://ivscc.gsfc.nasa.gov/publications/newsletter/issue61.pdf [Accessed 29 August 2022].

Bester, R. (2007). *Measurement Results for the Integrated KAT Antenna Structure. KAT7200PR1003*, iss. 1. November 2007. KAT7200PR1003_MeasurementResults_Issue1.

Bizouard, C., Lambert, D., Gattano, C., Becker, O. & Richard, J-Y. (2019). The IERS EOP 14C04 solution for Earth Orientation Parameters consistent with ITRF 2014. *Journal of Geodesy*, **93**(5):621-633 pp. DOI:10.1007/s00190-018-1186-3

Böhm, J., Böhm, S., Boisits, J., Girdiuk, A., Gruber, J., Hellerschmied, A., Krásná, H., Landskron, D., Madzak, M., Mayer, D., McCallum, J., McCallum, L., Schartner, M., Teke, K. (2018). Vienna VLBI and Satellite Software (VieVS) for geodesy and astrometry, *Publications of the Astronomical Society of the Pacific*, **130**(986): 044503. DOI:10.1088/1538-3873/aaa22b

Böhm, S., Böhm, J., Gruber, J., Kern, L., McCallum, J., McCallum, L., McCarthy, T., Quick, J.F.H. & Schartner, M. (2022). Probing a Southern Hemisphere VLBI Intensive baseline configuration for UT1 determination. *Earth, Planets and Space*, **74**:118. DOI: 10.1186/s40623-022-01671-w

Capitaine, N., Wallace, P.T. & Chapront, J. (2003). Expressions for IAU 2000 precession quantities. *Astronomy and Astrophysics*, 412(2):567-586 pp. DOI: 10.1051/0004-6361:20031539

Charlot, P., Jacobs, C.S., Gordon, D., Lambert, S., de Witt, A., Böhm, J., Fey, A.L., Heinkelmann, R., Skurikhina, E., Titov, O., Arias, E.F., Bolotin, S., Bourda, G., Ma, C., Malkin, Z., Nothnagel, A., Mayer, D., MacMillan, D.S., Nilsson, T., Gaume, R. (2020). The third realization of the International Celestial Reference Frame by Very Long Baseline Interferometry. *Astronomy and Astrophysics*, **644**: A159. DOI: 10.1051/0004-6361/202038368

Clark, T.A. & Thomsen, P. (1988). Deformations in VLBI antennas. *NASA Technical Memorandum*, 100696, NASA, Greenbelt. NASA-TM100696.

Combrinck, W.L. & Merry, C.L. (1997). Very Long Baseline Interferometry antenna axis offset and intersection determination using GPS. *Journal of Geophysical Research*, **102**(B11): 24741–24744 pp. DOI: 10.1029/97JB02081

Combrinck, W.L. & Schmidt, M. (1998). Physical site specifications: geodetic site monumentation. *Proceedings of the IGS Network Workshop*. Annapolis USA, November 1998, 91-107 pp. C.E. Noll, K.T. Gowey and V. Neilan, (eds.).

Combrinck, W.L. & Combrink, A.Z.A. (2004). Proposed new international space geodesy facility for southern Africa. *35th COSPAR Scientific Assembly*. 270 p. Paris, France. 18-25 July 2004.

Combrinck, W.L., Botha, R.C., Mey, P., de Witt, A. & Quick, J.F.H. (2015). Contributions of HartRAO to space geodesy, astrometry and related disciplines. *Proceedings of the 22nd European VLBI Group for Geodesy and Astrometry Working Meeting*. Ponta Delgada, Azores. 18-21 May 2015. 85-89 pp. DOI: 10.13140/RG.2.1.3897.8002

Combrink, A.Z.A., Combrinck, W.L. & Moraal, H. (2004). Near real-time detection of atmospheric water vapour using the SADC GPS network. *South African Journal of Science*, 100. September/October 2004. Review Articles, 436-442 pp.

Committee on the National Requirements for Precision Geodetic Infrastructure; Committee on Seismology and Geodynamics; National Research Council. (2010). *Precise geodetic infrastructure: national requirements for shared resources*. Washington DC: National Academic Press.

De Witt, A. (2014). Completing the K-band Celestial Reference Frame in the Southern Hemisphere. *IVS 2014 General Meeting Proceedings "VGOS: The New VLBI Network"*, Beijing, China: Science Press. 433-437 pp. D. Behrend, K.D. Baver and K.L. Armstrong (eds.).

De Witt, A., Charlot, P., Gordon, D. & Jacobs, C.S. (2022). Overview and status of the International Celestial Reference Frame as realized by VLBI. *Universe* 2022, **8**: 374. DOI: 10.3390/universe8070374

Desai, S.D. (2002). Observing the pole tide with satellite altimetry. *Journal of Geophysical Research (Oceans)*, **107**(C11), 3186, 7-1-1-13. DOI: 10.1029/2001JC001224

Egbert, G.D. & Erofeeva, S.Y. (2002). Efficient inverse modeling of barotropic ocean tides. *Journal of Atmospheric and Oceanic Technology*, **19**(2): 193-204 pp. DOI: 10.1175/1520-0426(2002)019<0183:EIMOBO>2.0.CO;2

Eisenträger, P., Herold, S. & Hartmann, S. (2016). Structural analysis: VGOS South Africa. *MT Mechatronics GmbH*. Document number, 163461.4230-4430 SPEC AZ EL Getriebe R00.

Eisenträger, P., Herold, S. & Kreth, S. (2017). Performance analysis: VGOS telescope. *MT Mechatronics GmbH*. Document number, VLBI-D-REP-0000-004.

Eubanks, T.M. (1991). A consensus model for relativistic effects in geodetic VLBI. *Proceedings of the U.S. Naval Observatory Workshop on Relativistic Models for Use in Space Geodesy*. U.S. Naval Observatory Washington D.C. 20392-5100, U.S.A., 60-82 pp. T.M. Eubanks (ed.).

Folkner, W.M., Williams, J.G. & Boggs, D.H. (2009). *The Planetary and Lunar Ephemeris DE 421*. *IPN Progress Report*. 42-178 pp. https://ipnpr.jpl.nasa.gov/progress_report/42-178/178C.pdf [Accessed 29 August 2022].

Gaylard, M. (2011) *Radio astronomy sensitivity with a single-dish radio telescope. Hartebeesthoek Radio Astronomy Observatory*. HartRAO. April 26, 2011.

Gipson, J. (2018). Sked: VLBI Scheduling Software. NASA Goddard Spaceflight Centre. October 12, 2018. https://ivscc.gsfc.nasa.gov/IVS_AC/sked_cat/SkedManual_v2018October12.pdf [Accessed 29 August 2022].

Gipson, J. (2020). IVS Contribution to ITRF2020. *IVS Newsletter*, 58. December 2020. https://ivscc.gsfc.nasa.gov/publications/newsletter/issue58.pdf [Accessed 29 August 2022].

Global Geodetic Observing System (GGOS). (2022). GGOS Core Sites. https://ggos.org/item/ggos-core-sites/ [Accessed 29 August 2022].

Gross, R., Beutler, G. & Plag, H.-P. (2009). Integrated scientific and societal user requirements and functional specifications for the GGOS. *Global Geodetic Observing System*. Springer, Berlin, Heidelberg, 209-224 pp. H.-P. Plag and M. Pearlman M. (eds.). DOI: 10.1007/978-3-642-02687-4_7

Gruber, J., Jaron, F., Nothnagel, A. & Böhm, J. (2021). Vienna correlation center report 2019-2020. *International VLBI Service for Geodesy and Astrometry 2019+2020 Biennial Report, NASA-TP-20210021389.* 164-167 pp. D. Behrend, K.D. Baver and K.L. Armstrong (eds.).

Hartebeesthoek Radio Astronomy Observatory (HartRAO). (n.d.). HartRAO 15m Radio Telescope Details: Coordinates. http://www.hartrao.ac.za/ht15m_factsfile.html [Accessed 29 August 2022].

Heinkelmann, R., Böhm, J., & Schuh, H. (2005). Homogenization of surface pressure recordings and its impact on long-term series of VLBI tropospheric parameters. *EVGA 2005 Working Meeting.* 74-79 pp.

Himwich, E., Van den Berg, N., Gonzalez, R., & Holmström, C. (2003). New developments in the NASA Field System. *New technologies in VLBI, Proceedings of a symposium of the International VLBI Service for Geodesy and Astrometry*. Gyeong-ju, Korea. November 5-8, 2002. ASP Conference Series, 306. Astronomical Society of the Pacific.193–198 pp.

Holland-Muter & Associates CC. (2006). *Engineering geological investigation for the Hartebeesthoek radio telescope foundations*. *Report no: LM 647/06.* September 2006.

Institut Géographique National Direction de la Production Service de Géodésie et de Nivellement (IGN). (2005). Hartebeesthoek co-location survey: reports and results. *RT/G 61*. https://itrf.ign.fr/doc_ITRF/hartebeesthoek_Co-location_Survey_v3.pdf [Accessed 29 August 2022].

International Earth Rotation and Reference Systems Service (IERS). (2005). Recommendations. *Proceedings of the IERS Workshop on site Co-location*. *IERS Technical Note, 33.* Matera. October 2003. Verlag des Bundesamts für Kartegrophie und Geodäsie. Frankfurt am Main. https://www.iers.org/shareddocs/publikationen/EN/IERS/publications/tn/TechnNote33/tn33.pdf [Accessed 29 August 2022].

International Earth Rotation and Reference Systems Service (IERS). (2010). IERS Conventions 2010. *IERS Technical Note, 36*. Frankfurt am Main: Verlag des Bundesamts für Kartographie und Geodäsie, 179 pp. G. Petit and B. Luzum (eds.).

International VLBI Service for Geodesy and Astrometry (IVS). (2019). Surveys of radio telescopes for modeling of gravitational deformation. *IVS Resolution 2019-0. IVS-Res-2019-01*. https://ivscc.gsfc.nasa.gov/about/resolutions/IVS-Res-2019-01-TelescopeSurveys.pdf [Accessed 29 August 2022].

International VLBI Service for Geodesy and Astrometry (IVS). (2021a). Continuous recording and submission of meteorological and clock offset data. *IVS Resolution 2021-01*. https://ivscc.gsfc.nasa.gov/about/resolutions/IVS-Res-2021-01-Met-n-Clock.pdf [Accessed 29 August 2022].

International VLBI Service for Geodesy and Astrometry (IVS). (2021b). Monitoring of critical telescope parameters. *IVS-Res-2021-02, 2021*. https://ivscc.gsfc.nasa.gov/about/resolutions/IVS-Res-2021-02-MonitorAntPar.pdf [Accessed 29 August 2022].

International VLBI Service for Geodesy & Astrometry (IVS). (2022). International VLBI Service for Geodesy & Astrometry. https://ivscc.gsfc.nasa.gov [Accessed 29 August 2022].

Jacobs, C.S., García-Miró, C., Horiuchi, S. & Snedeker, L.G. (2017). Twin telescope tests: assessing station oriented systematic errors. *Proceedings of the 23rd European VLBI Group for Geodesy and Astrometry Working Meeting*. May 2017, Gothenburg, Sweden, 226-230 pp. R. Haas and G. Elgered (eds.).

Klein, B. (2008). Holographic Measurement of the 26m HartRAO Telescope. *A dissertation submitted to the Faculty of Engineering and the Built Environment, University of the Witwatersrand, Johannesburg.* In fulfilment of the requirements for the degree of Master of Science in Engineering.

Kleinhans, I. (2002). A critical appraisal of regional geotechnical mapping in South Africa. *A dissertation submitted to the University of Pretoria, South Africa.* In fulfilment of the requirements for the degree of Master's degree.

Koch, K-R. (1999). *Parameter estimation and hypothesis testing in linear models.* Berlin, Heidelberg: Springer. DOI: 10.1007/978-3-662-03976-2

Kotary, N. (2021). T2++ Countdown! *IVS Newsletter*, 59. April 2021. https://ivscc.gsfc.nasa.gov/publications/newsletter/issue59.pdf [Accessed 29 August 2022].

Krásná, H., Nickola, M. & Böhm, J. (2014). Axis offset estimation of VLBI telescopes. *IVS 2014 General Meeting Proceedings "VGOS: The New VLBI Network*". Beijing, China: Science Press, 339-343 pp. D. Behrend, K.D. Baver and K.L. Armstrong (eds.).

Kurdubov, S. & Skurikhina, E. (2010). Antenna axis offset estimation from VLBI. *IVS 2010 General Meeting Proceedings*. Greenbelt, MD: NASA. 247–250 pp. D. Behrend, K.D. Baver & K. Armstrong (eds.).

Landskron, D. & Böhm, J. (2018). Refined discrete and empirical horizontal gradients in VLBI analysis. *Journal of Geodesy*, **92**: 1387-1399 pp. DOI: 10.1007/s00190-018-1127-1

Lösler, M., Haas, R. & Eschelbach, C. (2019). Gravitational deformation of ring-focus antennas for VGOS – First investigations at the Onsala Twin Telescopes project. *Journal of Geodesy,* **93**:2069-2087 pp. DOI:10.1007/s00190-019-01302-5

Lyard, F., Lefevre, F., Letellier, T. & Francis, O. (2006). Modelling the global ocean tides: modern insights from FES2004. *Ocean Dynamics*, **56**(5-6): 394–415 pp. DOI: 10.1007/s10236-006-0086-x

Madzak, M., Böhm, J., Böhm, S., Krásná, H., Nilsson, T., Plank, L., Tierno Ros, C., Schuh, H., Soja, B., Sun, J. & Teke, K. (2013). Vienna VLBI software – current release and plans for the future. *21st Meeting of the European VLBI Group for Geodesy and Astronomy.* Espoo, Finland. March 5-8, 2013. Zubko and M. Poutanen (eds.). https://www.oso.chalmers.se/evga/21_EVGA_2013_Espoo.pdf [Accessed 29 August 2022].

Mathews, P.M., Herring, T.A. & Buffett, B.A. (2002). Modeling of nutation and precession: New nutation series for nonrigid Earth and insights into the Earth's interior. *Journal of Geophysical Research*, **107**(B4, 3186). DOI: 10.1029/2001JB000390

Mayer, D., Böhm, J., Combrinck, W.L., Botai, J. & Böhm, S. (2014). Importance of the Hartebeesthoek Radio Astronomy Observatory for the VLBI network. *Acta Geodaetica et Geophysica*, **49**(3):313-325 pp. DOI: 10.1007/s40328-014-0063-7

Muller, J.-M., Pesce, D. & Collilieux, X. (2020). Hartebeesthoek co-location survey reprocessing report. *IGN Service de Géodésie et de Métrologie*, 2020.

Munghemezulu, C., Combrinck, W.L., Mayer, D. & Botai, O.J. (2014). Comparison of site velocities derived from collocated GPS, VLBI and SLR techniques at the Hartebeesthoek Radio Astronomy Observatory (comparison of site velocities). *Journal of Geophysical Science,* **4**:1-7 pp. De Gruyter Open. DOI:10.2478/jogs-2014-0002

Munghemezulu, C, Combrinck, W.L, Botai, J. & Quick, J.F.H. (2016). Analysis of the performance of hydrogen maser clocks at the Hartebeesthoek Radio Astronomy Observatory. *South African Journal of Geomatics*, **5**(3). November 2016. DOI: 10.4314/sajg.v5i3.5

NASA Goddard Space Flight Center (GSFC). (1993). VLBI System documentation: Mark IV field system. *NASA/Goddard Space Flight center. Space Geodesy Project.* Ver. 8.2. September 1, 1993. https://www.naic.edu/~astro/aovlbi/fsdoc/fshome.html [Accessed 29 August 2022].

Niell, A., Whitney, A., Petrachenko, B., Schlüter, W., Vandenberg, N., Hase, H., Koyama, Y., Ma, C., Schuh, H. & Tuccari, G. (2005). VLBI2010: Current and future requirements for geodetic VLBI systems. *Report of Working Group 3 to the IVS Directing Board.* IVS Memorandum 2006-008v01.

Niell, A., Whitney, A., Petrachenko, B., Schlüter, W., Vandenberg, N., Hase, H., Koyama, Y., Ma, C., Schuh, H. & Tuccari, G. (2006). VLBI2010: current and future requirements of geodetic VLBI systems. *International VLBI Service for Geodesy and Astrometry 2005 Annual Report, NASA/TP-2006-214136*. 13-40 pp. D. Behrend and K. Baver (eds.).

Nilsson, T., Karbon, M., Mora-Diaz, J.A., Raposo-Pulido, V. Soja, B., Heinkelmann, R. & Schuh, H. (2015). Antenna axis offsets estimated in VLBI data analysis. *Proceedings of the 22nd European VLBI Group for Geodesy and Astrometry Working Meeting*. Ponta Delgada, Azores. 18-21 May 2015. 177-180 pp. https://www.oso.chalmers.se/evga/22_EVGA_2015_Ponta_Delgada.pdf [Accessed 29 August 2022].

Nilsson, T., Mora-Diaz, J.A., Raposo-Pulido, V., Heinkelmann, R., Karbon, M., Liu, L., Lu, C., Soja, B., Xu, M. & Schuh, H. (2017). Antenna axis offsets and their impact on VLBI derived reference frames. *REFAG 2014 Proceedings of the IAG Commission 1 Symposium*. Kirchberg, Luxembourg, October 13-17, 2014. IAG Symposia Springer. T. van Dam (ed.). DOI: 10.1007/1345_2015_126

Nothnagel, A., Pilhatsch, M. & Haas, R. (1995). Investigations of thermal height changes of geodetic VLBI radio telescopes. *Proceedings of the 10th working meeting on European VLBI for geodesy and astrometry*, 121-133 pp. R. Lanotte and G. Bianco (eds.).

Nothnagel, A. (2009). Conventions on thermal expansion modelling of radio telescopes for geodetic and astrometric VLBI. *Journal of Geodesy*, **83**(9):787-792 pp. DOI: 10.1007/s00190-008-0284-z

Nothnagel, A., Artz, T., Behrend, D. & Malkin, Z. (2017). International VLBI Service for Geodesy and Astrometry – Delivering high-quality products and embarking on observations of the next generation. *Journal of Geodesy*, **91**(7): 711-721 pp. July 2017. DOI: 10.1007/s00190-016-0950-5

Nothnagel, A. (2018). Elements of Geodetic and Astrometric Very Long Baseline Interferometry. *Handbuch der Geodasie.* Springer Reference Naturwissenschaften Book Series. Heidelberg, Berlin: Springer Spektrum.1-58 pp. W. Freeden and R. Rummel (eds.). DOI: 10.1007/978-3-662-46900-2_110-1

Petrachenko, B., Niell, A., Behrend, D., Corey, B., Böhm, J., Charlot, P., Collioud, A., Gipson, J., Haas, R., Hobiger, T., Koyama, Y., MacMillan, D., Malkin, Z., Nilsson, T., Pany, A., Tuccari, G., Whitney, A. & Wresnik, J. (2009). Design aspects of the VLBI2010 system. *International VLBI Service for Geodesy and Astrometry 2008 Annual Report, NASA/TP-2009-214183*. D. Behrend and K. Baver (eds.).

Petrachenko, B., Behrend, D., Gipson, J., Hase, H., Ma, C., MacMillan, D., Niell, A., Nothnagel, A. & Zhang, X. (2014). VGOS observing plan. *IVS 2014 General Meeting Proceedings*. Beijing: Science Press. 17-19 pp. D. Behrend, K. Baver and L. Armstrong (eds.).

Petrachenko, B. (2015). VGOS operational readiness. *Proceedings of the 22nd European VLBI Group for Geodesy and Astrometry Working Meeting.* Ponta Delgada, Azores. May 18-21, 2015.1-5 pp.

Plag, H.-P., Altamimi, Z., Bettadpur, S., Beutler, G., Beyerle, G., Cazenave, A., Crossley, D., Donnellan, A., Forsberg, R., Gross, R., Hinderer, J., Komjathy, A., Ma, C., Mannucci, A.J., Noll, C., Nothnagel, A., Pavlis, E.C., Pearlman, M., Poli, P., Schreiber, U., Senior, K., Woodworth, P. L., Zerbini, S. & Zuffada, C. (2009). The future Global Geodetic Observing System. *Global Geodetic Observing System*. Berlin, Heidelberg: Springer, 237-272 pp. H.-P. Plag and M. Pearlman (eds.). DOI:10.1007/978-3-642-02687-4_2

Plank, L. (2014). *Sibling radio telescopes for geodesy: optimising the use of co-located VLBI telescopes in the southern hemisphere.* Proposal. University of Tasmania, 2014:1-20 pp.

Plank, L., Lovell, J.E.J., McCallum J.N., Mayer, D., Reynolds, C., Quick, J.F.H., Weston, S., Titov, O., Shabala, S.S., Böhm, J., Natusch, T., Nickola, M. & Gulyaev, S. (2017). The AUSTRAL VLBI observing program. *Journal of Geodesy*, **91**. 803-817 pp. https://link.springer.com/article/10.1007/s00190-016-0949-y [Accessed 29 August 2022].

Rothacher, M., Beutler, G., Behrend, D., Donnellan, A., Hinderer, J., Ma, C., Noll, C., Oberst, J., Pearlman, M., Plag, H.-P., Richter, B., Schöne, T., Tavernier, G. & Woodworth, P. L. (2009). The future Global Geodetic Observing System. *Global Geodetic Observing System*. Berlin, Heidelberg: Springer, 237-272 pp. H.-P. Plag and M. Pearlman (eds.). DOI:10.1007/978-3-642-02687-4_9

Sarti, P. & Abbondanza, C. (2010). Gravitational Deformations of VLBI Telescopes and Their Impact on Geodetic Results. *IVS Newsletter*. December 28, 2010. 2-3 pp. IVS Coordinating Center, NASA GSFC.

Sarti, P., Abbondanza, C., Petrov, L. & Negusini, M. (2011). Height bias and scale effect induced by antenna gravitational deformations in geodetic VLBI data analysis. *Journal of Geodesy*, **85**(1):1-8 pp. DOI:10.1007/s00190-010-0410-6

Schartner, M. & Böhm, J. (2019). VieSched++: a new VLBI scheduling software for geodesy and astrometry. *Publications of the Astronomical Society of the Pacific*, **131**: 084501. DOI: 10.1088/1538-3873/ab1820

Schuh, H. & Behrend, D. (2012). VLBI: A fascinating technique for geodesy and astrometry. *Journal of Geodynamics*, **61**. 68-80 pp. DOI: 10.1016/j.jog.2012.07.007

Schuh, H. & Böhm, J. (2013). Very Long Baseline Interferometry for Geodesy and Astrometry. *Sciences of Geodesy II, Innovations and Future Development.* Heidelberg: Springer-Verlag, 339-376 pp. G, Xu. (ed.). DOI: 10.1007/978-3-642-28000-9_7

Sovers, O.J., Fanselow, J.L. & Jacobs, C.S. (1998) Astrometry and geodesy with radio interferometry: experiments, models, results. *Review of Modern Physics*, **70**:1393-1454 pp. DOI:10.1103/RevModPhys.70.1393.

Takahashi, F., Kondo, T., Takahashi, Y. & Koyama, Y. (2000). *Very Long Baseline Interferometry*. Tokyo, Japan: Ohmsha, Ltd. 139-147 pp.

Teke, K., Nilsson, T. & Böhm, J. (2013). Troposphere delays from space geodetic techniques, water vapor radiometers, and numerical weather models over a series of continuous VLBI campaigns. *Journal of Geodesy*, **87**: 981-1001 pp. DOI:10.1007/s00190-013-0662-z

United Nations General Assembly Resolution 69/266. (2015). A global geodetic reference frame for sustainable development. https://ggim.un.org/documents/A_RES_69_266_E.pdf [Accessed 29 August 2022].

Van Zyl, P. (2016). Radio emission from gamma-ray flare sources discovered by Fermi-Lat. *A dissertation submitted to the Faculty of Science, University of the Witwatersrand, Johannesburg*. In fulfilment of the requirements for the degree of Master of Science.

Ware, R.H., Avery, S.K., Fulker, D.W., Stein, S.A., Anderson, D.N., Kuettner, J.P., Clark, R.D., Droegemeier, K.K., Minster, J.B. & Sorooshian, S. (2000). SuomiNet: A real-time national GPS network for atmospheric research and education. *Bulletin of the American Meteorology Society*, **81**, 677-694 pp.

Wijaya, D.D., Böhm, J., Karbon, M., Krásná, H. & Schuh, H. (2013). Atmospheric pressure loading. *Atmospheric effects in Space Geodesy*. Berlin, Heidelberg: Springer-Verlag. J. Böhm and H. Schuh (eds.). DOI:10.1007/978-3-642-36932-2_4

WMO. (2018). WMO Guide to Meteorological Instruments and Methods of Observation. *CIMO Guide, WMO-No. 8.* https://library.wmo.int/index.php?id=12407&lvl=notice_display#.YRuBwM-xWCh [Accessed 29 August 2022].

Wresnik, J., Böhm, J., Haas, R. & Schuh, H. (2007). Thermal deformation of radio telescopes Onsala and Wettzell. *International VLBI Service for Geodesy and Astrometry 2006 General Meeting proceedings.* 300-303 pp. NASA/CP-2006-214140. D. Behrend & K. Baver (eds.).

APPENDIX A

A.1 WMO CIMO GUIDELINES

Table A.1 WMO CIMO guidelines to be followed with the installation of HartRAO meteorological equipment.

Parameter	WMO CIMO standard for siting and exposure of meteorological equipment
1. General	- level piece of ground; no steeply sloping ground in vicinity; not in hollow - ground cover: short grass or surface representative of locality - away from trees, buildings, walls or other obstructions - all instruments preferably on same site - possible "same site" exceptions: wind (due to height), solar radiation (if trees or buildings obstruct horizon significantly) - obstacle: • effective angular width > 10° • tall, thin obstacles with effective angular width < 10° and height > 8 m • cluster of tall, thin obstacles will have similar effect to single wider obstacle • changes of altitude in landscape not representative of landscape - station should provide measurements that are representative of surrounding area - topography is representative of surrounding area - electrical interference: electronic sensors to be shielded; keep away from sources of strong magnetic fields such as transformers, computers, radar, *etc*. - instruments and equipment should be set out in a definite order, in several rows or lines
2. Temperature:	- installation height = 1.25 - 2 m (never < 1.25 m) - not on top of buildings - representative of free air conditions surrounding station, freely exposed to sunshine and wind

Table A.1 (Continued)

	- level ground (slope < 19°); avoid sites on steep slopes or in hollows - ground cover: natural ground, short grass, no surrounding vegetation within 100 m - avoid shading by nearby obstacles - not shielded by, or close to, trees, buildings and other obstructions - no unnatural surfaces or neighbouring artificial surfaces (concrete, asphalt, buildings) - > 100 m away from heat sources: reflective surfaces (*e.g.* buildings, concrete surfaces) and water or moisture sources (*e.g.* ponds, lakes, irrigated areas) (unless water sources representative or significant in region) - no artificial heating or reflective source
3. Humidity:	- installation height = 1.25 - 2 m (never < 1.25 m) - avoid shading by nearby obstacles - > 100 m away from heat sources: reflective surfaces (*e.g.* buildings, concrete - surfaces) and water or moisture sources (*e.g.* ponds, lakes, irrigated areas) (unless water sources representative or significant for region) - protection from direct solar radiation, atmospheric contaminants, rain and wind
4. Pressure:	- installation height = 1.2 - 2.0 m above ground level - solid, non-vibrating mounting - draught-free environment; prevent any artificial wind impact, gusty wind - shielded from direct sunshine; not affected by radiation - kept at a constant temperature; not affected by temperature variations - no strong magnetic fields
5. Wind:	- installation height = 10 m above ground surface - if on top of a building, raise at least one building width above top - keep away from local obstructions - numerous obstacles higher than 2 m: place 10 m above average height of obstacles - level and on open ground; obstacles situated at minimum distance equal to at least 10x their height; when distance < 20x height of obstacle, measured value can be erroneous by up to 25%; when distance = 10x height of obstacle, measured value can indicate opposite direction - observed wind representative of wind over area of at least few kilometres - homogeneous surface cover
6. Rain:	- installation height: local requirements; heights level with local ground surface (0 m), thereafter 0.5 - 1.5 m commonly used

Table A.1 (Continued

	- objects (including fence): not closer to gauge than distance of 2x their height above gauge orifice, preferably 4x times height - anything that subtends more than 10° of a 360° degree circle around gauge must be 4x height difference away - obstacle should not occupy more than 10 m - obtain sample representative of true amount falling over area - avoid sites on slope or roof of building - ensure minimal wind disturbances from nearby structures - protect against wind; use ground-level gauge or wind screen at same height as orifice of gauge - non-splashing ground surface; short grass, gravel or shingle; avoid hard, flat surfaces, such as concrete, to prevent excessive insplashing - vegetation should be kept at same level as gauge orifice
7. Solar radiation:	- installation height = 1.5 m or unobstructed height - mounted on rigid, stable stand/base plate to avoid shocks, vibrations, heating due to sunshine and movement due to wind - flat roof or stand placed some distance from buildings or other obstructions - keep plane of sensor horizontal - field of view of pyranometer shall be 180° - no obstruction above plane of sensing element - no obstacles in line of sight between sun and instrument during day - no obstructions that may shadow it at any time of the year; nothing should shade instrument height if sun is above 3° on any day of year - no non-shading but reflecting obstacles (albedo > 0.5) with angular height > 5° and total angular width > 10° - not close to light-coloured walls or other objects likely to reflect solar energy onto it - avoid close obstacles (non-reflecting obstacles below the visible horizon can be neglected) - anything taller than 4 m must be 10 m its height away - no exposure to artificial radiation sources

A.2 JUPITER GAIN CALIBRATION FOCUS SETTING CURVES

A.2.1 First set of sub-reflector focus offset gain curve observations at 22 GHz – 2020d224-225 (11-12 August 2020)

In Figure A.2.1a, for the focus offset of -0.5, the peak fit location for the half-power South left circular polarisation (HPS LCP) scan at an elevation of 26° with Jupiter rising could not be accurately established and is therefore absent from the figure.

In Figure A.2.1b, for the focus offset of -1.0, the peak fit locations for the Half Power North left circular polarisation (HPN LCP) and half-power South right circular polarisation (HPS RCP) scans at an elevation of 28° with Jupiter setting could not be accurately established and are therefore absent from the figure.

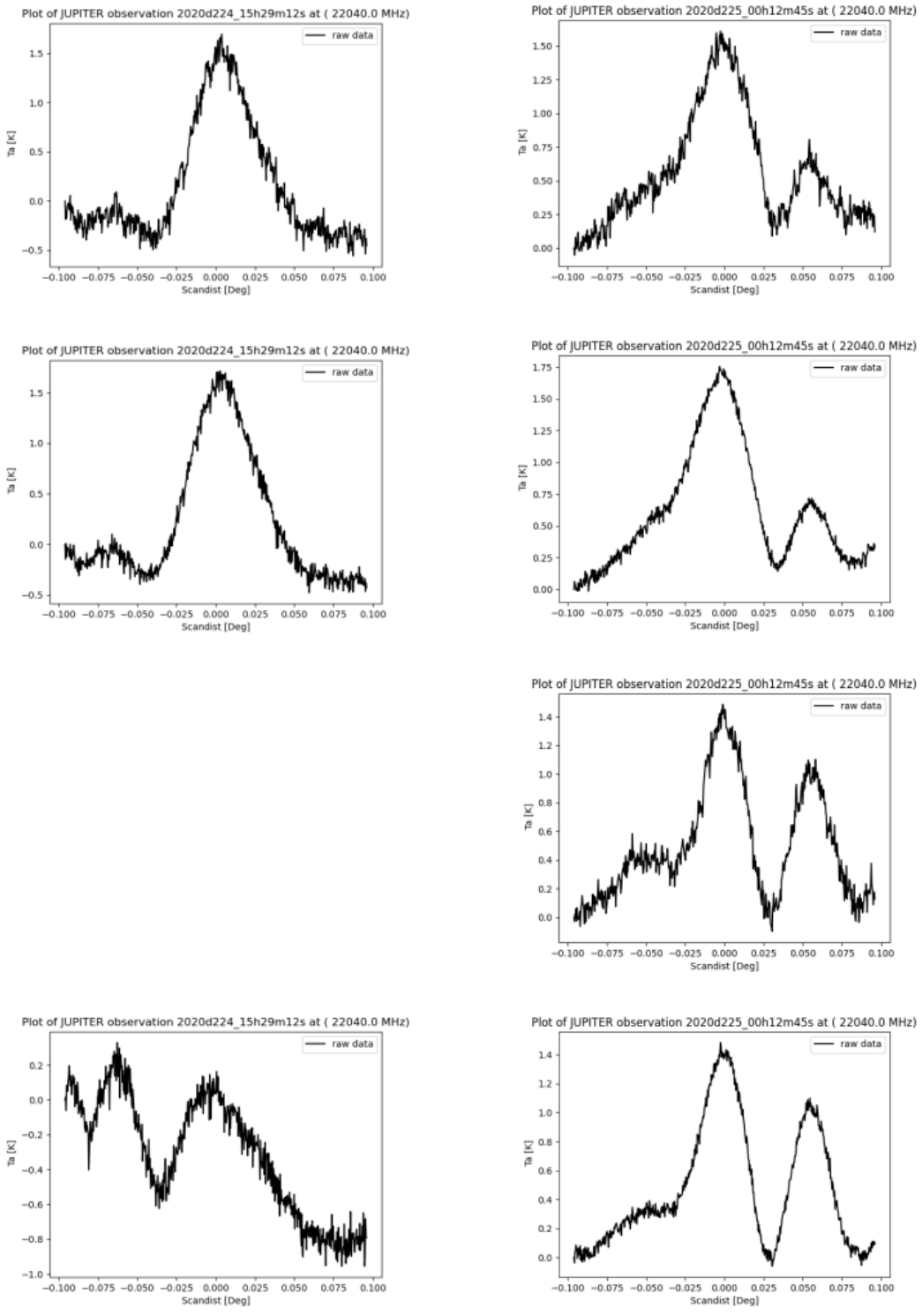

Figure A.2.1a. Raw plots – 2020d224-225 – varying sub-reflector focus settings – focus setting = -0.5 – left, top to bottom: HPN L&RCP and HPS RCP scans at elevation of 26° with Jupiter rising; right, top to bottom: HPN L&RCP and HPS L&RCP scans at elevation of 34° with Jupiter setting.

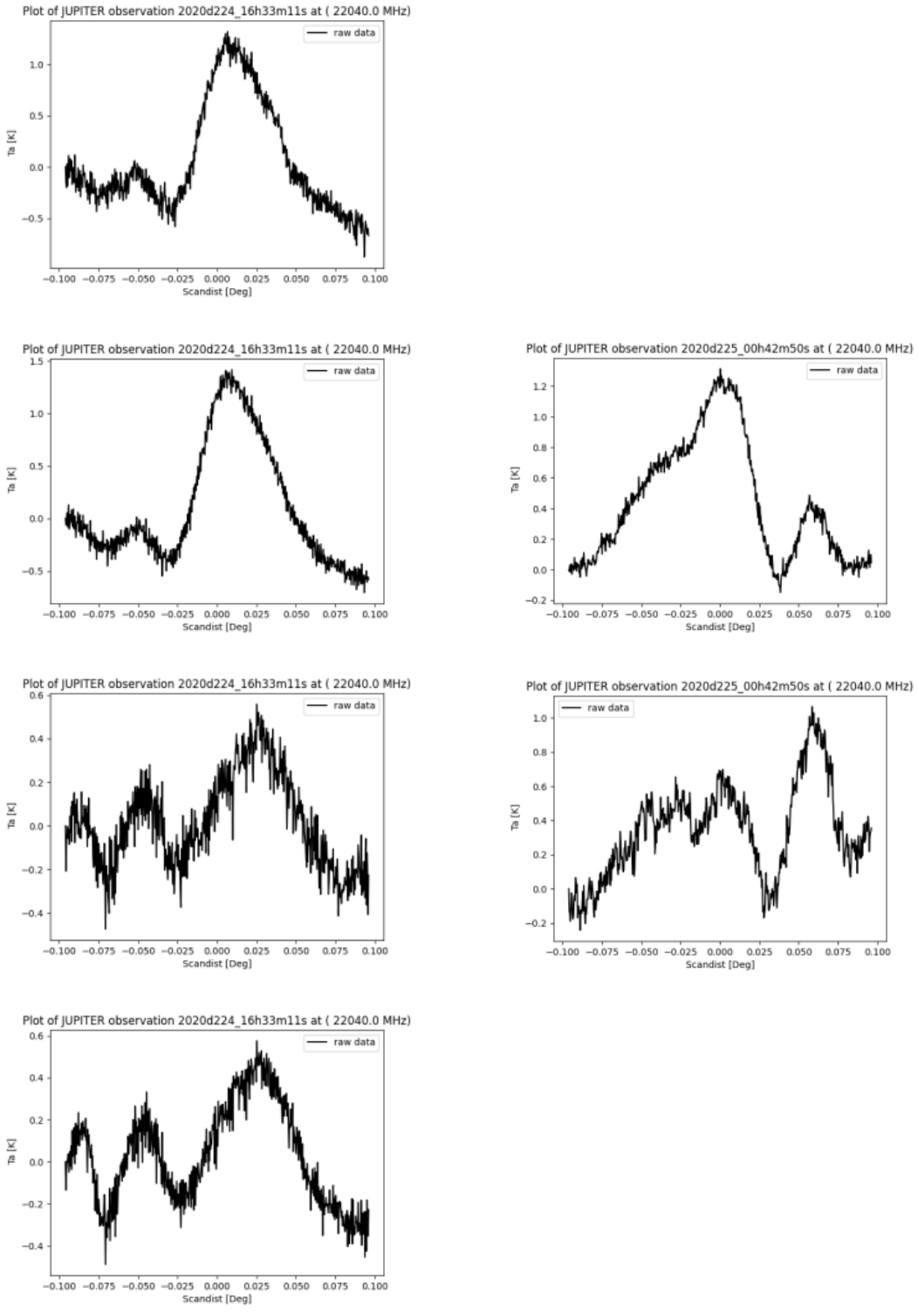

Figure A.2.1b. Raw plots – 2020d224-225 – varying sub-reflector focus settings – focus setting = -1.0 – left, top to bottom: HPN L&RCP and HPS L&RCP scans at elevation of 41° with Jupiter rising; right, top to bottom: HPN RCP and HPS LCP scans at elevation of 28° with Jupiter setting.

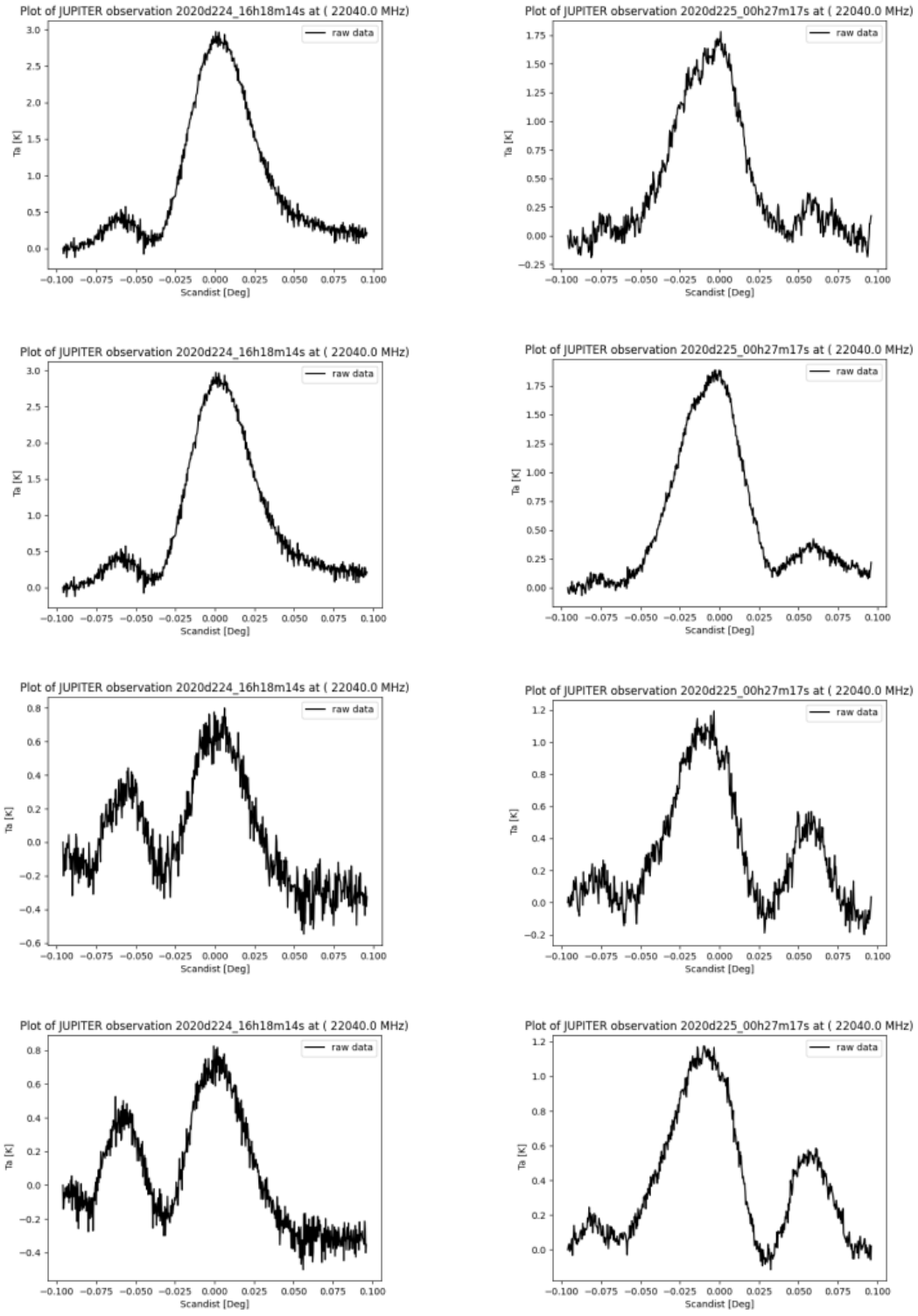

Figure A.2.1c. Raw plots – 2020d224-225 – varying sub-reflector focus settings – focus setting = +1.0 – left, top to bottom: HPN L&RCP and HPS L&RCP scans at elevation of 37° with Jupiter rising; right, top to bottom: HPN L&RCP and HPS L&RCP scans at elevation of 32° with Jupiter setting.

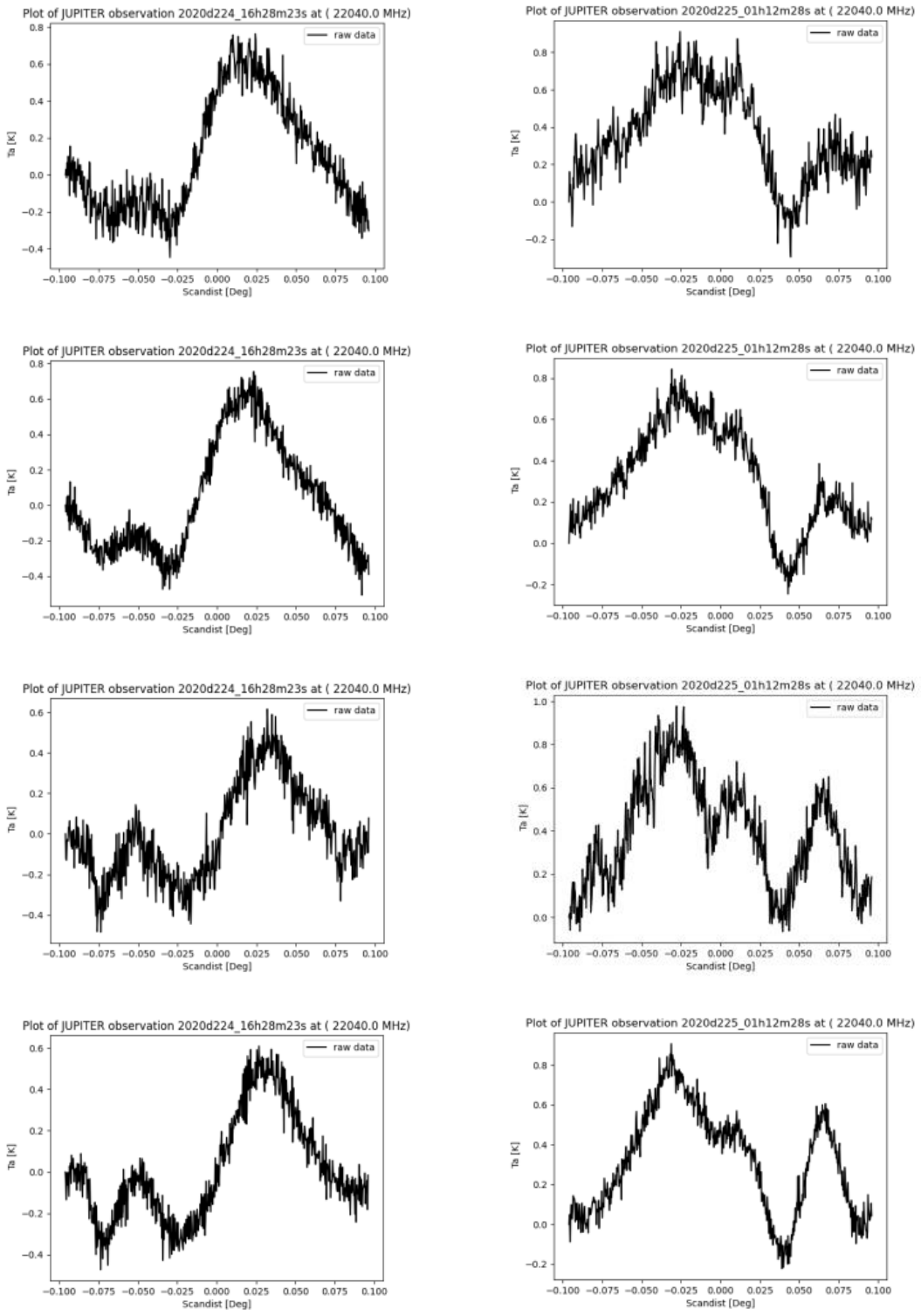

Figure A.2.1d. Raw plots – 2020d224-225 – varying sub-reflector focus settings – focus setting = -1.5 – left, top to bottom: HPN L&RCP and HPS L&RCP scans at elevation of 39° with Jupiter rising; right, top to bottom: HPN L&RCP and HPS L&RCP scans at elevation of 22° with Jupiter setting.

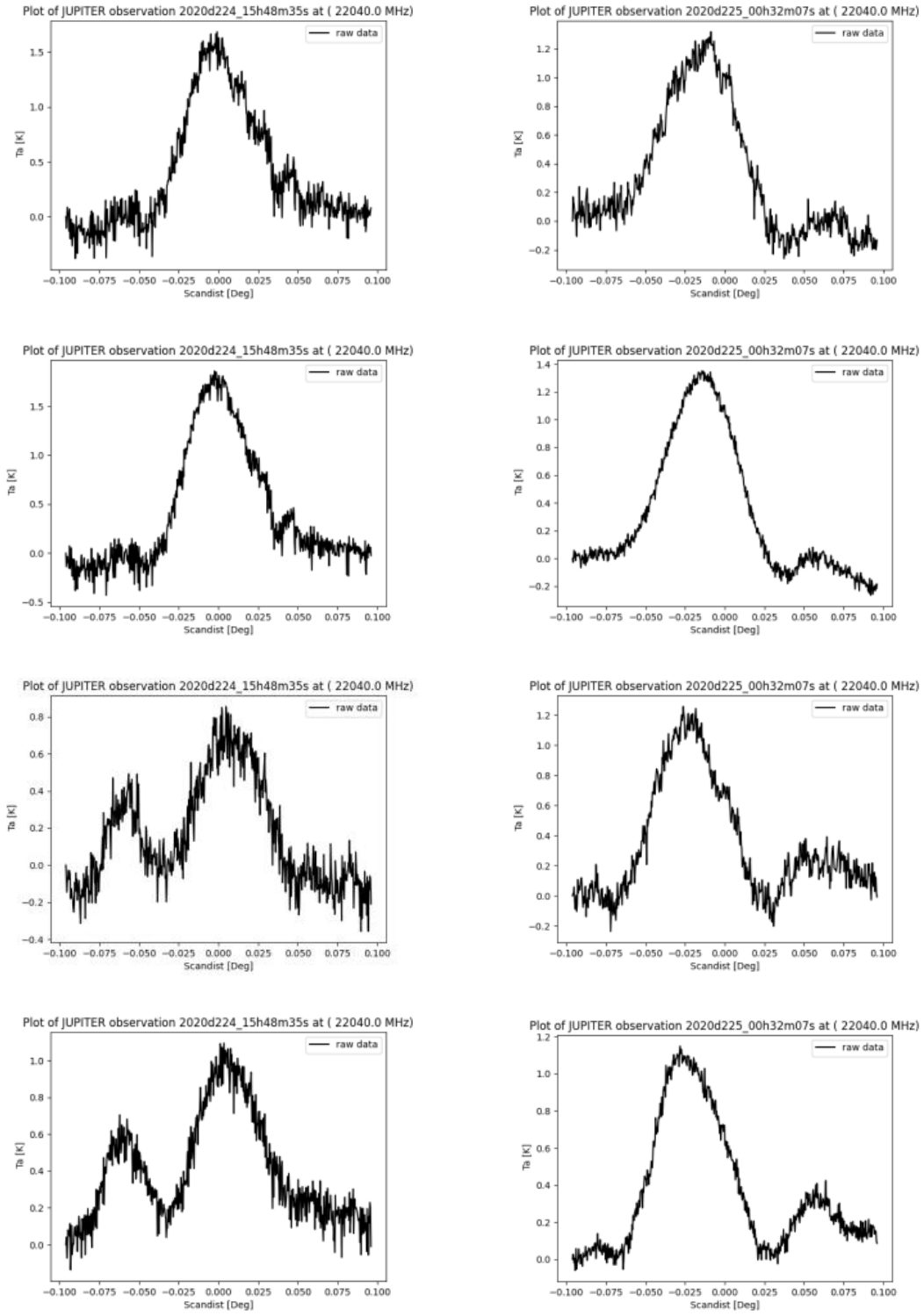

Figure A.2.1e. Raw plots – 2020d224-225 – varying sub-reflector focus settings – focus setting = +1.5 – scans at elevation of 31° – left, top to bottom: HPN L&RCP and HPS L&RCP scans with Jupiter rising; right, top to bottom: HPN L&RCP and HPS L&RCP scans with Jupiter setting.

A.2.2 Second set of sub-reflector focus offset gain curve observations at 22 GHz – 2021d117 (27 April 2021)

In Figure A.2.2a, for the focus offset of -0.25, the peak fit location for the HPN LCP scan at an elevation of 19° with Jupiter setting could not be accurately established and is therefore absent from the figure.

In Figure A.2.2c, for the focus offset of -0.5, the peak fit locations for the HPN LCP scan at an elevation of 21° with Jupiter setting could not be accurately established and is therefore absent from the figure.

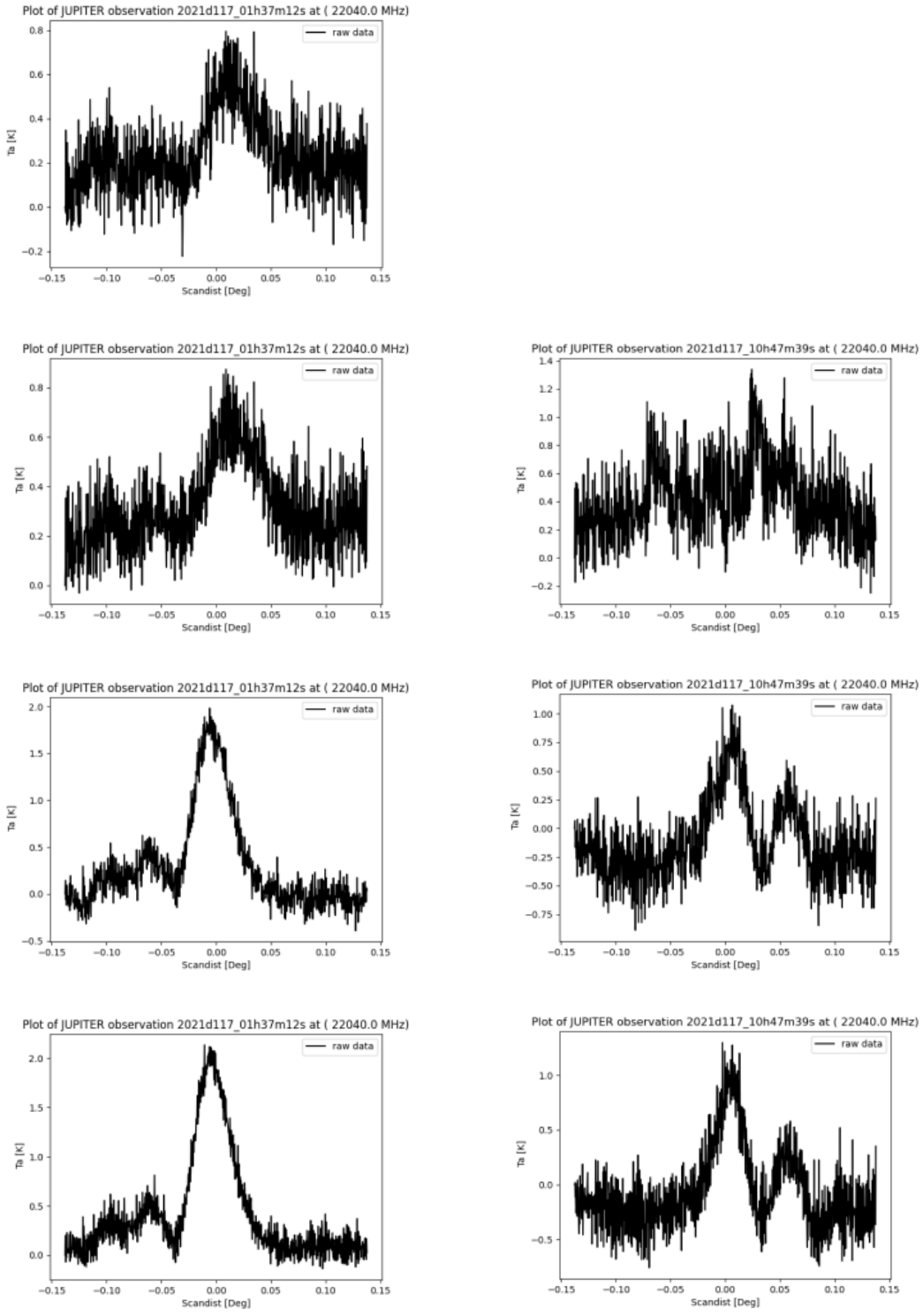

Figure A.2.2a. Raw plots – 2021d117 – varying sub-reflector focus settings – focus setting = -0.25 – left, top to bottom: HPN L&RCP and HPS L&RCP scans at elevation of 29° with Jupiter rising; right, top to bottom: HPN RCP and HPS L&RCP scans at elevation of 19° with Jupiter setting.

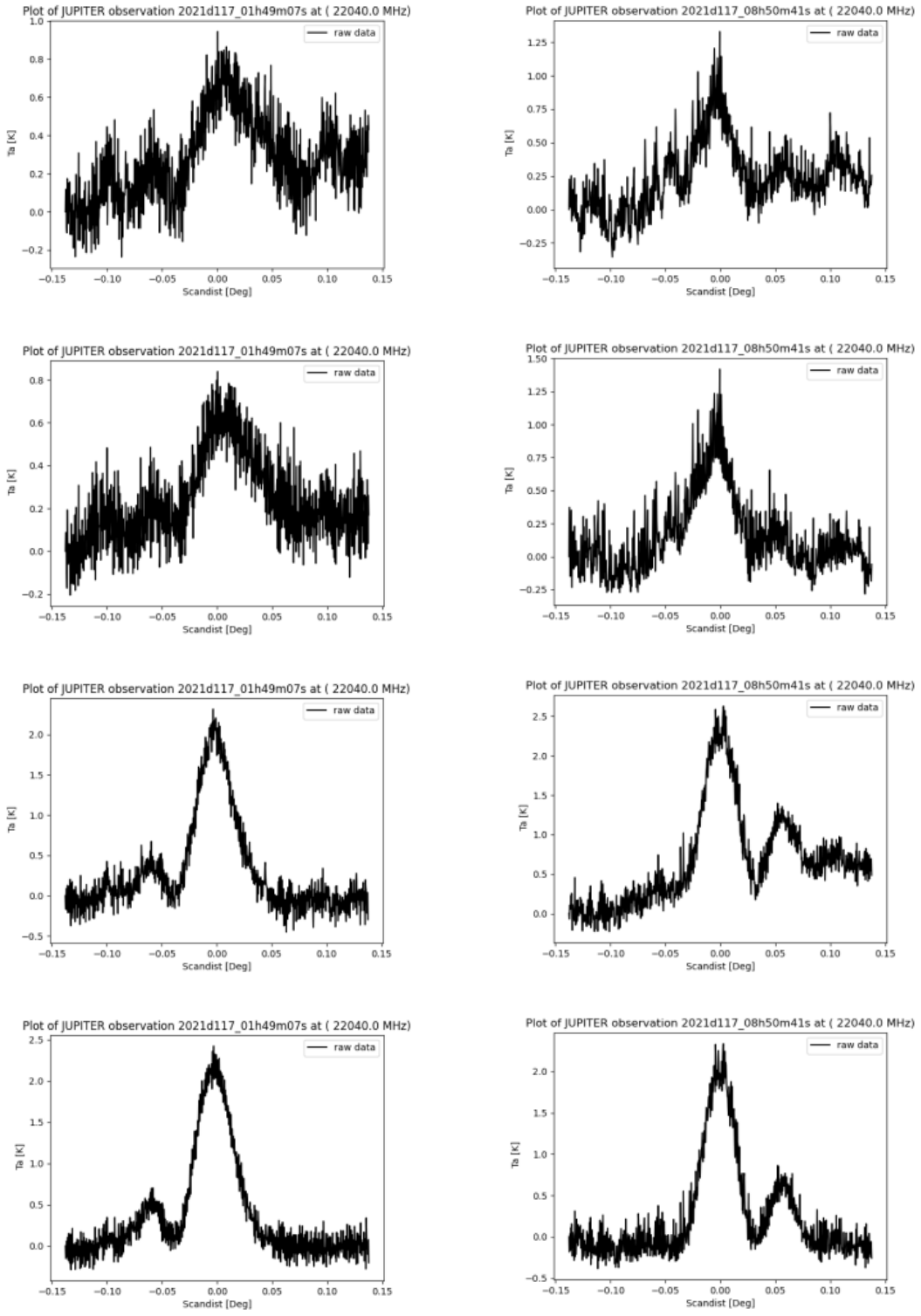

Figure A.2.2b. Raw plots – 2021d117 – varying sub-reflector focus settings – focus setting = +0.25 – left, top to bottom: HPN L&RCP and HPS L&RCP scans at elevation of 32° with Jupiter rising; right, top to bottom: HPN RCP and HPS L&RCP scans at elevation of 46° with Jupiter setting.

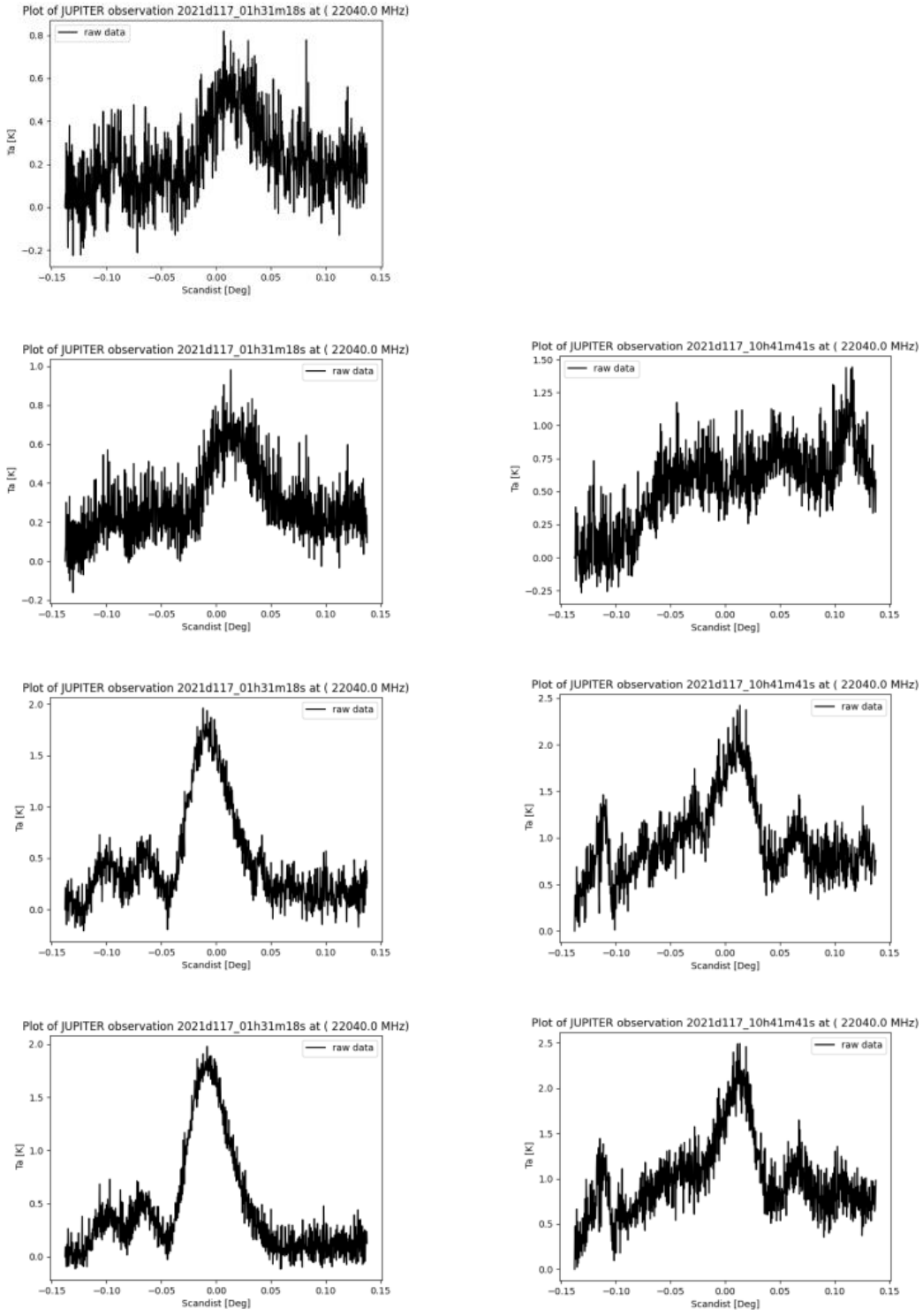

Figure A.2.2c. Raw plots – 2021d117 – varying sub-reflector focus settings – focus setting = -0.5 – left, top to bottom: HPN L&RCP and HPS L&RCP scans at elevation of 28° with Jupiter rising; right, top to bottom: HPN RCP and HPS L&RCP scans at elevation of 21° with Jupiter setting.

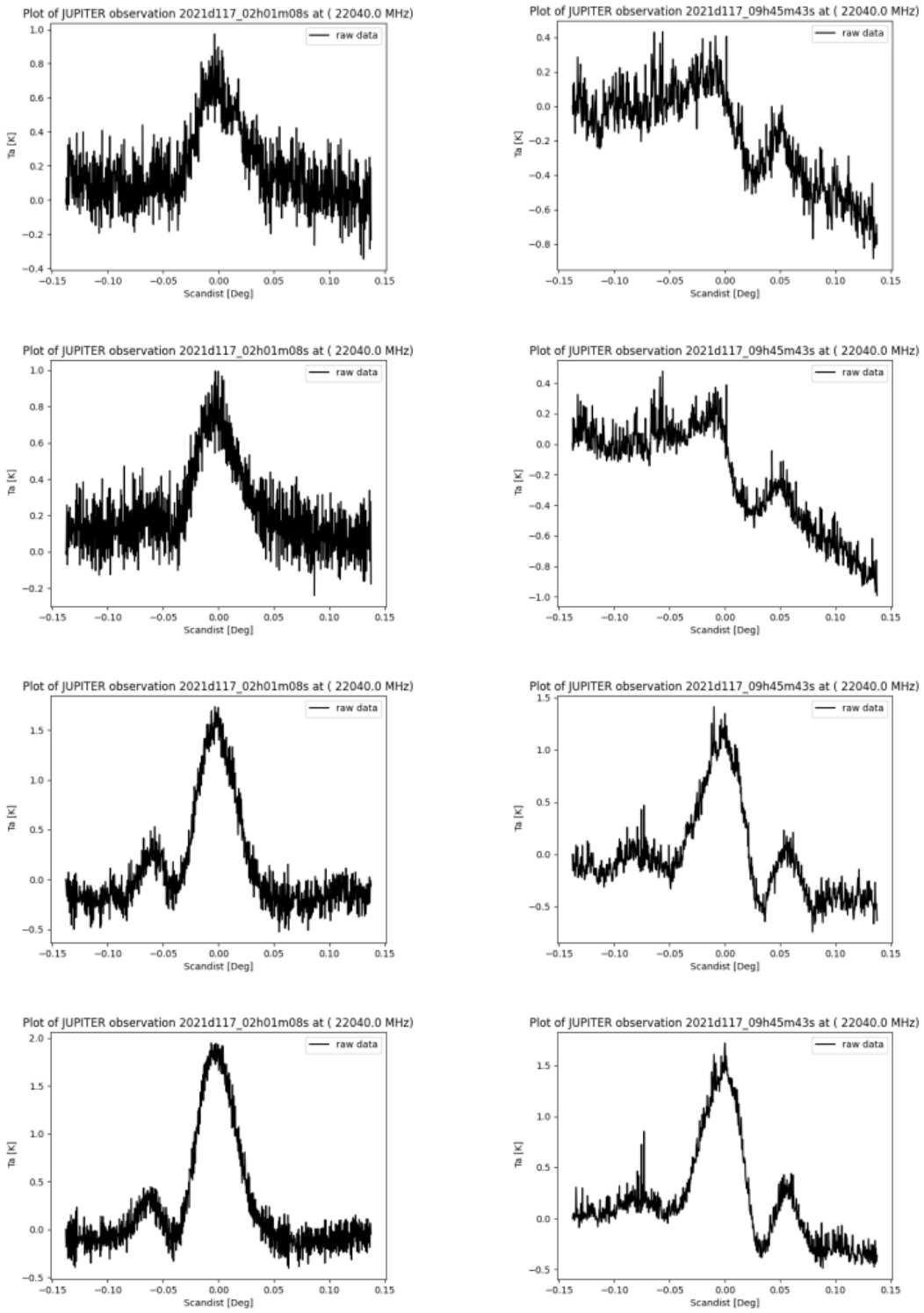

Figure A.2.2d. Raw plots – 2021d117 – varying sub-reflector focus settings – focus setting = +0.75 – left, top to bottom: HPN L&RCP and HPS L&RCP scans at elevation of 35° with Jupiter rising; right, top to bottom: HPN L&RCP and HPS L&RCP scans at elevation of 33° with Jupiter setting.

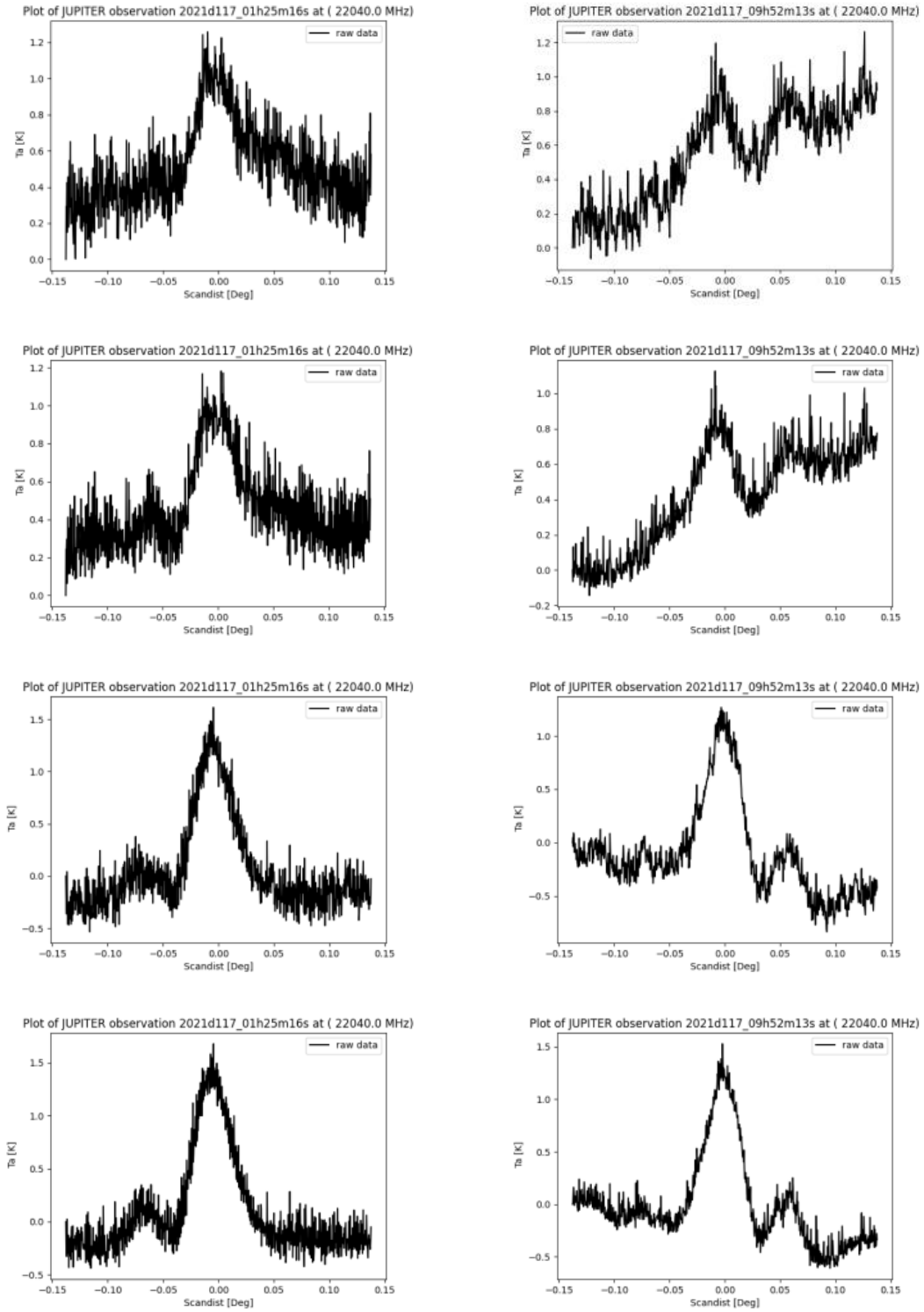

Figure A.2.2e. Raw plots – 2021d117 – varying sub-reflector focus settings – focus setting = +1.0 – left, top to bottom: HPN L&RCP and HPS L&RCP scans at elevation of 27° with Jupiter rising; right, top to bottom: HPN L&RCP and HPS L&RCP scans at elevation of 32° with Jupiter setting.